

# Modelling and Control of Three-Way Catalytic Converters



Diss. ETH No. 16018

# **Modelling and Control of Three-Way Catalytic Converters**

A dissertation submitted to the  
**SWISS FEDERAL INSTITUTE OF TECHNOLOGY  
ZURICH**

for the degree of  
**Doctor of Technical Sciences**

presented by  
Theophil Sebastian Auckenthaler  
Dipl. Masch.-Ing. ETH  
born 21 March 1970  
citizen of Pully, VD and Zürich, ZH

accepted on the recommendation of  
Prof. Dr. H.P. Geering, examiner  
Prof. Dr. A. Baiker, co-examiner  
Prof. Dr. Ph. Rudolf von Rohr, co-examiner

2005

contact: [theophil.auckenthaler@alumni.ethz.ch](mailto:theophil.auckenthaler@alumni.ethz.ch)

ISBN 3-906483-08-8

IMRT Press  
c/o Institut für Mess- und Regeltechnik  
ETH Zentrum  
8092 Zürich  
Schweiz

07/2005

“Nothing shocks me. I’m a scientist.”  
(Harrison Ford, as Indiana Jones)

*To Anna-Lena, Benjamin and Julian*



# Acknowledgements

This thesis was written at the Measurement and Control Laboratory of the Swiss Federal Institute of Technology (ETH) in Zürich from 1999 to 2005. It was carried out with the support of the Robert Bosch GmbH, Germany.

I would like to thank my supervisor, Prof. Dr. H.P. Geering for his support, trust, and for generously overlooking minor deficiencies in the planning of the schedule during the whole project.

Furthermore I would like to thank Prof. Dr. A. Baiker and Prof. Dr. Ph. Rudolf von Rohr for accepting to be my co-examiners.

Very special thanks go to Dr. Chris Onder for his immense support, the many fruitful discussions and inputs during the entire project.

I would like to thank everybody of the Robert Bosch GmbH, who contributed to the project, especially E. Schnaibel, Dr. J. Frauhammer and Dr. R. Hotzel for their patience, the many rewarding discussions, for introducing me to the secrets of engine control in the real world, and last but not least, for the unbu-reaucratic and generous support during the entire project.

Many thanks go to Dr. M. Votsmeier of the Umicore AG for all the discussions, his support and the generous contribution of the five TRI/X5 catalytic converters.

Special thanks go to the technical staff of the laboratory, Dani Matter, Jan Prikryl, Oskar Brachs and of course Hansueli Honegger, who contributed, apart from his support, a lot to the great atmosphere and the fun in the catacombs of the laboratory.

It was always a big pleasure to meet my coworkers in the field, Dr. Mario Balenovic and Dr. James Peyton-Jones, who contributed a lot to the project with their openness, the many fruitful discussions, and feedbacks.

For their search for the many errors and typos in the thesis I would like to thank Roman Möller, Brigitte Rohrbach, Delia Ajtay, and of course Jenny Johansson and Mikaela Waller of the Linköping University, Sweden.

Many thanks go to Prof. Dr. Eigenberger of the Institute for Chemical Processes Engineering of the University of Stuttgart for providing the PDEX solver.

In the context of this thesis, I had to learn a lot about chemical engineering. I would like to thank Dr. Esther Hammerschmied and Dr. Stefan Menzi for

opening some doors to the cryptic world of chemical engineering.

The time at the Measurement and Control Laboratory was particularly funny and entertaining thanks to the gang of the F-floor, especially Dr. Marzio Locatelli, Dr. Michael Simons, and Dr. Simon Frei. It was their contribution, which lead to the solution of many open questions vital for the welfare of mankind. These range from the development of the OB-Space and the hierarchy in the Swiss Army to the fine details regarding the formulation of high-performance lubricants.

The period at the Measurement and Control Laboratory was both instructive and entertaining. I would like to thank everybody at the IMRT for the great atmosphere, the good humour, support, and cooperation during the last five years.

The education of a student with sometimes extravagant ideas about the planning of his career can be costly and nerve wracking. I would like to thank my parents who spared no effort to make my education possible.

Last but not least, I would like to express my sincerest gratitude to my wife Anna-Lena for all her constant support, her care, her encouragement, and patience, especially during the last part of the project.



# Abstract

Three-Way Catalytic Converters (TWC) have been in use for the exhaust gas aftertreatment of spark-ignited engines for more than two decades now. During this period, emission limits enforced by legislation in Europe and elsewhere have been roughly cut in half every five years. In addition to these limits, regulations were introduced, which make the persistent monitoring and the indication of malfunctions of the exhaust gas aftertreatment system including the sensors compulsory.

In order to meet the stringent regulations, various concepts have been developed which not only aim at the stoichiometric control of the raw exhaust gas entering the TWC, but also at internal states of this device, usually the oxygen storage level. Often, the stored oxygen is estimated from the information provided by  $\lambda$  sensors which are located upstream and downstream of the TWC. Problems arise frequently because the sensor signals are considerably distorted by hydrogen. The hydrogen concentration of the raw exhaust gas from the engine can be predicted quite accurately using static functions or maps. However, its production and/or oxidation in the TWC is a highly dynamic process, which changes both with the engine operation point and over the TWC's lifetime.

In this thesis, an observer-based control and diagnosis concept has been developed, which not only accounts for the oxygen storage dynamics of the TWC, but also predicts the hydrogen concentration in the exhaust gas and its distortion of the  $\lambda$  sensor signals.

In order to identify the mechanisms driving the composition of the most important exhaust gas species in terms of legislation and sensor signal distortion, a detailed 1-D model of a TWC has been derived, which reflects the dynamical behaviour during low-frequency  $\lambda$  excitations very well. It has been found that during rich engine operation, i. e., with excess fuel, the TWC is deactivated by the adsorption of hydrocarbons. This leads to a significant decrease of the water-gas shift and steam-reforming activities, which in turn changes the ratio between hydrogen, carbon monoxide, and hydrocarbons, independently of the air-to-fuel ratio. This effect is more pronounced with an increased ageing level of the TWC.

The influence of the exhaust gas composition on the response of a switch-type  $\lambda$  sensor, which is usually located downstream, has been investigated by

means of a detailed process model, including diffusion effects and reaction kinetics both on the electrodes and the electrolyte. It has been found that under rich engine operation, the sensor response is mainly driven by the chemical potential of the hydrogen and carbon monoxide oxidation, rather than by a shortage of oxygen in the exhaust.

From the process models, a simplified control-oriented model for the TWC and the  $\lambda$  sensors has been deduced, which accounts for the deactivation and oxygen storage dynamics, the temperatures, and the concentrations of oxygen, carbon monoxide, and hydrogen with their influence on the switch-type  $\lambda$  sensor. The model very well reflects the behaviour of both the TWC and the sensor in a wide range of operating points and ageing levels. A procedure has been developed which allows an automated calibration of the model using measurements obtained from an engine with standard production-type sensor equipment.

The control-oriented model has been incorporated in an extended Kalman filter. This filter allows the online estimation of the oxygen storage levels and the storage capacity, the latter being used for diagnosis purposes. Thus, it is persistently adapted to the changing dynamics of the TWC due to ageing. The filter performed robustly and reliably, such that storage capacities of differently aged converters could be identified within a few hundred seconds with arbitrary initial values.

An LQ regulator with an integrator extension has been designed to control the levels of the stored oxygen. The regulator can be tuned with mainly two parameters, by means of which the balance between the conversion rates of oxidising and reducing species can be adjusted and the signal energy of the control signal can be altered, the latter being closely related to the conversion rates of carbon monoxide and nitric oxide. The controller has been tested in FTP cycles with frequent fuel cut-offs. As compared to a simple  $\lambda$  control concept, the conversion rates of the species limited by legislation were improved and stabilised for ageing levels ranging from considerably aged to fresh. The integrating extension of the controller was demonstrated to master the estimation of the offset of the wide-range  $\lambda$  sensor located in the raw exhaust, which is valuable for the diagnosis of this device.

# Zusammenfassung

Dreiwegekatalysatoren für die Abgasnachbehandlung von Ottomotoren werden nun seit über 20 Jahren eingesetzt. Während dieser Zeit wurden die Emissionsgrenzwerte innerhalb und ausserhalb Europas ungefähr alle fünf Jahre halbiert. Neben den Grenzwerten wurden auch Vorschriften erlassen, welche die permanente Überwachung des Abgasnachbehandlungssystems und die Anzeige allfälliger Fehlfunktionen zwingend erfordern.

Um den strengen Anforderungen gerecht zu werden, wurden Konzepte entwickelt, welche neben der Regelung des Luft/Brennstoffgemisches am Eingang des Katalysators auch dessen interne Zustände, wie zum Beispiel den Füllstand des Sauerstoffspeichers einbeziehen. Normalerweise wird die Menge des gespeicherten Sauerstoffs aus den Lambda-Sensorsignalen vor und nach dem Katalysator berechnet. Oft ergeben sich jedoch Probleme, weil die Sensoren durch den Einfluss des Wasserstoffs stark gestört werden. Die Wasserstoffkonzentration im Rohabgas des Motors kann relativ genau mit statischen Funktionen oder Kennfeldern bestimmt werden. Die Oxidation bzw. Produktion im Katalysator ist jedoch ein dynamischer Prozess, welcher sich sowohl in Abhängigkeit des Motorbetriebspunktes als auch der Katalysatoralterung ändert.

Im Rahmen dieser Abhandlung wurde ein Konzept für die Regelung und Diagnose von Dreiwegekatalysatoren entwickelt, welches nicht nur die Sauerstoffspeicherdynamik einbezieht, sondern auch die Wasserstoffkonzentration und deren Einfluss auf die Lambdasonden berücksichtigt.

Um die Mechanismen zu identifizieren, welche die Zusammensetzung der wichtigsten Abgaskomponenten in Bezug auf die Gesetzgebung und den Einfluss auf die Sensorsignale beeinflussen, wurde ein detailliertes 1-D Modell eines Dreiwegekatalysators hergeleitet, welches das dynamische Verhalten während tieffrequenter Anregungen durch das Luft/Brennstoffverhältnis sehr gut abbildet. Es hat sich herausgestellt, dass der Dreiwegekatalysator durch die Adsorption von Kohlenwasserstoffen beim fetten Betrieb, d.h. mit Brennstoffüberschuss, deaktiviert wird. Dadurch wird die Aktivität der Wasser-Gas-Shift- und der Steam-Reforming-Reaktionen stark reduziert, was einen erheblichen Einfluss auf das Verhältnis zwischen Wasserstoff, Kohlenmonoxid und Kohlenwasserstoffen zur Folge hat. Dieser Effekt verstärkt sich mit zunehmender Alterung des Katalysators.

Der Einfluss der Abgaszusammensetzung auf eine Zweipunkt-Lambdasonde, welche normalerweise hinter dem Katalysator eingesetzt wird, wurde anhand eines detaillierten Prozessmodells untersucht. Dabei wurde die Diffusion sowie die Reaktionskinetik und den Elektroden und am Elektrolyten berücksichtigt. Es zeigte sich, dass das Sensorsignal beim fetten Betrieb hauptsächlich vom chemischen Potential der Wasserstoff- und Kohlenmonoxidoxidation beeinflusst wird und nicht von einer allfälligen Sauerstoffknappheit im Abgas.

Ausgehend von den detaillierten Prozessmodellen wurde ein vereinfachtes Katalysator- und Sondenmodell für Regelzwecke abgeleitet. Dieses berücksichtigt die Deaktivierung, die Sauerstoffspeicherdynamik, die Temperaturen und die Konzentrationen von Sauerstoff, Wasserstoff und Kohlenmonoxid sowie deren Einfluss auf die Spannung der Zweipunkt-Lambdasonde. Das Modell widerspiegelt das Verhalten des Katalysators und der Sensoren sehr gut über einen weiten Bereich von Motorbetriebspunkten und Alterungsstufen. Es wurde ein Verfahren entwickelt, welches eine automatisierte Parametrierung des Modells aus Messungen eines Motors mit Standardsensorik ermöglicht.

Anhand des vereinfachten Modells wurde ein erweitertes Kalmanfilter entwickelt. Dieses schätzt die Füllstände des Sauerstoffspeichers und die Speicherkapazität im laufenden Betrieb. Letztere kann für Diagnosezwecke verwendet werden. Damit wird das Modell ständig an die fortschreitende Alterung des Katalysators angepasst. Das Filter wurde an verschieden stark gealterten Katalysatoren mit unterschiedlichen Startwerten für die Schätzung der Speicherkapazität getestet. Diese konnte in allen Experimenten zuverlässig und robust innerhalb weniger hundert Sekunden ermittelt werden.

Für die Regelung der Sauerstofffüllstände wurde ein LQ-Regulator mit Integrator-Erweiterung ausgelegt. Dieser kann hauptsächlich mit zwei Parametern eingestellt werden. Der erste Parameter beeinflusst die Balancierung zwischen den Konversionsraten reduzierender und oxidierender Gaskomponenten. Mit dem zweiten Parameter wird die Energie des Regelsignals justiert, welche eng mit den Konversionsraten von Stickstoffoxid und Kohlenmonoxid zusammenhängt. Der Regler wurde im FTP-Zyklus mit häufigen Schubabschaltungssequenzen getestet. Die Konversionsraten der gesetzlich limitierten Abgaskomponenten konnten im Vergleich zu einer reinen  $\lambda = 1$  Strategie generell für stark gealterte bis hin zu frischen Katalysatoren verbessert und stabilisiert werden. Es zeigte sich, dass die Integratorerweiterung des Reglers für die Schätzung des Fehlers der Lambda-Weitbereichssonde im Rohabgas verwendet werden kann. Dies ist eine wertvolle Information für die Diagnose dieser Sonde.

# Contents

<b>Acknowledgements</b>	<b>vii</b>
<b>Abstract</b>	<b>ix</b>
<b>Zusammenfassung</b>	<b>xi</b>
<b>Nomenclature</b>	<b>xvii</b>
<b>1 Introduction</b>	<b>1</b>
1.1 Main Pollutants in the Exhaust of Gasoline Engines . . . . .	1
1.1.1 Carbon Monoxide (CO) and Hydrocarbons (HC) . . . . .	2
1.1.2 Hydrogen (H <sub>2</sub> ) . . . . .	3
1.1.3 Nitrogen Oxides (NO <sub>x</sub> ) . . . . .	3
1.2 Legislation . . . . .	4
1.3 Three-Way Catalytic Converters . . . . .	7
1.4 Scope of this Thesis . . . . .	11
<b>2 Engine Test Bench</b>	<b>15</b>
2.1 Engine Control System . . . . .	16
2.2 Exhaust Gas Measurements . . . . .	17
2.2.1 NO: Cambustion fNO <sub>x</sub> 400 . . . . .	18
2.2.2 HC: Cambustion HFR 400 . . . . .	19
2.2.3 CO/CO <sub>2</sub> : Horiba MEXA 1300 FRI . . . . .	19
2.2.4 H <sub>2</sub> /O <sub>2</sub> /H <sub>2</sub> O/N <sub>2</sub> : Pfeiffer Omnistar . . . . .	20
2.3 λ Sensors . . . . .	22
2.4 Temperature and Mass Flow Sensors . . . . .	23
2.5 Three-Way Catalytic Converters . . . . .	23
<b>3 Modelling of a Three-Way Catalytic Converter</b>	<b>25</b>
3.1 Introduction . . . . .	25
3.2 Focus of the TWC Model . . . . .	26
3.3 Process Model of the TWC . . . . .	29
3.3.1 Thermodynamic Model of the TWC . . . . .	30

3.3.2	Kinetics of the TWC . . . . .	34
3.3.3	Simulation and Model Calibration . . . . .	39
3.4	Simulation Results vs Measurements . . . . .	44
3.4.1	Concentration downstream of the TWC . . . . .	44
3.4.2	Occupancy and Concentration Profiles . . . . .	49
3.4.3	Temperature Profiles . . . . .	54
3.5	Conclusion . . . . .	56
<b>4</b>	<b>Modelling of a Solid-Electrolyte Oxygen Sensor</b>	<b>57</b>
4.1	Introduction . . . . .	57
4.2	Structure and Working Principle . . . . .	59
4.3	Process Model . . . . .	61
4.3.1	Protection Layer . . . . .	63
4.3.2	Electrode . . . . .	65
4.3.3	Electrolyte . . . . .	68
4.4	Steady-State Simulation Results vs Measurements . . . . .	74
4.5	Aspects of the Wide-Range $\lambda$ Sensor . . . . .	80
4.6	Conclusion . . . . .	82
<b>5</b>	<b>Observer of a Three-Way Catalytic Converter</b>	<b>83</b>
5.1	Introduction . . . . .	83
5.2	Control-Oriented Modelling of the Exhaust Gas Aftertreatment System	85
5.2.1	Control-Oriented Raw Exhaust Gas Model . . . . .	87
5.2.2	Control-Oriented Model of a Switch-Type $\lambda$ Sensor . . . . .	90
5.2.3	Control-Oriented Model of a TWC . . . . .	96
5.3	Model Calibration . . . . .	103
5.3.1	Simulation Results vs Measurements . . . . .	111
5.4	Online Adaptation Strategy . . . . .	117
5.4.1	Extended Kalman Filter for the TWC . . . . .	117
5.4.2	Performance of the Extended Kalman Filter in the FTP Cycle	126
5.5	Conclusion . . . . .	130
<b>6</b>	<b>Control of a Three-Way Catalytic Converter</b>	<b>131</b>
6.1	Introduction . . . . .	131
6.2	Control of TWCs and $\lambda = 1$ Strategies . . . . .	132
6.2.1	Challenges of TWC Control . . . . .	132
6.2.2	Observer based TWC Control Strategies . . . . .	134
6.3	Control of the Relative Oxygen Storage Levels . . . . .	142
6.3.1	Design of an LQ Regulator for the TWC . . . . .	142
6.3.2	Controller Performance on the Engine Test Bench . . . . .	148
6.3.3	Sensor Diagnosis . . . . .	157

6.4 Conclusion . . . . .	161
<b>7 Conclusions</b>	<b>163</b>
<b>A Determination of <math>\lambda</math> from Exhaust Gas Components:</b>	<b>167</b>
A.1 Evaluation Procedure for the Exhaust Gas Measurements . . .	167
A.2 Error Calculation . . . . .	172
<b>B TWC Model</b>	<b>175</b>
B.1 Derivation of the Mass Balance Equation . . . . .	175
B.2 Model Parameters . . . . .	176
<b>C Switch-Type Sensor Model</b>	<b>179</b>
C.1 Model Parameters . . . . .	179
<b>D Observer of a Three-Way Catalytic Converter</b>	<b>183</b>
D.1 Model Parameters . . . . .	183





# Nomenclature

## Symbols

Variable	Unit	Description
$A$	$s^{-1}$	Pre-exponential factor (Langmuir-Hinshelwood)
$A$	$s^{-1}/(\text{molm}^{-3})$	Pre-exponential factor (Eley-Rideal)
$A_{cat}$	$\text{m}^2/\text{m}^3$	Specific catalytic active surface
$A_{cs}$	$\text{m}^2$	Catalyst cross-sectional area
$A_{\text{electrode}}$	$\text{m}^2$	Electrode surface
$A_{geo}$	$\text{m}^2/\text{m}^3$	Specific geometric catalyst surface
$A_{\text{sensor}}$	$\text{m}^2/\text{m}^3$	Specific diffusion cross-sectional area
$A_{TWC}$	$\text{m}^2$	Outer TWC surface
$A_{\lambda st} \dots F_{\lambda st}$	V, 1/ppm	Coefficients switch-type sensor model
$D$	m	Diameter
$D_i$	m/s	Convection mass transfer coefficient of $i$
$D_{iN_2}$	$\text{cm}^2/\text{s}$	Binary diffusion coefficient of $i$ in $N_2$
$D_{eff}$	$\text{kg}/(\text{ms})$	Gas dispersion coefficient
$E$	$\text{kJ}/\text{mol}$	Activation energy
$F_\lambda$	-	Signal of the $\lambda$ feedback-controller
$G(s)$		Plant transfer function
$J$	$\text{mol}/(\text{m}^2\text{s})$	Mole flux
$J$	-	Quadratic cost function
$K(s)$		Controller transfer function
$L$	$\text{mol}/\text{m}^2$	Adsorption capacity
$L_e(s)$		Loop gain transfer function
$M$	$\text{kg}/\text{mol}$	Molar mass
$Nu_D$	-	Nusselt Number
$Q$	J	Thermal energy
$SC$	$\text{mol}/\text{m}^3$	Storage capacity
$Sh_D$	-	Sherwood number
$R$	$\text{J}/(\text{kgK})$	Specific gas constant
$R$	$\text{mol}/(\text{m}^2\text{s})$	Production rate
$T$	K	Temperature
$T_{\text{sensor}}$	K	Sensor temperature

$U$	V	Voltage
$V$	$m^3$	Volume
$\dot{V}$	$m^3/s$	Volumetric flow
$a_{O^{2-}}$	-	Activity of oxygen ions
$a_{\eta_{comb}}$	-	Coefficient exhaust gas model
$b_{\eta_{comb}}$	1/K	Coefficient exhaust gas model
$c$	$mol/m^3$	Concentration
$c_p$	J/(kgK)	Specific heat capacity
$d_{diff}$	m	Strength diffusion layer
$h_s$	s	Sample rate
$k$	$s^{-1}$	Reaction rate
$l$	%	Load
$m$	kg	Mass
$\dot{m}$	kg/s	Mass flow
$n$	rpm	Speed
$n_c$	-	Number of discrete cells
$\dot{n}_e$	C/( $m^2s$ )	Electron current
$p$	Pa	Pressure
$q, r$		Weighting factor
$s$	-	Sticking probability
$t$	s	Time
$v, w$	-	Mass fraction
$w_{\lambda st}^{eq}$	-	CO/H <sub>2</sub> -ratio switch-type sensor model
$y$	-	Mole fraction
$z$	m	Axial position
$\Delta G$	kJ/mol	Chemical/electrostatic potential
$\Delta H_i$	kJ/mol	Reaction Enthalpy of $i$
$\Sigma_{v,i}$	$cm^3/mol$	Diffusion volume of $i$
$\alpha$	W/( $m^2K$ )	Heat-transfer coefficient TWC → exhaust
$\alpha_{th}$	%	Throttle angle
$\alpha_{TWC}$	W/( $m^2K$ )	Heat-transfer coefficient TWC → ambient
$\epsilon$	-	Volume fraction of gas phase
$\epsilon_{wc}$	-	Washcoat porosity
$\epsilon/q$	-	Porosity/Tortuosity factor
$\eta_{comb}$	-	Inverse combustion efficiency
$\eta_{CO}$	-	Number of sites occupied by CO
$\eta_i$	-	Conversion efficiency of species $i$
$\theta$	-	Occupancy on noble metal
$\vartheta$	-	Occupancy on electrolyte
$\lambda$	-	Air-to-fuel ratio

$\lambda$	W/(mK)	Heat conductivity
$\nu$	-	Stoichiometric coefficient
$\nu_O^{2+}$	-	Positive vacancy in electrolyte
$\rho$	kg/m <sup>3</sup>	Density
$\phi_{H_2/CO}$	-	H <sub>2</sub> /CO ratio (raw exhaust)

## Vectors and Matrices

Variable	Description
<b>f</b>	Dynamics function of state-space system
<b>h</b>	Measurement function of state-space system
<b>u</b>	Control vector
<b>x</b>	State vector
<b>y</b>	Measurement vector
<b>v, w</b>	Uncorrelated white noise process
<b>A</b>	System dynamics matrix
<b>B</b>	Control matrix
<b>C</b>	Measurement matrix
<b>D</b>	Feedthrough matrix
<b>G</b>	State feedback gain matrix (LQ regulator)
<b>H</b>	Observer gain matrix (Kalman filter)
<b>H</b>	Measurement matrix
<b>I</b>	Identity matrix
<b>K</b>	Kalman Gain matrix
<b>P</b>	Covariance matrix of the estimate error
<b>Q</b>	Covariance matrix of process white noise (Kalman Filter)
<b>Q</b>	Weighting matrix for the state vector (LQ cost function)
<b>R</b>	Covariance matrix of measurement white noise (Kalman Filter)
<b>R</b>	Weighting matrix for the control vector (LQ cost function)
<b><math>\Phi</math></b>	Fundamental matrix

## Constants

Constant	Value/Unit	Description
<b>F</b>	96485 C/mol	Faraday number
<b><math>\mathfrak{R}</math></b>	8.31451 J/molK	Universal gas constant

## Subscripts

Subscript	Description
<i>Cer</i>	Ceria
<i>KF</i>	Kalman filter
<i>NM</i>	Noble metal
<i>Temp</i>	Temperature
<i>TWC</i>	Three-way catalyst
<i>V</i>	Vacant surface
<i>a</i>	Backward reaction
<i>ads</i>	Adsorption
<i>amb</i>	Ambient
<i>calc</i>	Calculated
<i>ch</i>	Channel (outer gas phase)
<i>chan</i>	Channel
<i>chem</i>	Chemical
<i>des</i>	Desorption
<i>el</i>	Electrostatic
<i>eng</i>	Engine
<i>eq</i>	Equilibrium
<i>exh</i>	Exhaust gas (upstream of TWC)
<i>f</i>	Forward reaction
<i>g</i>	Gas phase
<i>meas</i>	Measured
<i>ref</i>	Reference
<i>tp</i>	Tailpipe (downstream of TWC)
<i>wc</i>	Washcoat (inner gas phase)
<i>reac</i>	Reaction
<i>s</i>	Solid phase, surface
<i>stst</i>	Steady-state
<i>λst</i>	Switch-type $\lambda$ sensor

## Acronyms

BIBO	Bounded Input, Bounded Output
ECE	Economic Commission for Europe
EKF	Extended Kalman Filter
EUDC	Extra Urban Driving Cycle
FTP	Federal Test Procedure
GUI	Graphical User Interface

LEV	Low Emission Vehicle
LPV	Linear Parameter Variation
LQ	Linear Quadratic
LQG	Linear Quadratic Gaussian
NEDC	New European Driving Cycle
NMOG	Non-Methane Organic Gas
SFTP	Supplemental Federal Test Procedure
SULEV	Super Ultra Low Emission Vehicle
TWC	Three-Way Catalytic converter
ULEV	Ultra Low Emission Vehicle



# 1 Introduction

At the turn of the 19th century the door towards individual mobility was opened with the start of the mass production of automobiles. During the 20th century, the number of gasoline-driven cars increased from a few thousand to several hundred million on the planet. By the year 2000, approximately 500'000'000 passenger cars were registered world-wide<sup>1</sup>. This dramatic increase, which is expected to continue at least for the next three decades, is accompanied by a corresponding growth of pollutants in the atmosphere, since almost every vehicle is driven by an internal combustion engine. Because these pollutants affect both the environment and the human health in many unpleasant ways, it became clear during the second half of the 20th century that measures had to be taken to reduce the levels of the emissions to tolerable limits. Soon it became apparent that the improvement of the combustion in gasoline engines alone was not sufficient to reach the desired emission levels. Therefore, exhaust gas aftertreatment systems were introduced, which are capable of completing the combustion by means of catalysts, thus reducing the levels of undesired emission components to very low concentrations.

## 1.1 Main Pollutants in the Exhaust of Gasoline Engines

Ideally, the emissions of an internal combustion engine only consist of carbon dioxide ( $\text{CO}_2$ ), water ( $\text{H}_2\text{O}$ ), and nitrogen ( $\text{N}_2$ ), when it is operated at stoichiometry. Under lean operation, i. e., with excess air, additional oxygen ( $\text{O}_2$ ) is emitted. Under rich operation, i. e., with excess fuel, mainly additional carbon monoxide ( $\text{CO}$ ) and hydrogen ( $\text{H}_2$ ) arise.

In reality, the combustion is never complete, since the air-to-fuel mixture is not entirely homogenous. Thus, the gasoline is not entirely burned, resulting in carbon monoxide ( $\text{CO}$ ), hydrogen ( $\text{H}_2$ ), and hydrocarbon ( $\text{HC}$ )<sup>2</sup> emissions.

---

<sup>1</sup>see e. g. [hypertextbook.com/facts/2001/MarinaStasenko.shtml](http://hypertextbook.com/facts/2001/MarinaStasenko.shtml)

<sup>2</sup>The correct chemical expression for unburned hydrocarbons is  $\text{C}_x\text{H}_y$ . For simplicity, the term HC will be applied throughout the thesis. Notice that here, only the compounds containing hydrogen and carbon are considered. In reality, other carbon-containing compounds are emitted, as well. However, they are not considered in this thesis. The term HC refers both to the singular and plural form.

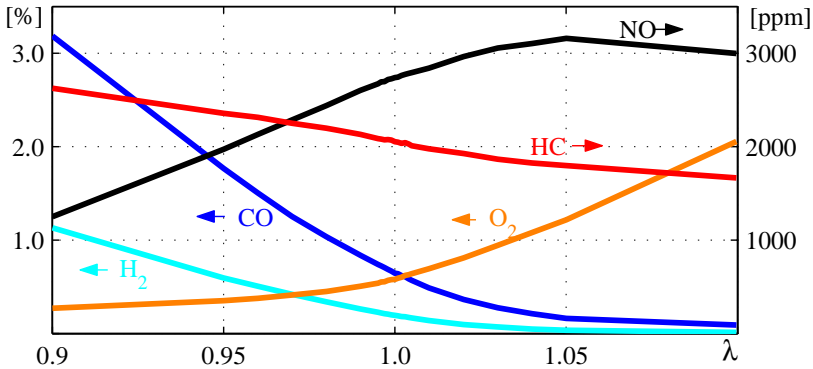


Figure 1.1: Measured concentrations of NO, CO, HC, H<sub>2</sub>, and O<sub>2</sub> in the raw exhaust gas of a port-injected spark-ignited engine versus the air-to-fuel ratio  $\lambda$ . The measurement data have been obtained on the testbench described in Chapter 2.

Since the combustion in the cylinder occurs at high temperatures, oxides of nitrogen (NO, NO<sub>2</sub> and very little N<sub>2</sub>O) are generated, as well. Their formation is highly dependent on the operating condition of the engine. In the following, they will be collected in the term NO<sub>x</sub>. All the emissions mentioned occur simultaneously, at any operable air-to-fuel ratio. Figure 1.1 shows a typical example of the exhaust gas composition of a commercial type spark-ignited engine at different air-to-fuel ratios.

### 1.1.1 Carbon Monoxide (CO) and Hydrocarbons (HC)

Carbon monoxide is an odourless and colourless gas. Since it exhibits a higher affinity to haemoglobin than oxygen, it is very toxic. It blocks the supply of oxygen to the body tissue, thus leading to suffocation. A concentration of a few thousand ppm is already fatal. Carbon monoxide is generated when the combustion occurs under oxygen-deficient conditions. Thus, CO is mainly generated when rich air-to-fuel mixtures are burned. However, even under lean conditions, CO occurs because of incomplete combustion.

The group of unburned hydrocarbons (HC) contains many compounds consisting of carbon and hydrogen. The most important groups are alkanes, alkenes, alkynes, and aromatics. Molecules which only contain single hydrogen-carbon bonds, i. e., the alkanes, are called “saturated”. Alkenes and alkynes are unsaturated. Hydrocarbons consist mainly of partially oxidised fuel molecules.



However, few molecules arise from unburned fuel, such as benzene ( $C_6H_6$ ). In addition to the hydrocarbons, oxygenates occur also, i. e., organic compounds containing oxygen, such as formaldehyde (HCHO). Usually their fraction is low as compared to the HC concentration.

Like CO, HC occur under rich operating conditions, i. e., when excess fuel is present. Additionally, they occur when the combustion is locally disturbed or hindered. This can for example be caused by the cylinder geometry, by quenching of the flame or by absorption of fuel in the oil [47]. Alkenes and alkynes are slightly sweet smelling, whereas alkanes are odourless. Many HC cause coughing, drowsiness or even have a narcotic effect. Benzene is toxic and carcinogenic. It is believed that internal combustion engines in cars are the cause of about 80% of the benzene in the atmosphere. Apart from the direct impact on the human health, some HC such as alkenes react with  $NO_x$  in the atmosphere to form secondary pollutants such as tropospheric ozone and photochemical smog. Ozone in turn has again a significant impact on the human health, affecting the respiratory tract.

### 1.1.2 Hydrogen ( $H_2$ )

Hydrogen is not a real pollutant. It is not toxic and has no significantly malign effect on the atmosphere. Therefore, it is not regulated by legislation. However, it has a very strong impact on the  $\lambda$  sensor signals, as will be shown in this thesis. Its very high agility as compared to other species and its considerable chemical activity are the causes of these sensor signal distortions.

### 1.1.3 Nitrogen Oxides ( $NO_x$ )

Nitrogen Oxides mainly occur in the form of nitric oxide (NO) and nitrogen dioxide ( $NO_2$ ). Nitrous oxide ( $N_2O$ ) only occurs in small amounts in the raw emissions of an internal combustion engine. However, the concentration may increase in a three-way catalytic converter under certain circumstances. Nitrogen dioxide is reddish-brown with a pungent smell and toxic, damaging the lung tissue. Already small concentrations of around 1 ppm are harmful. Nitric oxide is odourless and colourless and relatively harmless, as compared to  $NO_2$ . Both NO and  $NO_2$  play an important role in the formation of acid rain, photochemical smog and the depletion of the ozone layer. Nitrous oxide is an important greenhouse gas. Usually, the fraction of NO in the  $NO_x$  emissions of a gasoline engine is well above 98%. Therefore, only NO will be considered, the other nitrogen oxides will be neglected in this thesis.

Table 1.1: Limits according to the Californian LEV II emission standards.

Standard	NMOG g/mile	CO g/mile	NO <sub>x</sub> g/mile	HCHO g/mile
LEV	0.090	4.2	0.07	0.018
ULEV	0.055	2.1	0.07	0.011
SULEV	0.010	1.0	0.02	0.004

The limits are valid for the first 100'000 miles [35], [9].

## 1.2 Legislation

The introduction and development of exhaust gas aftertreatment systems is certainly a major success in the automobile industry. The reduction of pollutants has led to a considerable improvement of the air quality, especially in urban areas. However, this effort was of course connected with substantial costs and investments and would have hardly been taken without fierce legislative action.

The United States were the first to introduce very stringent limits for exhaust gas components as a response to the severe air pollution in urban areas. In Los Angeles for example, the smog was worse in 1955 than in Mexico City today [11]. As a consequence, Congress passed the Clean Air Act Amendments of 1970. Originally, a 90% reduction of HC, CO, and NO<sub>x</sub> emissions over uncontrolled levels was required within six years. However, these limits turned out to be too stringent for an implementation in the given time frame and the deadlines had to be postponed. Finally, all gasoline driven passenger cars in the U.S. had to meet the tight limits by the model year 1983. The general path towards a substantial reduction of the emissions was being kept and improved continuously.

With the Clean Air Act Amendments of 1970, the State of California was authorised by Congress to introduce its own motor vehicle emission control programme [11]. After that, California took the lead in emission control legislation and worked in a way as a “proving ground” for very stringent exhaust gas limits. Table 1.1 shows the emission limits according to the California LEV II emission standards for passenger cars. These standards will be phased in from 2004 to 2010. As for the hydrocarbons, only the non-methane organic gases (NMOG) are limited. Unlike in the European standards, also formaldehyde (HCHO) emissions are limited. The positive experience in the U.S. soon made Japan and Europe introduce the use of automotive catalysts, the latter in 1986 [90]. The emission standards in Europe are covered by the directives 93/59/EC

Table 1.2: Limits according to the European emission standards.

Standard	HC + NO <sub>x</sub> g/km	HC g/km	NO <sub>x</sub> g/km	CO g/km
EURO I (1992)	0.97			2.72
EURO II (1996)	0.50			2.2
EURO III (2000)		0.2	0.15	2.3
EURO IV (2005)		0.1	0.08	1.0

The year of introduction is indicated in parentheses [35], [9].

and 96/69/EC for EURO I/II, and by 98/69/EC for EURO III/IV standards, respectively. The emission limits according to these standards are shown in Table 1.2. In Europe, the total HC are limited, whereas there are no rules for formaldehyde. Under EURO I and EURO II, only the sum of the HC and NO<sub>x</sub> was limited.

In order to obtain comparable and reproducible conditions for emission measurements, special driving cycles have been developed, where the vehicle speed and load, the gear shift events, the braking, idle, and standstill phases as well as the ambient conditions, such as the temperature, pressure, and humidity are exactly defined. In the U.S. the FTP 75 (Federal Test Procedure) is one example. Its duration is approximately 20 minutes with a break of 10 minutes, where the engine is shut off. It contains three sections, which are set up from real vehicle speed profiles. These have been recorded during the morning rush hour in Los Angeles [9]. Today, there exist additional cycles for emission testing in the U.S. (SC03, US06), which also cover aggressive driving, different speed transient patterns, engine startup, engine shut-off phases and the operation of the air conditioning system. The vehicles have to pass both the FTP 75 and the SFTP (Supplemental FTP) tests. The latter is a combination of the FTP 75, SC03 and the US06 cycles.

In Europe, the ECE 15 (Economic Commission for Europe) + EUDC (Extra Urban Driving Cycle) driving cycles are applied for emission testing. The former is a synthetic cycle covering mainly urban driving with low vehicle speed, low engine load and low exhaust gas temperatures. The latter is an extension which also covers aggressive driving with speeds of up to 120 km/h. With EURO III, a 40 s engine warm-up period, where no emissions were measured, has been eliminated. Thus, emissions are measured from the beginning of the cold-start under EURO III and IV. This new cycle is also referred to as NEDC (New European Driving Cycle). Some characteristic figures of the mentioned

Table 1.3: Characteristic figures of different driving cycles [35], [9].

Cycle	FTP75	SC03	US06	ECE 15	EUDC
Distance [km]	17.87	5.76	12.87	4.05	6.96
Duration [s]	1877	594	600	780	400
Average speed [km/h]	34.1	34.9	77.3	18.7	62.6
Max speed [km/h]	91.2	88.2	129.2	50	120.0

cycles are listed in Table 1.3.

Not only the driving cycles per se are important and subject to legislation nowadays, but also the ambient conditions and the monitoring during a vehicle's lifetime. Additional issues are addressed in the latest exhaust gas regulations, such as

- **Cold-Start Conditions**

Cold-start conditions are now set to  $-7^{\circ}\text{C}$ , to which the system has to be conditioned before the test starts. The air-to-fuel mixture is enriched, i. e., more fuel is injected during startup in order to build up the wall film. Since the combustion is rather inefficient in a cold engine, large amounts of HC are emitted during this phase. Additionally, the exhaust gas aftertreatment system works efficiently only after catalyst light-off<sup>3</sup>. More stringent cold-start conditions thus force the optimisation of the startup of both the engine and the aftertreatment system during which most HC are emitted.

- **Onboard Diagnosis**

All relevant parts in the exhaust gas aftertreatment system, such as the  $\lambda$  sensors or the catalytic converter, as well as exhaust-relevant malfunctions such as misfire, have to be monitored and a malfunction has to be indicated to the driver.

- **Evaporative Emissions**

Evaporative emissions occur from gasoline which evaporates directly from the tank and from leakages in the gasoline supply system. These emissions are measured during increasing ambient temperatures with open windows and hood (SHED test).

- **Durability of the exhaust gas aftertreatment system**

Emission levels have to be kept during at least 80'000/100'000 km (EU)

---

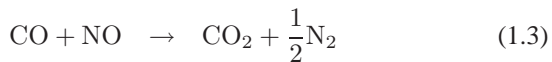
<sup>3</sup>Catalyst light-off is reached when at least 50% of the HC are converted.

or 50'000/100'000 miles (U.S. LEV II). Additionally, field monitoring is ensured by testing the emissions of a vehicle in certain time periods.

## 1.3 Three-Way Catalytic Converters

The tight limits for emissions described above cannot be reached by optimisation of the combustion in the engine alone. Ideally, i. e., with a perfect combustion, the exhaust gas only consists of nitrogen, carbon dioxide, and water, when the air-to-fuel ratio is stoichiometric. Real combustion is never complete, i. e., the exhaust gas leaving the cylinder has not reached the chemical equilibrium. Theoretically, this equilibrium can be reached without any additional treatment, however only very slowly, i. e., within days or weeks. Therefore, a catalyst<sup>4</sup> is used, which accelerates this process such that the state of the exhaust gas comes close to the equilibrium before being released to the atmosphere. With the latest figures of the legislation (EURO IV of SULEV), the catalyst has to reach conversion efficiencies of more than 96% for the CO, HC, and NO<sub>x</sub> during more than 100'000 km!

The most common aftertreatment device for gasoline engines nowadays is the three-way catalytic converter (TWC). It is named after its ability to promote the following three chemical reactions simultaneously:



The activity of the three reactions and thus the reduction of the HC, CO, and NO<sub>x</sub> significantly depends on the air-to-fuel ratio  $\lambda$ . Throughout this thesis,  $\lambda$  is defined as follows:

$$\lambda = \frac{2y_{CO_2} + y_{CO} + 2y_{O_2} + y_{NO} + y_{H_2O}}{2y_{CO_2} + 2y_{CO} + y_{H_2} + \left(2x + \frac{y}{2}\right) y_{C_xH_y} + y_{H_2O}} \quad (1.4)$$

where  $y_i$  denotes the mole fraction of the species  $i$ . Thus,  $\lambda$  is 1 in a stoichiometric mixture. A value above one indicates a lean mixture, i. e., excess O<sub>2</sub> and NO<sub>x</sub>, whereas a value below one indicates a rich mixture with excess CO, HC, and H<sub>2</sub>. In order to oxidise the CO and HC, a strategy with a stoichiometric or

---

<sup>4</sup>The term "catalyst" was first used by the Swedish Chemist Berzelius. A catalyst is a substance which alters the rate of a chemical reaction but remains chemically unchanged.

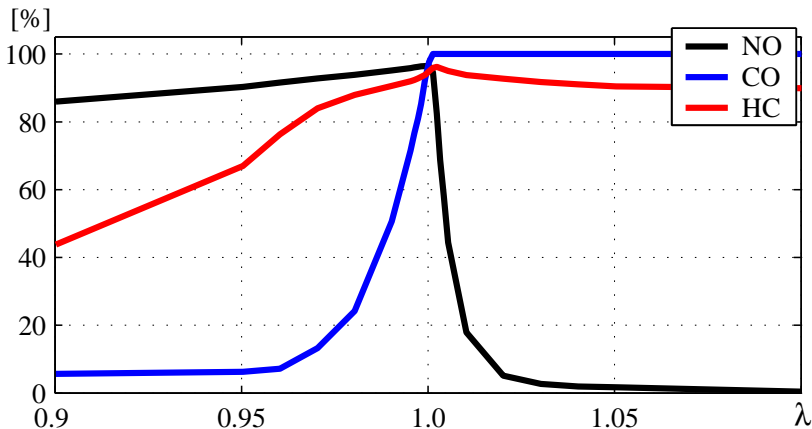
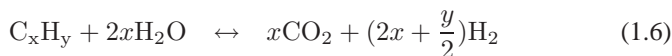


Figure 1.2: Measured conversion rates of NO, CO, and HC versus  $\lambda$  in a thermally aged TWC.

lean operation is necessary. However, under lean operation, the reaction (1.2) is dominant over (1.3). It is therefore necessary to operate the engine very close to stoichiometry, i. e., with  $\lambda = 1$ . Figure 1.2 shows the conversion efficiencies of NO, HC, and CO as a function of  $\lambda$ . As can be seen, only very close to stoichiometry all three components can be reduced significantly.

The design of TWCs nowadays not only aims at the promotion of the reactions described above, but also of the water-gas shift and the steam-reforming reactions. In the former reaction, water oxidises the carbon monoxide to produce carbon dioxide and hydrogen. In the latter process, the hydrocarbons are oxidised accordingly. Chemically, the two reactions are formulated as follows:



The role of these two reactions will be focused on in more detail in Chapter 3. It will be shown that the promotion of these reactions significantly changes with the ageing of the TWC. This leads to a substantial change of the hydrogen output of the TWC over its lifetime, which has a strong impact on  $\lambda$  sensors located downstream of the converter.

Figure 1.3 illustrates an example of the structure of a three-way catalytic converter. The core is a monolith (cordierite or metal), which is also called

substrate or carrier. On the monolith the washcoat is deposited. The washcoat is a layer of oxide ceramic, mainly alumina with a certain percentage of ceria added. Ceria is widely used because of the stability of its surface area, its reversibility of sulfur poisoning and its rapid kinetics of oxygen storage and release [95]. Hence, the TWC can store and release considerable amounts of oxygen. The washcoat is very porous in order to increase the area between the gas phase and the catalyst. The actual catalytically active materials are precious metals, such as platinum, palladium, and rhodium, which lie on the washcoat. Additionally, some stabilisers are used, which slow down the thermal ageing process. The exact composition and structure of a three-way catalytic converter is usually a secret well guarded by the manufacturer. The topic of catalyst composition and design shall not be discussed in this thesis. More information on the history, design, and composition of TWCs can be found in [90] or [38]. In order to reduce the emissions as demanded by legislation, the TWC has to be operated in a very tight window around stoichiometry, see also Figure 1.2. This requires an accurate control of the air-to-fuel ratio  $\lambda$ , which can only be achieved with an electronic fuel injection system. A typical setup of a  $\lambda$  control system is shown in Figure 1.4. The controller consists of two paths. In the feedforward path, the injected fuel mass is calculated from the air mass entering the cylinder. Thereby, the dynamics of the intake manifold have to be taken into account, since the air mass flow meter measures the air mass entering the intake manifold, rather than the one entering the cylinder. Because the fuel is injected onto the wall of the inlet duct and the intake valves, the dynamics of the evaporation have to be considered as well, in order to obtain an accurate estimate of  $\lambda$  in the cylinder. The actual  $\lambda$  is measured at the outlet of the cylinder. This signal is used by a feedback controller to correct the amount of injected fuel that was estimated by the feedforward controller. Notice that this correction is multiplicative, not additive, as probably expected. The reason for this can be explained as follows: The feedback (sensor) signal provides the air-to-fuel ratio. The controller only calculates a corrective signal  $F_\lambda$  relative to the current air mass in the cylinder. When  $F_\lambda$  is multiplied, the amount of injected fuel is automatically adjusted to the current air mass flow. This control structure has been thoroughly investigated and is well documented in the literature, see e. g. [9] or [86].

Because of the different dynamics of the air and the fuel paths, temporary excursions of the air-to-fuel ratio occur, especially during fast transients, such as aggressive acceleration or braking of the vehicle. Even the most sophisticated  $\lambda$  controllers cannot maintain the air-to-fuel ratio in a range where the TWC conversion rate is optimal. Today's TWCs are able to store a certain amount of oxygen. This oxygen storage allows to buffer a temporary shortage or surplus of oxygen in the exhaust gas. For this purpose, the oxygen storage level has to

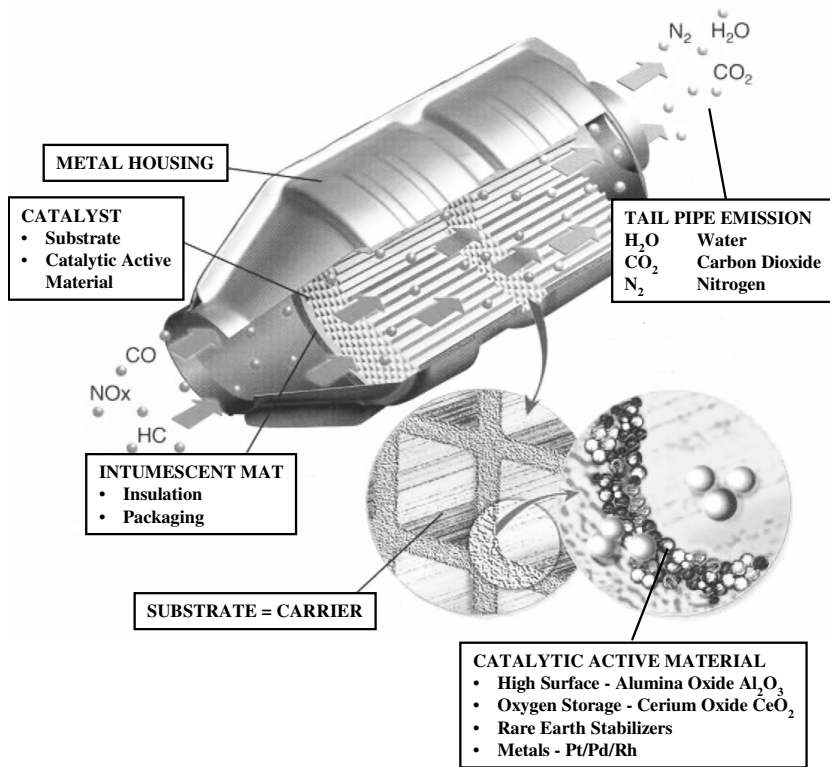


Figure 1.3: Structure of a TWC. Reprinted with permission of the Umicore AG.

be controlled in a way which allows optimal conversion rates of the TWC, even during transient operation.

Apart from the oxygen, other species are stored in the TWC, leading to a complex transient behaviour. This means that the conversion rate of the TWC is not only dependent on the air-to-fuel ratio of the inlet gas, but also on the catalyst state, which is determined by the temperature and the storage levels of the different species. As will be shown, a high oxygen storage level can inhibit the NO conversion. Another very important effect is the TWC deactivation by other species, which changes the composition of the exhaust gas significantly. This is very important when exhaust gas sensors downstream of the TWC are used for diagnosis and control purposes, since the signals of these sensors can be considerably distorted by the changes of the exhaust gas compo-



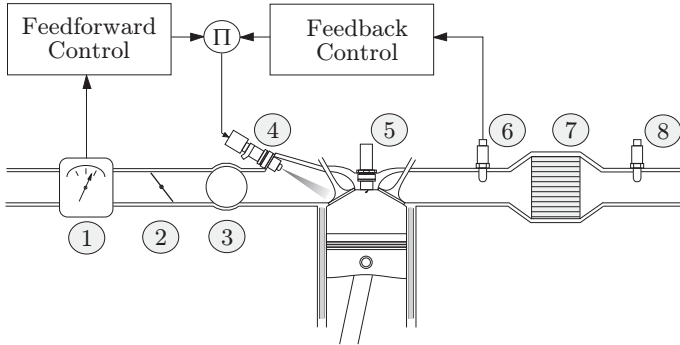


Figure 1.4: Sketch of the  $\lambda$  control system with the following components: 1 Air mass flow meter; 2 Throttle; 3 Intake manifold; 4 Fuel injection valve; 5 Spark plug; 6  $\lambda$  sensor upstream; 7 TWC; 8  $\lambda$  sensor downstream.

sition. Above all, the TWC changes its transient behaviour during its lifetime because of ageing. This can occur by poisoning, i. e., a deactivation of the catalytic activity by components such as sulfur or oil additives. Another form is thermal ageing, which leads to sintering of the porous catalytically active material and the loss of dispersion of the noble metal. Both ageing phenomena lead to a reduced catalytically active surface.

## 1.4 Scope of this Thesis

The goal of this thesis is to develop a control strategy for the TWC in order to maintain the required conversion rates under all operating conditions throughout the TWC's lifetime. This includes permanent monitoring of the parameters which are relevant for the TWC dynamics as well as an adaptation algorithm which accounts for the changing of these parameters during the TWC's lifetime. The diagnostics of TWCs, i. e., the link between the monitored parameters and the actual conversion efficiency of the TWC is only discussed briefly.

Control-oriented TWC modelling often addresses mainly the oxygen storage dynamics. In this thesis, also the deactivation of the TWC by reducing species is discussed. This plays an important role for the dynamics of the ratio between HC, CO, and  $H_2$  downstream of the TWC. This ratio significantly influences the  $\lambda$  sensor signals. This impact, especially on the switch-type sensors, is thoroughly investigated. Additionally, a method is presented which allows the

adaptation of the controller to the changing dynamics of the TWC because of ageing.

The setup of the addressed system corresponds mainly to the one shown in Figure 1.4. Thus, only port-injected spark-ignited engines are discussed. This thesis focuses on the use of a wide-range  $\lambda$  sensor upstream and a switch-type  $\lambda$  sensor downstream of the TWC. In addition to the sketched system, it is assumed that a temperature sensor for the raw exhaust gas or at least an accurate estimate is available. Auxiliary systems such as secondary air injection, canister purge, exhaust gas recirculation, turbochargers or other devices are not discussed. Only the air-to-fuel ratio or rather the amount of injected fuel is considered as an actuator. The spark advance and dwell angles are not taken into account as additional degrees of freedom.

Modern exhaust gas aftertreatment systems consist of two TWCs in the exhaust path. Mounted close to the engine, the close-coupled device is designed for fast light-off in order to minimise the hydrocarbon emissions which arise during warmup. It is usually reasonably small and robust against the thermal stress occurring close to the engine. The underfloor catalyst is mounted further downstream. It is larger in volume and often designed to efficiently remove the  $\text{NO}_x$  emissions. This thesis only covers aspects of the close-coupled TWC. The extension of the concept to systems with two TWCs is straightforward.

The thesis is divided into a process modelling part (Chapters 3 and 4), a control-oriented modelling part (Chapter 5) and a control part (Chapter 6). The Chapters are structured as follows:

In Chapter 3, a detailed process model of the TWC is developed in order to gain insight into its dynamic behaviour. Here, the focus is on the oxygen storage and the deactivation dynamics. It is shown how these dynamics drive the transients of the most important exhaust gas components, especially the ones which contribute to the sensor output downstream of the TWC.

Chapter 4 focuses on the  $\lambda$  sensors. A detailed process model of the switch-type sensor is developed in order to obtain a thorough understanding of its working principle and also of the advantages and difficulties of its use. The wide-range sensor is addressed shortly in the second part of this chapter. It is demonstrated that the signal can be significantly distorted. It is further discussed why the switch-type sensor is preferred downstream of the TWC.

Based on the process models, a control-oriented model of the TWC and the  $\lambda$  sensors is presented in Chapter 5. The TWC model accounts for both the most important dynamics and the exhaust gas components which mainly drive or distort the sensor signals. The sensor model considers the influence of the exhaust gas components provided by the TWC model. Based on the simplified model, an extended Kalman filter is developed which allows the online estimation of the relative oxygen level in the TWC, the deactivation, and the

oxygen storage capacity. These quantities are crucial for both the control and the diagnosis of the TWC.

The state observer allows the use of a model-based controller of the TWC. This is presented in Chapter 6. Different strategies are discussed which address various issues of combined  $\lambda$  and TWC control. An LQ controller with an integrator extension is developed which not only accounts for the TWC control but also estimates the offset of the wide-range  $\lambda$  sensor located upstream of the TWC. Apart from the controller, the question of the setpoint management in terms of emission-optimal operation is discussed, as well.

Finally, some conclusions are drawn and an outlook with recommendations for future research is presented.

All measurements presented throughout this thesis have been performed on the engine test bench of the Measurement and Control Laboratory at ETH Zürich. A description of this test bench with all the measurement devices and sensors is given in Chapter 2.



## 2 Engine Test Bench

All measurements presented in this thesis have been performed on the engine test bench of the Measurement and Control Laboratory at ETH Zürich. This test bench is equipped with an AUDI V6 30V engine with a displacement of 2.8 litres. The power output is 142 kW at 6000 rpm. The engine is connected to a highly dynamic direct current generator which can be run in speed or torque controlled mode. A detailed description of the setup can be found in [73] and [88]. The generator can be run in all operating conditions, i. e., it can be used both to brake and to drag the engine, for example to emulate the use of the engine as a brake. Thus, driving cycles such as the FTP cycle (cf. Section 1.2) can be run on the test bench. The FTP cycle measurements presented in this thesis are based on chassis dynamometer measurements at the Robert Bosch GmbH, where the engine speed and the throttle angle were recorded during a test on a vehicle equipped with the same engine. The vehicle used for the recording had a manual transmission, which leads to a frequent occurrence of fuel cut-offs during deceleration periods. Figure 2.1 shows a comparison of the recorded (setpoint) and the actually obtained engine speed and throttle angle during a significantly transient period of the FTP cycle. The agreement of the signals is excellent, which shows that the conditions occurring in the cycle can be emulated well. A major advantage of this procedure is the very accurate reproducibility of the driving cycle. This facilitates the comparison of the different control strategies for the three-way catalytic converter. In order to enhance this reproducibility, also the trigger for the fuel cut-off has been recorded. Thus, fuel cut-offs always occur at the same time in all cycle measurements.

In its present configuration, the engine is not equipped with any turbocharger or exhaust gas recirculation. The camshaft timing and the intake manifold volume may be varied, but this has not been used in any experiment presented here.

The test cell is not air conditioned, which leads to slightly varying ambient conditions, depending on the time of the year. Usually, the ambient temperatures during the measurements are between 25 °C and 35 °C. Ambient pressure and humidity only vary little. Since no cold start experiments were conducted, no special attention was paid to the ambient conditions.

The engine has two exhaust gas lines which are completely separated. Each line is equipped with  $\lambda$  sensors and three-way catalytic converters and is con-

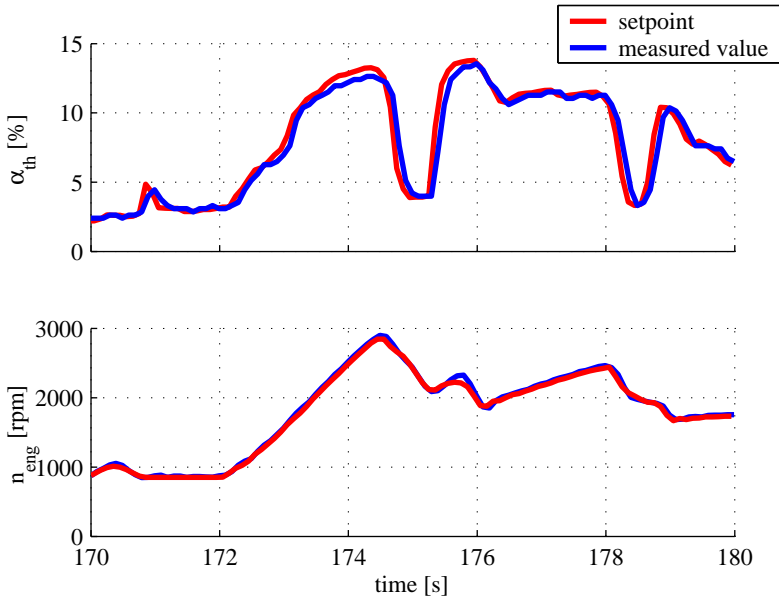


Figure 2.1: Comparison of the setpoints with the actual values of the throttle angle and the engine speed between 170 s and 180 s. Notice that the time scale differs from the original FTP cycle because data recording starts prior to the actual cycle.

trolled independently. The experiments presented here have been performed on one exhaust gas line, only.

## 2.1 Engine Control System

For the engine control system a rapid prototyping system from DSpace<sup>TM</sup> has been used. It contains the controllers for the air-to-fuel ratio and the ignition, the data acquisition system and the setpoint maps for the throttle and dynamometer speed controllers. The complete system runs at a sampling frequency of 1 kHz.

The pulses for the injection and ignition are generated by an in-house developed chip, ICX 3, see [41]. The ICX 3 receives updates of the injection angle, the ignition duration, the dwell and the spark advance angles from the DSpace<sup>TM</sup> system at a rate of 1 kHz. Being connected to an incremental encoder (resolution  $0.025^\circ$ ) and the camshaft sensor, the engine crank angle is

exactly known. Thus, accurate timing for the injection and the ignition pulses is possible. These pulses are sent to the power amplifier for the injection valves and the spark coils. Hence, the ICX 3 allows the separation of the engine's crank angle domain and the control system's time domain. In addition to the described features, the ICX 3 also provides a very accurate signal of the engine speed and the crank angle position. More details on the control system can be found in [61].

Unless stated otherwise, an air-to-fuel ratio controller has been used, which was developed at the Measurement and Control Laboratory at the ETH Zürich. A sketch of the air-to-fuel ratio controller is depicted in Figure 1.4 in the previous chapter. It consists of a feedforward path, which accounts for the intake manifold and the wall-wetting dynamics. A detailed description can be found in [61]. The feedback controller accounts for the dynamics of the engine and the  $\lambda$  sensor. It is described in e. g. [86]. The ignition (dwell and spark advance) angles are calculated from maps, depending on the operating point of the engine.

The throttle position is controlled by an external nonlinear extended PID controller of the Robert Bosch GmbH. The setpoint can be adjusted manually or from the DSpace™ system, e. g. to run driving cycles, see also Figure 2.1.

In all experiments, gasoline with a rather low sulfur content (17 wtppm) has been used. It is therefore assumed throughout the thesis, that sulfur only plays a minor role here for the TWC dynamics.

A considerable set of sensors is mounted on the engine. The ones which are relevant for the experiments in this thesis will be described in detail in the subsequent sections.

## 2.2 Exhaust Gas Measurements

The engine testbench is equipped with fast exhaust gas measurement devices. The concentrations of NO, total HC, CO, CO<sub>2</sub>, H<sub>2</sub>, O<sub>2</sub>, H<sub>2</sub>O, and N<sub>2</sub> could be measured with a response time ( $T_{90}$ ) of well below 100 ms. The measurement devices are described in detail further below.

Measurements have been performed upstream and downstream of the close-coupled TWC. The NO, HC, CO, and CO<sub>2</sub> concentrations could be measured simultaneously on both sides of the TWC. For the other components, which were obtained from the mass spectrometer, only one channel was available. A setup of the TWC with the mounted exhaust gas-, temperature- and  $\lambda$  sensors is depicted in Figure 2.2.

Most components could not be obtained directly from the measurements. A postprocessing procedure was necessary for all components, except for the HC.

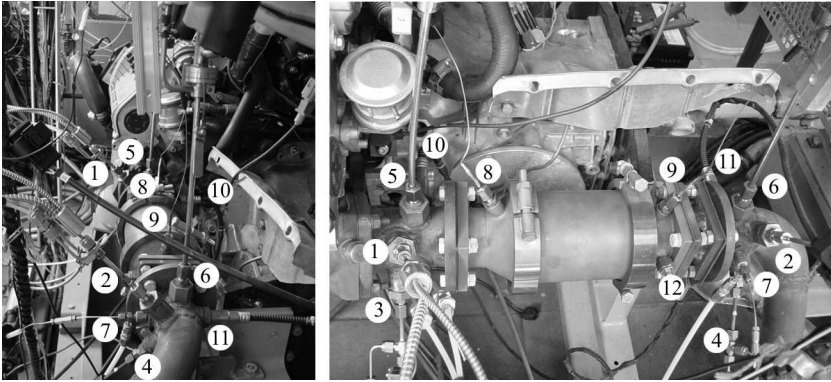


Figure 2.2: Pictures of the close-coupled TWC with mounted sensors. Left-hand side: view from the TWC outlet, right-hand side: View from the side, exhaust gas flow direction from left to right. Legend: 1/2 - upstream/downstream NO, 3/4 - upstream/downstream HC, 5/6 - upstream/downstream CO/CO<sub>2</sub>, 7 - downstream mass spectrometer, 8/9 - upstream/downstream temperature, 10/11 - upstream/downstream wide-range  $\lambda$ , 12 - downstream switch-type  $\lambda$ .

This is further discussed in the following subsections, where the measurement devices are described. The postprocessing procedure including an error calculation is presented in Appendix A.

### 2.2.1 NO: Cambusion fNOx 400

Nitric oxide was measured with a Cambusion fNOx 400. This device was originally developed at the Measurement and Control Laboratory at the ETH Zürich, see [8]. The measurement principle is chemiluminescence, where the light emission from NO reacting with ozone is collected and measured by a photo-multiplier. The very compact design with thin heated sample capillaries and analysers mounted close to the measurement probe results in an extremely short response time of the sensor, which is well below 10 ms, including both the transport delay and the time constant.

The analyser provides an NO concentration signal of the wet exhaust gas. However, calibration was done with dry calibration gas, which consisted of 1000 ppm NO in N<sub>2</sub>. Hence, the quenching effect of the water which slightly hinders the chemiluminescence reaction has to be accounted for. Additionally, quenching by the CO<sub>2</sub> also influences the signal. The total quenching effect is



0.7% per 1% water concentration and 0.3% per 1% CO<sub>2</sub> concentration.<sup>1</sup>

The NO concentration in the calibration gas used for the NO measurements had a relative accuracy of  $\pm 2\%$ , i. e.,  $\pm 20$  ppm. The linearity of the device is  $\pm 1\%$  of full scale to 5000 ppm NO [28]. The total maximum error of the uncorrected NO signal was assumed to be  $\pm 100$  ppm at all levels of NO. Notice that only the NO concentration has been measured, all other forms of NO<sub>x</sub> have been neglected.

### 2.2.2 HC: Cambustion HFR 400

For the measurement of the hydrocarbons, a Cambustion HFR400 fast FID 400 was used. The measurement principle is flame ionisation detection. It exploits the phenomenon that ions are produced when hydrocarbons are burned. The number of these ions is roughly proportional to the number of the carbon atoms in the HC compounds. In the FID, the exhaust gas enters a hydrogen flame, which by itself only produces very few ions. Hence, the ions detected by the sensor stem from the hydrocarbons in the exhaust gas. The design is similar to the NO analyser, which again results in very short response times of less than 10 ms.

The FID exhibits different sensitivities for the various hydrocarbon compounds. However, the most important components (low valued alkanes and alkenes) all have relative sensitivities close to 1. This factor was chosen for all HC. The device contains no drier, i. e., the total wet concentrations are measured directly. Therefore, no postprocessing of these measurements was necessary.

The calibration gas used for the measurements consisted of 1000 ppm CH<sub>4</sub> in N<sub>2</sub> with a relative accuracy of  $\pm 2\%$ , i. e.,  $\pm 20$  ppm. The device exhibits a precision of  $\pm 2\%$  and a drift of  $\pm 2\%$  of full scale per 8 hours [27]. The complete maximum error of the HC signal was assumed to be  $\pm 50$  ppm at all levels.

### 2.2.3 CO/CO<sub>2</sub>: Horiba MEXA 1300 FRI

Carbon monoxide and dioxide concentrations were measured with a Horiba MEXA 1300 FRI. This device uses the nondispersive infrared analysis method (NDIR). This method exploits the fact that each molecule absorbs infrared rays of a specific wavelength range. Thereby, the absorption intensity is proportional to the concentration of this molecule in the gas.

---

<sup>1</sup>Dr. M. Peckham, Cambustion Limited, personal communication.

The design of the device is quite compact. The sensor is mounted approximately 1 m from the tip of the probe. The exhaust gas is dehumidified before entering the measurement chamber. All this leads to a response time of 30 ms with a transport time delay from the probe to the sensor of 70 ms.

Since concentrations of the dried exhaust gas are measured, postprocessing of the data is necessary to obtain the absolute concentrations of the wet gas. Thereby, it is assumed that the exhaust gas is saturated at 5°C, to which it is cooled in the dehumidifier.

The calibration gas used for the measurements consisted of 10% CO and 14% CO<sub>2</sub> in N<sub>2</sub> at a relative accuracy of ±2%, i. e., ±0.2% CO and ±0.28% CO<sub>2</sub>, respectively. The precision of the device is ±1%. It exhibits a linearity of ±1% and a drift of ±2% per hour, all of the full scale [49]. All accuracies are provided by the manufacturer, which certainly include considerable safety factors. Tests revealed an excellent reproducibility of the signal levels, even after 24 h. Therefore, the overall maximum error of the (dry) CO and CO<sub>2</sub> signals was assumed to be 250 ppm for CO and 1000 ppm for CO<sub>2</sub> at all levels.

### 2.2.4 H<sub>2</sub>/O<sub>2</sub>/H<sub>2</sub>O/N<sub>2</sub>: Pfeiffer Omnistar

For the measurement of H<sub>2</sub>, O<sub>2</sub>, H<sub>2</sub>O, and N<sub>2</sub> a mass spectrometer Omnistar of Pfeiffer was used. This device uses quadrupole mass spectrometry to obtain the concentrations. The gas components are ionised in a vacuum chamber with a pressure of approximately 10<sup>-6</sup> mbar. They are accelerated such that all ions have approximately the same speed. Then, they have to pass an electrical field generated by a quadrupole, where the two opposite poles have the same potential. With the potentials imposed on the poles, the current of the ions passing the quadrupole can be focused such that only ions with a specific mass/charge ratio pass to a receiver, which measures the ion current. All other ions are deflected, leave the quadrupole in the lateral direction, and do not reach the receiver. Hence, the measured ion current at the receiver is proportional to the partial pressure of the specific species in the vacuum chamber.

The design of the mass spectrometer was modified in order to minimise the response time. Finally, the components could be measured with a response time of 12 ms per species and a transport delay of 70 ms. Since four species were measured, a total response time of approximately 120 ms resulted.

The ionisation of the gas species is obtained here by an electron bombardment, with an energy of about 90 eV. This leads not only to an ionisation of the gas components, but also to a fragmentation. This means that for example N<sub>2</sub> is not only ionised to N<sub>2</sub><sup>+</sup>, but also fragmented to N<sup>+</sup>. Since a part of the nitrogen consists of the <sup>15</sup>N isotope, signals are visible for the masses 28 (N<sub>2</sub><sup>+</sup>), 14 (N<sup>+</sup>), 29 (<sup>15</sup>N<sup>14</sup>N<sup>+</sup>), and 15 (<sup>15</sup>N<sup>+</sup>). Hence, overlapping can occur, if for

example  $\text{N}_2$  and  $\text{CO}$ , which both have a molecular mass of 28 g/mol occur simultaneously. Of course, the masses are not exactly the same, but the tiny difference cannot be resolved by this device, at least not when it is operated with the highest sampling rate.

$\text{H}_2$  is measured with the mass 2,  $\text{H}_2\text{O}$  with 17,  $\text{N}_2$  with 14, and  $\text{O}_2$  with 32. Potential interference on the mass 14 may arise from  $\text{CO}$  and  $\text{HC}$ . However, the sensitivity is very low, i. e., 0.8% ( $\text{CO}$ ) and 2.3% ( $\text{C}_3\text{H}_8$ ) of their total concentrations are detected on 14, with an ionisation energy of 90 eV [96]. Considering the low concentrations of these species as compared to the high concentration of  $\text{N}_2$  in the exhaust, this can be neglected. It is sometimes stated in the literature that water, which is present in the exhaust at a concentration of about 14%, also influences the hydrogen signal [33]. This is certainly true, if hydrogen is measured with the mass 1. However, if measured with 2, the sensitivity is very low. Tests have shown that a water concentration of roughly 40% causes an error of the hydrogen concentration of below 50 ppm. Hence, this influence can be neglected. Finally, methane ( $\text{CH}_4$ ) fragments are detectable both on the mass 14 (16%) and on 17 (1.2%). Since both the nitrogen and the water concentrations are very high as compared to the methane concentration in the exhaust, this cross sensitivity is also neglected.

In order to increase the sensitivity of the device, the secondary electron multiplier was used for every measurement. This led to a certain parallel drift of the ion currents. Hence, only the relative concentration of the four species could be obtained accurately, but not their absolute values.

In a first approach, the total mole fraction of the four species  $\text{H}_2$ ,  $\text{H}_2\text{O}$ ,  $\text{N}_2$ , and  $\text{O}_2$  was scaled to 100%. Together with the concentrations obtained from the other devices ( $\text{NO}$ ,  $\text{HC}$ ,  $\text{CO}$ , and  $\text{CO}_2$ ), the correct fractions could then be calculated by rescaling such that the total sum of all eight measured fractions in the exhaust was 100%. This procedure is described in more detail in Appendix A.

For the calibration of  $\text{H}_2$ ,  $\text{O}_2$ , and  $\text{N}_2$ , gas mixtures with 5000 ppm of  $\text{H}_2$  or  $\text{O}_2$  in  $\text{N}_2$  were available. The accuracy of the concentrations was  $\pm 1\%$ , i. e.,  $\pm 50$  ppm. Water was calibrated in saturated air. It is clear that both the water and the nitrogen calibrations are quite inaccurate, which was also reflected in the measurements, where a variance of up to  $\pm 1\%$  on a calibration to calibration basis occurred. Therefore, these two species were recalibrated on the running engine. Thereby, the engine was operated 10% lean, i. e., with a  $\lambda$  of 1.1. In this operating point, the  $\lambda$  sensor, upon which the engine was controlled, was assumed to be sufficiently accurate, i. e., the error was assumed to be below 0.5% in  $\lambda$ . Downstream of the TWC,  $\text{CO}$ ,  $\text{H}_2$ , and  $\text{HC}$  concentrations can be assumed to be zero at this operating point. Hence, the expected concentrations of  $\text{O}_2$ ,  $\text{H}_2\text{O}$ ,  $\text{N}_2$ , and  $\text{CO}_2$  could be calculated from stoichiometric considera-

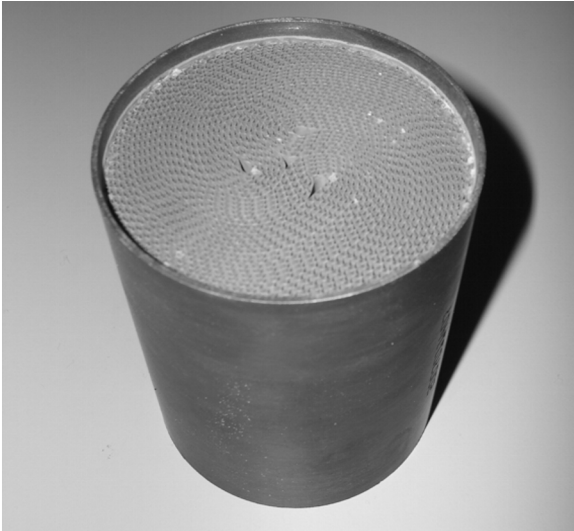


Figure 2.3: The TRI/X5 of the Umicore AG with a diameter of approximately 80 mm and a length of approximately 90 mm.

tions, taking into account the measured NO concentration. This recalibration procedure led to sufficiently accurate and reproducible results, both for N<sub>2</sub> and H<sub>2</sub>O. The procedure is described in more detail in Appendix A.

### 2.3 $\lambda$ Sensors

The wide-range  $\lambda$  sensors used in this investigation are heated, planar-type LSU 4 of the Robert Bosch GmbH. The manufacturer specifies the response time below 100 ms. Internal studies revealed that the response time of the sensors together with the evaluation unit lies well below 40 ms. The sensor was mounted directly behind the exhaust manifold, see Figure 2.2, which resulted in small transport time delays. Some aspects of the accuracy and use of the wide-range  $\lambda$  sensor are addressed in Section 4.5.

As for the switch-type  $\lambda$  sensors, the heated, planar-type LSF 4.7 of the Robert Bosch GmbH were used. The response time in a propane burner is asymmetric, i. e., dependent on whether the air-to-fuel ratio is switched from lean to rich or vice versa. The lean–rich response time is faster and specified below 60 ms. In the other direction, the sensor has a response time below 125 ms

according to the manufacturer. The sensor was only used downstream of the TWC, where it was mounted immediately behind the outlet, see Figure 2.2. The temperature of the sensor was neither controlled nor measured. Since the sensor clearly exhibited a temperature-dependent signal under rich operation, i. e., with  $\lambda < 1$ , the exhaust gas temperature was taken as a reference. This is discussed further in Chapter 5. A detailed model of a switch-type  $\lambda$  sensor is presented in Chapter 4.

## 2.4 Temperature and Mass Flow Sensors

The exhaust gas temperatures upstream and downstream of the TWC were measured with Phillips PT100 sensors. Their accuracy is  $\pm 0.5$  °C. The response time lies below 5 s. They can be applied in a temperature range from 0 °C to 1200 °C. The sensors were mounted approximately 1 cm away from the TWC, see also Figure 2.2.

The air mass flow was measured with a Hitachi hot film meter. The mass flow signal was integrated over one stroke at a rate of 256 kHz in order to obtain the air mass per cylinder. The integrator was triggered with the ICX3, see also Section 2.1. The air mass flow signal was calibrated against steady-state measurements, where the calibrated  $\lambda$  sensor and an accurate fuel meter (Flowtronic of the Quickly AG, Zürich) was used to calculate the steady-state reference air mass flow.

## 2.5 Three-Way Catalytic Converters

For every measurement in this thesis TRI/X5 converters of the Umicore AG have been used. These TWCs are coated with a double-layer washcoat. The lower layer is a mixture of palladium and oxygen storage material. The upper layer consists of platinum, rhodium, and oxygen storage material. The ratio of Pt/Pd/Rh is 1/8/1, the loading 100 g/ft<sup>3</sup>. The oxygen storage material mainly consists of oxides of cerium, which are doped with additives in order to increase the number of grid imperfections, which in turn enhances the mobility of the oxygen ions. Oxides of zirconium are also added, in order to increase the thermal stability of the washcoat. The washcoat lies on a metal substrate from Emitec, its cell density is 400 cells/in<sup>2</sup>.

The converter volume used for the experiments was 0.45 l. Since the engine was equipped with two exhaust gas lines, a displacement/TWC volume ratio of approximately 3 resulted. A picture of a TRI/X5 is shown in Figure 2.3.

Five TWCs at different ageing levels were available. Ageing had been performed with a hydrothermal procedure, where the converters had been exposed to a mixture of  $\text{H}_2\text{O}$ ,  $\text{CO}_2$ , and  $\text{N}_2$  during 24 hours at different temperatures. There was one fresh converter available, the others were aged at  $1100\text{ }^\circ\text{C}$ ,  $1000\text{ }^\circ\text{C}$ ,  $900\text{ }^\circ\text{C}$ , and  $800\text{ }^\circ\text{C}$ , respectively. It is somewhat difficult and arbitrary to compare this procedure to a corresponding field or dynamometer ageing, where e. g. a duration could be given in miles or kilometres. Therefore, such as reference has not been given here. To get a feeling of the ageing level, the relative storage capacities are depicted in Figure 2.4. Absolute values depend on the method of obtaining the storage capacity and are therefore somewhat arbitrary. The relative values presented here were obtained using the procedure described in Chapter 5.

The converters were mounted close to the engine, just behind the exhaust manifold, see also Figure 2.2. They were placed in a steel canning which was designed to allow an easy and quick exchange.

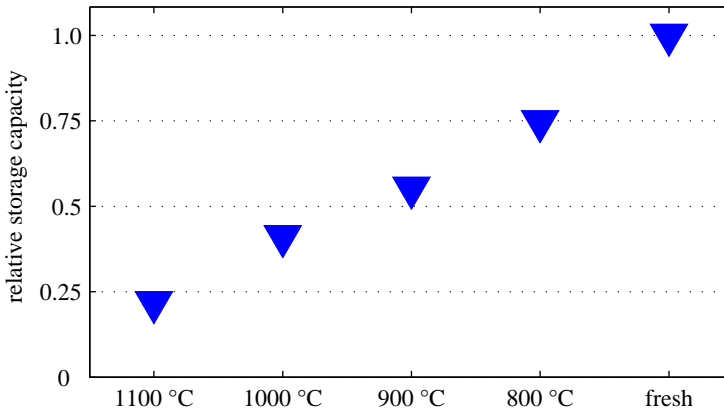


Figure 2.4: Relative storage capacities of the differently aged TRI/X5 converters. The fresh TWC has a relative capacity of 1. The temperatures of the ageing procedure are denoted on the abscissa.

# 3 Modelling of a Three-Way Catalytic Converter

## 3.1 Introduction

Three-way catalytic converters are very complex chemical reactors. Unfortunately, these reactors are not placed in a protected environment with constant ambient conditions. Mounted in the engine compartment of a car, they are subject to rapidly changing temperatures and fed with exhaust gas with a wide range of thermodynamical and chemical conditions, depending on the ambient conditions, the combustion in the engine, the driving mode, and the fuel. A detailed process model of a TWC can hardly cover all these conditions. Fortunately, this is not necessary, since a model usually addresses only few specific issues, leaving ample space for simplifications.

Various detailed TWC models have been presented in the literature. They usually account for the oxidation of CO and HC, and the reduction of NO. Often, the HC are represented by one or two specific HC components. In [6], a model has been developed, which includes a detailed kinetic reaction scheme of various species, except hydrogen. The storage mechanisms of oxygen and other species both on the noble metal and the ceria are described in detail. The model covers the dynamics both during cold start and hot operation of the TWC. Another very detailed model, which additionally includes hydrogen, has been presented in [31]. This model describes the kinetics on a Pt/Rh catalyst without ceria. A very complex scheme of elementary reactions is used. In this investigation, only steady-state results are presented. In [78] and [58], a model has been developed, which uses rather global kinetics including the water-gas shift reaction. The main focus is on the prediction of the cumulative emissions during a driving cycle. A model with a rather detailed water-gas shift and steam-reforming mechanism, taking into account the interaction of the noble metal and the ceria, has been presented in [54]. Additionally, this model also includes a sulfur reaction mechanism.

The latter model has been chosen as a basis for the one presented here, since it provides the main ideas for the description of the focused phenomena which will be discussed below. In the following, the focus of the model will be explained at first, using a measurement sample exhibiting some interesting as-

pects of the TWC dynamics. In the subsequent sections, the thermodynamics, the kinetics and the solution of the resulting equations including the parametrisation will be derived. Finally, a comparison of simulation samples with measurements will be presented.

## 3.2 Focus of the TWC Model

The model presented in this thesis focuses on the behaviour of the exhaust gas species limited by regulations (CO, HC, NO) and especially of the species driving the  $\lambda$  sensor output ( $O_2$ ,  $H_2$ ) during lean–rich and rich–lean transients. The goal is to determine the main dynamic phenomena in order to derive a simplified, control-oriented model which accounts for the storage effects of oxidising and reducing species and for distortions of the  $\lambda$  sensor signal, mainly induced by the ratio between  $H_2$ , CO, and HC. To illustrate these phenomena, some transients are presented in Figures 3.1 and 3.2. Concentration and  $\lambda$  measurements on a fresh and a considerably aged catalyst are shown. Both figures are based on the same measurements, where the inlet  $\lambda$  of the TWC has been switched from 1.05 (lean) to 0.95 (rich) at 10 s and back to 1.05 at 40 s. The engine was operated at a speed of 1500 rpm and a load of 30%.

After the lean–rich step, the stored oxygen is depleted by the reducing species. This leads to a delayed increase of these species, depending on the ageing of the TWC. The  $CO_2$  concentration increases during the depletion, since temporarily, more CO and (stored) oxygen are available. The subsequent rich phase exhibits significant differences between the two differently aged TWCs. The fresh catalyst shows a much higher water-gas shift and steam-reforming activity than the aged one. The ratio between  $H_2$  and CO is much closer to the expected equilibrium, which would be at around 3–4 at this temperature. Thus, with increased ageing, the TWC operates further away from equilibrium. Considering the aged TWC, it can even be seen that the hydrogen concentration increases at first after the lean–rich step and then decreases again after approximately 15 s. This indicates a phenomenon which obviously hinders the catalytic activity, moving the TWC away from equilibrium.

After the rich–lean step, the  $O_2$  and NO breakthroughs are delayed, because oxygen is being stored. After a negative peak of the  $CO_2$  concentration caused by a corresponding peak of the TWC inlet  $\lambda$ , the level is temporarily increased. This is very clearly visible for the fresh TWC between 40 and 50 s. Since the inlet CO and HC concentrations are low at this point, this additional  $CO_2$  can only stem from stored carbonaceous species. This has been suspected in the literature, see e. g. [52].



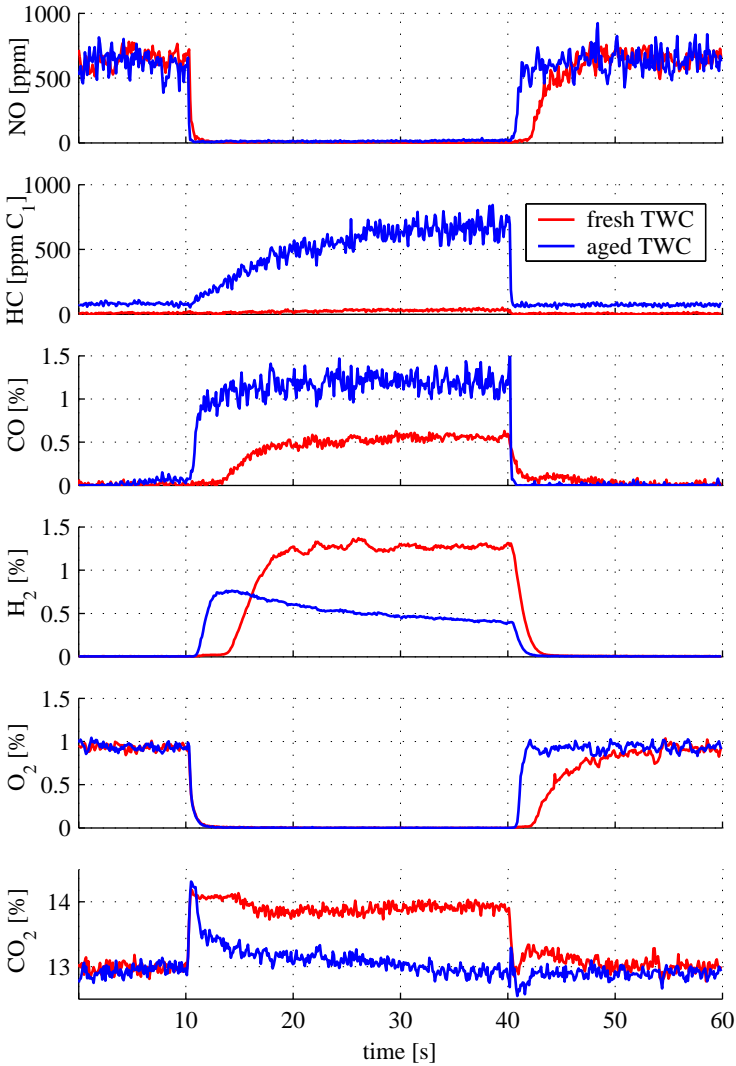


Figure 3.1: Concentrations of NO, HC, CO, H<sub>2</sub>, O<sub>2</sub>, and CO<sub>2</sub> downstream of the TWC during  $\lambda$  steps from 1.05 to 0.95 at 10 s and at back to 1.05 at 40 s.

The  $\lambda$  sensor signals in Figure 3.2 show a significant sensitivity to the ratio between H<sub>2</sub>, CO, and HC. This has already been found in earlier investigations,

### 3 Modelling of a Three-Way Catalytic Converter

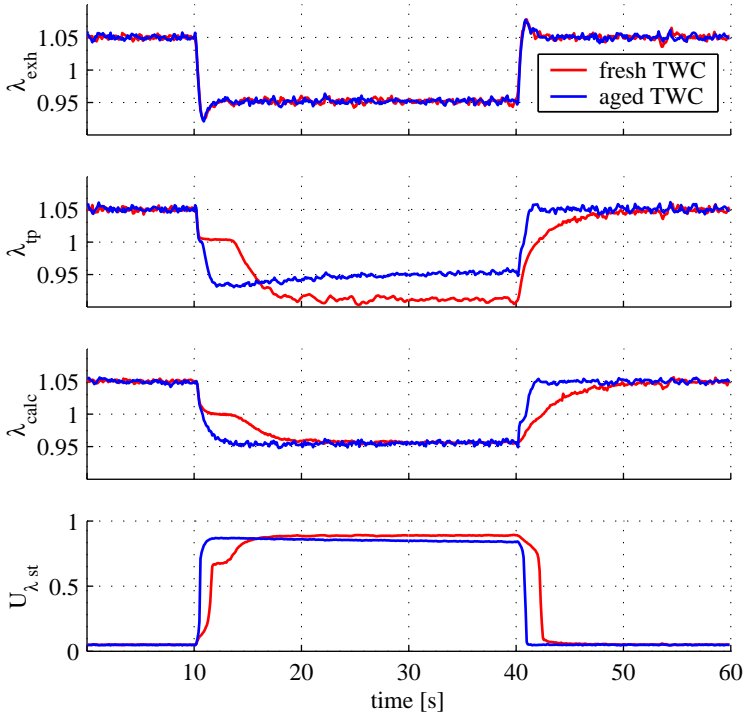


Figure 3.2: Transients of the  $\lambda$  upstream and downstream of the TWC measured with the wide-range  $\lambda$  sensor ( $\lambda_{exh}$  and  $\lambda_{tp}$ ), of the  $\lambda$  downstream calculated from (1.4) ( $\lambda_{calc}$ ), and of the switch-type  $\lambda$  sensor downstream ( $U_{\lambda, st}$ ) during  $\lambda$  steps from 1.05 to 0.95 at 10 s and at back to 1.05 at 40 s.

see [2], [4], or [42]. Here, also the “true”  $\lambda$  has been calculated from the measured species, using (1.4). It can be clearly seen that the steady-state value of this signal matches the one of the inlet  $\lambda$ , which is of course expected. However, both the wide-range and the switch-type  $\lambda$  sensor signals are significantly distorted by the hydrogen. The wide-range  $\lambda$  sensor signal downstream of the fresh TWC exhibits an offset of approximately 80% during the rich phase!

The goal of the model presented here is to account for the phenomena described above. If the main issues such as catalyst deactivation, the ratio between  $H_2$ , CO, and HC, and storage dynamics can be covered and understood, they can be incorporated in a control-oriented model, which is used both for TWC diagnosis and control. The key is thereby to account for the distortion of the

$\lambda$  sensor signal, which is obviously closely related to the ageing of the TWC. Hence, the distortion is used to obtain additional information on the system, which is essential for diagnosis, see also [79].

The kinetics of the model presented here are deliberately kept as slim, global, and “phenomenological” as possible, which might disturb a reader with a chemical-engineering background. A deeper understanding of both the deactivation mechanism and the water-gas shift or steam-reforming mechanisms are not subject of this thesis since a proper investigation of this kind is certainly in better hands when pursued by chemical engineers with the appropriate infrastructure.

The model presented here has already been published in [5]. Here, it will be explained in more detail. Additionally, results from differently aged TWCs at various operating points will be presented.

### 3.3 Process Model of the TWC

The TWC model presented in the following is referred to as the “process model”, because its goal is to understand the most important dynamics as described above, rather than the use in a control system. For that purpose, a much simpler model will be derived in Chapter 5. The model should be able to reproduce the dynamic input-output behaviour of all measured species at least qualitatively. The concentrations of NO, CO, HC, CO<sub>2</sub>, H<sub>2</sub>, O<sub>2</sub>, H<sub>2</sub>O, and N<sub>2</sub> have been considered. Since only the total HC concentration could be measured, C<sub>3</sub>H<sub>6</sub> has been used as a “representative” for the hydrocarbon species, following the investigation presented in [54].

The cross sectional distributions of the flow velocity, temperature, and concentration profiles in the exhaust upstream of the TWC have been assumed to be uniform. In reality, this is hardly the case. However, the focus here is on the main dynamic phenomena, rather than on the TWC’s overall performance, which can be significantly influenced by the flow velocity profile. Hence, only one channel has been modelled, using a one-dimensional approach. Geometry and material parameters such as storage capacities have been assumed to be constant along the flow axis. In reality, ageing mechanisms close to the inlet are different from those close to the outlet of the TWC. At the inlet, TWC deactivation occurs mainly because of poisoning. Towards the tail, more thermal effects are dominant, such as sintering. Additionally, deactivation does not occur uniformly on the TWC cross section, it is rather dependent on the exhaust gas flow velocity profile at the inlet of the TWC, see e. g. [55]. All phenomena eventually lead to a reduction of the oxygen storage capacity [93].

The cross sectional flow velocity profile in one channel is not constant along

the flow axis. Especially close to the inlet, the boundary layers are built up and some lateral inlet flow disturbances might still be effective. Since the length of one channel exceeds its diameter by two orders of magnitude, these effects have been neglected. A constant, fully developed flow velocity profile has been assumed throughout the channel [50].

#### 3.3.1 Thermodynamic Model of the TWC

The thermodynamic model has been derived from [6]. Figure 3.3 shows a sketch of the heat and mass transfer terms and of the cross sectional geometry of the TWC. Two gas phases and one solid phase have been considered. The first (outer) gas phase includes the gas in the core of the channel. Hence, convective mass flow and heat transfer in the axial direction are considered. Additionally, mass is exchanged with the second gas phase by means of radial diffusion. The second (inner) gas phase contains the washcoat and the boundary layers. Here, no axial convection occurs. Mass is exchanged in the radial direction with the outer gas phase on the one hand by means of diffusion, and with the solid surface on the other hand by means of adsorption or desorption, respectively.

One mass balance per gaseous species can be formulated for the inner and the outer gas phases. Additionally, mass balances for the adsorbed species establish the kinetic model. The axial temperature distribution is assumed to be identical for the two gas phases. Hence, two energy balances, one for the gas and one for the solid phase, can be derived.

The mass balance for the gas phase species  $i$  in the channel consists of a convective term, an axial diffusion term and a radial diffusion term, which describes the mass exchange between the two gas phases. Mathematically, this can be expressed as follows:

$$\begin{aligned} \varrho_g \varepsilon \frac{\partial w_i}{\partial t} &= \varepsilon D_{eff} \frac{\partial^2 w_i}{\partial z^2} - \frac{\dot{m}_{exh}}{A_{cs}} \frac{\partial w_i}{\partial z} - D_i A_{geo} (\varrho_g w_i - \varrho_{wc} v_i) \\ &\quad + w_i \sum_j D_j A_{geo} (\varrho_g w_j - \varrho_{wc} v_j) \end{aligned} \quad (3.1)$$

$w_i$  denotes the mass fraction of the species  $i$  in the channel along the axial coordinate  $z$ ,  $v_i$  the mass fraction in the washcoat. On the right-hand side of the equation, the first and the second terms stand for the diffusive and the convective mass transport. The former is small as compared to the latter and has mainly been accounted for to increase the numerical stability of the solver. The gas dispersion coefficient  $D_{eff}$  and the exhaust gas mass flow  $\dot{m}_{exh}$  are assumed to be constant throughout the TWC. The last two terms on the right denote the radial mass exchange between the channel and the washcoat. The

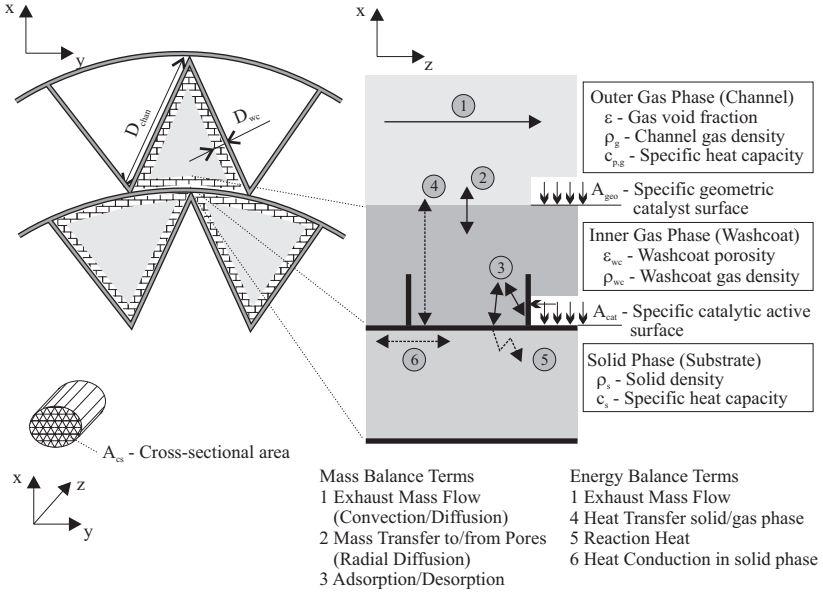


Figure 3.3: Sketch of the TWC structure and the terms of the balance equations. View from the front (on the left) and from the side (on the right) of the TWC.

last term is necessary to keep the sum of all mass fractions at 1, see also Appendix B.1. The geometry parameters are illustrated in Figure 3.3.  $D_i$  is the radial mass transfer coefficient. With mass flows ranging from 5 to 50 g/s and a viscosity of  $3.4 \cdot 10^{-5}$  Ns/m<sup>2</sup> (at 800 K), the Reynolds number hardly exceeds 500. Hence, the flow is laminar and a constant Sherwood number  $Sh_D$  of 2.47 can be assumed for a triangular shaped tube, see [50].  $D_i$  can be calculated from the Sherwood number:

$$Sh_D = 2.47 = \frac{D_i D_{chan}}{D_{iN_2}} \quad (3.2)$$

$D_{iN_2}$  is the binary diffusion coefficient of the species  $i$  in  $N_2$ . It is calculated as proposed by Füller et. al., see [84]:

$$D_{iN_2} = \frac{143 \cdot T_g^{1.75}}{p_{exh} \sqrt{M_{i,N_2}} \left[ \sum_{v,i}^{1/3} + \sum_{v,N_2}^{1/3} \right]^2} \quad (3.3)$$

### 3 Modelling of a Three-Way Catalytic Converter

where  $\Sigma_v$  is the diffusion volume and

$$\sqrt{M_{i,N_2}} = \frac{\sqrt{2}}{\sqrt{\frac{1}{M_i} + \frac{1}{M_{N_2}}}}. \quad (3.4)$$

Notice that the units of  $M_{i,N_2}$  and  $D_{iN_2}$  are g/mol and cm<sup>2</sup>/s, respectively.

The mass balance for the species  $i$  in the inner gas phase does not contain any convective or axial diffusion terms, only radial mass transport occurs. On the channel side, mass is exchanged with the channel phase by means of radial diffusion. On the solid surface side, mass is exchanged by means of adsorption and desorption. Since the shape of one channel is roughly an isosceles triangle, the reference volumes for the washcoat and the gas phase have been assumed as follows:

$$\begin{aligned} dV_{wc} &= 3D_{wc}D_{chan}dz \\ dV_g &= \frac{\sqrt{3}}{4}D_{chan}^2dz \end{aligned}$$

Hence, the mass balance equation for species  $i$  in the washcoat/boundary layer reads as follows:

$$\begin{aligned} \rho_{wc}\varepsilon_{wc}\frac{4\sqrt{3}D_{wc}}{D_{chan}}\frac{\partial v_i}{\partial t} &= D_iA_{geo}(\rho_g w_i - \rho_{wc} v_i) \\ &\quad - v_i \sum_j D_j A_{geo}(\rho_g w_j - \rho_{wc} v_j) \\ &\quad + \Delta r_i - v_i \sum_j \Delta r_j \end{aligned} \quad (3.5)$$

Notice that no gas phase reactions have been assumed to occur. The first two terms on the right-hand side denote the mass exchange with the channel phase. The subsequent terms describe the mass exchange with the solid phase by means of sorption. Thereby,  $\Delta r_i$  stands for the mass transfer of species  $i$ . Again, a balancing term is required, which ensures that the sum of all mass fractions remains 1. The mass transfer term is calculated from the reaction rates involving sorption. For species  $i$  with a total sorption rate  $r_{sorption}$  e. g. from the noble metal, the mass transfer rate is obtained as follows:

$$\Delta r_i = r_{sorption,i}L_sA_{cat}M_i \quad (3.6)$$

The calculation of  $r_{sorption}$  will be discussed in Section 3.3.2.  $L_s$  is the surface storage capacity of the noble metal ( $L_{NM}$ ) or the ceria ( $L_{Cer}$ ).

The energy balance for the gas phase incorporates a heat conduction term and a convective heat transport term in the axial direction (1<sup>st</sup> and 2<sup>nd</sup> term in (3.7)). In the radial direction, heat is exchanged with the solid phase by means of “convective” heat transfer (3<sup>rd</sup> term in (3.7)). Thus, the energy balance for the gas phase can be formulated accordingly:

$$\rho_g \varepsilon c_{p,g} \frac{\partial T_g}{\partial t} = \varepsilon \lambda_g \frac{\partial^2 T_g}{\partial z^2} - \frac{\dot{m}_{exh}}{A_{cs}} c_{p,g} \frac{\partial T_g}{\partial z} + \alpha A_{geo} (T_s - T_g) \quad (3.7)$$

Notice again that no gas phase reactions have been assumed to occur.  $\lambda_g$  denotes the heat conductivity in the gas phase,  $\alpha$  the heat-transfer coefficient between the gas and the solid phase. Again, a constant Nusselt number of 2.47 can be assumed in the laminar flow, see also [50]. Thus,  $\alpha$  can be calculated using the following expression:

$$Nu_D = 2.47 = \frac{\alpha D_{chan}}{\lambda_g} \quad (3.8)$$

The energy balance for the solid phase only includes axial heat conduction (1<sup>st</sup> term in (3.9) with the heat conductivity  $\lambda_s$ ) and the heat transfer (2<sup>nd</sup> term) in the radial direction. Additionally, heat production from the chemical reactions on the solid surface occurs (3<sup>rd</sup> term):

$$\rho_s (1 - \varepsilon) c_s \frac{\partial T_s}{\partial t} = (1 - \varepsilon) \lambda_s \frac{\partial^2 T_s}{\partial z^2} - \alpha A_{geo} (T_s - T_g) + A_{cat} \sum_j -\Delta H_j \cdot R_j \quad (3.9)$$

$\Delta H_j$  denotes the enthalpy of the species  $j$ ,  $R_j$  the net production rate.

Since the heat production of each reaction is somewhat difficult to estimate, only the net production (if negative: consumption) rates of CO, CO<sub>2</sub>, H<sub>2</sub>O, C<sub>3</sub>H<sub>6</sub>, and NO have been accounted for. The enthalpies of O<sub>2</sub>, H<sub>2</sub>, and N<sub>2</sub> are zero. Additionally, the reaction enthalpy of the ceria oxidation has been taken into account:



The values for the enthalpies used in the model are listed in Appendix B.2. This simple approach of course influences the transient behaviour of the TWC temperature. Since temperature changes on the solid phase occur relatively slowly, as long as phenomena such as light-off are omitted, this method for the calculation of the heat production has been assumed to be sufficiently accurate.

### 3.3.2 Kinetics of the TWC

The mass balances of the adsorbed species on the solid phase are obtained using Langmuir-Hinshelwood and Eley-Rideal mechanisms. Thereby, the occupancies<sup>1</sup> of each species  $i$  on the noble metal ( $\theta_i$ ) and the ceria surfaces ( $\Psi_i$ ) are calculated as follows:

$$\frac{\partial \theta_i}{\partial t} = r_{\text{adsorption},i} - r_{\text{desorption},i} + \sum_j (\nu_{i,j} \cdot r_{\text{reaction},j})$$

The noble metal and the ceria surfaces are modelled as two different independent storage capacities which exchange mass with the gaseous phase via sorption. On the noble metal, various species compete for the same surface sites, whereas on the ceria, only oxygen adsorption is taken into account. The surface diffusion has been assumed to be instantaneous, i. e., there is perfect mixing of the adsorbed species.

The adsorption rate is calculated using statistical thermodynamics, see e. g. [1] or [44]. It is dependent on the number of molecule-surface collisions per time unit and on the relative vacant surface  $\theta_V$ , which is defined as

$$\theta_V = 1 - \sum_i \theta_i \quad i = \text{O, CO, H, } \dots \quad (3.11)$$

The adsorption rate can be formulated as follows:

$$r_{\text{adsorption},i} = s \sqrt{\frac{\mathfrak{R}T_g}{2\pi M_i}} \frac{1}{L_s} c_i \theta_V \quad (3.12)$$

$s$  denotes the sticking probability, which is mainly a correction factor. Although some adsorption reactions also contain dissociation mechanisms, as will be shown further below, no extensions such as Arrhenius terms have been used for the adsorption, i. e., it has been assumed that the adsorption itself is always rate determining.

The desorption rate coefficient is obtained from an Arrhenius-Ansatz. The rate is dependent on the availability of the species on the surface  $\theta_i$ , and on the solid surface temperature  $T_s$ :

$$r_{\text{desorption},i} = A_{des} e^{\frac{-E_{des}}{\mathfrak{R}T_s}} \theta_i \quad (3.13)$$

$A_{Des}$  is the pre-exponential factor,  $E_{Des}$  denotes the activation energy.

<sup>1</sup>The occupancy  $\theta_i$  denotes the fraction of the surface which is covered with the species  $i$ .

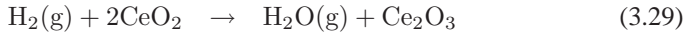
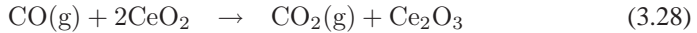
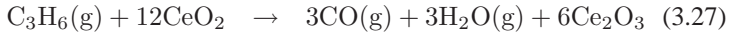
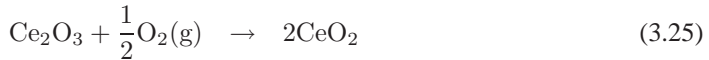
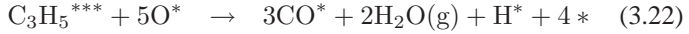
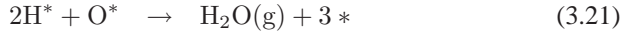
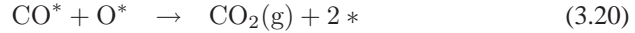
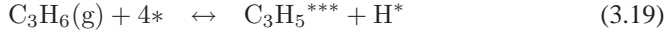


The reaction rate coefficient is also determined from the Arrhenius-Ansatz. The rate is dependent on the occupancies of the reacting species, if Langmuir-Hinshelwood kinetics are applied:

$$r_{\text{reaction,LH}} = A_{\text{reac,LH}} e^{\frac{-E_{\text{reac}}}{\mathfrak{R}T_s}} \theta_i \theta_j \quad (3.14)$$

As for the Eley-Rideal kinetics, the rate is dependent on the occupancy of the

Table 3.1: Reaction scheme of the TWC model.



The reaction scheme has been mainly derived from [54]. \* denotes a vacant site on the noble metal. Superscript \* stands for adsorbed species (on the noble metal). The number of \* represents the number of vacant sites occupied by the adsorbed species.

adsorbed species and on the concentration of the gaseous species. Theoretically, similar considerations should be made as for the adsorption rates. However, for the sake of simplicity, also the Arrhenius-Ansatz is applied. Notice

that the unit of the pre-exponential factor  $A_{\text{reac,ER}}$  has to be adapted accordingly.

$$r_{\text{reaction,ER}} = A_{\text{reac,ER}} e^{\frac{-E_{\text{reac,LH}}}{RT_s}} \theta_i c_j \quad (3.30)$$

Table 3.1 shows the reaction scheme used in the model. Reactions on the noble metal surface (3.15–3.24) are modelled using Langmuir-Hinshelwood kinetics. Reactions on the ceria (3.25–3.27) follow the Eley-Rideal mechanism. In [6], also the adsorption of CO, NO, and NO<sub>2</sub> on the ceria surface has been taken into account. Additionally, species adsorbed on the noble metal can be oxidised by oxygen adsorbed on the ceria surface. This has been omitted here in order to keep the model as simple as possible.

#### Oxygen Storage

Oxygen can adsorb on the noble metal (3.15) and on the ceria (3.25). The desorption has been assumed to be very weak. Therefore, it has been neglected in the parametrisation of the models. The adsorption and dissociation are modelled in one step, where the adsorption is the rate determining step.

No exchange of oxygen between the noble metal and the ceria has been modelled. For simplicity, the two phases have been kept separated, which is certainly not the case in reality. Reducing species adsorbed on the noble metal react with oxygen from the ceria at the phase boundary [6]. Additionally, it has been shown that in reality, oxygen is exchanged between the noble metal and the ceria [95].

The ceria mainly contributes to the oxygen storage capacity. Oxygen storage in the bulk has not been taken into account, i. e., the total storage capacity has been collected in one surface capacity.

#### NO Reduction

The reduction of NO occurs via adsorption (3.18), dissociation (3.23) and N<sub>2</sub> formation (3.24). This implies that vacant surface sites are necessary. During lean operation, the surface is mainly occupied by oxygen. Therefore, the NO dissociation is hindered. Because of the abundance of oxygen, the back reaction of (3.23) is additionally dominant. Hence, oxygen is preferred for the oxidation of reducing species. Under rich operation, the NO reduction is efficient, as long as the surface is rather free. With increasing deactivation, presumably by carbonaceous species, also the NO dissociation becomes more inhibited. This leads to a reduced NO conversion under rich operation, as has been reported in e. g. [29].

Other compounds of N and O, such as  $\text{N}_2\text{O}$  or  $\text{NO}_2$  have been neglected. Reaction schemes including  $\text{NO}_2$  have been presented in [53] and [6].

## CO Oxidation

The CO oxidation occurs on the noble metal via (3.16) and (3.20), and on the ceria via (3.28). The first reaction path is straightforward and widely applied in the literature, see e. g. [54], [6], or [31]. The  $\text{CO}_2$  adsorption has been omitted here, no back reaction of (3.20) occurs. The oxidation with oxygen from ceria might also be modelled with CO adsorbed on the noble metal instead of the gaseous form, as has been proposed in [24]. However, in [95], it has been observed that only a limited amount of oxygen on the ceria is accessible for the oxidation of adsorbed CO on the noble metal. In [6], even the adsorption of CO on the ceria and on the oxidised noble metal surface (to form OCO) had been accounted for. From a phenomenological and thus much simplified point of view it is important that the presence of ceria significantly increases the CO oxidation. This has been taken into account here by the application of the Eley-Rideal mechanism, where the two reactants do not compete for the same surface sites.

## HC Oxidation

The HC are represented by propene,  $\text{C}_3\text{H}_6$ . This choice follows the model presented in [54]. Often, propene or propane are chosen as a replacement for all HC. In [6],  $\text{C}_2\text{H}_2$  and  $\text{C}_2\text{H}_4$  have been used to represent slow and fast oxidised hydrocarbons. With the approach chosen here, the specific properties of different hydrocarbons (alkanes, alkenes, aromates etc.) are collected in the one chosen species,  $\text{C}_3\text{H}_6$ . Hence, also properties such as coking, which are more attributed to alkanes, see [10], [25], or [13], are modelled with propene.

The oxidation of  $\text{C}_3\text{H}_6$  in the model takes place on the noble metal via (3.19) and (3.22) and on the ceria via (3.27). The scheme has been adopted from [54]. The adsorption on the noble metal includes the dissociation, where the breaking of one C-H bond is involved. The oxidation to adsorbed CO, H, and gaseous water has been modelled in one step. A very detailed scheme, where the breaking of each C-H bond was taken into account, has been presented in [31]. It has been assumed that one adsorbed  $\text{C}_3\text{H}_5$  molecule occupies three sites on the noble metal. This is again a rough assumption, based on phenomenological observations. It will be shown that in this model, the deactivation under rich operation mainly occurs because of site occupation by hydrocarbons. In reality, it is not entirely clear, what species actually occupies the sites. From exhaust gas measurements, see also Figure 3.1, it is evident that some carbona-

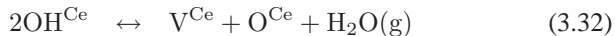
ceous species are involved. It has been assumed that one surface site is used per C atom, which leaves space for interpretation about the form of the adsorbed species. Above all, this assumption has brought about the best simulation results. In [62], it has been shown that “coking” with  $\text{CH}_x$  indeed occurs on a Rh/alumina/ceria catalyst, when exposed to propane pulses. Additionally, it has been shown there that the conversion rate for the steam-reforming reaction rapidly decreases after the first pulse because of coking.

HC oxidation on the ceria is implemented using an Eley-Rideal mechanism. No competition for vacant surface site between the reactants occurs. As on the noble metal,  $\text{C}_3\text{H}_6$  is oxidised to gaseous CO and water.

## **H<sub>2</sub> Oxidation and H<sub>2</sub>O Dissociation**

The oxidation of the H<sub>2</sub> occurs, like the CO and the HC, both on the noble metal via (3.17) and (3.21), and on the ceria via (3.29). The mechanism is in both cases simple and straightforward.

In [54], a reaction path on the ceria has been proposed, where adsorbed hydrogen (on the noble metal) and oxygen (on the ceria) react to form OH on the ceria as an intermediate product. Two OH ions may react to water, leaving an oxidised and an empty site on the ceria:



The corresponding back reactions describe the adsorption and dissociation of water, providing the necessary steps for the water-gas shift and the steam-reforming reactions. Also other authors have described the occurrence of OH, see e. g. [34] or [98]. In [62], it has even been shown that hydroxyl is very mobile and spillover to the noble metal occurs.

In [34], it has been stated that the OH occupancy is responsible for the deactivation of the water-gas shift reaction under rich operation. That investigation was made with Rh/Al<sub>2</sub>O<sub>3</sub> catalysts, where only the water-gas shift reaction was focused on, i. e., hydrocarbons were not present. Considering the transient behaviour of the aged TWC in Figure 3.1, it can be seen that the water-gas shift reaction is deactivated rather fast after the lean–rich step (approximately after 5 s). However, the deactivation of the steam-reforming reaction is much slower (approximately 20 s after the step). Hence, another mechanism must be responsible for this deactivation. Since no increased water or hydrogen concentrations have been observed after the rich–lean step, it has been concluded that the OH occupancy is only responsible for the “fast” deactivation of the water-gas shift reaction.

The goal of this investigation was to keep the reaction scheme as slim as possible. Therefore, the water adsorption and dissociation was considered more on a phenomenological level. It is described by reaction (3.26). Hence, water is adsorbed on the ceria and dissociated to adsorbed hydrogen on the noble metal and oxygen on the ceria, if vacant sites are available both on the noble metal and on the ceria. Under lean operation, the occupancy on the surfaces by oxygen inhibits the adsorption of water. Additionally, hydrogen from the water dissociation is immediately oxidised because of the abundance of oxygen. Under rich operation, water adsorption is inhibited, if the noble metal surface is coked, i. e., covered with hydrocarbons. It will be shown that this very simple approach suffices to describe the rather complex behaviour of the  $H_2$ , CO, and HC concentrations during a lean–rich step. The same mechanism, which inhibits the water-gas shift reaction will be shown to also hinder the NO dissociation. It is clear that this is a purely phenomenological approach, but hopefully it provides some inspiration for more detailed reaction schemes.

### The Role of Sulfur

Basically, sulfur plays an important role in the deactivation of the TWC, especially during rich operation, see e. g. [29]. It occurs in the exhaust mainly as  $SO_2$  and is assumed to inhibit the water-gas shift and the steam-reforming reactions, especially on Pd and ceria [70]. Additionally, it has been found to hinder even NO reduction under rich operation [29]. Exactly these phenomena are focused on here and can be reproduced by the TWC model (see Figures 3.7–3.9). For all experiments presented in this thesis, a fuel with a rather low sulfur content (17 wtppm) was used. Therefore, sulfur was neglected. However, there is no contradiction of this thesis with the cited work, since it is still possible that sulfur promotes the mechanisms presented here. This means that the TWC is deactivated by stored carbonaceous species, but the storage mechanism itself can be enhanced by the presence of sulfur. In fact, it has been observed in [10] that  $SO_2$  promotes the coking of the TWC, when alkanes are present.

### 3.3.3 Simulation and Model Calibration

For eight gas species in two phases, seven adsorbed species and two temperatures (gas phase and solid phase), a total of 23 mass balances and 2 energy balances have to be calculated simultaneously. The balance equations were solved with PDEXPACK [72]. PDEXPACK is a method-of-lines solver for systems of parabolic differential equations in one space dimension. For the spatial discretisation, second order finite differences are applied. For the time discretisation, a semi-implicit Euler method is used, which combines the ad-

vantages of an implicit method (stability) with the advantages of an explicit method (no iteration). A two dimensional extrapolation method is applied to calculate solutions of higher order and to estimate separate errors of the state variables in time and space. Based on these error estimations, an equilibration of the errors is achieved through inserting gridpoints in regions of high errors and cancelling gridpoints in regions of small errors (local regridding). Finally, such a combination of spatial grid, time step and extrapolation order, promises an optimised performance of the method for a user specified tolerance.

In order to facilitate the use of this package, a Matlab<sup>TM</sup> GUI was developed. This GUI allows an efficient parametrisation of both the model and the solver, and a convenient and flexible handling of the input and the output data. Since the GUI runs under Matlab<sup>TM</sup>, powerful graphical tools are accessible directly from the GUI.

For the model parameters describing the TWC geometry, physically reasonable values were chosen. They are presented in Appendix B.2. As for the kinetic parameters and the storage capacities, a different approach was taken. Since the model uses rather global kinetics, parameters could not be obtained from the literature. Therefore, they were calculated using an optimisation routine which minimises the error between measured and simulated transients of the gas concentrations during steps between lean and rich inlet exhaust gas mixtures. For this purpose, the model and the solver had to be simplified, since one simulation of 100 s takes approximately 10-60 minutes with the PDEXPACK<sup>2</sup>. The longitudinal axis was divided into five cells. Then, an implicit Rosenbrock algorithm of 4th order was applied to solve the set of ordinary differential equations, see [83]. The calculation demand for this model is considerably reduced as compared to the original model.

The simplified model was used for an automated adjustment to measured concentration transients by means of a non-linear leastsquares algorithm [64]. The reference measurements consisted of low-frequency  $\lambda$  excitations at steady-state engine operating points. Thereby,  $\lambda$  was switched between 0.97 and 1.03 every 30 s. In order to keep the calculation burden manageable, only three operating points and three ageing levels of the TWC were considered for the parameter fitting procedure. The resulting reaction constants were fitted according to the Arrhenius-Ansatz (pre-exponential factor  $A$  and activation energy  $E$ ).

The parameters were obtained in three iterations. In the first iteration, all parameters were identified. In the second iteration, the sticking probabilities  $s$ , and in the third iteration additionally the storage capacities  $L_{NM}$  and  $L_{Cer}$  were fixed.

---

<sup>2</sup>All Simulations were performed on a PC with a Pentium IV processor (3.2 GHz) running under Windows XP.

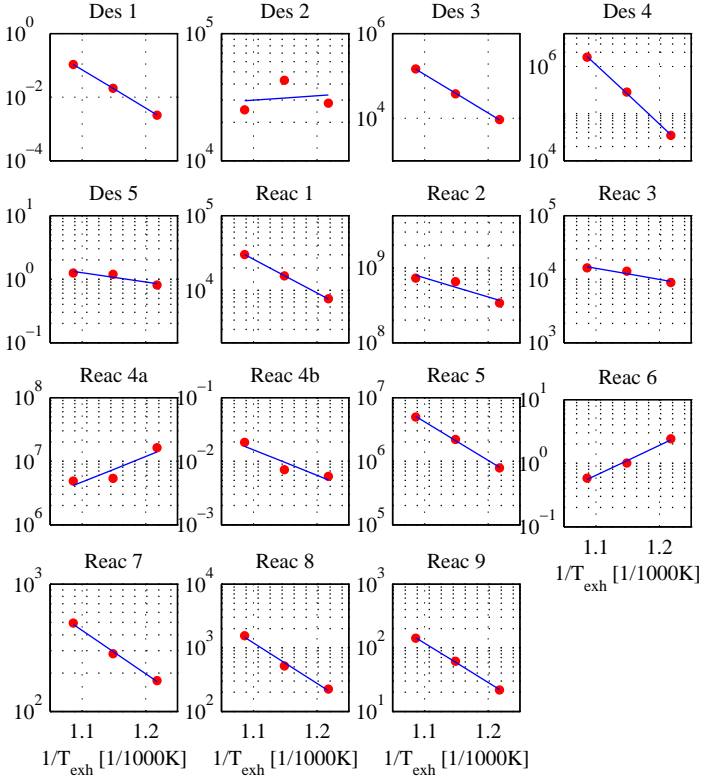


Figure 3.4: Kinetic parameters obtained from the calibration. Des 1 – Des 5 denote the kinetic parameters according to (3.13) of the desorption reactions (3.15)–(3.19). Reac 1 – Reac 9 denote the kinetic parameters according to (3.14) and (3.30) of the reactions (3.20) – (3.29). The dots mark the value obtained by the optimisation, the lines are fitted according to the Arrhenius Ansatz using a least-squares algorithm.

An example of the desorption and reaction parameters is presented in Figure 3.4. The three operating points, where the model was calibrated are depicted in Table 3.2. The TWCs used for the procedure were considerably aged (at 1100 °C), moderately aged (at 900 °C) and fresh, see also Section 2.5. The storage capacities of the noble metal ( $L_{NM}$ ) and the ceria ( $L_{Cer}$ ) obtained from the calibration are shown in Figure 3.5. Actually, the total storage capacity is dependent on both the specific capacity  $L_{NM}$  or  $L_{Cer}$  and on the catalyst

### 3 Modelling of a Three-Way Catalytic Converter

Table 3.2: Operating points for the calibration of the TWC model.

Nr	$n_{eng}$ [rpm]	load [%]	$T_{exh}$ [K]	$\dot{n}_{exh}$ [g/s]
1	1500	30	775	7.5
2	1750	35	830	10.4
3	2000	40	875	13.8

The exhaust gas mass flow corresponds only to one exhaust gas line here.

surface  $A_{cat}$ . Ageing might in fact influence both parameters. Presumably, thermal ageing leads to a reduction of  $A_{cat}$ , whereas poisoning affects  $L_{NM}$  and  $L_{Cer}$ . However,  $A_{cat}$  has been assumed to remain constant here, whereas  $L_{NM}$  and  $L_{Cer}$  have been assumed to be subject to ageing.

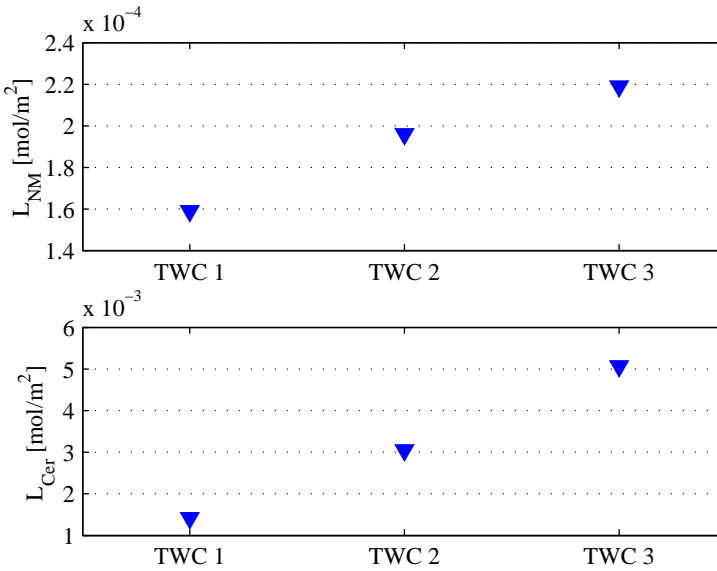


Figure 3.5: Storage capacities  $L_{NM}$  and  $L_{Cer}$  of the differently aged TWCs. TWC 1 denotes the considerably aged (at 1100 °C) converter. TWC 2 is moderately aged (at 900 °C), and TWC 3 is fresh.



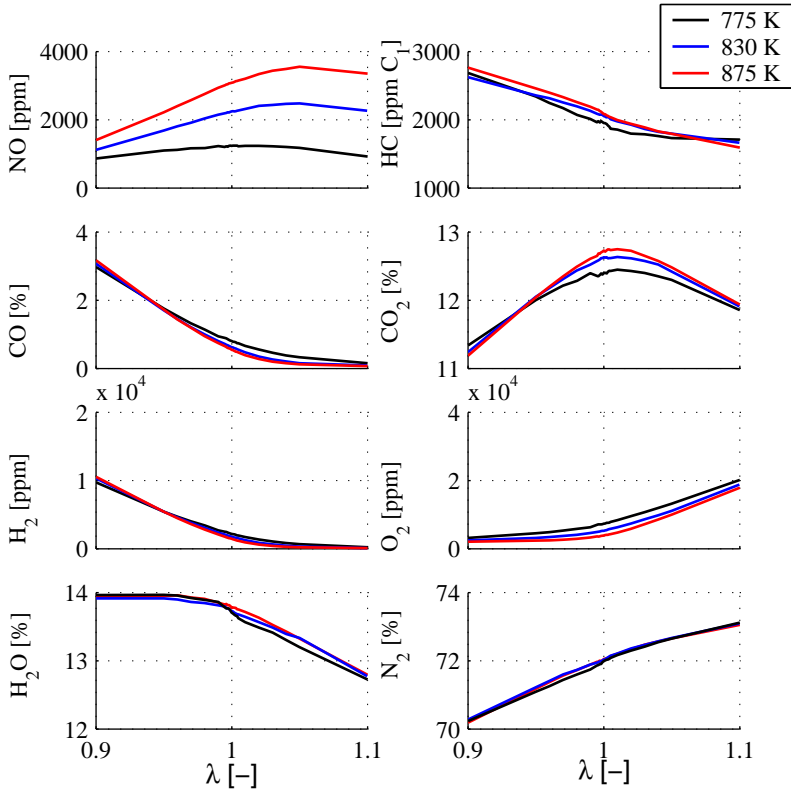


Figure 3.6: Measured raw exhaust gas concentrations dependent on  $\lambda$  at different engine operating points corresponding to the exhaust gas temperature depicted in the legend.

The inlet concentrations were obtained from steady-state measurements. The concentrations are dependent on the air-to-fuel ratio  $\lambda$  and on the engine operating point, i. e., the exhaust gas temperature. They are shown in Figure 3.6. The instantaneous inlet concentration of each species was calculated by interpolation using the  $\lambda$  value from the sensor and the exhaust gas temperature. All parameters obtained from the calibration procedure are presented in Appendix B.2.

## 3.4 Simulation Results vs Measurements

Simulations have been performed in various operating points with differently aged TWCs. For all simulations, the same kinetic parameters have been used (see Appendix B.2) apart from the storage capacities, of course, which are dependent on the ageing level of the TWC. Here, a selection of results is presented. In the first part, the transients of measured and simulated concentrations downstream of the TWC are compared for three differently aged converters at different engine operating points. In the second part, the profiles of the occupancies and the concentrations during lean–rich and rich–lean transients are presented. Finally, the temperature profiles are shown and discussed.

### 3.4.1 Concentration downstream of the TWC

Figures 3.7–3.9 show the measured and simulated concentration transients downstream of the TWC. In all three figures, the TWC was operated at  $\lambda = 1.03$  at the beginning. At 10 s, the inlet  $\lambda$  was switched to 0.97, at 40 s back to 1.03. Transients of a considerably aged TWC at engine operating point 3, of a moderately aged TWC at point 2, and of a fresh TWC at point 1 are shown, see Table 3.2 for the specification of the engine operating points. This selection was made because the sensitivity of the transient behaviour of the ratio between  $H_2$ , CO, and HC towards both the engine operating points and the ageing level can be very clearly pointed out.

Generally, the agreement of the simulated and the measured exhaust gas concentrations is very good for all species. Some steady-state offsets mainly occur from errors of the inlet concentrations, which is the case for NO and  $CO_2$ . The larger offsets of the  $H_2O$  and  $N_2$  concentrations in Figure 3.8 are caused by the air humidity, which was significantly higher, when these measurements were performed. The inlet water concentration was not adjusted in the simulation.

After the lean–rich step at 10 s, the stored oxygen is depleted at first, leading immediately to a low concentration of all species, except for the reaction products  $CO_2$  and  $H_2O$ , whose levels are increased temporarily. The duration of the depletion is dependent on the amount of stored oxygen. This in turn is dependent on the storage capacity, which is reduced with ageing, see Figure 3.5.

The transient behaviour of the  $H_2$ , CO, and HC concentrations after a lean–rich step at 10 s is remarkably well reproduced by the model. After the depletion of the stored oxygen, the hydrogen concentration level strongly increases. This is mainly caused by the water–gas shift reaction, which needs free catalyst surface, see reaction (3.26). As will be shown in the next section, hydrocarbons start to cover the surface slowly, hindering the water adsorption. Hence, the hydrogen production and concentration level decreases. With this coking

of the catalyst surface, the HC emissions also increase. This effect is most pronounced, when an aged TWC with a high throughput is considered, such as in Figure 3.7. In Figure 3.9, where the exhaust mass flow is smaller and the catalyst surface is very large, coking is very slow and thus, deactivation of the water-gas shift reaction becomes hardly visible within 30 s. The CO concentration increases quite fast to reach a steady-state level after the depletion of the oxygen in the catalyst, in all three cases. Notice that the increased  $H_2$  concentration with the fresher TWC goes hand in hand with lower CO and HC levels. Hence, the air-to-fuel ratio remains unchanged by the deactivation of the TWC, which is of course expected. The coking of the catalyst surface even affects the NO conversion under rich operation. In Figure 3.7, a slight increase of the NO concentration after the depletion of the stored oxygen occurs, which is also reflected by the model.

When a step from rich to lean occurs, as at 40 s, the concentration of the reducing species is expected to drop. Oxygen and NO are not expected to increase, until the oxygen storage is filled. In reality, the CO and HC concentrations drop immediately after the step. However, the hydrogen concentration only decreases slowly, especially, when the storage capacity of the TWC is large, such as in Figure 3.9. This is caused by a persistent water adsorption, which is declining with the increasing level of stored oxygen. The model reflects the time of both the  $O_2$  and the NO breakthrough after the filling of the oxygen storage quite inaccurately. The reason for this is not entirely clear. An apparent measure would be to reduce the storage capacities. However, this leads to a poorer agreement of the concentration transients of the reducing species during the rich period. Here, the model certainly needs an improvement.

The behaviour of the  $H_2O$ ,  $CO_2$ , and  $N_2$  concentrations also agrees well with the measured values. Notice that in Figure 3.9, both the  $H_2O$  and the  $CO_2$  concentrations are slightly increased after the rich–lean transient between 42 s and 46 s after a negative peak caused by an overshoot of the inlet  $\lambda$ . This increase may only come from stored carbonaceous species containing hydrogen. This is a clear indication that indeed coking of the catalyst is caused by hydrocarbons and not by carbon monoxide. However, this only addresses the relatively slow coking effect and not the very fast deactivation of the water-gas shift reaction caused by other phenomena, as proposed in [34] and [98].

### 3 Modelling of a Three-Way Catalytic Converter

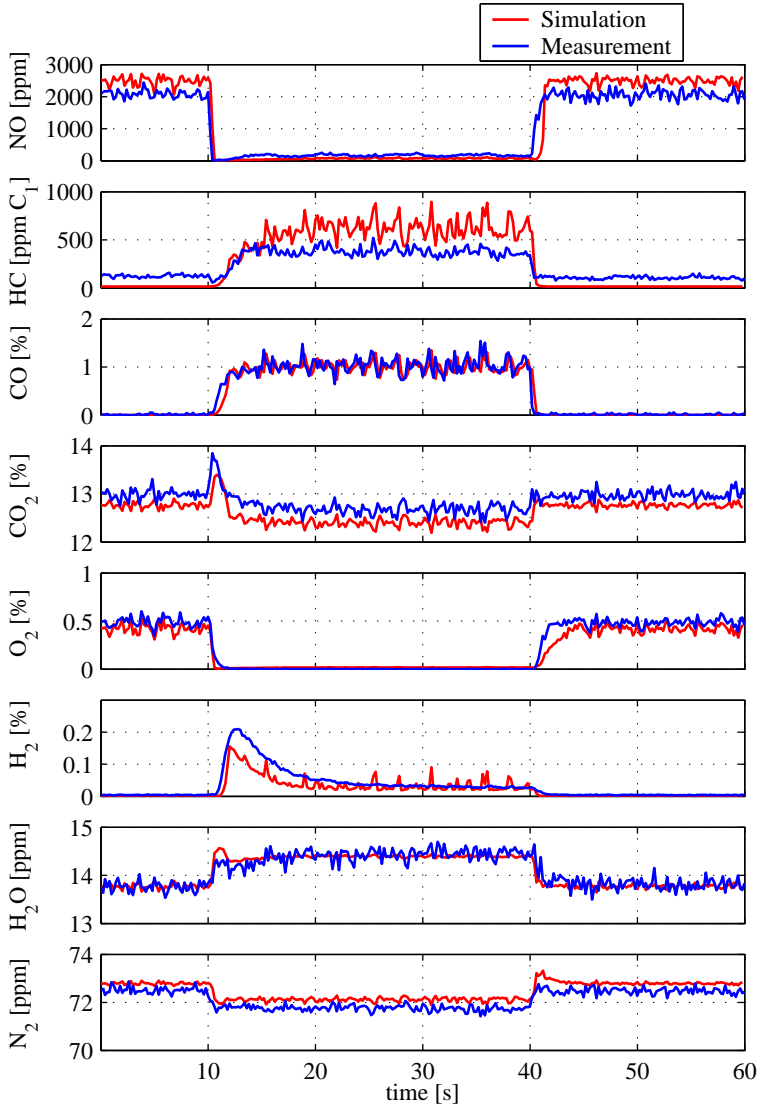


Figure 3.7: Simulated and measured exhaust gas concentrations downstream of a considerably aged TWC (at 1100 °C) and operating point 3 (see Table 3.2). The raw exhaust  $\lambda$  was switched from 1.03 to 0.97 at 10 s and from 0.97 to 1.03 at 40 s.

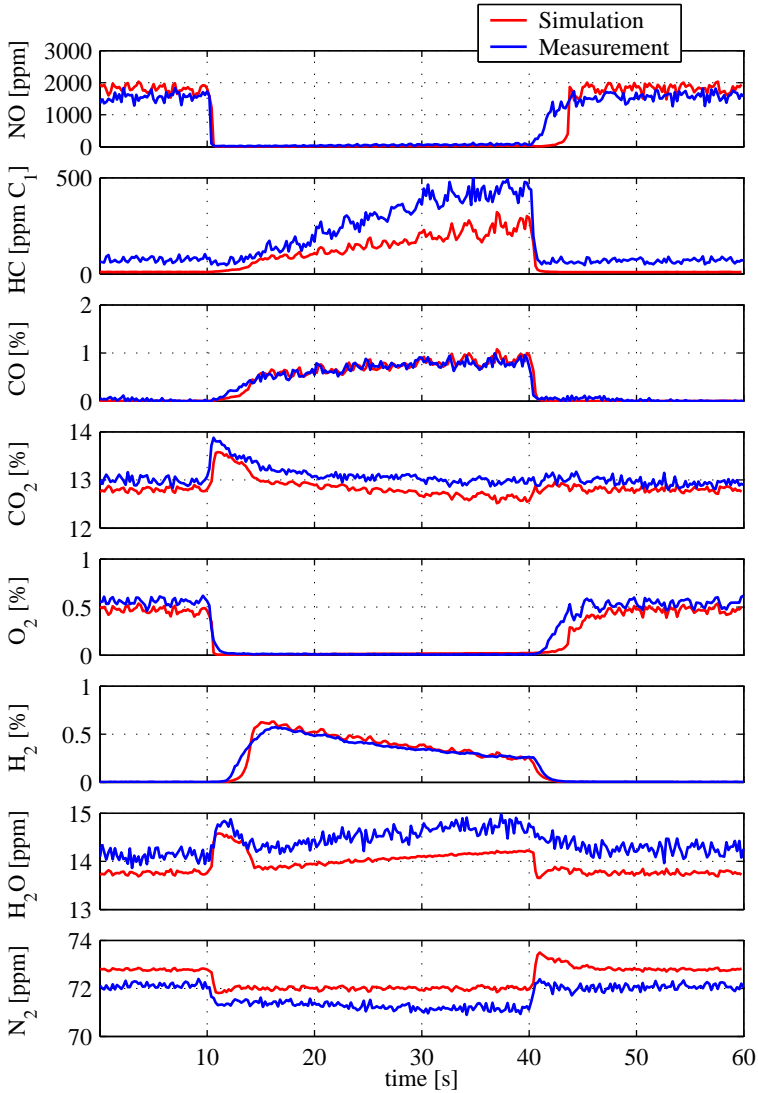


Figure 3.8: Simulated and measured exhaust gas concentrations downstream of the moderately aged TWC (at 900 °C) and operating point 2 (see Table 3.2). The raw exhaust  $\lambda$  was switched from 1.03 to 0.97 at 10 s and from 0.97 to 1.03 at 40 s.

### 3 Modelling of a Three-Way Catalytic Converter

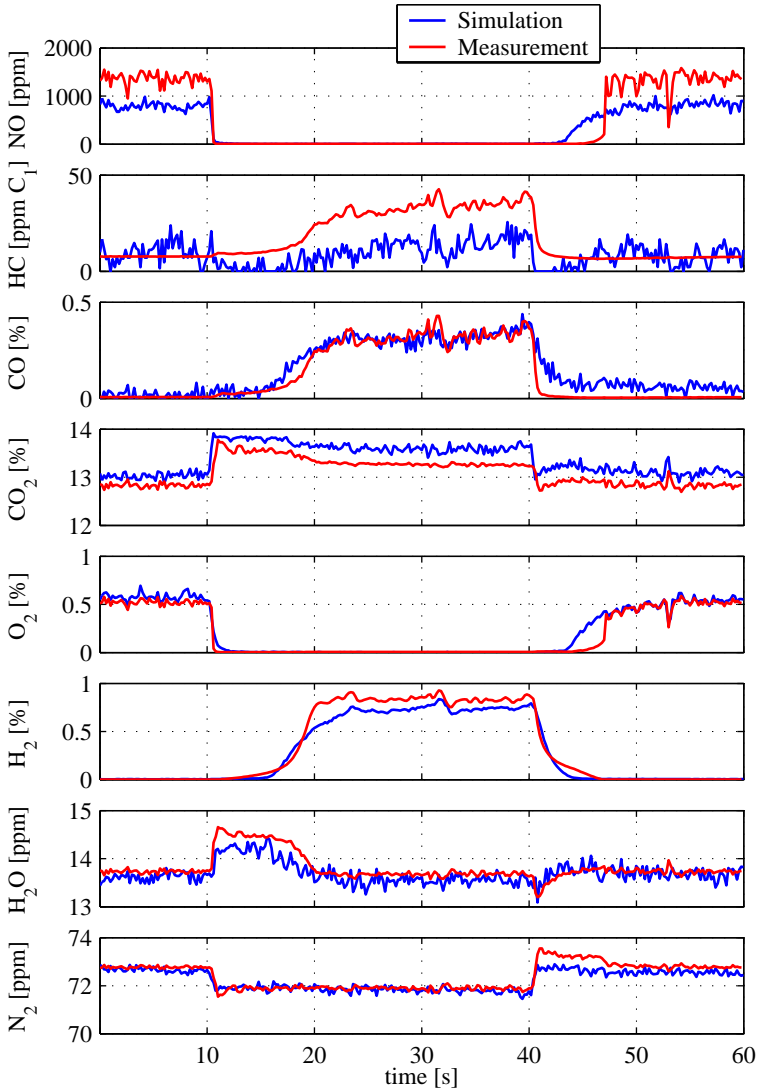


Figure 3.9: Simulated and measured exhaust gas concentrations downstream of the fresh TWC and operating point 1 (see Table 3.2). The raw exhaust  $\lambda$  was switched from 1.03 to 0.97 at 10 s and from 0.97 to 1.03 at 40 s.

### 3.4.2 Occupancy and Concentration Profiles

In Figures 3.10 and 3.11, the profiles of the occupancies and the concentrations along the TWC axis during the step from lean to rich at 10 s is presented. Figures 3.12 and 3.13 show the profiles during the step from rich to lean at 40 s. All profiles are from the moderately aged TWC.

After the switch of the TWC inlet  $\lambda$  from lean to rich at 10 s, stored oxygen is depleted at first. On the noble metal, this happens rapidly within 1.5 s with a steep front moving from the inlet to the tail of the TWC. However, the profile of the oxygen on the ceria ( $\theta_{O,Ce}$ ) is much more evenly distributed. Additionally, oxygen depletion is much slower. It takes approximately 5 s, until the storage is completely empty. The small amount of NO on the catalyst disappears almost immediately. As for the CO and the H, reasonable amounts are stored on the noble metal within 5 s. After that, both are steadily replaced by the  $C_3H_5$  from the front to the tail, the TWC is being coked. The gas concentration profiles are much more evenly distributed, because of the axial convection. NO and  $O_2$  drop almost immediately to low levels. CO breaks through after the noble metal is saturated. The same is valid for the hydrogen, however, the source is different: Whereas the adsorbed CO comes from direct adsorption, the hydrogen comes mainly from the water adsorption and dissociation, i. e., reaction (3.26). This reaction is more and more hindered by the coking, by which the adsorbed hydrogen is displaced. Hence, less of it desorbs, which leads to a lower hydrogen gas concentration. Notice that this concentration is increasing from the TWC front to the tail, at least, as long as adsorption of the abundantly available water is present. As for the CO, the opposite is true, since adsorbed CO mainly comes from the gaseous CO entering the TWC. The water concentration of course increases with decreasing adsorption and water-gas shift activity. This in turn leads to a decreasing  $CO_2$  concentration.

After the rich to lean step of the inlet  $\lambda$  at 40 s, oxygen is stored both on the noble metal and the ceria. Again, the front on the noble metal is quite steep, moving from the inlet of the TWC to the tail. At the front, where mainly  $C_3H_5$ , but also the remaining small amounts of CO and H are oxidised, some free surface is available, leading to a small peak of NO and N moving to the tail. The profile of the oxygen on the ceria is much more evenly distributed than on the noble metal. Again, the abundantly available water contributes additional oxygen. This leads to the phenomenon that the water-gas shift activity “fades out” with the level of the oxygen storage, when the exhaust gas turns lean, leading to a comparatively smooth decrease of the gaseous hydrogen concentration at the tail, whereas CO and  $C_3H_6$  break down immediately.

### 3 Modelling of a Three-Way Catalytic Converter

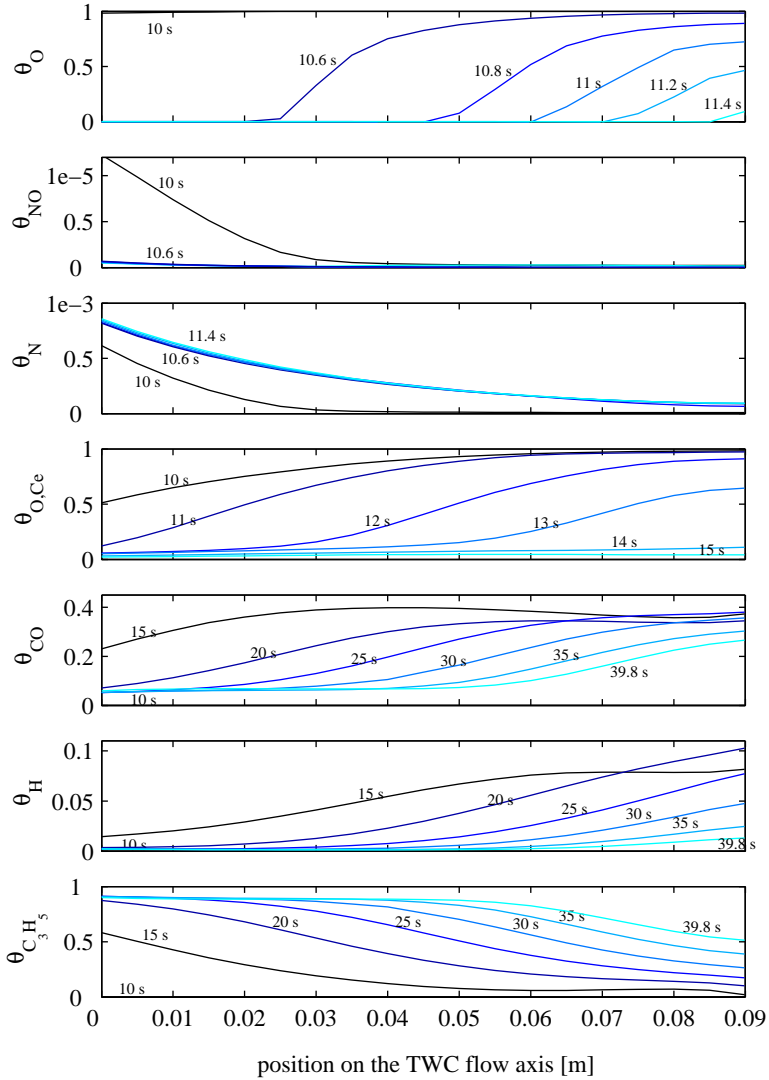


Figure 3.10: Occupancies during the step from lean to rich at 10 s. The profiles are from the moderately aged TWC. Notice the varying time scale.



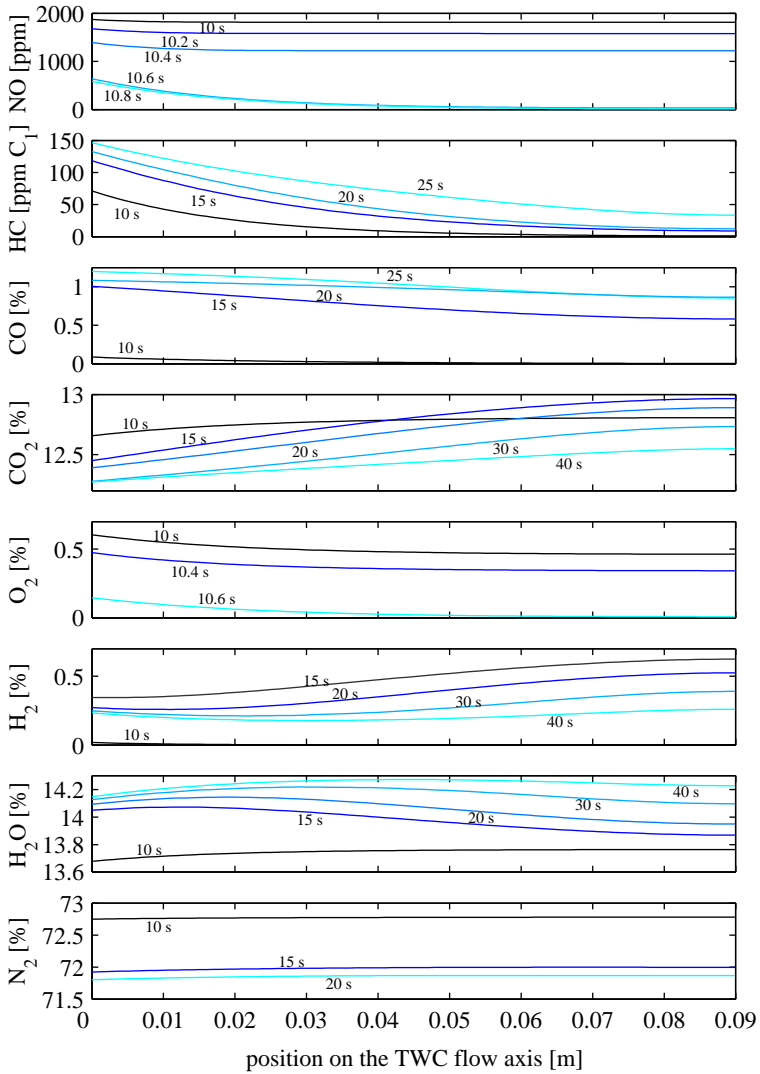


Figure 3.11: Concentration profiles during the step from lean to rich at 10 s. The profiles are from the moderately aged TWC. Notice the varying time scale.

### 3 Modelling of a Three-Way Catalytic Converter

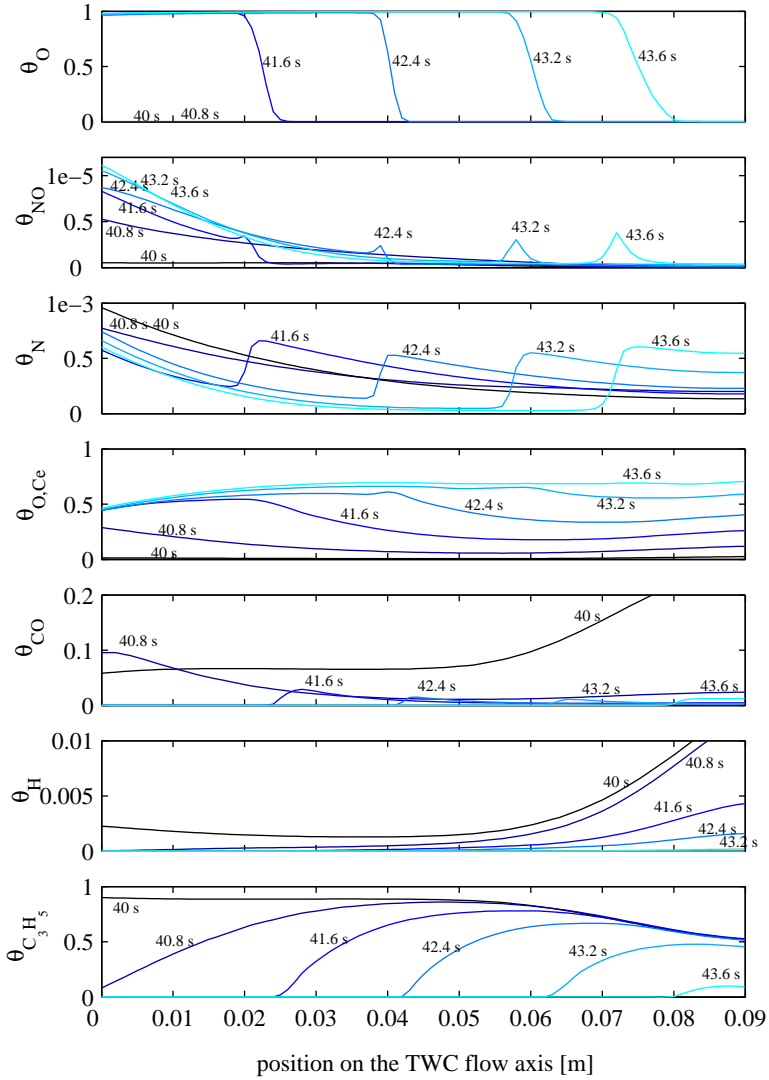


Figure 3.12: Occupancies during the step from rich to lean at 40 s. The profiles are from the moderately aged TWC. Notice the varying time scale.

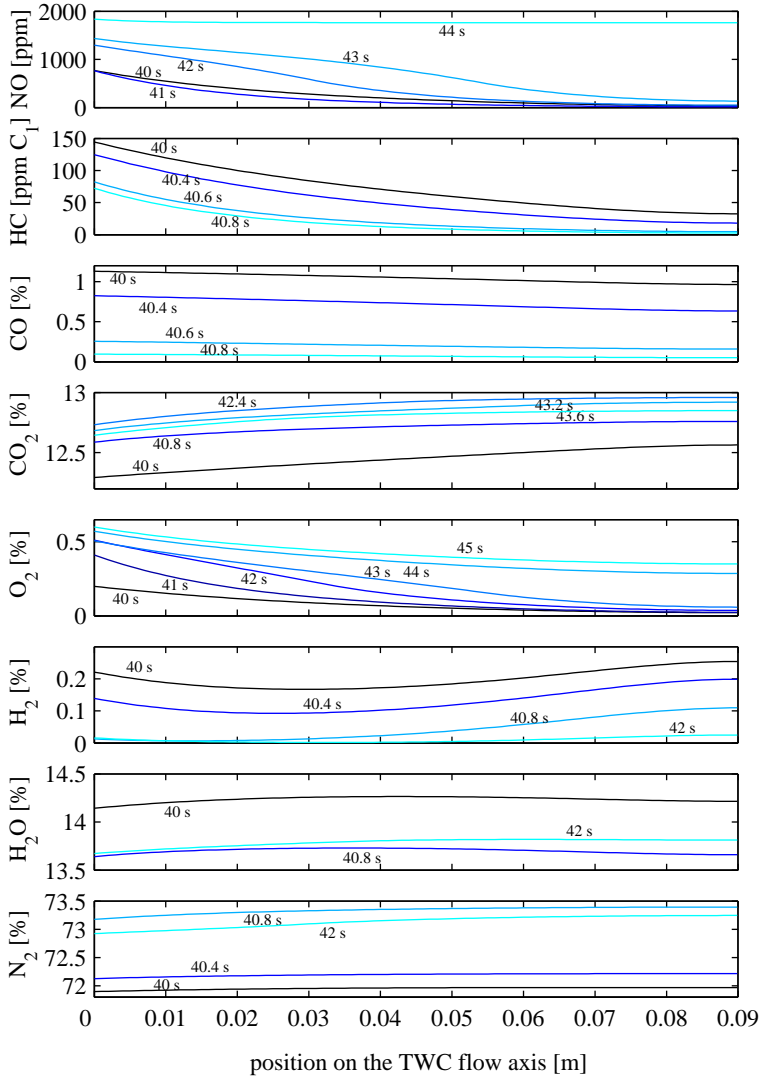


Figure 3.13: Concentration profiles during the step from rich to lean at 40 s. The profiles are from the moderately aged TWC. Notice the varying time scale.

### 3.4.3 Temperature Profiles

The temperatures at the outlet of the three TWCs during the  $\lambda$  steps are shown in Figure 3.14. The temperature profiles of the moderately aged TWC along the axial direction are presented in Figure 3.15.

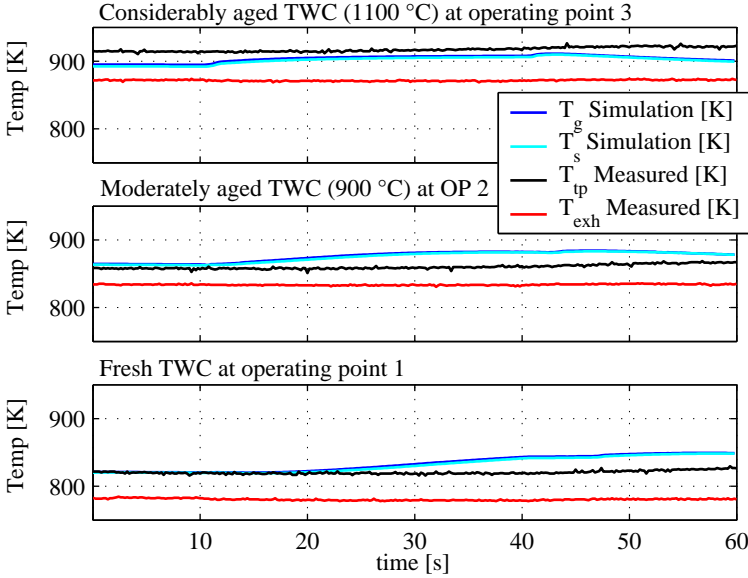


Figure 3.14: Tail-pipe temperatures of the three TWCs during the inlet  $\lambda$  steps from lean to rich at 10 s and rich to lean at 40 s.  $T_{exh}$  denotes the measured temperature of the raw exhaust gas at the TWC inlet.  $T_{tp}$  is the measured temperature at the TWC tail, see also Figure 2.2.

Generally, the temperatures were far too high when the first simulations were performed. This comes from the assumption of the TWC being an adiabatic system. In reality, both heat radiation and convection occur, which lead to a substantial heat loss in the radial direction. Therefore, a very simple heat loss term was added to (3.9):

$$\Delta Q = -(T_s - T_{amb})\alpha_{TWC} \frac{A_{TWC}}{V_{TWC}} \quad (3.33)$$

$T_{amb}$  denotes the ambient temperature,  $\alpha_{TWC}$  is the heat transfer coefficient.  $A_{TWC}$  stands for the outer TWC surface and  $V_{TWC}$  for the TWC volume.

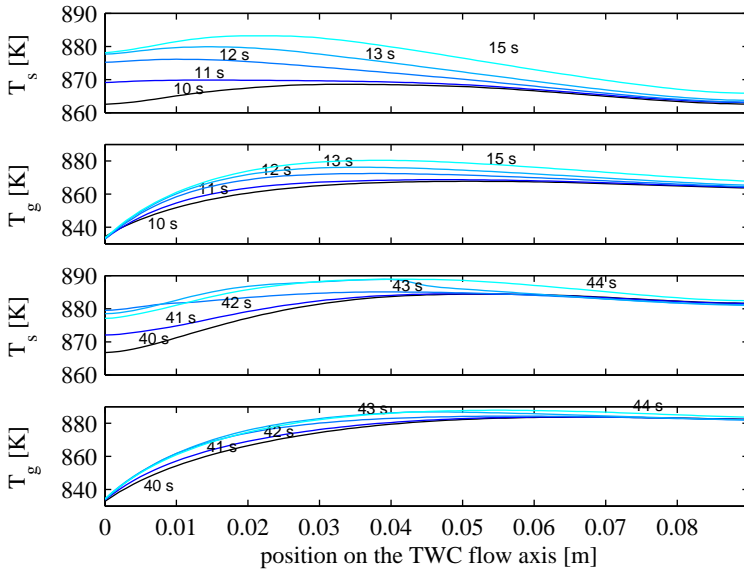


Figure 3.15: Temperature profiles during the inlet  $\lambda$  steps from lean to rich at 10 s (above) and from rich to lean at 40 s (below). The profiles are from the moderately aged TWC.

With this heat loss term, the temperature levels could be corrected to more reasonable values. However, the transient behaviour is still too aggressive as compared to the measured values because of the following reasons: First, the TWC is modelled as one homogeneous solid object. In reality, it is surrounded with an insulating material and a steel canning, which adds substantially to the total thermal inertia. Secondly, the temperature sensors apparently are comparatively slow. Despite these drawbacks the result is considered to be sufficient for the purpose of the model.

As for the temperature profiles, it can be generally stated that the temperature within the TWC of course increases because of the enthalpy of the exothermal reactions. However, towards the tail of the converter, the temperature decreases again because of the heat loss.

## 3.5 Conclusion

A process model of the TWC has been derived. This model accounts for all measured species, including NO, HC, CO, CO<sub>2</sub>, O<sub>2</sub>, H<sub>2</sub>, H<sub>2</sub>O, and N<sub>2</sub>. The model is based on published work, mainly from [54] and [6]. The hydrocarbons are represented by C<sub>3</sub>H<sub>6</sub>. The main focus of the model was to correctly reflect the behaviour of the concentrations during steps of the air-to-fuel ratio at the inlet of the TWC at different engine operating points and varying TWC ageing levels. The goal was thereby to identify the main mechanisms which drive the ratio between H<sub>2</sub>, CO, and HC. The model generally provides a very good agreement between measured and simulated transients of the exhaust gas concentrations. It has been shown that not only the oxygen storage dynamics are relevant, but also the deactivation of the TWC by coking or coverage of carbonaceous species. This phenomenon hinders the water-gas shift reaction under rich operation. This leads to variations of the ratio between H<sub>2</sub>, CO, and HC, depending on the engine operating point and on the catalyst surface, which decreases with ageing. It has been shown that even the NO conversion is deactivated by coking under rich operation.

The dynamics of the deactivation are rather slow as compared to the oxygen filling/depleting dynamics. The ratio of H<sub>2</sub> and CO/HC is very important for the  $\lambda$  sensor output, as will be shown in the next chapter. Therefore, the dynamics of the deactivation of the water-gas shift reaction must be accounted for in a TWC observer, which is supported with a  $\lambda$  sensor. This model identifies the main phenomena and thus is highly suitable as a starting point for the development of a simplified control-oriented model. This task will be pursued in Chapter 5.

# 4 Modelling of a Solid-Electrolyte Oxygen Sensor

## 4.1 Introduction

Solid-electrolyte oxygen sensors are used both upstream and downstream of the TWC. In the configuration applied in this investigation, a wide-range  $\lambda$  sensor is used upstream of the TWC, i. e., in the raw exhaust. Downstream of the TWC, a switch-type  $\lambda$  sensor is mounted, see also Figure 1.4. In Figure 3.2 of the previous chapter, it has been shown that these sensors are not only sensitive to the oxygen concentration and/or the air-to-fuel ratio, but also to the ratio between  $H_2$ , CO, and HC. This is a minor problem in the raw exhaust, where this ratio roughly remains constant for one specific  $\lambda$ . However, downstream of the TWC, it can vary considerably, independent of  $\lambda$ . It is thus essential to understand the working principle of the solid-electrolyte oxygen sensors and how their outputs depend on the exhaust gas concentrations. In the following, mainly the switch-type  $\lambda$  sensor will be focused on, because only this type is used downstream of the TWC throughout this thesis. Sometimes, the use of a wide-range  $\lambda$  sensor is proposed also downstream of the TWC. This will be addressed briefly at the end of this chapter.

Figure 4.1 shows typical steady-state characteristics of a switch-type  $\lambda$  sensor downstream of a fresh and an aged TWC, respectively. On the lean side, i. e., where  $\lambda > 1$ , the voltage is mainly below 200 mV and roughly identical for both cases. On the rich side, i. e., where  $\lambda < 1$ , the voltage is well above 600 mV, and a significant difference between the two characteristics is visible. Whereas the characteristic of the sensor downstream of the fresh TWC increases persistently with a decreasing  $\lambda$ , downstream of the aged TWC the increase is somewhat unsteady with a “terrace” at  $\lambda = 0.98$ . It will be shown that this stems from differences in the ratios between  $H_2$ , CO, and HC.

The use of a  $\lambda$  sensor downstream of the TWC fulfills mainly two purposes. The first application is for TWC diagnostics. From the delayed response as compared to the one of the sensor upstream, the TWC storage capacity and thus the state of ageing can be determined. The second application is the calibration of the sensor upstream. When the sensor upstream fails to establish a chemical equilibrium at its electrodes, a bias of the measured  $\lambda$  occurs. Down-

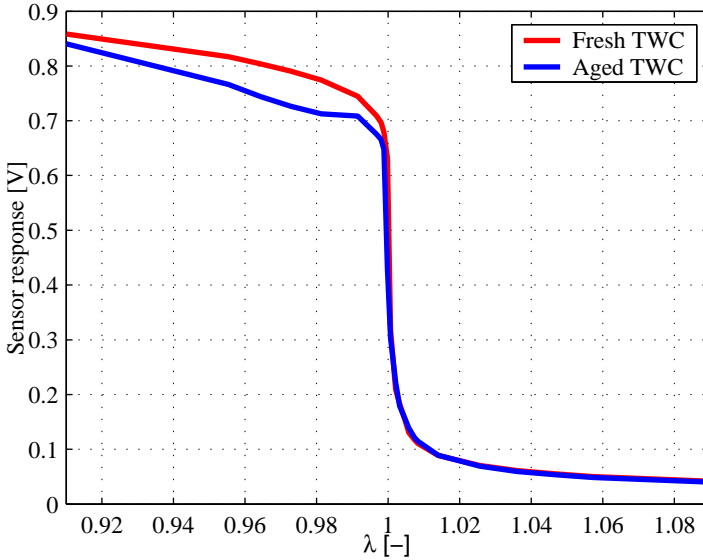


Figure 4.1: Switch-type  $\lambda$  sensor characteristics downstream of a fresh and an aged TWC.

stream of the TWC, where the exhaust gas is close to equilibrium, the switch-type  $\lambda$  sensor delivers a very precise information about the stoichiometric point, i. e., where the switch of the sensor characteristic is located. This information is used for the calibration of the sensor upstream. Both sensor calibration and TWC diagnostics could theoretically be implemented using the location of the switch, only. However, as can be seen from Figure 4.1, there is much more information in the sensor signal. Its sensitivity to the hydrogen concentration is both disturbing but also a chance to obtain additional information about the TWC's level of ageing, since this is strongly connected to the hydrogen emissions, as has been shown in the previous chapter. Hence, a model shall be developed, which accounts for the main exhaust gas components, with a special focus on the ones mainly driving the sensor voltage, such as oxygen, hydrogen, carbon monoxide, and hydrocarbons.

It is clear from the considerations above that models which exclusively take into account the oxygen concentration in the exhaust gas cannot describe the characteristics as shown in Figure 4.1, irrespective of whether the oxygen concentrations in the exhaust are used or the equilibrium concentrations above the



electrodes. Such models have been presented in [73] and [79]. A simple test, where the sensor is exposed to an inert gas such as helium or nitrogen, reveals that the voltage will only reach about 300 – 400 mV, although no oxygen is present, see e. g. [14]. Hence, not only the diffusivity but also the chemical potentials of the reducing and oxidising species have to be taken into account.

The model developed here is mainly based on the work presented in [21] and [16]. Parts of it have been published already in [2], however some minor modifications have been made. It accounts for the most important exhaust gas species. Diffusion to the electrodes, reaction kinetics on the electrodes and the electrolyte have been considered. The purpose is to reproduce the dependencies on the exhaust gas species on a qualitative level only, i. e., no extensive tuning will be applied. Hence, the model serves as a basis for the development of a simplified control-oriented model, which can be used in an engine control system, where the computational resources are rather limited. Such a model will be presented in Chapter 5.

In the following, the structure and the working principle of the switch-type  $\lambda$  sensor will be discussed at first. Then, the process model with the different modules, such as the protection layer, the electrode and the electrolyte is developed. Finally, a selection of simulation results in comparison with measurements is presented.

## 4.2 Structure and Working Principle

Modern  $\lambda$  sensors are planar-type, i. e., they consist of different horizontal layers, where the outermost one is exposed to the exhaust gas, the innermost one to the reference gas, which is air in this case. Sensors of older types consist of concentric layers, where the outside is exposed to the exhaust gas and the inner tube to the reference gas.

A sketch of a planar type sensor is depicted in Figure 4.2. The actual sensor element is shielded by a protection tube with small openings or slots to allow the exhaust gas to pass inside. The tube protects the sensor against particles, small droplets and the direct exposure to the exhaust gas. Additionally, the heat transfer from the heated sensor element is reduced, whereas the mass transfer from the exhaust gas to the sensor is enhanced. The flow pattern with the heat and mass transfer between the exhaust gas and the sensor has been investigated in detail in [57]. The sensor element consists of various layers. The first one, which is exposed to the exhaust gas, is a porous ceramic and serves to protect the electrode and as a diffusion barrier. Under the protection layer, a porous catalytic electrode is located, which consists mainly of platinum. The kernel of the sensor is an electrolyte, usually zirconia ( $ZrO_2$ ) with additives to enhance

#### 4 Modelling of a Solid-Electrolyte Oxygen Sensor

the mobility of the oxygen ions. The reference side is built accordingly. The cathode of the sensor is located at the measurement side, the anode at the reference side. Modern switch-type  $\lambda$  sensors are heated, in order to keep the sensor element at approximately 700 °C.

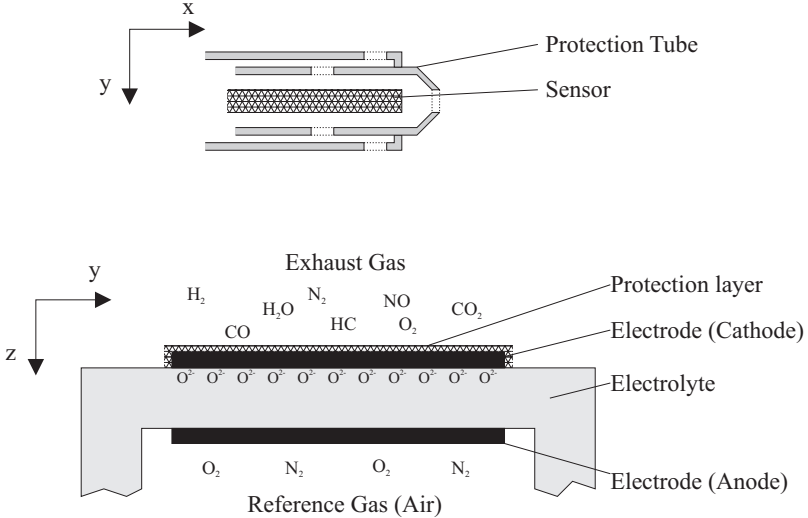


Figure 4.2: Sketch of the working principle and the structure of a switch-type  $\lambda$  sensor. View from the side (top) and cross-sectional view of the sensor element (bottom).

The exhaust gas components diffuse through the protection layer onto the electrodes. The electrodes are catalytic, which brings the exhaust gas close to a chemical equilibrium. This is enhanced by the protection layer, which additionally serves as a diffusion barrier. Thereby, a concentration gradient between adsorbed oxygen on the electrode on the one hand and oxygen ions in the electrolyte on the other hand arises, which causes the oxygen ions to migrate to the electrode (or vice versa), donating (or receiving) two electrons to (or from) the electrode. Additionally, oxygen ions react directly with reducing species such as H<sub>2</sub>, CO, or HC, donating additional electrons. The electrons leaving the electrolyte or rather the positively charged vacancies in the electrolyte grid build up an electrostatic potential, which finally is in equilibrium with the chemical potential of the exhaust gas. The same process occurs on

the reference side. Hence, a concentration gradient of oxygen ions in the electrolyte is established. It has been shown that this concentration gradient is located in the outermost layer of the electrolyte, see [43], [82], or [37]. The potential occurring from the electrons migrating to or from the electrodes is finally measured as the sensor output voltage. Thus, the concentration or better the activity gradient of the oxygen ions between the exhaust and the reference side is measured, rather than the concentration gradient of the oxygen in the exhaust gas. The activity of the oxygen ions on the measurement side in turn is dependent on the gas composition, i. e., on the concentrations of *both oxidising and reducing* species in the exhaust gas. Occasionally,  $\lambda$  sensors are referred to as oxygen sensors. This can be obviously misleading, especially, when switch-type  $\lambda$  sensors are used.

### 4.3 Process Model

The structure of the sensor model follows the one of the real sensor, which basically consists of four elements: The thimble, the protection layer, the porous electrodes, and the electrolyte. This is reflected in the model, which is divided into three modules. A sketch of the sensor model structure is shown in Figure 4.3. The thimble and the protection layer are collected in the first module where mainly diffusion phenomena are accounted for. Here, the gas concentrations at the electrode  $c_i^{\text{electrode}}$  are calculated from the exhaust gas concentrations  $c_i^{\text{exhaust}}$  and the mass transfer rates  $\dot{m}_i^{\text{sorption}}$  between the electrode and the gas phase due to sorption. The second one represents the catalytic electrodes where the most important chemical reactions are modelled. In this module, the occupancies of the adsorbed species  $\theta_j$  are calculated from the exhaust gas concentrations at the electrode. The third module incorporates the electrolyte with the three-phase boundary between the gas, the electrode and the electrolyte. Here, the sensor voltage  $U_{\lambda st}$  is obtained from the occupancies on the electrode.

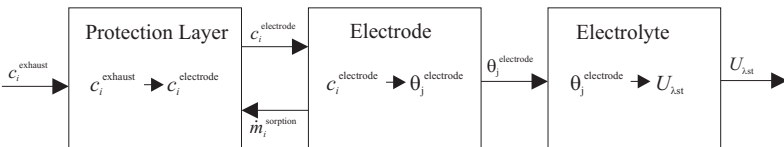


Figure 4.3: Structure of the sensor model.

The goal of the model is to reproduce the sensor output qualitatively correct in steady-state conditions, in order to understand the main mechanisms, especially the role of oxygen, hydrogen and carbon monoxide. Hence, the following simplifying assumptions have been made:

**Plane geometry** The sensor geometry is not exactly plane. However, effects arising from this are neglected.

**Uniform temperature distribution** In reality, the temperature distribution depends on the location of the heater, the flow pattern inside and outside the protecting tube, which is in turn dependent on the mounting in the exhaust, and on the sensor geometry. Here, only one gas temperature and one solid temperature have been assumed.

**Uniform concentration profiles** The flow pattern inside the protection tube depends on various factors, such as the geometry or the position in the exhaust gas pipe. This has been investigated in detail in [57]. Hence, the concentration profiles at the protection layer are very complex and rapidly changing. Here, perfect mixing has been assumed inside the protection tube, which leads to uniform concentration profiles.

**Efficient gas exchange inside the tube** It has been assumed that the tube does not significantly hinder the gas transport between the exhaust and the sensor element, as compared to the porous protecting layer. Hence, only the sensor element has been taken into account.

Notice that the third and the fourth assumptions are also based on the condition that only steady-state simulations are performed.

The exhaust gas has been assumed to consist of  $O_2$ ,  $CO$ ,  $H_2$ ,  $NO$ ,  $CO_2$ ,  $H_2O$ , and  $N_2$ . The HC have been neglected, since their concentrations remain rather low as compared to  $CO$  and  $H_2$  during normal operation downstream of the TWC. In order to maintain a correct  $\lambda$ , the measured HC concentrations have been added to the  $CO$  and  $H_2$  concentrations, where a C:H ratio of 1:2 was assumed. In reality, the HC consist of many components [87], which certainly have differing influences on the sensor output, depending on the agility of the molecules and their reactivity on the electrode. Since only the total HC were measured, their composition could not be determined. The  $NO_x$  apart from  $NO$  have also been neglected, partly because of their usually low concentrations and partly because they were not measured. Notice that both the HC and the  $NO_x$  may have a considerable effect on the sensor output, if they occur in considerable quantities. This might for example be the case in the exhaust of engines fuelled with natural gas, where a lot of methane is present in the exhaust [69].

### 4.3.1 Protection Layer

The mass transfer in the protection layer is purely diffusive, as has been pointed out in the previous section. Stefan-Maxwell equations have been applied to account for the diffusion in the porous material. These equations are generally not as well-known as the Fick's law. The latter equations only account for the concentration gradient of a species to drive the diffusion. They do not account for the fact that if a species A diffuses into B, B is displaced and has to diffuse in the opposite direction in order to maintain the overall pressure equilibrium. The Stefan-Maxwell equations account for this displacement and can hence be considered to be "more fundamental". A detailed derivation of these equations can be found in [63] or [84].

Since the protection layer consists of a porous ceramic material, diffusion is hindered. In order to facilitate the numerical solution of the problem, the layer has been divided into finite volumes. The concentration of  $c_i$  of the species  $i$  has been assumed to be uniform within the finite volume. Its change in time is calculated by use of a mass balance and the gas equation, and can thus be expressed as follows:

$$\frac{\partial c_i}{\partial t} = (J_{i,in} - J_{i,out}) \cdot A_{\text{sensor}} \quad (4.1)$$

$J_i$  is the mole flux of the species  $i$ ,  $A_{\text{sensor}}$  denotes the specific flux area of the layer. Notice that the temperature has been assumed constant.

The fluxes between the finite volumes are calculated from the concentrations using the Stefan-Maxwell equations. For a mixture of  $n$  species, they are expressed as follows:

$$J_i = \frac{-\frac{p_{exh}}{\Re T_{exh}} \nabla c_i + c_i \sum_{\substack{j=1 \\ j \neq i}}^n \frac{J_j}{D_{ij}}}{\sum_{\substack{j=1 \\ j \neq i}}^n \frac{c_j}{D_{ij}}} \quad (4.2)$$

$\nabla c_i$  denotes the concentration gradient of the species  $i$ ,  $D_{ij}$  stands for the binary diffusion coefficient of species  $i$  diffusing into  $j$ . It is the same as has been used for the TWC model in the previous chapter, see (3.3). However, here the diffusion is hindered since it occurs in the porous material. Therefore, the coefficient is extended with the porosity-tortuosity factor  $\epsilon/q$  as follows:

$$D_{ij} = \frac{\epsilon}{q} \frac{143 \cdot T_{exh}^{1.75}}{p_{exh} \sqrt{M_{i,j}} \left[ \Sigma_{v,i}^{1/3} + \Sigma_{v,j}^{1/3} \right]^2} \quad (4.3)$$

$\epsilon$  is the volume fraction of the gas in the porous material.  $q$  is a measure for the increase of the diffusion path due to the curvature of the pores.

The Stefan-Maxwell equations as denoted in (4.2) are implicit and have to be rearranged for the direct calculation of the fluxes  $J_i$ . They are transformed to a linear equation system of the form

$$\mathbf{A} \cdot \mathbf{x} = \mathbf{b}, \quad (4.4)$$

where the elements of  $\mathbf{A}$ ,  $\mathbf{b}$ , and  $\mathbf{x}$  can be expressed as follows:

$$A_{ij} = \begin{cases} -\frac{\frac{c_i}{D_{ij}}}{n} & \text{if } i \neq j \\ \sum_{\substack{k=1 \\ k \neq i}} \frac{c_k}{D_{ik}} & \\ +1 & \text{if } i = j \end{cases} \quad (4.5)$$

$$b_i = -\frac{\frac{p_{exh}}{\mathcal{R}T_{exh}}}{n} \nabla c_i \quad (4.6)$$

$$\sum_{\substack{k=1 \\ k \neq i}} \frac{c_k}{D_{ik}}$$

$$x_i = J_i \quad (4.7)$$

The concentration gradient  $\nabla c_i$  is approximated by a simple forward difference scheme. Hence, with the length  $d$  of the finite volume  $k$  it reads

$$\nabla c_i|_k \approx \frac{c_{i,k+1} - c_{i,k}}{d}. \quad (4.8)$$

Since the Stefan-Maxwell equations are inherently consistent with the overall pressure equilibrium, only  $n - 1$  equations are linearly independent, if applied to  $n$  components. Hence, the matrix  $\mathbf{A}$  in (4.5) is only of rank  $n - 1$ . One possibility to resolve this is to replace one row in  $\mathbf{A}$  by ones and setting the corresponding element in the vector  $\mathbf{b}$  to zero. Physically, this expresses the balance of all fluxes, of which the sum must be zero. However, this approach leads to a badly conditioned matrix  $\mathbf{A}$ . This may cause numerical problems, when the equation system is solved, especially, if the efficient LU (Lower - Upper triangular) decomposition is applied. Therefore, another approach has been chosen.

If the Matrix  $\mathbf{A}$  is replaced by the identity matrix  $\mathbf{I}$ , the equation system (4.4) represents the Fick's law. The idea is now to separate the identity part from  $\mathbf{A}$

and add the remaining matrix with the outer diagonal elements of  $\mathbf{A}$  with a weighting factor  $\mu$ , which is 1 in the exact case:

$$\mathbf{A} \approx \mathbf{I} + \mu\mathcal{A}, \quad (4.9)$$

where

$$\mathcal{A} = \mathbf{A} - \mathbf{I}. \quad (4.10)$$

As long as the weighting factor  $\mu$  is smaller than 1,  $\mathbf{A}$  is not singular. Tests have revealed that a factor of 0.9999 provides sufficiently accurate and numerically stable results with the LU decomposition. The error which occurs from the weighting factor is very small as compared to one occurring from the simplifying assumptions.

The boundary conditions on the exhaust gas side are the concentrations of the gas species. On the electrode side, the mass flux arising from adsorption and desorption on the electrode is fed into the diffusion model.

### 4.3.2 Electrode

In this module, the occupancies of the adsorbed species are calculated from the concentrations of the gas species in the protection layer at the electrode surface. These are provided by the first module. Again, a number of simplifying assumptions have been made:

**Uniform and constant temperature profile** The temperature profile is uniform and constant. There are no local temperature peaks, i. e., the reaction enthalpy is set to zero for all reactions.

**Langmuir-Hinshelwood kinetics** All reactions have been modelled using Langmuir-Hinshelwood kinetics. Hence, reactions only occur amongst adsorbed species. All species compete for the same surface sites on one adsorption layer.

**Uniform distribution of occupancies** The adsorbed species are uniformly distributed on the surface, i. e., surface diffusion is assumed to be instantaneous.

The adsorption, desorption and reaction rates have been calculated as described in Chapter 3. For convenience, they are repeated here. The balance equation for the species  $i$  on the surface reads as follows:

$$\frac{\partial \theta_i}{\partial t} = r_{\text{adsorption},i} - r_{\text{desorption},i} + \sum_j (\nu_{i,j} \cdot r_{\text{reaction},j})$$

#### 4 Modelling of a Solid-Electrolyte Oxygen Sensor

The adsorption rate is dependent on the concentration  $c$  of the gaseous species  $i$ , on the availability of free surface sites  $\theta_V$  and on the gas temperature  $T_{exh}$ :

$$r_{\text{adsorption},i} = s \sqrt{\frac{\mathfrak{R}T_{exh}}{2\pi M_i}} \frac{1}{L_{\text{electrode}}} c_i \theta_V \quad (4.11)$$

Accordingly, the desorption rate is dependent on the occupancy  $\theta$  of the species  $i$  on the surface and on the sensor temperature  $T_{\text{sensor}}$ :

$$r_{\text{desorption},i} = A_{des} e^{\frac{-E_{des}}{\mathfrak{R}T_{\text{sensor}}}} \theta_i \quad (4.12)$$

The reaction rate depends on the availability, i. e., the occupancies  $\theta$  of the reactants  $i$  and  $j$ , and on the sensor temperature  $T_{\text{sensor}}$ :

$$r_{\text{reaction,LH}} = A_{\text{reac,LH}} e^{\frac{-E_{\text{reac,LH}}}{\mathfrak{R}T_{\text{sensor}}}} \theta_i \theta_j \quad (4.13)$$

The complete reaction scheme applied in the model is depicted in Table 4.1. The adsorbed species taken into account in the reaction scheme include C, CO, O, H, OH, H<sub>2</sub>O, NO, and N.

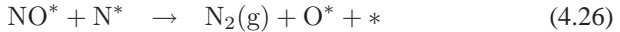
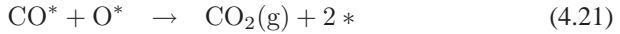
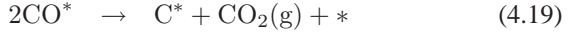
The C-O-CO (4.14–4.15, 4.19–4.21) and the H-O-OH (4.14, 4.16, 4.18, 4.22–4.24) reaction schemes follow mainly the proposals presented in [48]. However, some modifications have been made.

Since the  $\lambda$  sensor works at temperatures around 700 °C, no direct decomposition of CO has been taken into account. Instead, the Boudroie reaction (4.19) has been introduced. The occurrence of pure carbon on the sensor electrode is probably somewhat controversial. In [30], it has been shown that the exposure of the sensor to a gas mixture consisting of O<sub>2</sub>, CO, and N<sub>2</sub>, which changes between lean and rich at low frequencies reveals an asymmetric response of the sensor voltage. The sensor follows the switch from rich to lean immediately, whereas the voltage only saturates slowly in the other direction. This test was simulated with the model. The asymmetric behaviour could only be reproduced, if the occurrence of C was taken into account. The occurrence of C has been documented in [76], however in a system, where only CH<sub>4</sub> was tested and no gaseous CO. As long as the engine is not operated with a very rich air-to-fuel ratio during a longer period, the occurrence of C on the sensor plays a minor role. Therefore, the parameters of the reactions involving adsorbed C have been set to zero. However, the reactions have been documented for the sake of completeness.

The desorption of OH has not been taken into account here, since only very low rates are expected at the sensor's working temperature of 700 °C, see [48]

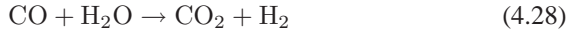


Table 4.1: Reaction scheme of the sensor electrode model.



\* denotes a vacant site on the noble metal. Superscript \* stands for adsorbed species (on the noble metal).

or [100].  $\text{CH}_4$  has not been taken into account. The hydrocarbons certainly have an impact on the sensor voltage. However, since they generally occur only in small quantities downstream of a TWC, they have not been incorporated in the sensor model. The water-gas shift reaction



is implicitly contained in the reaction scheme.

The N-O-NO reaction scheme (4.25–4.27) has been derived from [45]. The formation of  $\text{NO}_2$  has been neglected. The data for the kinetics have been taken from [71] and [77]. The former investigation was performed on a rhodium catalyst. However, NO concentrations are quite low in comparison with the  $\text{O}_2$  concentrations. Therefore, these data have been assumed to be sufficiently accurate.

Apart from the occupancies on the electrode, also the mass flows to and from the electrode by means of adsorption and desorption have to be calculated by the electrode model to obtain boundary conditions for the diffusion model, see Figure 4.3. The mass flows are calculated from the sorption rates, the adsorption storage capacity on the electrode  $L_{\text{electrode}}$ , the electrode surface  $A_{\text{electrode}}$ , and the molar mass  $M$  of the species  $i$ . Notice that the mass flow is positive in the direction from the electrode to the diffusion model.

$$\dot{m}_{\text{sorption},i} = (r_{\text{desorption},i} - r_{\text{adsorption},i})L_{\text{electrode}}A_{\text{electrode}}M_i \quad (4.29)$$

### 4.3.3 Electrolyte

The actual sensor output voltage, which is measured at the electrodes, is generated in the electrolyte. It arises from a concentration gradient of the oxygen ions in the outer layers of the electrolyte.

It has been illustrated in Section 4.2 that the oxygen ions migrate from the electrolyte, donating two electrons to the electrode at the three-phase boundary between the gas, the electrode, and the electrolyte. The switch-type  $\lambda$  sensor is a potentiometric sensor without induced ion current in the electrolyte. Hence, only the chemical potential of the redox reactions causes the oxygen ions to migrate. These reactions occur on the electrode, as has been shown in the previous section. In the literature, it has been shown that also species which are adsorbed on the electrolyte react with the oxygen, see [68] and [67]. Most of these reactions presumably occur at the three-phase boundary between the electrode, the electrolyte, and the gas. Hence, also surface diffusion plays an important role. In order to keep the model simple, such surface transport phenomena have not been modelled here. Additionally, the temperature has been assumed to be uniform and constant in the electrolyte.

Three algebraic models of the zirconia electrolyte have been derived. The first model only takes into account the oxygen concentrations on the electrodes. It is mainly based on [43] and [18]. In the second model, also reducing species adsorbed on the electrodes are regarded, as in [19]. The third model additionally accounts for adsorbed species on the electrolyte. It is based on the work presented in [59], [65], [85], and [37].

#### Model I: Oxygen on Electrodes

In an exhaust gas with a rich air-to-fuel ratio, i. e.,  $\lambda < 1$ , oxygen is almost completely reduced on the catalytically active electrode. Hence, a chemical potential between the oxygen adsorbed in the electrode and the ions in the electrolyte arises. The latter migrate to the electrode surface, until the chemical

potential  $\Delta G_{chem}$  balances the electrostatic potential in the electrolyte  $\Delta G_{el}$ . This can be expressed mathematically as follows [43]:

$$\begin{aligned} \Delta G_{chem} &= \Delta G_{el} \\ -\mathcal{R}T_{\text{sensor}} \ln \left( \frac{\theta_{\text{O}}}{a_{\text{O}^{2-}}} \right) &= 2FU_{\text{meas}} \end{aligned} \quad (4.30)$$

$\theta_{\text{O}}$  denotes the occupancy of oxygen on the electrode.  $a_{\text{O}^{2-}}$  stands for the activity of the oxygen ions in the electrolyte.  $F$  is the Faraday number and  $U_{\text{meas}}$  the voltage on the measurement side. At the reference electrode, the balance can be expressed accordingly:

$$\mathcal{R}T_{\text{sensor}} \ln \left( \frac{\theta_{\text{O}}^{\text{ref}}}{a_{\text{O}^{2-}}} \right) = 2FU_{\text{ref}} \quad (4.31)$$

The total sensor voltage output  $U_{\lambda st}$  is the sum of the two voltages on the measurement and the reference sides, respectively:

$$U_{\lambda st} = \frac{\mathcal{R}T_{\text{Sensor}}}{2F} \ln \left( \frac{\theta_{\text{O}}^{\text{ref}}}{\theta_{\text{O}}} \right) \quad (4.32)$$

This result is based on purely steady-state considerations. The same result can be derived from a dynamic analysis [18]. Such an analysis will be pursued for the next model. Notice that (4.32) is the Nernst equation, applied to the occupancies of the oxygen on the electrodes, instead of the oxygen concentrations.

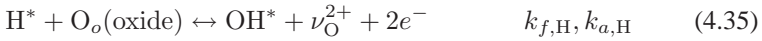
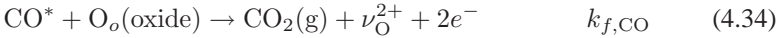
## Model II: Redox Reactions with Oxygen of the Electrolyte

This model is mainly based on the one presented in [19]. Not only adsorbed oxygen is taken into account, but also adsorbed reducing species such as hydrogen or carbon monoxide. Most probably, the reducing species contribute the main part for higher voltage outputs on the rich side. The chemical potential of the redox reactions is much higher than of concentration gradients between the electrode and the electrolyte. This can be verified by exposing a switch-type  $\lambda$  sensor to an inert gas, such as nitrogen. The voltage output hardly exceeds 350 mV, see also [14]. Metaphorically speaking, reducing species “pull” the oxygen ions out of the electrolyte against the electrostatic potential.

It is assumed that oxygen migrates between the electrode and the electrolyte and that oxygen on the electrolyte reacts directly with carbon monoxide and hydrogen, which are adsorbed on the electrode. This can be expressed as fol-

#### 4 Modelling of a Solid-Electrolyte Oxygen Sensor

lows:



$\text{O}_o(\text{oxide})$  denotes an oxygen ion in the electrolyte,  $\nu_{\text{O}}^{2+}$  a positive vacancy in the electrolyte grid and  $e^-$  stands for an electron.  $k_f$  and  $k_a$  are the reaction rate coefficients of the forward and backward reactions. Carbon is not taken into account, because it has been neglected in the electrode model. Considering the reaction scheme on the electrode (4.14–4.27), also other species might be accounted for, for example NO. In reality, the hydrocarbons, which have not been considered in the electrode model at all, certainly play an important role, as well. However, these have been omitted for the sake of simplicity. It will be shown that the reactions considered here are sufficient to get satisfactory results.

From the reaction scheme above, an expression for the electron current can be derived:

$$\dot{n}_e = k_f \theta_V - k_a \vartheta_{V_o} \theta_{\text{O}} + k_{f,\text{CO}} \theta_{\text{CO}} + k_{f,\text{H}} \theta_{\text{H}} - k_{a,\text{H}} \theta_{\text{OH}} \theta_V \quad (4.36)$$

$\vartheta_{V_o}$  denotes the fraction vacant sites in electrolyte grid, i. e., it corresponds to  $\nu_{\text{O}}^{2+}$  above. It is assumed that the availability of oxygen ions is not rate limiting, i. e., the reaction rates are independent of the oxygen concentration in the electrolyte. The first two terms on the right hand side denote the exchange of oxygen between the electrode and the electrolyte. In [37], it was assumed that the forward reaction was of order zero with respect to all reactants, i. e., the first term would then be only  $k_f$ . In the final model, as it will be derived in the following, this leads to infinitely high sensor voltage outputs, when the oxygen occupancy of the electrode is zero. In reality, this is never the case: Even, when the sensor is put in a pure inert gas, oxygen migrates from the electrolyte to the electrode. However, in the model developed here, the electrolyte model is algebraic without any feedback to the electrode. In other words, species migrating between the electrolyte and the electrode are not considered in the balance equations of the electrode model. Notice that this problem also arises in the simple model I, which has been presented above. The introduction of the dependency of the reaction rate on the availability of vacant sites on the electrode,  $\theta_V$ , solved the problem to a satisfactory level.

Assuming steady-state or better equilibrium, the electron current in (4.36) is zero. Hence,  $\vartheta_{V_o}$  can be expressed as follows:

$$\vartheta_{V_o} = \frac{k_f \theta_V + k_{f,\text{CO}} \theta_{\text{CO}} + k_{f,\text{H}} \theta_{\text{H}}}{k_a \theta_{\text{O}} + k_{a,\text{H}} \theta_{\text{OH}}} \quad (4.37)$$

The corresponding term can be found for the reference side. Here, the gas only consists of air, no hydrogen or carbon monoxide is present:

$$\vartheta_{V_o}^{ref} = \frac{k_f \theta_V^{ref}}{k_a \theta_O^{ref}} \quad (4.38)$$

These two terms for the vacant oxygen sites in the electrolyte can now be inserted in the Nernst equation. Of course, in a reciprocal way as compared to the model I, since now the oxygen vacancies are considered and not the activity of the ions.

$$U_{\lambda st} = \frac{\Re T_{\text{sensor}}}{2F} \ln \left( \frac{\theta_O^{ref} \left( \theta_V + \frac{k_{f,\text{CO}}}{k_f} \theta_{\text{CO}} + \frac{k_{f,\text{H}}}{k_f} \theta_{\text{H}} \right)}{\theta_V^{ref} \left( \theta_O + \frac{k_{a,\text{H}}}{k_a} \theta_{\text{OH}} \right)} \right) \quad (4.39)$$

Now the sensor voltage output is also dependent on the occupancies of CO, H, and OH, which are in turn dependent on the concentrations of CO, H<sub>2</sub>, and H<sub>2</sub>O. It will be shown that this model approach provides the best results of the three electrolyte models.

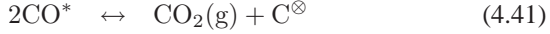
### Model III: Redox Reactions on the Electrolyte

This model was derived from a number of investigations performed by Mizusaki et al., see [65; 66; 68; 67] and [75; 76]. It has been assumed that various species migrate on the electrode surface to the three-phase boundary between the gas, the electrode, and the electrolyte, where they react with oxygen adsorbed on the electrolyte or migrate to the electrolyte surface. Additionally, species such as water or carbon dioxide adsorb on the electrolyte or react directly with the adsorbed species. Here, only the reactions are accounted for, which have been determined to be relevant in the mentioned investigations. It has to be pointed out that the two reaction groups, which will be presented below, have been derived in separate investigations. They have been combined in this thesis.

The first part accounts for reactions, which occur at the two-phase boundary between the electrode and the electrolyte. These reactions include both an exchange of adsorbed species and a transfer of charge carriers. Therefore, the reaction rates can be expressed as current densities,  $i$ . It is assumed that no current is present under steady-state conditions. Hence, all reaction currents can be summed and set to zero. An expression for the occupancy of the oxygen ions in the outer layer in the electrolyte,  $\Theta_{O_2^-}$  shall be derived, which can be inserted in the Nernst equation.

#### 4 Modelling of a Solid-Electrolyte Oxygen Sensor

Two types of reactions with CO adsorbed on the electrode might be considered:

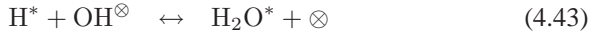


The superscript  $\otimes$  denotes a species adsorbed on the electrolyte. It has been shown in [76] that the first reaction is dominant in a  $\text{CO}_2$  rich environment, whereas the second one mainly occurs in a CO rich environment. The former is true for an engine exhaust environment, hence only reaction (4.40) will be considered. Instead of the reaction rate, the kinetic equation is expressed by means of a current density:

$$i_1 = k_1 \theta_{\text{CO}}^{0.5} \vartheta_{\text{O}}^{0.5} - k_1' c_{\text{CO}_2}^{0.5} \quad (4.42)$$

$\vartheta_{\text{O}}$  stands for the occupancy of oxygen on the electrolyte. The exponents of 0.5 arise from the assumption that this reaction takes place at the phase boundary [67].

Hydrogen adsorbed on the electrode reacts at the phase boundary as follows:



$\otimes$  denotes an empty site on the electrolyte surface. It has been shown in [67] that both reactions should be considered. The corresponding kinetic expressions are

$$i_2 = k_2 \theta_{\text{H}}^{0.5} \vartheta_{\text{OH}}^{0.5} - k_2' \theta_{\text{H}_2\text{O}}^{0.5} \vartheta_{\text{V}}^{0.5} \quad (4.45)$$

$$i_3 = k_3 \theta_{\text{H}}^{0.5} \vartheta_{\text{H}_2\text{O}}^{0.5} - k_3' \theta_{\text{H}_2\text{O}}^{0.5} \vartheta_{\text{H}}^{0.5} \quad (4.46)$$

It is assumed that oxygen atoms are transferred between the electrode and the electrolyte because of the surface concentration gradient:



The current density occurring from this reaction is

$$i_0 = k_0 \theta_{\text{O}}^{0.5} \vartheta_{\text{V}}^{0.5} - k_0' \vartheta_{\text{O}}^{0.5} \theta_{\text{V}}^{0.5} \quad (4.48)$$

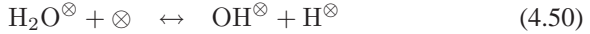
Other species are not accounted for here. In reality, hydrocarbons might play an important role. However, they have neither been considered in the exhaust gas

nor in the electrode model. All reactions occur in parallel. Hence, the current densities  $i_0$ – $i_3$  are added and set to zero, since steady-state is assumed:

$$\begin{aligned}
 0 &= +k_0\theta_{\text{O}}^{0.5}\vartheta_{\text{V}}^{0.5} - k'_0\vartheta_{\text{O}}^{0.5}\theta_{\text{V}}^{0.5} \\
 &+ k_1\theta_{\text{CO}}^{0.5}\vartheta_{\text{O}}^{0.5} - k'_1c_{\text{CO}_2}^{0.5} \\
 &+ k_2\theta_{\text{H}}^{0.5}\vartheta_{\text{OH}}^{0.5} - k'_2\theta_{\text{H}_2\text{O}}^{0.5}\vartheta_{\text{V}}^{0.5} \\
 &+ k_3\theta_{\text{H}}^{0.5}\vartheta_{\text{H}_2\text{O}}^{0.5} - k'_3\theta_{\text{H}_2\text{O}}^{0.5}\vartheta_{\text{H}}^{0.5}
 \end{aligned} \tag{4.49}$$

The second part of the model incorporates reactions which occur on the electrolyte. All reactions are assumed to be in equilibrium, which makes the use of the equilibrium constant  $K(T_{\text{sensor}})$  possible.

In [67], [75], and [76] it was shown that mainly water, hydrogen, and hydroxyl are adsorbed on the electrolyte. It was shown further that water is adsorbed directly from the gas, whereas hydrogen is formed by water or hydroxyl dissociation. Hydroxyl is formed by water dissociation or by hydrogen reacting with an oxygen ion. Both carbon and carbon monoxide have not been considered on the electrolyte. Oxygen occurs both on the surface ( $\text{O}^\otimes$ ) and in the grid ( $\text{O}^{2-}$ ). Hence, four reactions are taken into account:



The corresponding kinetic expressions are directly put in the equilibrium form:

$$0 = K_5\vartheta_{\text{H}_2\text{O}}\vartheta_{\text{V}} - \vartheta_{\text{OH}}\vartheta_{\text{H}} \tag{4.54}$$

$$0 = K_6\vartheta_{\text{H}}\Theta_{\text{O}^{2-}} - \vartheta_{\text{OH}} \tag{4.55}$$

$$0 = K_7\Theta_{\text{O}^{2-}}\vartheta_{\text{V}} - \vartheta_{\text{O}} \tag{4.56}$$

$$0 = K_8c_{\text{H}_2\text{O}}\vartheta_{\text{V}} - \vartheta_{\text{H}_2\text{O}} \tag{4.57}$$

The five equations (4.49) and (4.54)–(4.57) can now be applied to calculate  $\vartheta_{\text{H}}$ ,  $\vartheta_{\text{OH}}$ ,  $\vartheta_{\text{H}_2\text{O}}$ ,  $\vartheta_{\text{O}}$ , and  $\Theta_{\text{O}^{2-}}$ . The concentration of the oxygen ions in the outer layer of the electrolyte,  $\Theta_{\text{O}^{2-}}$ , can then be used for the calculation of the sensor voltage output applying the Nernst equation:

$$U_{\lambda st} = \frac{\Re T_{\text{Sensor}}}{2\text{F}} \ln \left( \frac{\Theta_{\text{O}^{2-}}^{\text{ref}}}{\Theta_{\text{O}^{2-}}} \right) \tag{4.58}$$

## 4.4 Steady-State Simulation Results vs Measurements

Only steady-state simulations have been performed. An engine testbench is not suitable for dynamic tests of the switch-type  $\lambda$  sensor, since it is very difficult to generate well-defined reproducible steps of the exhaust gas components. An analysis in the frequency domain, as can be performed for the wide-range  $\lambda$  sensor [74] cannot be accomplished because of the nonlinear characteristic of the sensor.

For the parameters of the diffusion model, physically reasonable values have been chosen. The parameters of the electrode model have been obtained from the literature, only minor adjustments have been made. As for the electrolyte model II, the parameters had to be tuned. The parameters of model III have been obtained from the literature, where available. Parameters have been tuned to one operating point only. All parameter values can be found in Appendix C.1.

The temperature dependence of the sensor has not been investigated. The reason is again that on an engine test bench, the exhaust gas temperature, composition, and mass flow as well as the sensor temperature cannot be varied independently.

### Exhaust Gas Concentrations

The model was tested on data obtained at an engine speed of 2000 rpm and a relative load of 40%. Figure 4.4 shows the exhaust gas concentrations at this operating point. Measurements have been performed with a considerably aged (at 1100 °C), a moderately aged (at 900 °C), and a fresh TWC, see also Section 2.5. Mainly the H<sub>2</sub>, CO, and HC concentrations exhibit variations. Accordingly, H<sub>2</sub>O and CO<sub>2</sub> concentrations also vary slightly. The concentrations of O<sub>2</sub> and NO are somewhat higher downstream of the aged TWC. Here, the exhaust gas composition is obviously further away from equilibrium, because the aged converter is less effective, which is of course expected. Hence, the sensitivity of the sensor to different ratios of rich species can be tested.

### Occupancies on the Measurement Electrode

The occupancies of the adsorbed species on the measurement electrode for the three TWCs are presented in Figure 4.5. They are shown in a logarithmic scale to elucidate their influence on the Nernst equations of models I and II. On the lean side, the electrode is mainly covered with oxygen, on the rich side with carbon monoxide. The occupancies of the other species are very low. However, the hydrogen coverage is clearly different for the three TWCs, which will be



#### 4.4 Steady-State Simulation Results vs Measurements

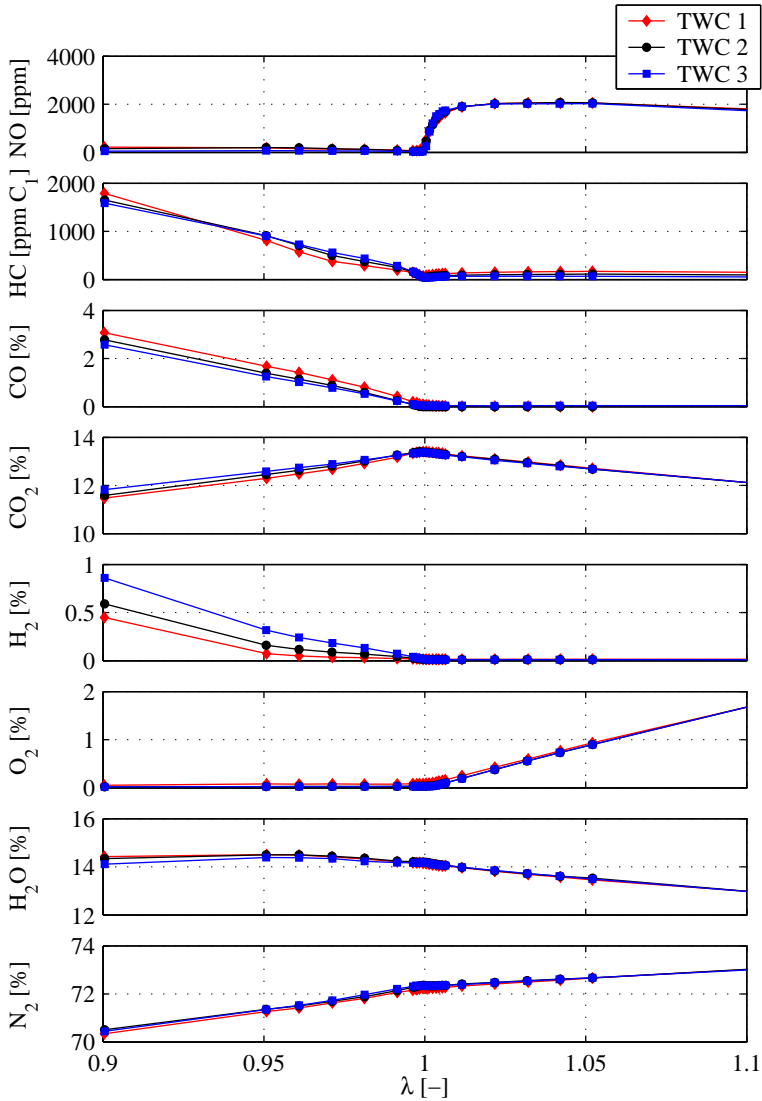


Figure 4.4: Steady-state concentrations of the measured components downstream of differently aged TWCs. TWC 1 is aged at 1100 °C, TWC 2 at 900 °C, and TWC 3 is fresh.

shown to be crucial for the sensor voltage. In fact, the hydrogen desorption was significantly increased as compared to the value obtained from the literature. This led to a reduction of the occupancy of three orders of magnitude, but to a much better result of the simulated sensor voltage, especially for model II.

### Sensor Voltage Outputs of Models I–III

The simulated sensor voltage of model I in comparison with the measured values is depicted in Figure 4.6. The accuracy is qualitatively correct but poor by means of absolute values. On the lean side ( $\lambda > 1$ ), the simulated voltage is far too low. There are two possible reasons for this: The oxygen occupancy is too high, or the occupancies of the other species play a role, even on the lean side, which is not reflected in the model. On the rich side ( $\lambda < 1$ ), the sensitivity to the different exhaust gas mixtures is qualitatively correct, i. e., a higher voltage is obtained downstream of the fresh TWC. However, this is not caused by the higher hydrogen concentration, but rather by the lower oxygen content. Notice that the voltage follows the inverse oxygen occupancy  $\theta_{\text{O}}$ , rather than the hydrogen occupancy,  $\theta_{\text{H}}$ . On an absolute level, the difference between the measured and the simulated voltage is quite large, i. e., up to 100 mV. This shows clearly that other species apart from oxygen have to be taken into account in the electrolyte model.

Figure 4.7 shows the simulated sensor voltage output of model II in comparison with the measured values. The accuracy of the model is very good, both on the lean and on the rich sides. Comparing the sensor voltage with the occupancies reveals that on the rich side the voltage is mainly driven by the hydrogen. Hence, the differences of the sensor voltage output on the rich side are clearly connected with the ratio between  $\text{H}_2$  and CO. Of course, hydrocarbons also play a role in reality, but they have not been taken into account in this model. The sensor characteristic on the rich side ( $\lambda < 1$ ) downstream of the aged TWC is somewhat unsteady. There is a step like saturation at approximately  $\lambda = 0.98$ , from where the voltage rises further on the rich side. This behaviour is obviously caused by the ratio between  $\text{H}_2$  and CO, as can be seen in Figure 4.4. Downstream of the fresh TWC, the characteristic is smoother on the rich side because of the more steady increase of the hydrogen concentration.

The simulated sensor voltage output of model III in comparison with the measured values is presented in Figure 4.8. For the calculation of the sensor voltage, the model was simplified by assuming the occupancy of the free surface sites on the electrolyte to be 1, i. e.,  $\vartheta_V = 1$ . On the lean side ( $\lambda > 1$ ), the agreement between the measured and the simulated values is very good. On the rich side ( $\lambda < 1$ ), the agreement is satisfactory. However, the characteristic is somewhat too steep. The dependency on the ratio between  $\text{H}_2$  and

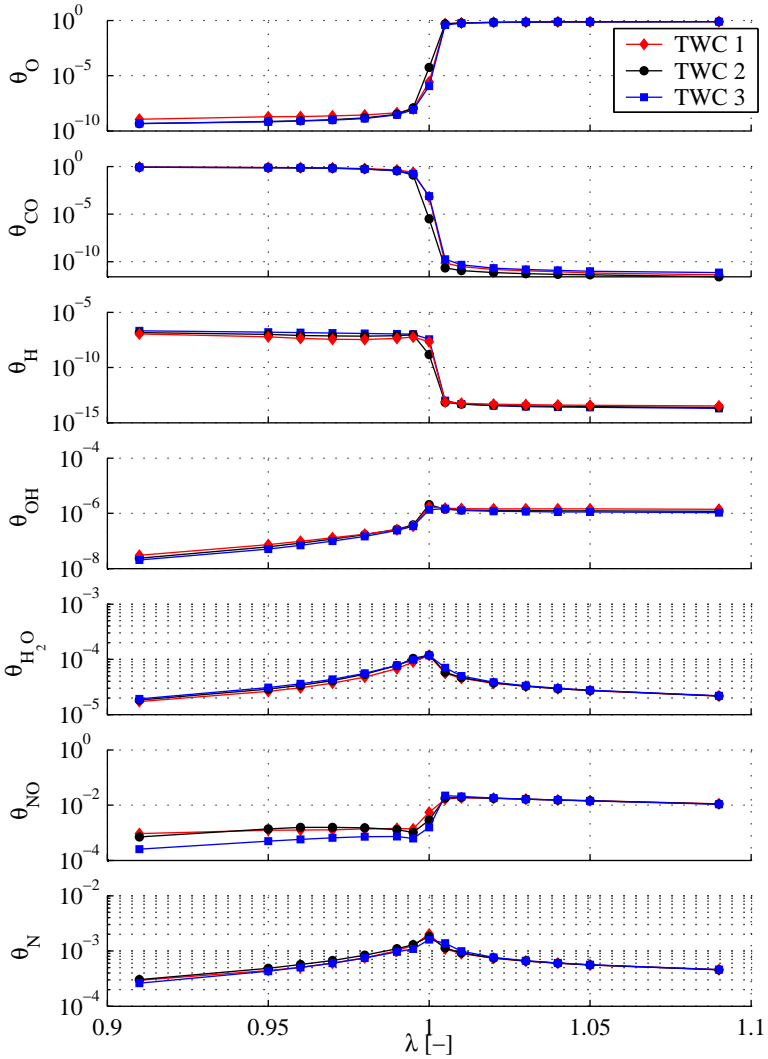


Figure 4.5: Simulated steady-state occupancies of the adsorbed species on the measurement electrode in a logarithmic scale. TWC 1 is aged at 1100 °C, TWC 2 at 900 °C, and TWC 3 is fresh.

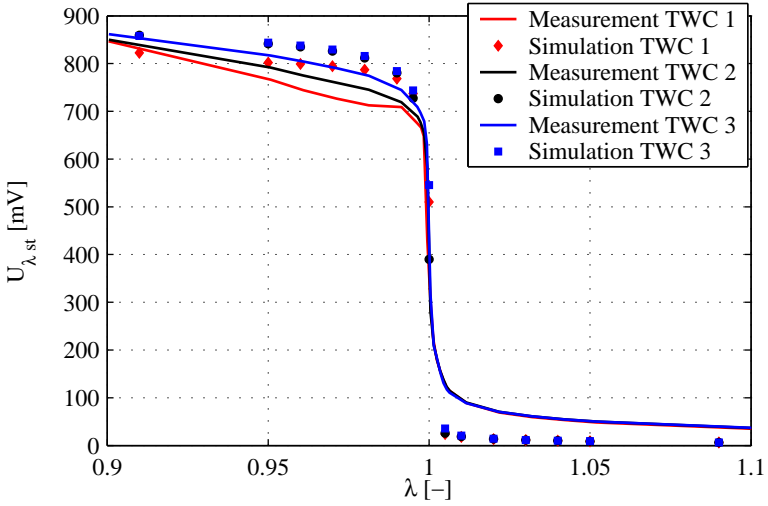


Figure 4.6: Simulated sensor voltage of model I in comparison with the measured values. TWC 1 is aged at 1100 °C, TWC 2 at 900 °C, and TWC 3 is fresh.

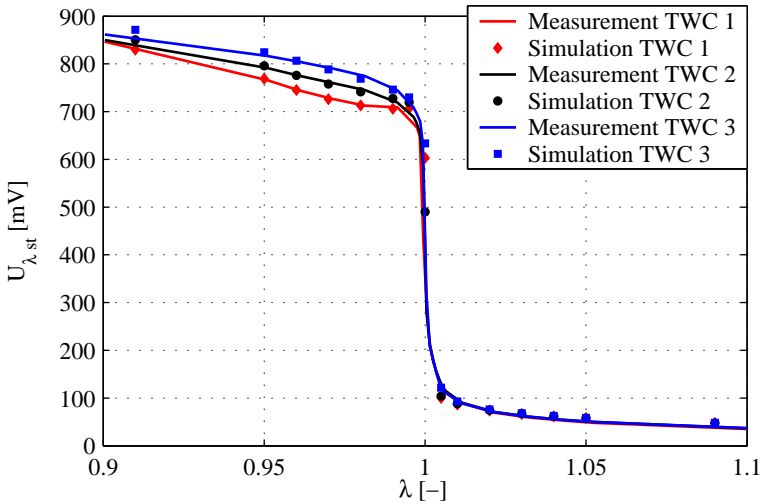


Figure 4.7: Simulated sensor voltage of model II in comparison with the measured values. TWC 1 is aged at 1100 °C, TWC 2 at 900 °C, and TWC 3 is fresh.

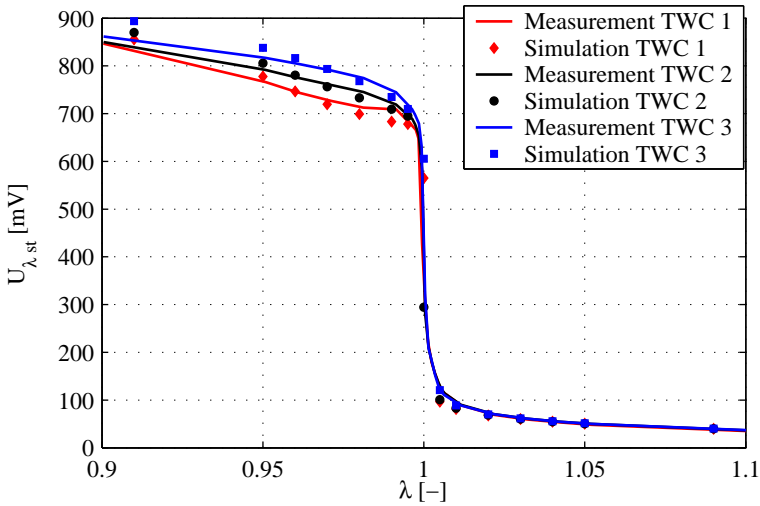


Figure 4.8: Simulated sensor voltage of model III in comparison with the measured values. TWC 1 is aged at 1100 °C, TWC 2 at 900 °C, and TWC 3 is fresh.

CO is reflected well. The consideration of feedback terms of the electrolyte module in the electrode model would probably improve the model and reproduce the saturation on the rich side in a more pronounced way, i. e., flatten the characteristic.

The models I–III revealed clearly that reducing species such as hydrogen or carbon monoxide have to be considered in a switch-type  $\lambda$  sensor model. The reason for this is the fact that the sensor voltage is driven by a shortage of oxygen ions in the electrolyte rather than in the exhaust gas outside the sensor or at the electrode. The shortage of oxygen ions leading to a high voltage output, i. e., over 450 mV is mainly driven by the reducing species. Hence, two conclusions can be drawn for the development of a simple control-oriented model: First, reducing species such as  $H_2$  and CO have to be considered. Secondly, the ratio of these two species has to be accounted for. This calls for a TWC model which calculates the concentrations of these two species correctly, if a physically meaningful model of the sensor is to be applied. This will be pursued in Chapter 5.

## 4.5 Aspects of the Wide-Range $\lambda$ Sensor

Occasionally, the use of wide-range  $\lambda$  sensors downstream of a TWC is proposed in the literature, see e. g. [51] or [39]. This setup has not been considered in this thesis for the following reasons:

First, wide-range  $\lambda$  sensor signals are also heavily distorted by the ratio between  $H_2$ , CO, and HC, as is the case with the switch-type  $\lambda$  sensors. This has been shown by various authors, see [42] or [79]. Also in this thesis, a very impressive example can be seen in Figure 3.2 of the previous chapter. Although the rich branch of the switch-type characteristic is also distorted by the exhaust gas composition, the position of the switch remains stable, especially downstream of the TWC. Hence, this sensor provides a very robust information about whether the exhaust gas is lean or rich during both the sensor's and TWC's lifetime. This cannot be achieved with a wide-range  $\lambda$  sensor.

Secondly, the wide-range  $\lambda$  sensor changes its characteristic during its lifetime. This goes hand in hand with the first reason: Since the position of the switch in the switch-type  $\lambda$  sensor characteristic is very robust against ageing, this sensor can be used both for the calibration and the diagnosis of the upstream sensor. This cannot be done with the wide-range  $\lambda$  sensor, whose characteristic is subject to a certain drift over its lifetime.

Thirdly, the switch-type  $\lambda$  sensor is cheaper. While this is certainly a killing point for commercial applications, it is not the most important aspect when pursuing new ways of TWC control or diagnosis in the research environment. However, since the application of the wide-range  $\lambda$  sensor does not really bring substantial advantages, it is somewhat hard to justify its use.

The distortion of the signal of the wide-range  $\lambda$  sensor used in this thesis has been investigated in more detail. It has to be pointed out that this was only done on one single sensor and on an engine test bench. This is of course not a suitable way and/or infrastructure for the determination of a systematic behaviour of this type or brand of sensors. However, the results will be presented in order to give an impression on how potential distortions may appear. Of course, the probably somewhat controversial comments above should be additionally supported.

Only the distortion of the wide-range  $\lambda$  sensor signal upstream of the TWC had been investigated. This was done by controlling the measured upstream  $\lambda$  to  $\pm 1$ , 3, and 5% off stoichiometry, i. e.,  $\lambda = 1 \pm 0.01, 0.03, 0.05$ . The "true"  $\lambda$  was then determined from the exhaust gas measurements. Thereby, (1.4) has been applied. For convenience, it is repeated here:

$$\lambda = \frac{2y_{CO_2} + y_{CO} + 2y_{O_2} + y_{NO} + y_{H_2O}}{2y_{CO_2} + 2y_{CO} + y_{H_2} + \left(2x + \frac{y}{2}\right) y_{C_xH_y} + y_{H_2O}}$$

This was done in five different operating points on all five TWCs used in this

thesis, see also Section 2.5. The measurements have been performed on different days with frequent calibration of all exhaust gas measurement devices. Exhaust gas concentration measurements are, of course, also afflicted with errors. Therefore, the maximum error propagation from the measurements to the estimated  $\lambda$  has been analysed. The methodology is presented in Appendix A.2.

The measured and the calculated  $\lambda$  values are shown in Figure 4.9. Also shown is the total maximum error of the calculated  $\lambda$ . Notice that the expected error is approximately one third of the maximum error. It can be clearly seen that the error of the sensor is dependent both on the operating point and on the  $\lambda$ . The error behaviour of the sensor is obviously dependent on whether it is operated in a lean or in a rich mixture.

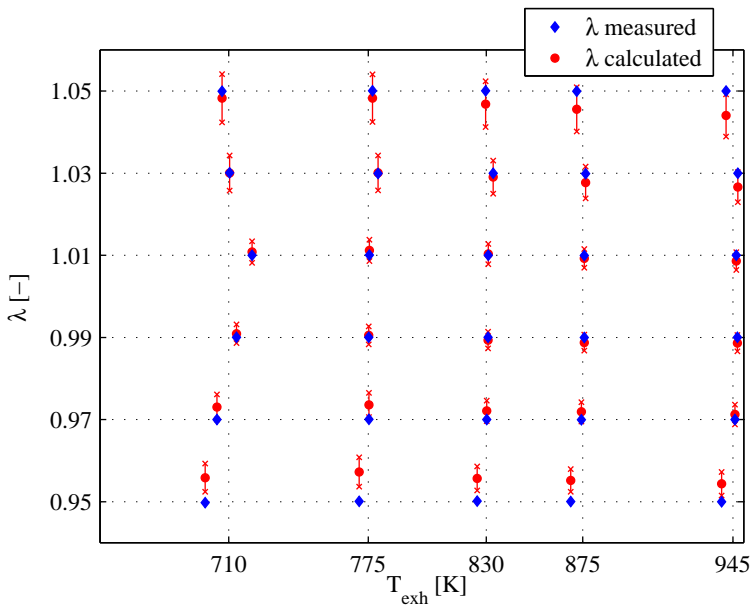


Figure 4.9: Measured and calculated  $\lambda$  at five different operating points (=exhaust gas temperatures). The error bars denote the maximum error.

## 4.6 Conclusion

A process model of a switch-type  $\lambda$  sensor, which accounts for  $O_2$ ,  $NO$ ,  $H_2$ ,  $CO$ ,  $H_2O$ , and  $CO_2$  in the exhaust gas has been developed. The goal was thereby to reproduce the sensitivity of the sensor signal to the different exhaust gas species, at least on a qualitative level. The model consists of three modules. The first module accounts for the diffusion of the exhaust gas species from/to the electrode through a porous protection layer. The second module incorporates the surface kinetics of the catalytically active electrode. The third module contains an algebraic model of the electrolyte. Three different electrolyte models have been developed. The first model, which only accounts for adsorbed oxygen on the electrodes, brought qualitatively correct but quantitatively poor results. Very good results have been obtained from the other two models, where the direct influence of adsorbed hydrogen and carbon monoxide on the electrode or even the electrolyte had been incorporated.

Generally, it could be shown that not only the oxygen, but also the reducing species such as carbon monoxide and hydrogen drive the sensor voltage, especially in a rich exhaust environment, i. e., where  $\lambda < 1$ . Thereby, the sensor voltage is very sensitive to the ratio between  $H_2$  and  $CO$ . This was tested in the exhaust of differently aged TWCs. The process model is able to reproduce this sensitivity accurately.

If a switch-type  $\lambda$  sensor is used to support an observer of the TWC, its sensitivity to the ratio between  $H_2$  and  $CO$  should be taken into account. Hence, this ratio should be reproduced by the TWC observer.

Wide-range  $\lambda$  sensors exhibit considerable offsets, which are dependent on the exhaust gas composition, the operating point, and the ageing level. This has been demonstrated by means of a comparison of the measured with the calculated  $\lambda$ , which was obtained from exhaust gas measurements. Unlike the switch-type  $\lambda$  sensor, the wide-range  $\lambda$  sensor cannot provide a robust and accurate information about the stoichiometric point. Therefore, this type of sensor has not been considered to be used downstream of the TWC throughout this thesis.



# 5 Observer of a Three-Way Catalytic Converter

## 5.1 Introduction

In the last two chapters, detailed process models of the TWC and the switch-type  $\lambda$  sensor have been derived. These models reflect the physics accurately. However, they are very complex and consume a considerable amount of CPU resources. For a control system, these models are far too complicated and thus have to be simplified substantially. Generally, the five most important issues concerning control-oriented modelling of an exhaust gas aftertreatment system can be described as follows:

- **Simplicity:** The model has to be as simple as possible in order to fit into an engine control system, where CPU resources are limited.
- **Accuracy of TWC model:** The control-relevant states such as the level of the stored oxygen or the reduction rates have to be estimated accurately.
- **Accuracy of sensor model:** In order to support state observers, e. g. a Kalman filter, the sensor signal downstream of a TWC has to be modelled properly. This requires, of course, an accurate estimation of the components which drive the sensor output, such as  $O_2$ ,  $H_2$ , or CO.
- **Adaptability:** Both TWC and  $\lambda$  sensors change their dynamical behaviour during their lifetime because of ageing. The model should not only be able to cope with ageing but also yield quantitative information about the TWC's state and performance.
- **Applicability:** A TWC model should be simple to apply and simple to parameterise to different TWCs without the price of extensive measurement campaigns.

In order to account for all stated issues, the use of a physical model is almost compulsory. Therefore, it has been decided to develop a physical control-oriented model of the TWC and the  $\lambda$  sensors from the process models presented in the previous two chapters.

A number of control-oriented models have been presented in the literature. In [89], the TWC was modelled as an integrator representing the oxygen storage. In [23], additionally saturation effects and asymmetric filling and depleting dynamics were introduced using nonlinear functions. A similar model was presented in [6]. This model was derived from a very complex and accurate TWC model presented in the same investigation. A model, where apart from the nonlinear filling and depleting dynamics also the  $\lambda$  sensor signal distortion was taken into account, was presented in [81]. In [80], the importance of the reversible TWC deactivation by a presumably carbonaceous species was pointed out.

The control-oriented model of the TWC and the  $\lambda$  sensor shall be implemented in an observer. Hence, an accurate TWC model is not sufficient. Also the  $\lambda$  sensor downstream has to be modelled properly, in order to obtain an estimated sensor signal which is necessary to close the observer loop. The observer developed in the following is an extended Kalman filter, which can be used as a state estimator on the one hand and for online parameter estimation on the other hand. Hence, the filter provides states such as the oxygen storage level in the TWC, which will be controlled, and additionally estimates the oxygen storage capacity, which can be used as a reference for the ageing of the TWC. Naturally, the model adapts to the ageing level of the TWC. Theoretically, also other diagnosis information such as the offset of the upstream  $\lambda$  sensor could be obtained from the extended Kalman filter. However, this has been found to be impractical, and a much more elegant way to obtain this information from the TWC controller will be presented.

In the following, a control-oriented model of the exhaust gas aftertreatment system will be derived. In the second part of this chapter, this model is incorporated in an extended Kalman filter, which serves both as a state and parameter estimator. It will be shown that the filter provides an excellent means of estimating the storage capacity of the TWC.

An extended Kalman filter of the exhaust gas aftertreatment system has already been presented in [4]. However, the model presented there exhibits some major differences as compared to the one developed here. In that publication, it was assumed that the TWC deactivation is mainly caused by the occupancy of the ceria by OH. This could not be verified. Especially the exhaust gas measurements of water and hydrogen did not show the expected behaviour such as peaks during the oxidation of an OH-layer. It was found that the assumption of the deactivation by carbonaceous species agreed much better with the measured exhaust gas components and the transient behaviour of the TWC in general<sup>1</sup>.

---

<sup>1</sup>The author wants to point out that the initial idea for this approach arose during a conversation with Dr. James Peyton-Jones, Villanova University.

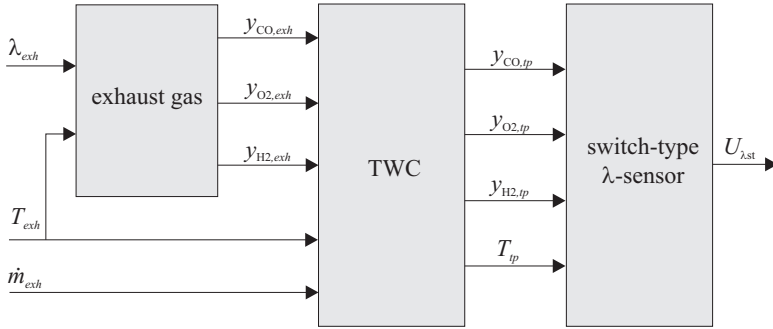


Figure 5.1: Structure of TWC observer model.

This does not mean that OH is not present on the ceria, it just does not play the role as a rate determining deactivator, as stated in the cited reference. Additionally, the model presented in this thesis has been significantly optimised in terms of the calculation effort.

## 5.2 Control-Oriented Modelling of the Exhaust Gas Aftertreatment System

The structure of the control-oriented model follows the physical setup. It is shown in Figure 5.1. The model is divided into three modules. The first module contains the model of the raw exhaust gas, where the mole fractions  $y_{i,exh}$  of the components  $i$  entering the TWC are calculated from the measured  $\lambda$  value,  $\lambda_{exh}$ . The second module consists of the TWC model. Here, the outlet mole fractions  $y_{i,tp}$  of the exhaust gas components  $i$  and the temperature at the TWC outlet  $T_{tp}$  are calculated from the exhaust gas mass flow  $\dot{m}_{exh}$ , the exhaust gas temperature  $T_{exh}$ , and the mole fractions provided by the wide-range  $\lambda$  sensor model. In the third module finally, which represents the switch-type  $\lambda$  sensor, the sensor voltage output  $U_{\lambda st}$  is calculated from the temperature and the mole fractions of the exhaust gas downstream of the TWC.

In the two preceding chapters it has been shown that the TWC deactivation by HC plays an important role for two reasons. Firstly, it influences directly the water-gas shift reaction, which has an impact on the amount of hydrogen in the exhaust at the tail of the TWC. Hydrogen or rather the ratio between  $H_2$ ,

CO, and HC in turn mainly drive the signal of the switch-type  $\lambda$  sensor, if the mixture is rich, i. e.,  $\lambda < 1$ . Secondly, the storage of HC, which is a slow process as compared to the storage behaviour of oxygen, has a significant impact on the general storage dynamics of the TWC. Therefore, the deactivation has been accounted for in the control-oriented model. Since the model is to be used in an observer loop, the voltage output of the downstream switch-type  $\lambda$  sensor must be estimated accurately. This can only be achieved, if the hydrogen concentration is accounted for, as has been shown in the previous chapter.

Apart from the accurate downstream sensor output, the model has to provide the quantities which are needed for control and diagnosis purposes. Any TWC control strategy naturally aims at minimising the concentrations of  $\text{NO}_x$ , CO, and HC. One way to achieve this might be to develop a model, which explicitly calculates these concentrations, and then to derive an optimal control strategy for the minimisation. A simpler approach is to balance the TWC to a (steady) state, where disturbances of the air-to-fuel ratio both to the lean or to the rich side can be buffered or at least damped to a satisfactory level. An obvious approach is therefore to control the oxygen storage level of the TWC. It is then sufficient that the control-oriented model provides the oxygen storage level, rather than the explicit concentrations of  $\text{NO}_x$ , CO, and HC.

As for the diagnosis, parameters are needed which reflect the performance of the TWC in terms of the conversion efficiency of  $\text{NO}_x$ , HC, and CO. Again, this might be achieved by directly estimating the concentrations of these three species. However, another approach is to estimate the storage capacity, which is assumed to be connected to the conversion efficiencies. A well-known assumption is the so called “hockey-stick” function, which links the oxygen storage capacity with the conversion efficiency of HC [46].

From the considerations above, it is apparent that the model should include the following features:

- Oxygen storage level as a state variable.
- Storage level of a deactivating species as a state variable.
- Concentrations of hydrogen, oxidising and additional reducing species as output variables (to feed the switch-type  $\lambda$  sensor model).
- Storage capacity of the TWC as a model parameter.

Hydrocarbons only occur in small quantities as compared to CO, at least during normal operation, i. e., after the TWC has lit off<sup>2</sup>. Hence, their influence on the

---

<sup>2</sup>Notice that this reasoning should be taken with care, if applied to natural gas engines, where high amounts of methane may occur.

sensor downstream of the TWC is limited. Therefore, the HC are incorporated in the CO concentration. Catalyst deactivation is accounted for by means of CO adsorption instead of HC adsorption, see Section 5.2.3. NO<sub>x</sub> also occur only in small quantities as compared to O<sub>2</sub>. Additionally, they always occur in parallel and have a similar influence on the  $\lambda$  sensor. Therefore, they are included in the O<sub>2</sub> concentration. With this, only three components have to be accounted for, namely CO, O<sub>2</sub>, and H<sub>2</sub>. The other components (H<sub>2</sub>O, CO<sub>2</sub>, and N<sub>2</sub>) only vary little in the operating range of the engine. Additionally, they are present in large quantities. Hence, their influence is not important, because it is roughly constant, independent of the  $\lambda$  or the operating point of the engine.

In the following sections, the three modules are presented. At first, models of the raw exhaust gas and of the switch-type  $\lambda$  sensor are discussed. These determine the inputs and outputs of the TWC model, which will be developed in the third part. Additionally, a procedure for the calibration of the model will be presented.

### 5.2.1 Control-Oriented Raw Exhaust Gas Model

In this module, the raw exhaust gas concentrations of CO, H<sub>2</sub>, and O<sub>2</sub> are calculated from the output of the wide-range  $\lambda$  sensor, which is located upstream of the TWC. Hence, the module actually contains an “inverted” model of the wide-range  $\lambda$  sensor.

Basically, the concentrations of the mentioned gas components could be obtained from lookup tables, as in the process model. However, this is not a very good approach for two reasons. Firstly, the use of lookup tables makes measurements with exhaust gas analysers necessary. Secondly, these measurements must be very accurate and consistent in terms of the air-to-fuel ratio. Naturally, the model is very sensitive to errors and inconsistencies of the inlet concentrations. This may lead to considerable offsets of the estimation of the storage capacity. Notice that these errors cannot be corrected by the downstream sensor, whereas a simple offset of the upstream sensor can be corrected because of the accurate and stable position of the downstream sensor’s switch.

A much better approach is the use of an exhaust gas model. It has been found that a very simple model suffices and presumably is generally valid for all modern port-injected spark-ignited gasoline engines.

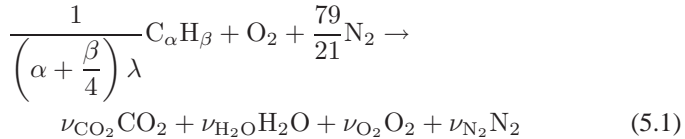
In Figure 3.6, profiles of measured raw exhaust gas components dependent on  $\lambda$  have been shown. The only component which significantly changes with the operating point is NO. The model only needs the sum of NO and O<sub>2</sub>, hence this dependency does not have to be accounted for. Apart from the NO, all other concentrations vary little with the operating point.

Generally, it can be observed that the concentrations of reducing and oxidising species decrease with higher temperatures because of a more efficient combustion. This should be accounted for in the model, because it directly affects the heat production in the TWC. The heat production is proportional to the amount of reactants, i. e., oxidising and reducing species. Metaphorically speaking, the less efficient the combustion was in the cylinder, the more has to be burned in the TWC, which causes additional heat.

The second important point is the ratio between  $H_2$  and CO in the raw exhaust. It can be observed in Figure 3.6 that the two concentration profiles are roughly parallel, from which it can be concluded that their ratio remains approximately constant. This is hard to see from the measurements, because the accuracy of the raw exhaust measurements is not very good, especially, when the concentrations are very small. Fortunately, the TWC model is not very sensitive to the ratio between  $H_2$  and CO in the raw exhaust gas. Therefore, a constant ratio has been assumed in the model.

The calculation of the exhaust gas concentrations is simple and straightforward. It is conducted in two steps. In a first step, only the excess rich or lean concentrations, dependent on whether  $\lambda$  is smaller or greater than 1, are calculated. In a second step, a model for the unburned components is developed.

If the engine is operated lean, and if the combustion is perfect, only oxidising species remain in the exhaust. All these species are collected in the  $O_2$  here. Hence, the  $O_2$  concentration can be calculated directly from  $\lambda$ . If the gasoline is assumed to be  $C_\alpha H_\beta$  and the ratio between  $O_2$  and  $N_2$  of the air is 21/79, the combustion reaction can be expressed as follows:

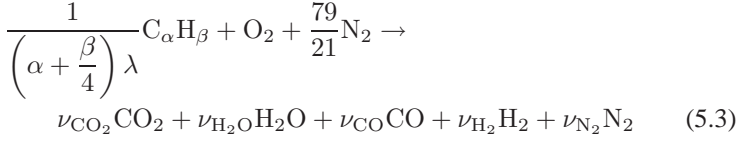


This equation can be easily extended, if humid air and a fraction of O in the gasoline are assumed. This has been done in Appendix A.1 for the evaluation of the exhaust gas measurements. Here, both have been neglected. From the combustion reaction, the mole fraction of  $O_2$  can be derived directly:

$$\begin{aligned} y_{O_2} &= \frac{\nu_{O_2}}{\sum_{i=CO_2, H_2O, O_2, N_2} \nu_i} \\ &= \frac{1 - \frac{1}{\lambda}}{\frac{\alpha + \beta/2}{(\alpha + \beta/4)\lambda} + \left(1 - \frac{1}{\lambda}\right) + \frac{79}{21}} \end{aligned} \quad (5.2)$$

## 5.2 Control-Oriented Modelling of the Exhaust Gas Aftertreatment System

Likewise, this can be done on the rich side, i. e., where  $\lambda < 1$ . Here, only CO and H<sub>2</sub> are present in the model. Their ratio  $\phi_{\text{H}_2/\text{CO}}$  is assumed to be constant. Hence, both species can be determined from  $\lambda$ . The combustion reaction is now



Again, the mole fractions of CO and H<sub>2</sub> can be obtained directly from the combustion reaction using  $\phi_{\text{H}_2/\text{CO}}$ :

$$y_{\text{CO}} = \frac{\frac{2}{1 + \phi_{\text{H}_2/\text{CO}}} \left(\frac{1}{\lambda} - 1\right)}{\frac{\alpha + \beta/2}{(\alpha + \beta/4)\lambda} + \frac{79}{21}}$$

$$y_{\text{H}_2} = \frac{\frac{2\phi_{\text{H}_2/\text{CO}}}{1 + \phi_{\text{H}_2/\text{CO}}} \left(\frac{1}{\lambda} - 1\right)}{\frac{\alpha + \beta/2}{(\alpha + \beta/4)\lambda} + \frac{79}{21}} \quad (5.4)$$

With equations (5.2) and (5.4), the concentrations of excess O<sub>2</sub> ( $\lambda > 1$ ), or CO and H<sub>2</sub> ( $\lambda < 1$ ) can be obtained from  $\lambda$ . To these concentrations the species are added, which occur because of incomplete combustion. To preserve the air-to-fuel ratio, the amount of added O<sub>2</sub> has to be stoichiometrically balanced to the amount of added CO and H<sub>2</sub>. For the actual concentration profile, a heuristic function has been found, which matches the measured profiles well. Tests have shown that the accuracy of the concentrations is not critical. However, it is very important that the final concentration profiles are consistent in terms of the air-to-fuel ratio  $\lambda$ . The heuristic function of the additional concentration profile can be expressed as follows:

$$\Delta y_{\text{O}_2} = 0.5(\Delta y_{\text{CO}} + \Delta y_{\text{H}_2}) = \frac{\eta_{\text{comb}}}{1 + 10|\lambda - 1|} \quad (5.5)$$

$\eta_{\text{comb}}$  can be interpreted as an inverse combustion efficiency. If the combustion is perfect, the factor becomes zero. The factor is dependent on the temperature and has a strong impact on the energy balance of the TWC. It generally decreases with increasing temperatures of the raw exhaust. A linear approximation of this dependency is sufficient. Thus,  $\eta_{\text{comb}}$  can be expressed as follows:

$$\eta_{\text{comb}} = a_{\eta_{\text{comb}}} + b_{\eta_{\text{comb}}} \cdot T_{\text{exh}} \quad (5.6)$$

The two coefficients  $a_{\eta_{comb}}$  and  $b_{\eta_{comb}}$  can be obtained from steady-state temperature and mass flow measurements using the energy balance equations. Alternatively, their values can be derived from concentration measurements of the raw exhaust gas.

Figure 5.2 shows the comparison between the measured and the calculated mole fractions of  $O_2$ , CO, and  $H_2$ . Notice that the measured  $O_2$  concentration includes NO, and the CO includes HC. A ratio between H and C of two has been assumed in the HC. Hence, the measured mole fractions of  $O_2$  and CO were obtained as follows:

$$y_{O_2} = y_{O_2}^{meas} + \frac{1}{2}y_{NO}^{meas} \quad (5.7)$$

$$y_{CO} = y_{CO}^{meas} + 3y_{HC}^{meas} \quad (5.8)$$

The parameters for the calculation of  $\eta_{comb}$  have been obtained from the exhaust gas measurements. They are given in Appendix D. The agreement is sufficiently good. The deviations mainly occur from the inclusion of HC in the CO concentration. This disturbs the ratio between CO and  $H_2$ , especially, where the concentrations are small, i. e., on the lean side. Theoretically, the HC could also be divided into a fraction added to the  $H_2$  and the rest added to the CO. However, in the TWC model, catalyst deactivation is caused by the adsorption of CO, unlike in the process model, where the adsorption of HC deactivates the TWC. Therefore, it has been decided to fully include the HC in the CO concentration. Since the deviation mainly occurs on the lean side, only a limited impact on the performance of the control-oriented model has to be expected.

### 5.2.2 Control-Oriented Model of a Switch-Type $\lambda$ Sensor

In Chapter 4, a process model of the switch-type  $\lambda$  sensor has been presented. It has been shown that not only the oxygen concentration is important for the sensor signal output, but also the concentrations of the reducing species. Especially  $H_2$  has been found to have a strong impact on the sensor voltage output, particularly under rich conditions, i. e., where  $\lambda < 1$ .

To derive a simple sensor model, a rather metaphorical approach is taken. Following the results of the process model, it could be stated that the oxygen ions are attached with a spring to the electrolyte and that the sensor voltage corresponds to the drag of the spring. If the sensor is exposed to a “neutral”, i. e., inert gas such as nitrogen, the springs are under a slight drag. The sensor



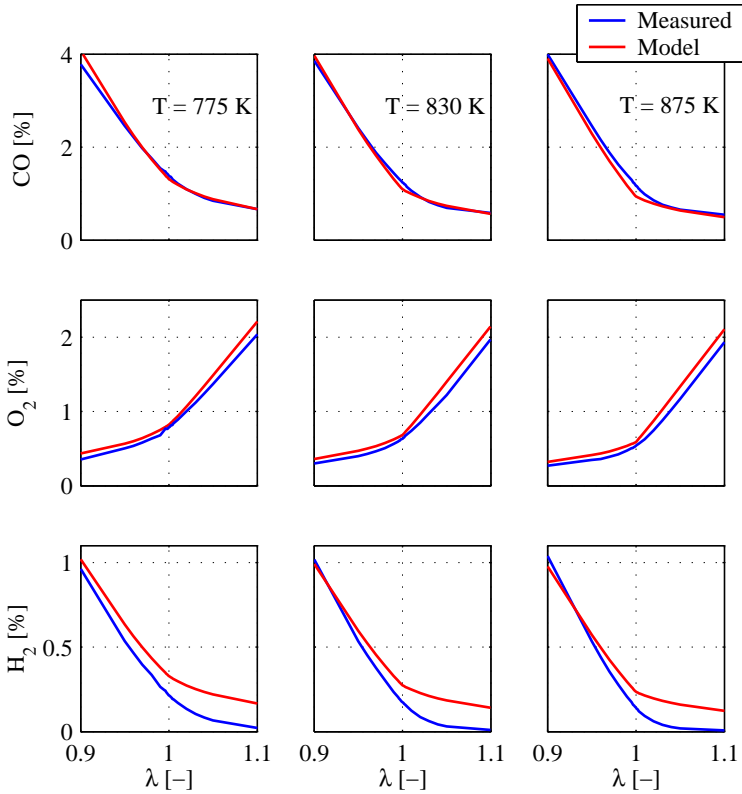


Figure 5.2: Comparison of the measured and calculated raw exhaust gas concentrations. The first column shows the concentrations at an exhaust gas temperature of 775 K, the second at 830 K, and the third at 875 K.

shows a voltage output of approximately 300-400 mV. If the sensor is exposed to a lean atmosphere with excess oxygen, the springs are released and the voltage drops. If exposed to reducing species, the oxygen ions are more attracted, the springs are stretched and a high voltage results. These considerations can be summarised with a simple mathematical formulation:

$$U_{\lambda st} = A_{\lambda st} + f(y_{CO}, y_{H_2}) - g(y_{O_2}) \quad (5.9)$$

Hence, if exposed to an inert gas, the sensor output is  $A_{\lambda st}$ . From here, CO or  $H_2$  pull the voltage up, whereas  $O_2$  takes it down.

An analysis of the measured exhaust gas components and the sensor voltage output reveals that the sensor output is mainly correlating with the logarithm of the exhaust gas components. This conclusion might also be drawn from the results of Chapter 4. However, there, the voltage was calculated from the adsorbed and not from the gaseous species. Hence, the functions  $f$  and  $g$  in (5.9) should contain the logarithms of the gas species' mole fractions. If exposed to a rich exhaust, i. e.,  $\lambda < 1$ , the sensitivity to  $\text{H}_2$  is dominant. However, if no  $\text{H}_2$  is present, still voltage outputs of 500 mV and more result, see [14]. This is considered by introducing a weighted sum of the CO and the  $\text{H}_2$  mole fractions. Additionally, the model should account for the fact that the sensor output is temperature dependent, if  $\lambda < 1$ , as has been shown in e. g. [73]. The sensor voltage decreases with increasing temperatures. Although a heated sensor was used here, it still exhibited a temperature dependence. This has been covered by an Arrhenius Ansatz. If all these considerations are accounted for, the following sensor model results:

$$\begin{aligned}
 U_{\lambda st} &= A_{\lambda st} \\
 &+ E_{A,\lambda st} \cdot \exp\left(\frac{-E_{E,\lambda st}}{\mathfrak{R}T_{tp}}\right) \cdot \log_{10}(1 + B_{\lambda st}y_{\text{CO}} + C_{\lambda st}y_{\text{H}_2}) \\
 &- F_{\lambda st} \cdot \log_{10}(1 + D_{\lambda st}y_{\text{O}_2})
 \end{aligned} \tag{5.10}$$

The 1 in the logarithmic expressions is necessary to prevent the term from becoming negative. With a concentration of zero, the term should naturally become zero, as well. Of course, also the natural logarithm could be used, the parameters would have to be adjusted accordingly.

The use of the gas temperature downstream of the TWC  $T_{tp}$  is a somewhat crude simplification. In this investigation, a heated sensor was used, where the heater was always on full power, i. e., the temperature was not controlled. A much better approach would be the use of a temperature controlled sensor. Additionally, the thermal model could be improved by accounting for the exhaust gas mass flow in addition to the exhaust gas temperature. With this, a proper heat balance could be calculated. However, the approach used here proved to be sufficient for the laboratory environment, as will be shown further below.

The model cannot be applied to the concentrations directly. In the real sensor, the exhaust gas is brought to a state close to the chemical equilibrium on the catalytically active electrodes. The calculation of the equilibrium would be far too complex here. Therefore, a simple approach has been taken. If the mixture is lean, i. e., excess oxygen is present, the following "equilibrium"

concentrations are used:

$$\begin{aligned} y_{\text{O}_2}^{eq} &= y_{\text{O}_2} - 0.5(y_{\text{H}_2} + y_{\text{CO}}) \\ y_{\text{CO}}^{eq} &= 0 \\ y_{\text{H}_2}^{eq} &= 0 \end{aligned} \quad (5.11)$$

Under rich operation, i. e., with excess CO and H<sub>2</sub>, the calculation is a bit more complicated, because CO and H<sub>2</sub> are oxidised simultaneously by the remaining O<sub>2</sub>. Hence, a weighting factor  $w_{\lambda_{st}}^{eq}$  has to be introduced:

$$\begin{aligned} y_{\text{O}_2}^{eq} &= 0 \\ y_{\text{CO}}^{eq} &= \max(y_{\text{CO}} - 2(1 - w_{\lambda_{st}}^{eq})y_{\text{O}_2} + \min(y_{\text{H}_2} - 2w_{\lambda_{st}}^{eq}y_{\text{O}_2}, 0), 0) \\ y_{\text{H}_2}^{eq} &= \max(y_{\text{H}_2} - 2w_{\lambda_{st}}^{eq}y_{\text{O}_2} + \min(y_{\text{CO}} - 2(1 - w_{\lambda_{st}}^{eq})y_{\text{O}_2}, 0), 0) \end{aligned} \quad (5.12)$$

If  $w_{\lambda_{st}}^{eq}$  is 0, the remaining O<sub>2</sub> in a rich gas only oxidises CO. If the factor is 1, only H<sub>2</sub> is oxidised. The probably somewhat unexpected “min” expression is necessary to cover the case, when the mixture is rich, but the O<sub>2</sub> concentration still is greater than one of the weighted CO or H<sub>2</sub> concentrations. In all simulations, it was assumed that CO is oxidised more efficiently at the electrode than H<sub>2</sub>. Therefore,  $w_{\lambda_{st}}^{eq}$  was chosen as follows:

$$w_{\lambda_{st}}^{eq} = \frac{0.3y_{\text{H}_2}}{0.3y_{\text{H}_2} + y_{\text{CO}}} \quad (5.13)$$

The response time of the sensor is assumed to be well below 100 ms. Considering the relatively slow dynamics of the exhaust gas composition downstream of the TWC, the sensor dynamics can be neglected. Thus, an algebraic model as presented should be sufficient.

### Simulation Results vs Measurements

The sensor model has been tested both with steady-state and transient measurements. The parameters have been obtained using a least-squares algorithm. They are depicted in Appendix D.1.

In order to test the model against both varying exhaust gas compositions and temperatures, measurements of all TWCs under different engine operating conditions were used. Thereby, the sensor voltage output was calculated from the measured exhaust gas concentrations using (5.11), (5.12), and (5.10).

Figure 5.3 shows the measured and the modelled steady-state sensor voltage output downstream of different TWCs at the same engine operating point and

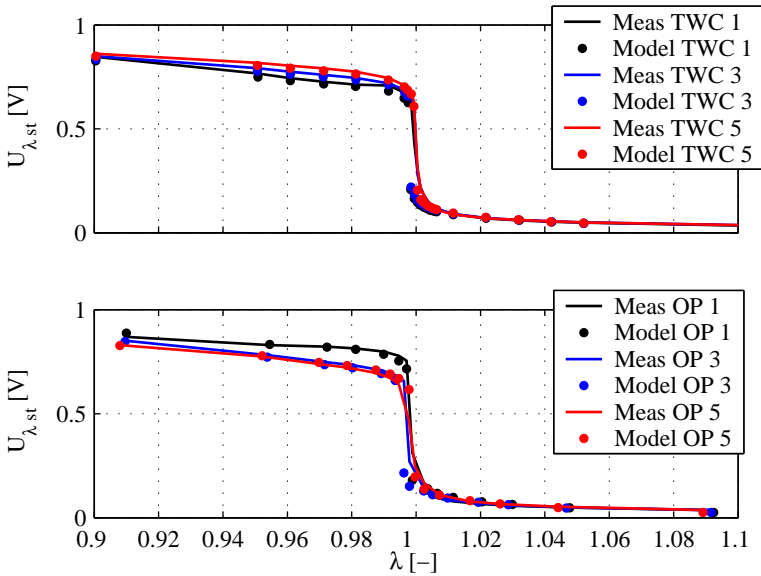


Figure 5.3: Calculated and measured switch-type  $\lambda$  sensor voltage output in steady-state conditions. The upper graph shows the output downstream of TWCs 1, 3, and 5 (aged at 1100 °C, 900 °C, and fresh, see Section 2.5). The lower graph shows one TWC at different engine operating points, which are (speed/load/raw exhaust temperature) (1) 1250 rpm/25 %/440 °C, (3) 1750 rpm/35 %/570 °C, and (5) 2500 rpm/50 %/680 °C.

downstream of one TWC at different engine operating points. The agreement is very good. It can be clearly seen that the model accounts both for the sensitivity towards varying exhaust gas compositions (different TWCs) and temperatures (different engine operating points). However, one small drawback is the behaviour close to the stoichiometric point on the lean side ( $\lambda > 1$ ). Here, the model is somewhat too sensitive. This might be a consequence of the rather rigorous “equilibrium” calculation (5.11–5.12). Tests have shown that care should be taken, if the model is to be used in the raw exhaust. In that case, an improved equilibrium model should be applied.

In Figure 5.4 measured and modelled sensor voltage outputs during  $\lambda$  steps are shown for all TWCs under various engine operating points. Again, the agreement is very good, although the sensor model is algebraic. This confirms the assumption of slow exhaust gas composition dynamics as compared to the

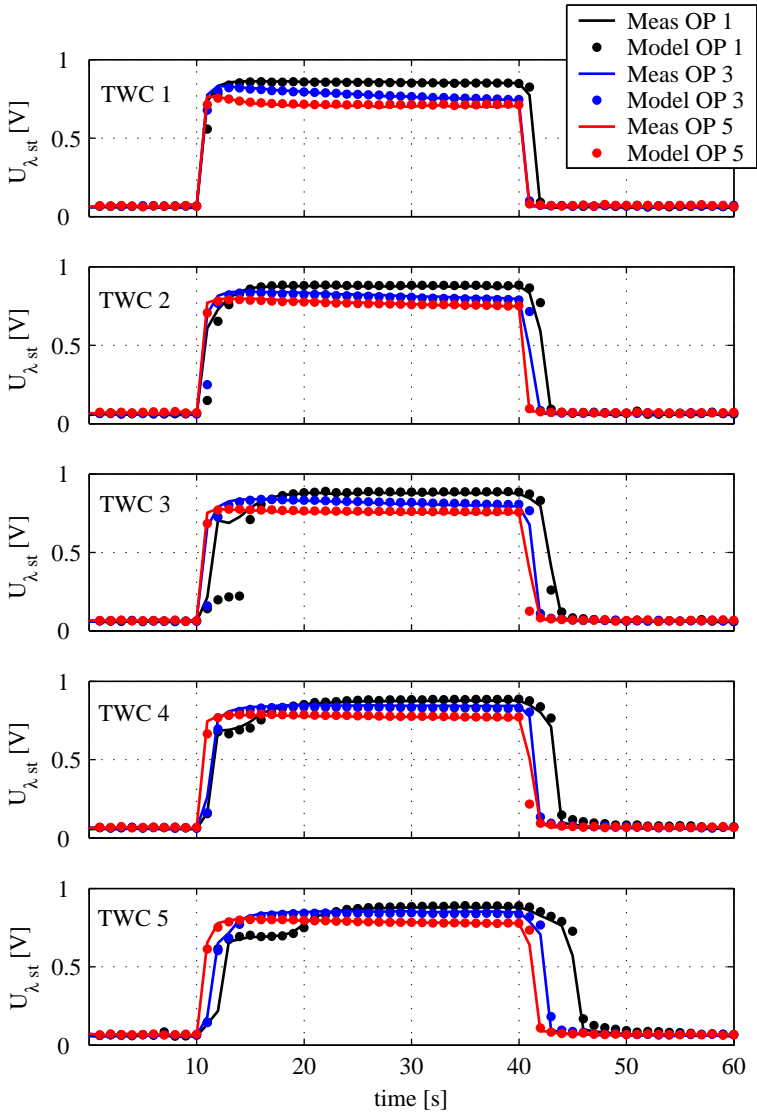


Figure 5.4: Calculated and measured switch-type  $\lambda$  sensor voltage output in transient conditions.  $\lambda$  of the raw exhaust is switched from 1.03 to 0.97 at 10 s and back to 1.03 at 40 s. TWC 1 refers to a considerably aged TWC, TWC 5 is fresh, see Section 2.5. The operating points are (speed/load/raw exhaust temperature) (1) 1250 rpm/25%/440 °C, (3) 1750 rpm/35%/570 °C, and (5) 2500 rpm/50%/680 °C.

sensor dynamics. In some points, the agreement is somewhat deteriorated during the  $\lambda$  steps, especially for the TWC 3. The reason for this is most likely an offset in the exhaust gas measurements, since this error only occurs here. Notice that already very small errors in the measured exhaust gas concentrations can lead to a delayed or accelerated switching behaviour, because the concentrations of all relevant species are very low during the transition phase from lean to rich or vice versa.

From the results, it can be concluded that the proposed switch-type  $\lambda$  sensor model is certainly suitable for the use in an observer. It is also clear that the concentrations of  $O_2$ , CO, and  $H_2$ , and additionally the gas temperature have to be provided by a preceding TWC model. This is the task of the next section.

### 5.2.3 Control-Oriented Model of a TWC

In Chapter 3, a process model has been derived, which is able to correctly reflect the behaviour of the TWC both in terms of the oxygen storage effects and the water-gas shift reaction with its deactivation by coking. Also, the changing behaviour over the TWC's lifetime was reproduced correctly. Therefore, a considerably simplified model of the TWC based on the process model shall be derived here, which accounts for the mentioned phenomena, but also is sufficiently simple to fit in a control system.

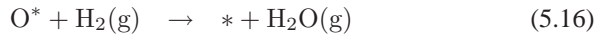
In the previous section, it has been shown that the  $O_2$ , CO, and  $H_2$  concentrations should be provided by the TWC model. Additionally, the outlet temperature  $T_{tp}$  should be calculated accurately. For control purposes, the model should provide an information about the oxygen storage level. Last but not least, one or two parameters should characterise the TWC's ageing level. From the process model it is clear that the storage capacity is a very suitable parameter for this task.

In order to keep the model transparent and easy to parameterise, the use of look-up tables or other heuristic elements is avoided, as far as possible. The ultimate goal is to find a model which can be parameterised automatically with few standardised measurements, which can be taken on a production type engine and/or car, i. e., without special exhaust gas measurement equipment. Therefore, the model will be kept to the  $\lambda$  sensor relevant components  $O_2$ , CO, and  $H_2$ . However, an extension to NO and HC is straightforward and relatively easy to implement because of the transparent structure of the model.

#### Kinetic and Thermodynamic Model

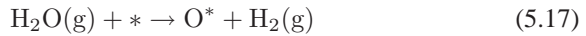
The control-oriented model has been derived from the process model. Starting point is therefore the set of chemical reactions, which are accounted for.

As has been discussed above, NO and HC are incorporated in the O<sub>2</sub> and CO concentrations. Therefore, all reactions, where these species are involved, are eliminated. Furthermore, only one storage capacity shall be assumed to be present, i. e., the noble metal and the ceria are “merged”. In a first step, oxygen adsorption and depletion by CO and H<sub>2</sub> are accounted for. However, it is assumed that only oxygen adsorbs. Its reduction by CO and H<sub>2</sub> is incorporated by means of Eley-Rideal mechanisms. This can be formulated with the following three chemical reactions:

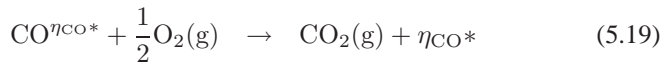
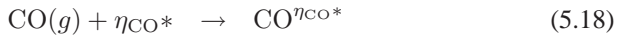


\* stands for a vacant site on the catalyst surface. O\* denotes adsorbed oxygen.

In the process model, water adsorption and dissociation was dependent on the availability of vacant surface sites both on the noble metal and on the ceria. Here, only one catalyst surface has been accounted for. Since only oxygen adsorption has been considered so far, the water dissociates directly into adsorbed oxygen and gaseous hydrogen:



Catalyst deactivation occurs from the adsorption of HC. Since these have been included in the CO concentration, CO adsorption is introduced. In the process model, only the deactivation of the noble metal surface had been considered. Here, only one type of surface is accounted for, which also contains the far greater ceria surface. Therefore, it is assumed that the adsorbed CO occupies a number of  $\eta_{\text{CO}}$  sites instead of only one. With  $\eta_{\text{CO}}$  being equal to 12, the best results were obtained. The adsorbed CO has to be oxidised under lean operation. This is again accounted for by means of an Eley-Rideal mechanism:



The calculation of the reaction rates is straightforward. All reaction rate constants are calculated using the Arrhenius-Ansatz. This is also the case for the

adsorption reactions. Hence,

$$\begin{aligned}
 r_{\text{O}_2}^{ads} &= k_1 c_{\text{O}_2}^{wc} \theta_V \\
 r_{\text{CO}}^{red} &= k_2 c_{\text{CO}}^{wc} \theta_{\text{O}} \\
 r_{\text{H}_2}^{red} &= k_3 c_{\text{H}_2}^{wc} \theta_{\text{O}} \\
 r_{\text{H}_2\text{O}}^{ads} &= k_4 \theta_V^2 \\
 r_{\text{CO}}^{ads} &= k_5 c_{\text{CO}}^{wc} \theta_V \\
 r_{\text{CO}}^{ox} &= k_6 c_{\text{O}_2}^{wc} \theta_{\text{CO}}
 \end{aligned}$$

$\theta_V$  denotes the fraction of vacant sites, i. e.,  $1 - \theta_{\text{O}} - \theta_{\text{CO}}$ .  $c_i^{wc}$  stands for the concentration of the species  $i$  in the washcoat.  $k_i$  denotes the reaction rate coefficient and is defined following the Arrhenius Ansatz:

$$k_i = A_i \exp\left(\frac{-E_i}{\Re T_s}\right), \quad i = 1 \dots 6 \tag{5.20}$$

Notice that the adsorption rate of  $\text{H}_2\text{O}$  is of second order in  $\theta_V$ . Additionally, it is independent of the water concentration, which is assumed to be constant and thus has been included in the pre-exponential factor  $A_4$ .

With these reaction rates, the balance equations for the occupancies of O and CO can be expressed as follows:

$$\frac{\partial \theta_{\text{O}}}{\partial t} = r_{\text{O}_2}^{ads} - r_{\text{CO}}^{red} - r_{\text{H}_2}^{red} + r_{\text{H}_2\text{O}}^{ads} \tag{5.21}$$

$$\frac{\partial \theta_{\text{CO}}}{\partial t} = \eta_{\text{CO}} (r_{\text{CO}}^{ads} - r_{\text{CO}}^{ox}) \tag{5.22}$$

The thermodynamic model has been derived from the process model. Starting point is the set of mass balance equations for the species in the channel and in the washcoat and of the energy equations for the solid and the gas phases, see Section 3.3.1. For convenience, the equations are repeated here. The mass balance for the gas channel reads

$$\begin{aligned}
 \varrho_g \varepsilon \frac{\partial w_i}{\partial t} &= \varepsilon D_{eff} \frac{\partial^2 w_i}{\partial z^2} - \frac{\dot{m}_{exh}}{A_{cs}} \frac{\partial w_i}{\partial z} - D_i A_{geo} (\varrho_g w_i - \varrho_{wc} v_i) \\
 &+ w_i \sum_j D_j A_{geo} (\varrho_g w_j - \varrho_{wc} v_j)
 \end{aligned}$$



For the washcoat, the mass balance is

$$\begin{aligned} \varrho_{wc} \varepsilon \varepsilon_{wc} \frac{4\sqrt{3}D_{wc}}{D_{chan}} \frac{\partial v_i}{\partial t} = & D_i A_{geo} (\varrho_g w_i - \varrho_{wc} v_i) \\ & - v_i \sum_j D_j A_{geo} (\varrho_g w_j - \varrho_{wc} v_j) \\ & + \Delta r_i - v_i \sum_j \Delta r_j \end{aligned}$$

In a first step, the mass balance for the species in the channel is simplified as follows: Since only three components are accounted for, the last term, which accounts for errors in the total mass balance due to inconsistent radial diffusion, is neglected. Additionally, axial diffusion is neglected, as well. The model is discretised along the flow axis into a small number  $n_c$  of cells. This number remains to be determined. If the mole concentrations  $c_i^{ch}$  and  $c_i^{wc}$  are used instead of the mass fractions  $w_i$  and  $v_i$  (by dividing the equation with the molar mass  $M_i$ ), the balance equation for cell  $j$  becomes

$$\varepsilon \frac{V_{TWC}}{n_c} \frac{\partial c_{i,j}^{ch}}{\partial t} = -\dot{V} (c_{i,j}^{ch} - c_{i,j-1}^{ch}) - \frac{V_{TWC}}{n_c} D_i A_{geo} (c_{i,j}^{ch} - c_{i,j}^{wc}) \quad (5.23)$$

$V_{TWC}$  denotes the total volume of the TWC,  $\dot{V}$  is the volumetric flow of the exhaust gas.  $c_i^{ch,j-1}$  stands for the concentration of species  $i$  in the preceding cell or at the TWC inlet, if  $j = 1$ . The other quantities are identical with the ones in the process model.

The mass balance for the species in the washcoat is simplified in a similar manner. Again, the correction terms for the radial transport phenomena are neglected, and instead of mass fractions, mole concentrations are used. This leads to the following expression for the mass balance for species  $i$  in the washcoat:

$$\varepsilon \varepsilon_{wc} \frac{4\sqrt{3}D_{wc}}{D_{chan}} \frac{\partial c_{i,j}^{wc}}{\partial t} = D_i A_{geo} (c_{i,j}^{ch} - c_{i,j}^{wc}) - r_{sorption,i,j} \cdot SC \quad (5.24)$$

$SC$  is the storage capacity of the TWC in mol/m<sup>3</sup>.

Of course, the explicit application of these balance equations would lead to a considerable consumption of CPU power, both because of the high number of state equations and because a very stiff system would be obtained. Generally, it has been found that the dynamics of the gas species are much faster than the ones of the oxygen storage and the deactivation. Therefore, the mass balance equations (5.23) and (5.24) can be applied as static equations. This is done by setting the left-hand side of the two equations to zero, isolating the washcoat

concentrations  $c_{i,j}^{wc}$  in (5.24), and inserting in (5.23). After some algebra the following terms are obtained for both the channel and the washcoat concentrations of  $O_2$ , CO, and  $H_2$ :

$$\begin{aligned}
 c_{O_2,j}^{ch} &= \frac{\dot{V}_{rel} c_{O_2,j-1}^{ch}}{\dot{V}_{rel} + \mathcal{D}_{O_2} \left( 1 - \frac{\mathcal{D}_{O_2}}{\mathcal{D}_{O_2} + 0.5(k_1\theta_{V,j} + k_6\theta_{CO,j})SC} \right)} \\
 c_{CO,j}^{ch} &= \frac{\dot{V}_{rel} c_{CO,j-1}^{ch}}{\dot{V}_{rel} + \mathcal{D}_{CO} \left( 1 - \frac{\mathcal{D}_{CO}}{\mathcal{D}_{CO} + (k_2\theta_{O,j} + k_5\theta_{V,j})SC} \right)} \\
 c_{H_2,j}^{ch} &= \frac{\dot{V}_{rel} c_{H_2,j-1}^{ch} + \frac{\mathcal{D}_{H_2} k_4 \theta_{V,j}^2 SC}{\mathcal{D}_{H_2} + k_3\theta_{O,j}SC}}{\dot{V}_{rel} + \mathcal{D}_{H_2} \left( 1 - \frac{\mathcal{D}_{H_2}}{\mathcal{D}_{H_2} + k_3\theta_{O,j}SC} \right)} \\
 c_{O_2,j}^{wc} &= \frac{\mathcal{D}_{O_2} c_{O_2,j}^{ch}}{\mathcal{D}_{O_2} + 0.5(k_1\theta_{V,j} + k_6\theta_{CO,j})SC} \\
 c_{CO,j}^{wc} &= \frac{\mathcal{D}_{CO} c_{CO,j}^{ch}}{\mathcal{D}_{CO} + (k_2\theta_{O,j} + k_5\theta_{V,j})SC} \\
 c_{H_2,j}^{wc} &= \frac{\mathcal{D}_{H_2} c_{H_2,j}^{ch} + k_4 \theta_{V,j}^2 SC}{\mathcal{D}_{H_2} + k_3\theta_{O,j}SC} \tag{5.25}
 \end{aligned}$$

where

$$\begin{aligned}
 \mathcal{D}_i &= D_i A_{geo} \\
 \dot{V}_{rel} &= \frac{\dot{V}}{V_{TWC}/n_c}
 \end{aligned}$$

With these equations, both the washcoat and the channel concentrations can be calculated from the occupancies and the temperatures. The channel concentrations of the last cell are the actual output variables which are fed into the switch-type  $\lambda$  sensor model. The washcoat concentrations in turn are used for the calculation of the reaction rates.

The temperatures are calculated from the energy balance equations for the gas phase and for the solid phase. Again, the starting point is the TWC process model. The two balance equations are repeated here for convenience. The

equation for the solid phase reads

$$\varrho_s (1 - \varepsilon) c_s \frac{\partial T_s}{\partial t} = (1 - \varepsilon) \lambda_s \frac{\partial^2 T_s}{\partial z^2} - \alpha A_{geo} (T_s - T_g) + A_{cat} \sum_k -\Delta H_k \cdot R_k$$

The corresponding equation for the gas phase is

$$\varrho_g \varepsilon c_{p,g} \frac{\partial T_g}{\partial t} = \varepsilon \lambda_g \frac{\partial^2 T_g}{\partial z^2} - \frac{\dot{m}_{exh}}{A_{cs}} c_{p,g} \frac{\partial T_g}{\partial z} + \alpha A_{geo} (T_s - T_g)$$

The dynamics of the exhaust gas temperature  $T_g$  are expected to be much faster than the one of the solid temperature  $T_s$ . The reason for this is the convection, which accounts for an efficient distribution of the heat in the axial direction. In the solid phase, however, only heat conduction is present, which is much less effective. Hence, the dynamics of the exhaust gas temperature are neglected. Additionally, heat conduction in the gas phase is also assumed to be of minor importance and therefore left out. Introducing the volume of one cell,  $V_{TWC}/n_c$ , the remaining energy balance of the gas phase can be used to obtain the exhaust gas temperature  $T_{g,j}$  of the cell  $j$  by means of an algebraic equation:

$$T_{g,j} = \frac{\frac{\dot{m}_{exh}}{V_{TWC}/n_c} c_{p,g} T_{g,j-1} + \alpha A_{geo} T_{s,j}}{\frac{\dot{m}_{exh}}{V_{TWC}/n_c} c_{p,g} + \alpha A_{geo}} \quad (5.26)$$

$T_{g,j-1}$  denotes the gas temperature of the preceding cell. In the first cell,  $T_{g,j-1}$  stands for the inlet gas temperature.

The dynamics of the solid temperature  $T_s$  are accounted for in the model. The solid energy balance equation of the process model is not simplified, since all terms are considered. However, the second derivative of the temperature has to be discretised, which is done with a backward difference scheme. When all cells have the same length  $dz$ , the term can be expressed for the cell  $j$  as follows:

$$\frac{\partial^2 T_{s,j}}{\partial z^2} \approx \frac{T_{s,j-1} - 2T_{s,j} + T_{s,j+1}}{dz^2} \quad (5.27)$$

As for the boundary conditions, the gradient of the solid temperature is assumed to vanish. Hence,

$$\begin{aligned} \frac{\partial^2 T_{s,j}}{\partial z^2} &\approx \frac{-T_{s,j} + T_{s,j+1}}{dz^2}, & \text{if } j = 1 \\ \frac{\partial^2 T_{s,j}}{\partial z^2} &\approx \frac{-T_{s,j} + T_{s,j-1}}{dz^2}, & \text{if } j = n_c \end{aligned}$$

Since only two global oxidation reactions occur, only the reaction enthalpies for the CO oxidation,  $\Delta H_{CO_2}$  and the H<sub>2</sub> oxidation,  $\Delta H_{H_2O}$  are needed. The fact that NO and HC are included in the O<sub>2</sub> and CO concentrations has been neglected. Notice that  $\Delta H_{CO_2}$  here denotes the reaction enthalpy, i. e., the difference of the enthalpies of CO<sub>2</sub> and CO (the one of O<sub>2</sub> is zero). The reaction enthalpy of the oxygen storage in the ceria has been neglected.

Since a considerable amount of heat is lost by convection and radiation, a heat convection term must be included as follows:

$$\Delta \dot{E}_{loss} = \alpha_{TWC}(T_s - T_{amb}) \frac{A_{TWC}}{V_{TWC}} = \alpha_{TWC}(T_s - T_{amb}) \frac{4}{D_{TWC}} \quad (5.28)$$

$\alpha_{TWC}$  denotes the heat transfer coefficient from the TWC to the ambient air.  $A_{TWC}$  is the outer TWC surface,  $D_{TWC}$  stands for the diameter of the TWC. Notice that the heat loss term  $\Delta \dot{E}_{loss}$  is expressed in specific form, i. e., with the unit W/(Km<sup>3</sup>).

In this investigation, all experiments have been conducted on an engine test bench without an external airstream. Therefore, only the temperature difference between the solid phase and the ambient has been accounted for. In a vehicle, the air flow around the TWC, which is dependent on the vehicle speed, should be considered, because it enhances the heat loss.

With all these assumptions, the energy balance of the solid phase for the cell  $j$  can be expressed as follows:

$$\begin{aligned} \frac{\partial T_{s,j}}{\partial t} = & \frac{(1 - \varepsilon)\lambda_s \frac{T_{s,j-1} - 2T_{s,j} + T_{s,j+1}}{dz^2} - \alpha A_{geo}(T_{s,j} - T_{g,j})}{\rho_s c_s (1 - \varepsilon)} \\ & + \frac{SC((-r_2 - r_6)\Delta H_{CO_2} + (-r_3 + r_4)\Delta H_{H_2O})}{\rho_s c_s (1 - \varepsilon)} \\ & - \frac{\alpha_{cat}(T_{s,j} - T_{amb}) \frac{4}{D_{TWC}}}{\rho_s c_s (1 - \varepsilon)} \end{aligned} \quad (5.29)$$

The complete TWC model is described with equations (5.21), (5.22), (5.25), (5.26), and (5.29). With the TWC discretised into  $n_c$  cells, a number of  $3n_c$  state variables results. The model geometry parameters are the same as in the process model. For the kinetic parameters and the storage capacities, a tuning procedure has been developed which will be described in detail in Section 5.3. There, also the number of cells will be discussed.

A fundamental difference to many models presented in the literature is the introduction of a state variable which accounts for the TWC deactivation. This is necessary for two reasons. Firstly, the estimation of the oxygen storage capacity is more accurate, since also the storage of reducing species and the water-gas

shift reaction are accounted for. Especially the latter can significantly distort an estimation of the oxygen storage capacity, which is based on the signals of upstream and downstream  $\lambda$  sensors, see [3]. Secondly, the TWC deactivation influences the ratio between  $H_2$  and CO, and additionally changes over the TWC's lifetime due to the changing TWC storage capacity. This ratio distorts the  $\lambda$  sensor signal, as has been shown in the previous section.

At first sight, the model appears to be somewhat complicated as compared to other models presented in the literature. However, additional phenomena are covered and so far no heuristic nonlinear function such as a lookup table has been introduced. In fact, it will be shown that the tuning of the parameters is very simple and can be performed on a standard production-type engine. The very transparent structure of the model makes extensions or simplifications easy to implement.

## 5.3 Model Calibration

The parameter set of the model can only partly be obtained from geometrical and thermodynamical considerations. For an accurate set of the kinetic parameters, the storage capacities, and some thermodynamical parameters, a calibration procedure has been developed. A relatively small set of standardised measurements is necessary, from which all parameters can be obtained by means of minimising the error between the measured and the simulated switch-type  $\lambda$  sensor and/or the measured exhaust gas components, if available. The goal of the procedure is to keep the necessary interaction with the application engineer as low as possible, i. e., to provide a fully standardised and automated method for the calibration of the model.

The method proposed in the following is only one possibility of how to fulfill the task. Depending on the needs, the procedure can of course deliberately be modified. The important point is the methodology and flexibility, which allows an easy and quick adaptation of the model to different systems, purposes, or a modified set of parameters.

The following set of parameters have to be obtained by calibration:

- Kinetic parameters: This includes the six pre-exponential factors  $A_i$  and activation energies  $E_i$ . Additionally, the number of occupied sites by CO ( $\eta_{CO}$ ) has to be obtained. However, it is expected that this parameter does not change and has therefore not been included in the procedure.
- Storage capacities: The storage capacities  $SC$  for different ageing levels have to be obtained simultaneously with the kinetic parameters for con-

sistency reasons. Later, a method will be presented, how these can be obtained online by means of an extended Kalman filter.

- Heat transfer coefficient between the TWC and the ambient air,  $\alpha_{cat}$ : This is one of the typical “additional” parameters, which have been included here, because its physical reasonable value is somewhat difficult to estimate due to the heterogenous structure of the TWC, the insulation material, and the steel canning. This demonstrates, how the method can be deliberately extended to almost any parameter.

A possible approach could be to use an existing driving cycle, which covers a large area of operating points, and then fit the parameters such that the relevant signals such as  $\lambda$  sensor outputs, temperatures, and concentrations are matched. Thereby, at least two major problems arise. Firstly, it is very difficult to reliably estimate a large set of parameters (here: 13 plus the storage capacity) simultaneously. Secondly, the sensitivities to the different parameters have to be accounted for. The model is extremely sensitive to the activation energies as compared to the pre-exponential factors.

To avoid these problems, a different approach was chosen. Thereby, data sets are used, where only the air-to-fuel ratio  $\lambda$  is excited, whereas the engine speed, the load conditions, and the temperatures remain roughly constant in one set. Instead of  $A_i$  and  $E_i$ , the reaction constants  $k_i$ , see (5.20), are obtained. In a second step, the required parameters  $A_i$  and  $E_i$  are calculated from the temperatures using a curve fit algorithm. This allows additionally to check, whether the Arrhenius-Ansatz is suitable, and if the reaction scheme really covers the most important phenomena.

The data sets consist of two parts per operating point.  $\lambda$  is excited with switches between rich and lean starting with long periods (30 s). The periods are then shortened in steps down to 1 s. Each of the two parts uses the same periods, but  $\lambda$  amplitudes of  $\pm 1\%$  and  $3\%$ . Figure 5.5 shows an example of one data set with the signals of the wide-range  $\lambda$  sensor at the inlet of the TWC and of the switch-type  $\lambda$  sensor at the outlet. The measurements have been taken at five engine operating points which are depicted in Table 5.1. Thereby, the following signals are recorded:

1.  $\lambda$  at the TWC inlet and outlet (switch-type  $\lambda$  sensor).
2. Temperatures at the TWC inlet and outlet.
3. Engine speed and air mass flow.
4. Concentrations of NO, HC, H<sub>2</sub>, CO, and O<sub>2</sub>

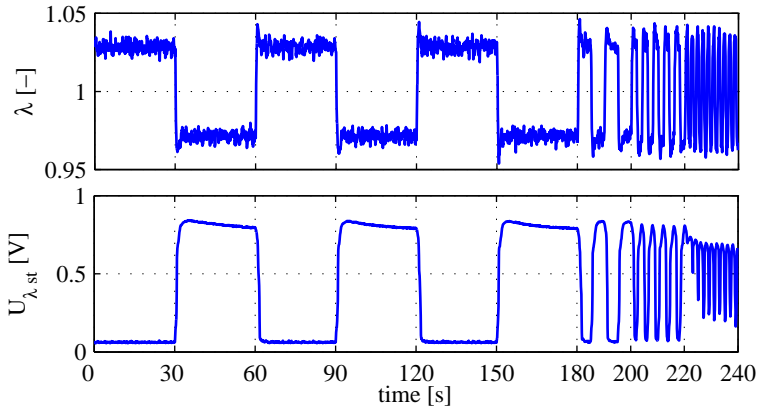


Figure 5.5: Example of a  $\lambda$  and switch-type  $\lambda$  sensor measurement for the model calibration.  $\lambda$  is switched between 3% rich and 3% lean, in the first part every 30 s, then every 5 s, followed by 2 s and 1 s. The measurement has been taken at operating point 3 with the moderately aged (at 900 °C) TWC .

Table 5.1: Operating points, where the model calibration measurements were taken.

Nr.	Engine speed [rpm]	Engine load [%]	Exhaust gas temperature [K]
1	1250	25	715
2	1500	30	780
3	1750	35	835
4	2000	40	880
5	2500	50	950

All values are approximate mean values over the whole measurement.

The concentration measurements are not necessary. However, they have been taken here in order to evaluate the performance of the model and the calibration procedure.

At each engine operating point, the parameters can now be obtained by minimising the sum of squares of the sampled error between measured and simulated switch-type  $\lambda$  sensor voltages, temperatures, or concentrations. For the minimisation, for example the nonlinear leastsquares algorithm “lsqnonlin” of the Matlab<sup>TM</sup> Optimization Toolbox [64] can be used.

The kinetic parameters and storage capacities can be obtained by minimising the errors of the switch-type  $\lambda$  sensor signal or the concentrations of  $O_2$  (including NO), CO (including HC), and  $H_2$ . The advantage of the concentration measurements is the linearity of the error at any concentration level. However, especially for small concentrations, the relative accuracy of the measurements is decreasing. Unfortunately, small concentrations occur during the transition between rich and lean mixtures. This transition however, is very important for the estimation of the storage capacity. This problem can be overcome with the switch-type  $\lambda$  sensor, which provides a very accurate information about the transition, i. e., the moment, when the exhaust gas at the TWC outlet turns rich or lean. The major disadvantage of the sensor, however, is the nonlinearity of its signal. The errors occurring from bad transition timing are much outweighed as compared to the errors during a rich or lean phase.

A practical solution is to use either a combination of the switch-type  $\lambda$  sensor and the concentration measurements or a combination of the sensor signal in the direct form and in a linearised form. This can be obtained by inverting the control-oriented model (5.10), which has been presented in Section 5.2.2. Thereby, the “equilibrium” concentration of  $O_2$  can be calculated, if the sensor voltage is below the inert value  $A$ , or a weighted sum of the  $H_2$  and CO concentrations is obtained, if the voltage is greater than  $A$ . Mathematically, this can be expressed as follows:

$$\begin{aligned}
 U_{\lambda st, lin} &= y_{H_2} + \frac{B}{C} y_{CO} - y_{O_2} \\
 &= \frac{1}{C} \left[ 10^{\left( \frac{\max(U_{\lambda st} - A, 0)}{E_A \exp\left(\frac{-E_E}{\Re T_{tp}}\right)}\right) - 1} \right] \\
 &\quad - \frac{1}{D} \left[ 10^{\left( \frac{\max(A - U_{\lambda st}, 0)}{F}\right) - 1} \right] \quad (5.30)
 \end{aligned}$$

With the combination of the linearised and the measured switch-type  $\lambda$  sensor signals, the use of concentration measurements is not necessary anymore. This



simplifies the calibration of the model substantially. Of course, this method relies on the accuracy of the sensor model. Therefore, it is always advantageous if concentration measurements are available for monitoring purposes.

As has been mentioned already, it is impractical to obtain all parameters simultaneously. The problem is that the influence of the parameters is not entirely orthogonal, i. e., some parameters may exhibit slight dependencies. For example, the storage capacities and the adsorption parameters are not entirely independent. The adsorption or storage rate might be influenced by both parameters. It is thus very important that the set of measurements for the calibration provides sufficient excitation in order to separate the influences of closely related parameters. This can be obtained by providing measurements covering a wide range of engine operating points with TWCs at different ageing levels. With the latter, the influence of the storage capacity can be separated from the storage rates.

The calibration of the model has been performed with TWCs at five different ageing levels (see Chapter 2) and with a set of five different operating points as depicted in Table 5.1. Thereby, the parameters were calibrated iteratively in the following order:

1. Kinetic parameters  $A_i/E_i$  and storage capacities  $SC$  (minimising switch-type  $\lambda$  sensor error)
2. Storage capacities  $SC$  only (minimising switch-type  $\lambda$  sensor error)
3. Heat transfer coefficient between the TWC and the ambient air,  $\alpha_{cat}$  (minimising temperature error)
4. Kinetic parameters  $A_i/E_i$  only (minimising switch-type  $\lambda$  sensor error)
5. Storage capacities  $SC$  only (minimising switch-type  $\lambda$  sensor error)
6. Kinetic parameters  $A_i/E_i$  only (minimising switch-type  $\lambda$  sensor error)
7. Storage capacities  $SC$  only (minimising switch-type  $\lambda$  sensor error)

For all parameters, good initial guesses were available. If only poor values are available, more iterations should be included.

### Validity of the Model over TWC Ageing

It has been assumed that the storage capacity is constant for all operating points. Additionally, it is the only parameter which is assumed to change with the ageing of the TWC. In the following, these two assumptions will be assessed.

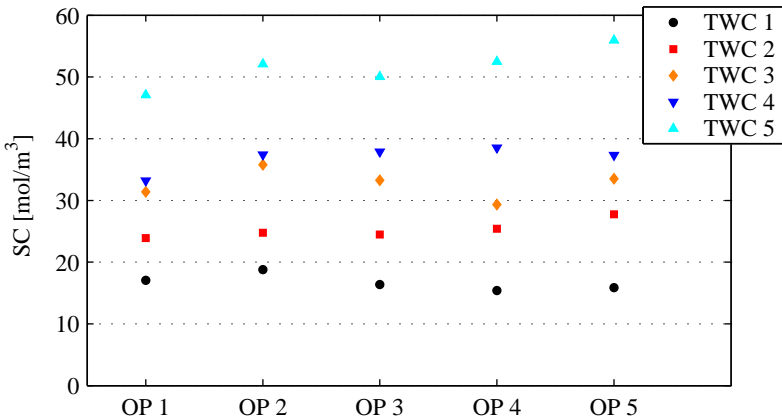


Figure 5.6: Estimated storage capacities of differently aged TWC at the five engine operating points. TWC 1 refers to the most aged, TWC 5 to the fresh TWC.

In the literature, it has been reported that the oxygen storage capacity is dependent on the temperature [51]. However, usually the “phenomenological” oxygen storage capacity is addressed. This means that the storage capacity is estimated upon comparison of the input and the output measurements of oxygen or  $\lambda$  during  $\lambda$  transients. This storage capacity is not identical with the one used here, i. e.,  $SC$ . The point is that the here used “physical” storage capacity is not necessarily fully exploited. In other words, it is possible that the catalytically active surface is not fully covered with oxygen during a lean phase or not completely empty during a rich phase. Additionally, storage of reducing species is accounted for here. Both phenomena are dependent on the temperature, which leads to a different oxygen input/output behaviour. Hence, the statement that  $SC$  is independent of the temperature does not a priori contradict the results presented in the literature.

Figure 5.6 shows the storage capacity of the five different TWC which has been estimated with the method described in the previous section at various engine operating points. At each point, the storage capacity has been obtained independently. Although slight variations are apparent, no trend indicating a temperature dependence is visible. The variations are more significant with a larger  $SC$ . From the diagnosis point of view this is of minor importance, since only close to the point, where the conversion rates of the TWC and the storage capacity are small, an accurate estimate is required. It has been concluded that the parameter  $SC$  is indeed independent of the engine operating point.

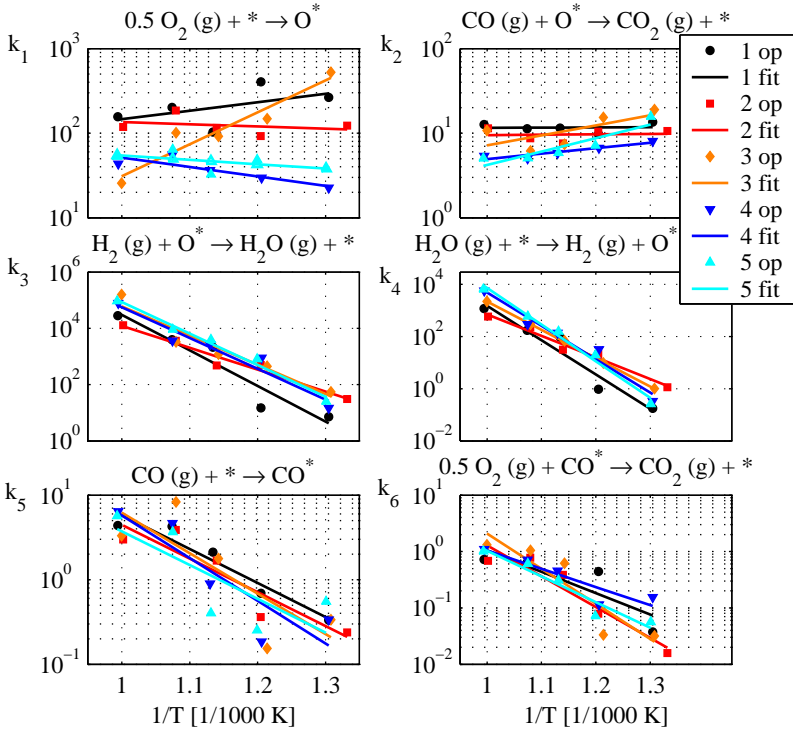


Figure 5.7: Kinetic parameters independently obtained for the five different TWCs. “op” refers to the parameter which was obtained independently at each operating point. “fit” is the corresponding curve fit following the Arrhenius Ansatz. TWC 1 is most aged, TWC 5 is fresh.

In order to demonstrate the general validity of the TWC model over the TWCs lifetime, the kinetic parameters have been estimated independently for all five differently aged TWCs. The result is presented in Figure 5.7. Thereby, the storage capacities  $SC$  have been used, which have been obtained from the overall calibration procedure including all TWCs simultaneously. The obtained parameters exhibit astonishingly little variation. Only the adsorption of oxygen (reaction 1) appears somewhat scattered as compared to the other parameters. The reason for this is assumed to be the strong connection of the oxygen storage capacity with this parameter. Already small offsets of  $SC$  may lead to significant variations of this parameter. Under this premise, the variation of the

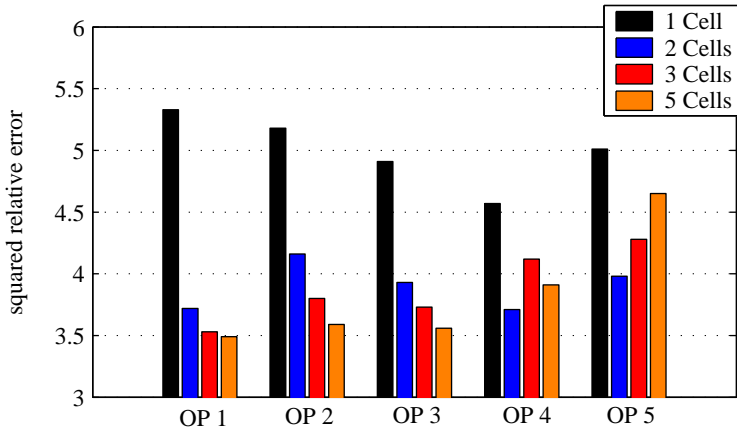


Figure 5.8: Residuals at Operating points (OP) 1-5 with 1, 2, 3, and 5 cells. All TWC ageing levels have been considered in the accumulated residuals.

parameter is acceptable.

These two tests have shown that the kinetic parameters are roughly valid throughout the TWCs lifetime and that the storage capacity is independent of the temperature. This is an important prerequisite for the online estimation of the storage capacity, which will be presented in Section 5.4.

### Number of Discrete Cells

The TWC model has been derived from one-dimensional partial differential equations. To transpose this distributed model to a lumped parameter model, it has been discretised along the flow axis into finite elements. Since every element or cell is described with three state variables, their number should be kept as low as possible. The model has been tested with different numbers of cells on all TWCs in order to determine a configuration, which provides sufficiently accurate results without a too high grade of complexity. Thereby, the accumulated residuals between measured and simulated transients of the switch-type  $\lambda$  sensor have been calculated. Both the linearised and the actual sensor signals have been accounted for. Notice that already relatively small disturbances of the measurements can influence the residuals considerably. Therefore, only significant variations of the residuals are actually meaningful. The accumulated residuals are shown in Figure 5.8. It can be clearly seen that the model with one cell exhibits a significantly increased residual as compared to the other con-

figurations. For operating points 1-3 the residuals decrease with an increasing number of cells, as expected. This is not the case for the two other operating points. The reason is that the transitions between the rich and the lean phases are very fast and thus, their influence on the residual decreases. Hence, operating points 1-3 should be focused on for the test. It can be seen that more than three cells do not significantly improve the result anymore. Therefore, three cells have been assumed to be a reasonable choice for the model.

### 5.3.1 Simulation Results vs Measurements

Figures 5.9–5.11 show measured and simulated switch-type  $\lambda$  sensor signals during  $\lambda$  excitations of 3% around stoichiometry at the five different engine operating points according to Table 5.1. Generally, the agreement is very good. Both the dependencies on the engine operating point and on the storage capacity, which considerably influences the high frequency behaviour, are reflected well by the model. Notice that only the storage capacity  $SC$  has been varied to obtain the simulation results for the three differently aged TWCs.

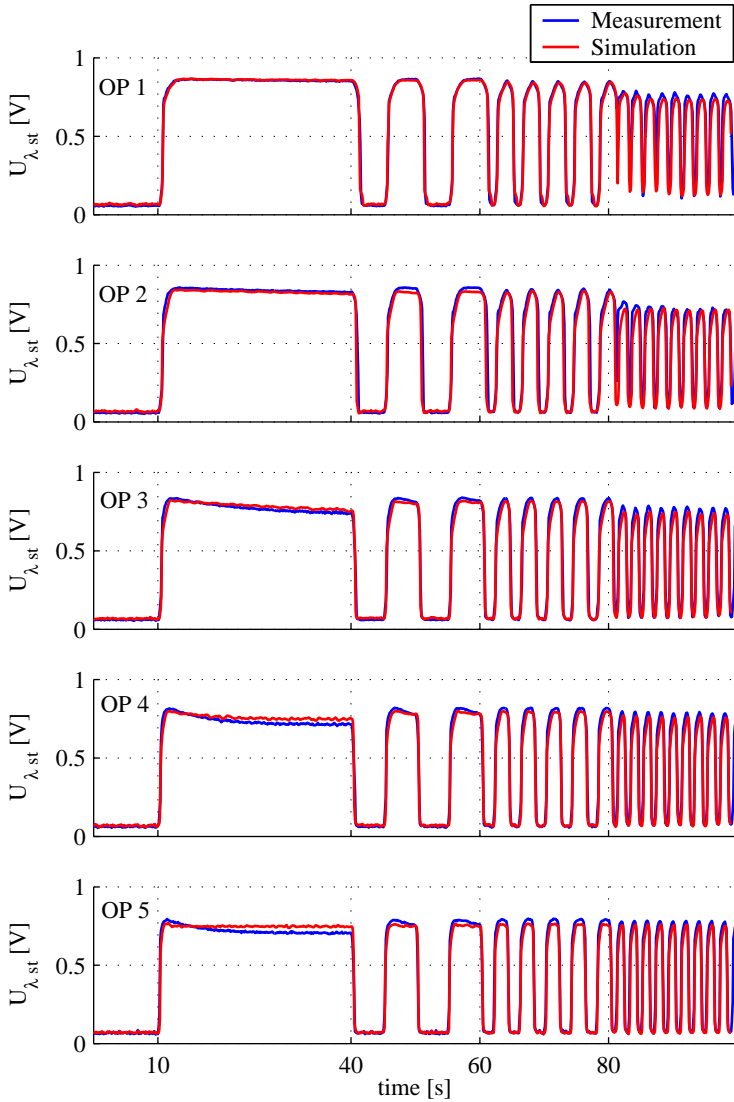


Figure 5.9: Comparison of the measured and the simulated switch-type  $\lambda$  sensor signal downstream of the considerably aged (at 1100 °C, see Section 2.5) TWC at all engine operating points (OP).

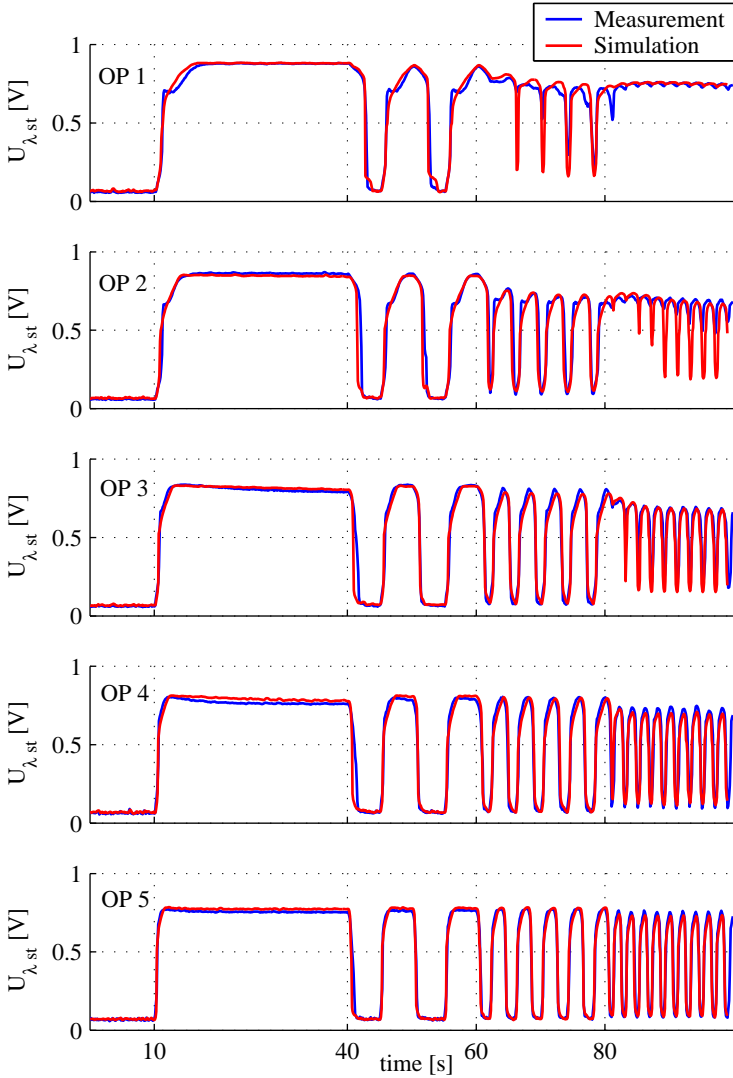


Figure 5.10: Comparison of the measured and the simulated switch-type  $\lambda$  sensor signal downstream of the moderately aged (at 900 °C, see Section 2.5) TWC at all engine operating points (OP).

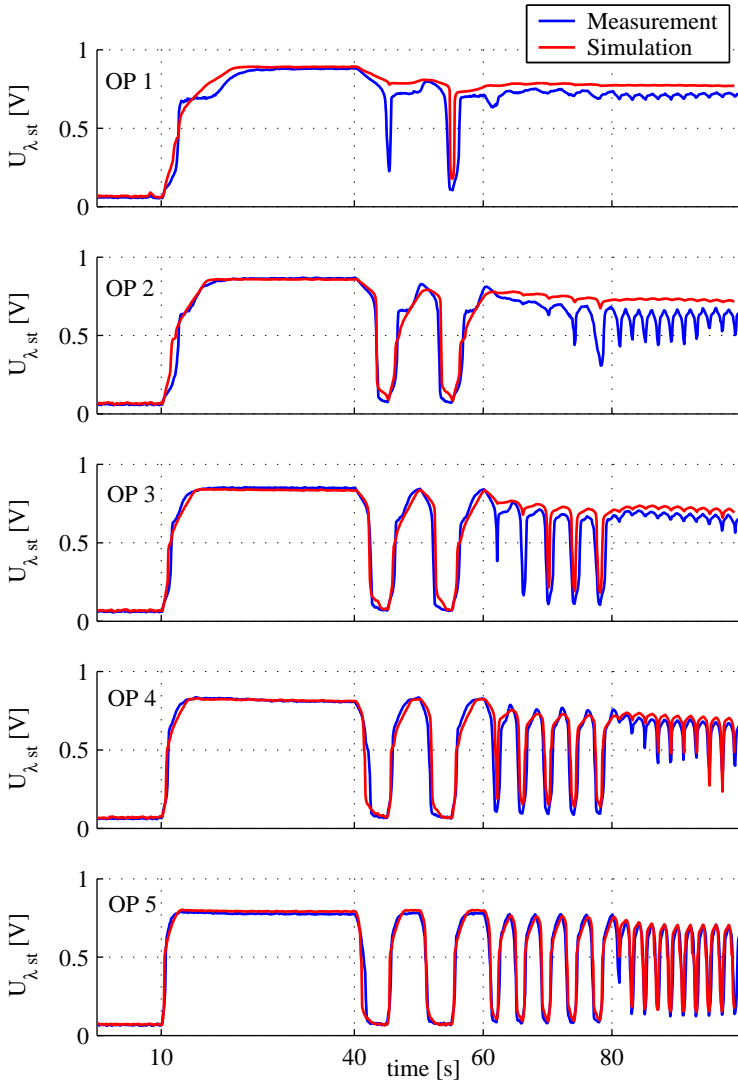


Figure 5.11: Comparison of the measured and the simulated switch-type  $\lambda$  sensor signal downstream of the fresh TWC at all engine operating points (OP).



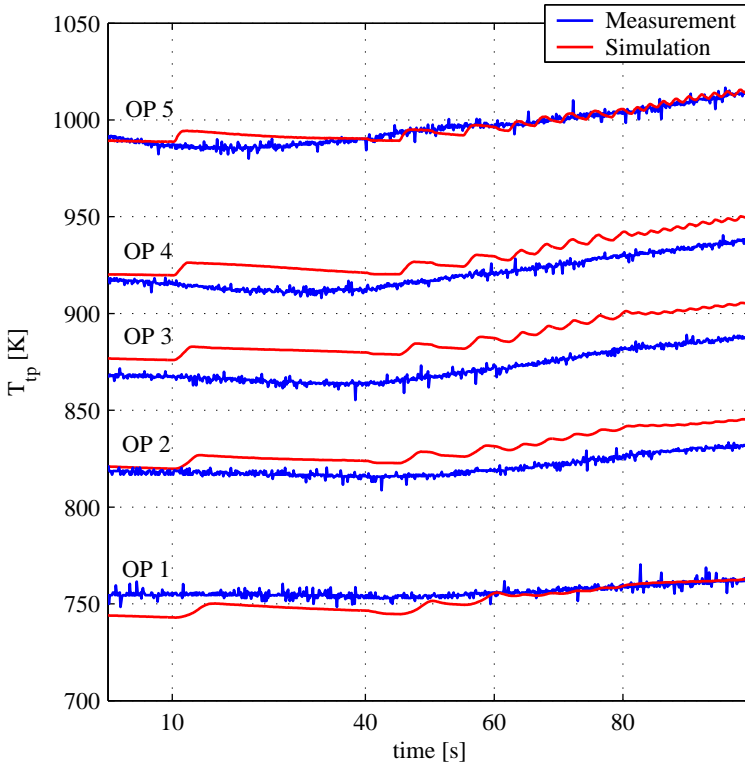


Figure 5.12: Comparison of the measured and the simulated tailpipe temperature  $T_{tp}$  downstream of the moderately aged (at 900 °C, see Section 2.5) TWC at all engine operating points (OP).

Figure 5.12 shows the measured and simulated tailpipe temperatures  $T_{tp}$  at the five different engine operating points in comparison. The agreement is generally good. However, since the engine operating point remains constant during the measurements, this test is not very meaningful. Therefore, an example of an FTP cycle measurement is depicted in Figure 5.13. Both the measured and simulated tailpipe temperatures and switch-type  $\lambda$  sensor voltages are shown. For reference, the engine speed and the measured TWC inlet  $\lambda$  are also displayed.

The agreement of the temperatures is good, except, where fuel cut-offs occur with an adjacent engine idle phase (e. g. between 130 s and 170 s). Here, the thermal inertia of the TWC and the canning is obviously not reflected very well in the model. However, the error remains within a limited band. Hence, the

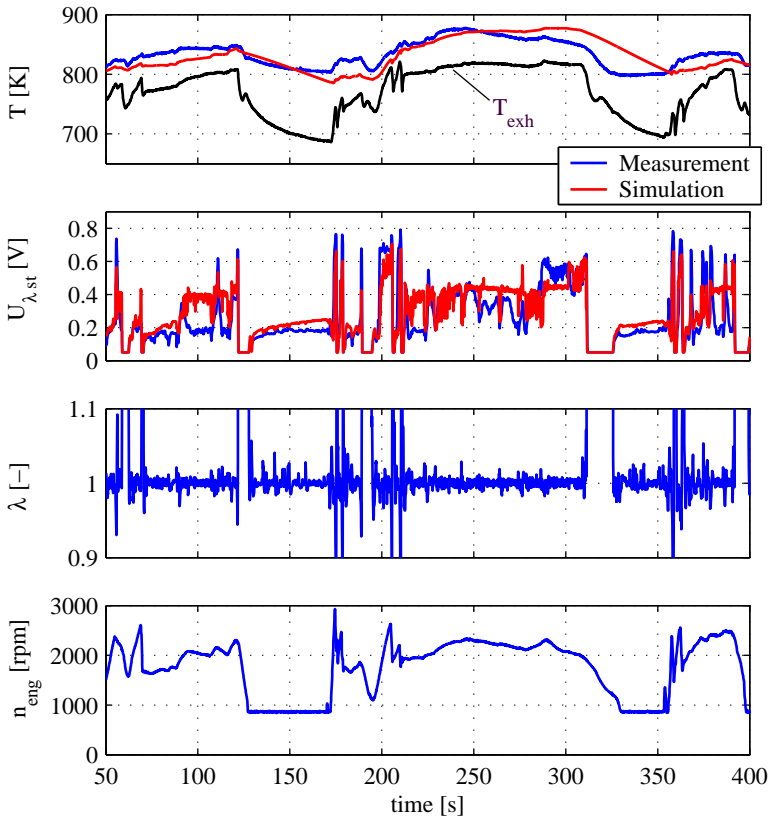


Figure 5.13: Comparison of the measured and the simulated switch-type  $\lambda$  sensor signal and the temperature downstream of the fresh TWC during a part of an FTP cycle.

accuracy of the temperature model is sufficient for the control-oriented model. If, however, some improvements are necessary, they have to consider the specific setup of the exhaust gas aftertreatment system. In that case, the convection around the TWC canning and the heat transfer through the insulation should be accounted for.

The agreement of the switch-type  $\lambda$  sensor signals is satisfactory. When evaluating the performance of the model just from the visual impression, it should be considered that close to stoichiometry, already very small disturbances in the inlet  $\lambda$  lead to a significant offset of the switch-type  $\lambda$  sensor voltage out-

put because of the nonlinear characteristic. With this challenge and the partly significant simplifications in the model in mind, the agreement of the measured and the simulated sensor signals can be considered good. For the purpose of diagnosis and control, the model can therefore be expected to be sufficiently accurate.

## 5.4 Online Adaptation Strategy

The ageing of the TWC is reflected in the model with the storage capacity  $SC$  which decreases over the TWC's lifetime. All other parameters are assumed to remain constant. It is intuitively clear that the storage capacity is strongly connected to the TWC's dynamics. Hence, the determination of  $SC$  is important from the point of views of both diagnostics and control. As for the former, the ageing level of the TWC can be determined or better, the knowledge of  $SC$  can be used to evaluate the TWC's performance. As for the latter, the controller can be adjusted to the changing dynamics of the TWC.

Of course, the estimation of  $SC$  should be performed autonomously by the control unit during operation, i. e., an online adaptation algorithm is required. The adaptation should be sufficiently fast, since a "bad" TWC should be detected within one driving cycle, such as FTP. This has to be done from an arbitrary initial value of  $SC$ , since the TWC might be exchanged or damaged between two engine starts. The same is true from the point of view of the controller. A fast and accurate adaptation to the "true"  $SC$  is essential for the correct estimation of the controlled internal state variables such as the oxygen storage level.

A concept which estimates both the internal state variables by means of an observer and additionally provides the online identification of certain parameters is the extended Kalman filter (EKF). Since this filter handles nonlinear models, it is a suitable choice for the described tasks. In the following, an EKF will be derived, which makes use of the control-oriented model presented above. Aspects such as numerical issues and excitation will be addressed, as well as possibilities for the extension to other parameters, such as sensor offsets. Finally, some results of the application in an FTP cycle will be presented.

### 5.4.1 Extended Kalman Filter for the TWC

A large number of very instructive and detailed books and papers on extended Kalman filters exist in the literature, see [102], [56], or [99]. Therefore, only a short summary of the algorithm shall be given here.

Consider a process described by the nonlinear state-space equations

$$\begin{aligned}\dot{\mathbf{x}} &= \mathbf{f}(\mathbf{x}, \mathbf{u}) + \mathbf{w} \\ \mathbf{y} &= \mathbf{h}(\mathbf{x}, \mathbf{u}) + \mathbf{v}\end{aligned}\quad (5.31)$$

$\mathbf{y}$ ,  $\mathbf{x}$ , and  $\mathbf{u}$  denote the output, the state and the control input vectors, respectively.  $\mathbf{w}$  stands for the process noise,  $\mathbf{v}$  for the measurement noise.  $\mathbf{v}$  and  $\mathbf{w}$  are uncorrelated, zero-mean white noise processes with covariance matrices  $\mathbf{Q}$  and  $\mathbf{R}$ , respectively:

$$\mathbf{Q} = E[\mathbf{w}\mathbf{w}^T] \quad (5.32)$$

$$\mathbf{R} = E[\mathbf{v}\mathbf{v}^T] \quad (5.33)$$

It is assumed that the process and measurement noise processes are additive to the state derivative and the output vectors. A more general approach, where also nonlinear noise models are accounted for, has been presented in [99].

The goal of the Kalman filter is to provide an estimate  $\hat{\mathbf{x}}$  of the state vector  $\mathbf{x}$ , where the covariance matrix  $\mathbf{P}$  of the estimate error is minimal.  $\mathbf{P}$  can be expressed as follows:

$$\mathbf{P} = E[(\mathbf{x} - \hat{\mathbf{x}})(\mathbf{x} - \hat{\mathbf{x}})^T] \quad (5.34)$$

The Kalman filter algorithm basically handles linear models. Therefore, the model has to be linearised around the current state estimate  $\hat{\mathbf{x}}$  to obtain the systems dynamics matrix  $\mathbf{F}$  and the measurement matrix  $\mathbf{H}$ :

$$\mathbf{F} = \left. \frac{\partial \mathbf{f}(\mathbf{x}, \mathbf{u})}{\partial \mathbf{x}} \right|_{\mathbf{x}=\hat{\mathbf{x}}} \quad (5.35)$$

$$\mathbf{H} = \left. \frac{\partial \mathbf{h}(\mathbf{x}, \mathbf{u})}{\partial \mathbf{x}} \right|_{\mathbf{x}=\hat{\mathbf{x}}} \quad (5.36)$$

The filter will eventually be required in the discrete form. In the discrete algorithm equations, the fundamental matrix  $\Phi_k$ <sup>3</sup> is required instead of the systems dynamics matrix  $\mathbf{F}$ .  $\Phi_k$  can be approximated by the first two terms of the Taylor-series expansion:

$$\Phi_k = e^{\mathbf{F}h_s} \approx I + \mathbf{F}h_s \left( + \frac{\mathbf{F}^2 h_s^2}{2!} + \frac{\mathbf{F}^3 h_s^3}{3!} + \dots \right) \quad (5.37)$$

---

<sup>3</sup>A more accurate denotation is  $\Phi((k+1)h_s, kh_s)$ , since the progression of the state vector between the two samples  $kh_s$  and  $(k+1)h_s$  is addressed. However, for the sake of readability, the simpler form  $\Phi_k$  is preferred.

$h_s$  denotes the sample time. A more robust possibility is the bilinear approximation. It should be used, when the model is stiff. The problem is, however, that a matrix inversion is required. The bilinear approximation  $\Phi_k$  can be expressed as follows [40]:

$$\Phi_k \approx \left[ \mathbf{I} - \frac{h_s}{2} \mathbf{F} \right]^{-1} \left[ \mathbf{I} + \frac{h_s}{2} \mathbf{F} \right] \quad (5.38)$$

The extended Kalman filter algorithm basically consists of two steps. In the first step, the “time update” or “extrapolation” step, the state vector estimate  $\hat{\mathbf{x}}$  and the covariance matrix  $\mathbf{P}$  are projected one step ahead:

$$\hat{\mathbf{x}}_k^- = \mathbf{f}(\hat{\mathbf{x}}_{k-1}, \mathbf{u}_{k-1}) \quad (5.39)$$

$$\mathbf{P}_k^- = \Phi_k \mathbf{P}_{k-1} \Phi_k^T + \mathbf{Q}_k \quad (5.40)$$

Notice that the nonlinear state-space equation is integrated directly without linearisation. The discrete process noise matrix  $\mathbf{Q}_k$  can be obtained from the continuous matrix  $\mathbf{Q}$  by integration over one time step:

$$\mathbf{Q}_k = \int_{(k-1)h_s}^{kh_s} \Phi(\tau) \mathbf{Q} \Phi^T(\tau) d\tau \quad (5.41)$$

In the second step, the “measurement update” or “correction” step, the state vector estimate  $\hat{\mathbf{x}}$  and the covariance matrix  $\mathbf{P}$  are corrected using the error between the projected output vector  $\mathbf{h}(\hat{\mathbf{x}}_k^-)$  and the measured vector  $\mathbf{z}_k$ , and measurement matrix  $\mathbf{H}_k$ , respectively:

$$\hat{\mathbf{x}}_k = \hat{\mathbf{x}}_k^- + \mathbf{K}_k (\mathbf{z}_k - \mathbf{h}(\hat{\mathbf{x}}_k^-, \mathbf{u}_k)) \quad (5.42)$$

$$\mathbf{P}_k = (\mathbf{I} - \mathbf{K}_k \mathbf{H}_k) \mathbf{P}_k^- \quad (5.43)$$

The Kalman gain  $\mathbf{K}_k$  is calculated from the discrete Riccati equation

$$\mathbf{K}_k = \mathbf{P}_k^- \mathbf{H}_k^T (\mathbf{H}_k \mathbf{P}_k^- \mathbf{H}_k^T + \mathbf{R}_k)^{-1} \quad (5.44)$$

The filter algorithm is established with equations (5.39)–(5.40) and (5.42)–(5.44). Their calculation has to be repeated every time step.

Theoretically, the covariance matrices  $\mathbf{Q}$  and  $\mathbf{R}$  describing the process and measurement noise processes, can be obtained from measurements. However, some of the internal state variables such as the occupancies of O or CO can hardly be measured. In practice, the two matrices are used as tuning parameters. To illustrate their influence, consider (5.44). If  $\mathbf{R}$  is chosen large and  $\mathbf{Q}$  small,  $\mathbf{K}_k$  becomes rather small. This means that due to the large measurement

error, the model is trusted more. Hence, the estimated state vector  $\hat{\mathbf{x}}$  is mainly calculated with the extrapolation step, the correction step only has a weak influence. Accordingly, the opposite is true, if  $\mathbf{Q}$  is chosen to be large and  $\mathbf{R}$  small. Since the model errors are in reality somewhat far away from white noise, especially in the example presented here, the two parameters have to be chosen carefully. Generally, the model noise is considered small as compared to the measurement noise, i. e., a relatively slow adaptation is preferred. This choice is based on the intention to filter out high frequency dynamics which are not reflected by the model.

### Implementation of the TWC Model

The TWC model is implemented in the form presented in Section 5.2. Thereby, the state-space equation contains the raw exhaust and the TWC models. The measurement equation incorporates the switch-type  $\lambda$  sensor model. Hence, the input, state, and output vectors are defined as follows:

$$\mathbf{u} = \begin{bmatrix} \lambda \\ \dot{n}_{exh} \\ T_{exh} \end{bmatrix}, \quad \mathbf{x} = \begin{bmatrix} \theta_{O,1} \\ \theta_{CO,1} \\ T_{s,1} \\ \theta_{O,2} \\ \vdots \\ T_{s,3} \end{bmatrix}, \quad \mathbf{y} = [U_{\lambda st}]$$

The model contains nine state variables, which is certainly the upper limit for control-oriented purposes. However, since the measurement vector is actually a scalar, the matrix inversion in the Riccati equation (5.44) reduces to a scalar inversion.

The filter is somewhat simplified by only including the occupancies in the measurement update step. The temperatures are estimated in the extrapolation step. This reduces the covariance matrix  $\mathbf{P}$  to 6<sup>th</sup> order. This choice is based on the fact that the coupling between the temperatures and the sensor output is relatively weak. Tests have shown that significant transients, as they occur e. g. during a fuel cut-off, may over-excite the temperature correction because of this weak coupling. This destabilising effect could only be partly damped by an adequate choice of the corresponding elements in the model noise covariance matrix  $\mathbf{Q}$ . The reduction of the problem considerably improved the robustness of the filter against the mentioned sudden transients.

The characteristic of the measurement equation  $h(\mathbf{x}, \mathbf{u})$  is strongly nonlinear. This nonlinearity arises from the considerably increased sensitivity of the sensor signal around stoichiometry, as compared to the zones, where  $\lambda$  is further

away from one. Basically, one would expect that the measurement covariance  $\mathbf{R}$  should be adjusted to the voltage level. An alternative approach could be to “invert” the sensor signal according to (5.30) of the model calibration section. This would considerably “flatten” the sensor characteristic.

In fact, neither has been done. The sensor signal has been used in its original nonlinear form and  $\mathbf{R}$  has been kept constant. As already stated in Chapter 4, the switch-type  $\lambda$  sensor provides a very accurate information about the position of the stoichiometric point. This is also the point, where the model should be accurate, since it is directly connected to the estimation of the storage capacity. Further off the stoichiometric point, i. e., where  $|\lambda - 1| > \epsilon$ , the sensor is less accurate. Its signal is distorted by the actual sensor temperature, which is unknown, and by the ageing of the sensor. Hence, choosing  $\mathbf{R}$  to be constant, naturally increases the weight of the measurement update step around stoichiometry, whereas it is decreased substantially, where some sensor inaccuracies might occur.

### Identification: State-Space Augmentation

Parameter identification with an extended Kalman filter can be implemented by replacing the estimated parameters by additional state variables. This is permitted, because the filter is not limited to linear state-space models.

The discrete form of the state-space model (5.31) is augmented with the following equation:

$$SC_{k+1} = SC_k + w_{SC,k} \quad (5.45)$$

$w_{SC,k}$  denotes a zero-mean scalar white noise process.  $SC$  is kept constant in the extrapolation step and is only adjusted in the measurement update step.  $\mathbf{Q}$  and  $\mathbf{P}$  have to be augmented accordingly. Notice that  $SC$  has been assumed to be identical for all cells.

Figure 5.14 shows a sketch of the realised extended Kalman filter in signal flow form. Notice that two different state vectors are used in the extrapolation and correction steps. As has been pointed out above, the temperatures are only calculated in the extrapolation step and then handled as model parameters. Hence, the two state vectors  $\mathbf{x}_{KF}$  and  $\mathbf{x}_{Temp}$  consist of the following elements:

$$\mathbf{x}_{KF} = \begin{bmatrix} \theta_{O,1} \\ \theta_{CO,1} \\ \theta_{O,2} \\ \theta_{CO,2} \\ \theta_{O,3} \\ \theta_{CO,3} \\ SC \end{bmatrix}, \quad \mathbf{x}_{Temp} = \begin{bmatrix} T_{s,1} \\ T_{s,2} \\ T_{s,3} \end{bmatrix}$$

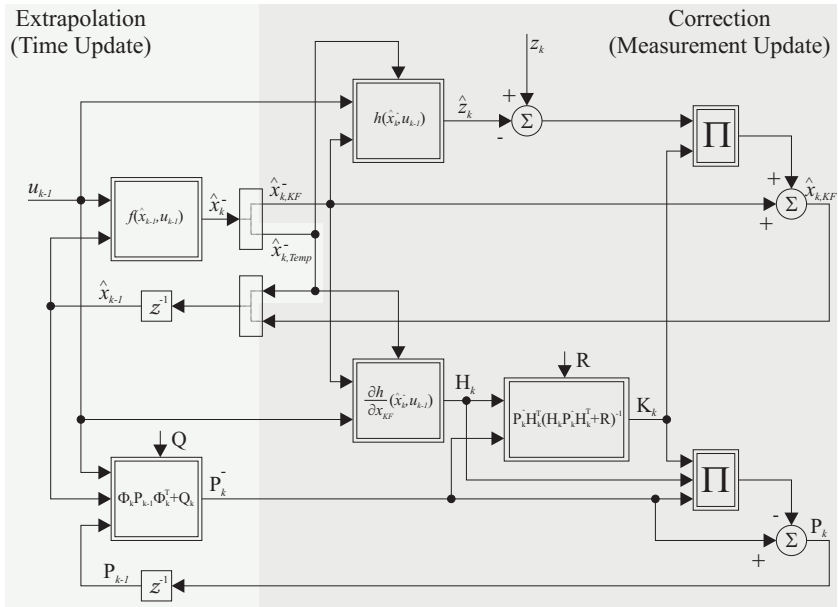


Figure 5.14: Sketch of the realised extended Kalman filter.

In the extrapolation step, both vectors are calculated in combination. In the correction step, only  $\mathbf{x}_{KF}$  is updated.

### Observability and Excitation

A very important prerequisite for the proper operation of an extended Kalman filter is the observability of the state-space model. For a nonlinear system, the global observability can be defined as follows [12]:

**Definition 5.1** *The nonlinear system  $\dot{\mathbf{x}} = \mathbf{f}(\mathbf{x}, \mathbf{u})$ ,  $\mathbf{x}(0) = \mathbf{x}_0$ ,  $\mathbf{y} = \mathbf{h}(\mathbf{x}, \mathbf{u})$ , where  $\mathbf{x} \in D_{\mathbf{x}} \subseteq R^n$ ,  $\mathbf{u} \in D_{\mathbf{u}} \subseteq R^m$ ,  $\mathbf{y} \in R^q$  is globally observable if all initial states  $\mathbf{x}_0$  can be determined uniquely from  $\mathbf{y}(t)$  and  $\mathbf{u}(t)$  in the entire domain  $\mathbf{x}_0 \in D_{\mathbf{x}}$ ,  $\forall \mathbf{u} \in D_{\mathbf{u}}$ .*

Less strict are the local and the operating point observabilities:

**Definition 5.2** *The nonlinear system  $\dot{\mathbf{x}} = \mathbf{f}(\mathbf{x}, \mathbf{u})$ ,  $\mathbf{x}(0) = \mathbf{x}_0$ ,  $\mathbf{y} = \mathbf{h}(\mathbf{x}, \mathbf{u})$ , where  $\mathbf{x} \in D_{\mathbf{x}} \subseteq R^n$ ,  $\mathbf{u} \in D_{\mathbf{u}} \subseteq R^m$ ,  $\mathbf{y} \in R^q$  is locally observable in a point  $\mathbf{x}_p$  if all initial states  $\mathbf{x}_0$  in the neighbourhood  $\|\mathbf{x}_0 - \mathbf{x}_p\| < \rho$  of  $\mathbf{x}_p$  can*



be determined uniquely from  $\mathbf{y}(t)$  and  $\mathbf{u}(t)$  in the entire domain  $\forall \mathbf{x}_p \in D_{\mathbf{x}}, \forall \mathbf{u} \in D_{\mathbf{u}}$ .

The system is observable in the operating point  $\mathbf{x}_s$ , if all initial states  $\mathbf{x}_0$  in the neighbourhood ( $\|\mathbf{x}_0 - \mathbf{x}_s\| < \epsilon_x, \|\mathbf{u} - \mathbf{u}_s\| < \epsilon_u$ ) of the steady-state operating point  $\mathbf{x}_s, \mathbf{u}_s$  with  $\mathbf{f}(\mathbf{x}_s, \mathbf{u}_s) = \mathbf{0}$  can be determined uniquely from  $\mathbf{y}(t)$  and  $\mathbf{u}(t)$ .

Notice that all three types are identical for linear systems. The determination of the global observability is difficult and awkward. Procedures concerning this task have been proposed in [12]. The determination of the operating point observability is much easier and can be performed using the tools from the linear theory, see [32]. However, care should be taken, since the eigenvalues of the system do not remain constant when the operating point is changing. Since the system focused on here is “well-tempered”, a more intuitive approach is taken to demonstrate the operability of the observer. “Well-tempered” means that the system is inherently stable. For exact definitions and concepts regarding stability, refer to [92]. To determine BIBO (bounded-input/bounded-output) stability, no mathematical analysis is required. Notice that the occupancies are physically limited. They cannot become negative and their sum cannot exceed 1. The temperature can never decrease below the ambient temperature. The heat production is dependent on the occupancies and therefore cannot increase indefinitely. Thus, all state variables remain bounded. Actually, the linearised system is asymptotically stable in any steady-state operating point.

For an intuitive approach to the observability of the TWC model, an equivalent system shall be derived, which is somewhat easier to understand. Consider three tanks in a row, which are filled with water. Each tank leaks water to the next tank, dependent on the water level. The size and geometry of the tanks as well as the correlation of the storage levels and the leakage are known. It is intuitively obvious that the levels of the three tanks can be determined, if the amount of water leaving the last tank is known. If oil is added to the water, and if the oil/water ratio is measured at the outlet, both the water and oil levels of each tank can be determined. This corresponds roughly to the oxygen and carbon monoxide storage levels in the three different cells. Notice that this is only the case because the concentrations of  $\text{O}_2$ ,  $\text{CO}$ , and  $\text{H}_2$  are calculated statically from the occupancies in the cells and the concentrations of the preceding cells. These considerations shall suffice to demonstrate the observability of the model. For future work, a more profound analysis is certainly recommended.

To guarantee convergence of the Kalman filter states to the “true” values, the model should be excited accordingly. The prerequisite of persistent excitation is described in [60] or [94]. Here, it shall be explained with a simple example for the reader who is not familiar with the concepts of parameter identification.

Consider a volume with entering and leaving mass flows. For example the intake manifold of an engine can be considered as such a volume. An identification algorithm shall now be developed, where the volume of the manifold is to be estimated. It is intuitively clear that under steady-state conditions, i. e., as long as the input and output mass flows are identical and constant, the volume cannot be determined. Only when at least one of the mass flows are excited, the volume can be determined from the relation of the two mass flows. This is a fundamentally valid, physically founded problem, independent of the identification algorithm. Hence, a system, where the input-output relation cannot be determined by steady-state considerations, has to be excited accordingly.

In the present model, the storage capacity can theoretically be determined from steady-state considerations, since the reaction rates and thus both the heat production and the tailpipe concentrations are dependent on  $SC$ . Even if this input-output link is too weak, excitation is not a problem, since the disturbances of the air-to-fuel ratio  $\lambda$  at the TWC inlet and the usually considerable transients of the exhaust gas mass flow are sufficient in most cases. On a highway, however, where driving may be constant during longer periods (which is not expected in central Europe considering the topography and the general traffic situation), these excitations can become very weak. Here, the steady-state input-output relation including  $SC$  has at least a stabilising effect in the sense that the identification process does not diverge. Concepts, where  $\lambda$  is permanently excited, i. e., where the so called “wobbling” is applied [97], are favourable, because they provide excellent excitation, which guarantees convergence within a few seconds. The concept presented in this thesis does not make use of any extra  $\lambda$  excitation.

### Aspects of the Numerics

The extended Kalman filter presented here has been tested with a sample rate of 1 kHz. With this rate, no major numerical problems occurred. The state vector in the extrapolation step was calculated using an Euler forward scheme. The Jacobians  $\mathbf{F}$  and  $\mathbf{H}$  were calculated numerically. For the fundamental matrix  $\Phi$ , the approximation from the Taylor series according to (5.37) was used. Hence, for every step, which might be numerically delicate, the simplest method provided stable and accurate results. This was possible for two reasons. First, the sample rate was about one order of magnitude higher as compared to what can be expected in a present production-type control unit. Second, with the steady-state implementation of the mass balances, the inherent stiffness of the system could be eliminated. If slower sampling rates are a premise and/or if for some reasons, the model is extended to dynamical mass balance equations, measures can be taken, which are described in the following. As a rule of

thumb, it can be generally stated that an improvement of the accuracy is more effective when applied in the extrapolation step [102].

The Jacobians of  $\mathbf{F}$  and  $\mathbf{H}$  can alternatively be calculated analytically. This is a somewhat awkward task, but certainly improves the accuracy and most probably reduces the consumption of CPU power.

The fundamental matrix  $\Phi$  can alternatively be calculated using the bilinear approximation according to (5.38). This involves a matrix inversion of the dimension of the state vector in the correction step. Here, this vector has dimension 7. Notice that the Gauss algorithm provides numerically more stable results than the LU decomposition, see [83], especially when the matrix is badly conditioned. Unfortunately, this is often the case, when stiff systems are linearised.

Instead of the Euler forward scheme, a semi-implicit Euler scheme can be applied for the integration of the nonlinear state-space system in the extrapolation step. This scheme can be derived from the implicit Euler backward integration. It is usually almost as stable as implicit schemes and therefore very suitable for stiff systems. Here, only a short derivation shall be given, details can be found in [83].

Consider an ordinary differential equation in  $\mathbf{x}$ . If the time step size  $h_s$  is assumed, the integration with the implicit Euler backward scheme can be expressed as follows:

$$\mathbf{x}_{k+1} = \mathbf{x}_k + h_s \cdot \mathbf{f}(\mathbf{x}_{k+1}) \quad (5.46)$$

This is a nonlinear equation system for  $\mathbf{x}_{k+1}$ . Such a system can be solved using an iterative method, which is not suitable for a real-time control system. Therefore, a linearised Ansatz for  $f(\mathbf{x}_{k+1})$  following Newton is applied:

$$\mathbf{f}(\mathbf{x}_{k+1}) \approx \mathbf{f}(\mathbf{x}_k) + \left. \frac{\partial \mathbf{f}}{\partial \mathbf{x}} \right|_{\mathbf{x}_k} (\mathbf{x}_{k+1} - \mathbf{x}_k) \quad (5.47)$$

Solving for  $\mathbf{x}_{k+1}$ , leads to

$$\mathbf{x}_{k+1} = \mathbf{x}_k + h_s \left( \mathbf{I} - h_s \left. \frac{\partial \mathbf{f}}{\partial \mathbf{x}} \right|_{\mathbf{x}_k} \right)^{-1} \cdot \mathbf{f}(\mathbf{x}_k) \quad (5.48)$$

This solution can be explicitly calculated, i. e., no iterative method is necessary. However, a matrix inversion is required, which leads to a significantly increased consumption of CPU power, as compared to the Euler forward integration scheme.

### $\lambda$ Sensor Offset

Both the wide-range and the switch-type  $\lambda$  sensor signals may be subject to offsets. As for the switch-type  $\lambda$  sensor, this is a problem, when the position of the switch is shifted. It is assumed that the position remains sufficiently stable, as long as the sensor is used downstream of the TWC. The influence of the sensor ageing has not been investigated in this thesis. This is certainly recommended for future work.

The wide-range  $\lambda$  sensor may exhibit a considerable offset, as has been shown in Chapter 4. This offset leads to a different estimated oxygen storage level as compared to the one calculated from an accurate sensor signal. The erroneous oxygen storage level in turn leads to a modified voltage output of the estimated switch-type  $\lambda$  sensor signal.

The extended Kalman filter forces the estimated and the measured switch-type  $\lambda$  sensor signals to converge to the same value. This can only be achieved by a modification of the estimated oxygen storage levels. If the estimated oxygen storage level is controlled to a constant value, a steady-state offset of the control signal  $\lambda$  is necessary to compensate for the sensor offset. This compensation can only be achieved by an I-controller. Thus, it can be concluded that if an I-controller is used, its steady-state output provides a signal which is proportional to the sensor offset at the inlet of the TWC. Hence, the controller can be used for the diagnosis of the wide-range  $\lambda$  sensor at the inlet of the TWC. This will be demonstrated in the next chapter.

Basically, the sensor offset could also be estimated directly with the filter by identification. Tests have shown that the tuning of the filter then becomes very delicate since the sensor offset and the storage capacity are not entirely independent. The separation of the sensor error and the storage capacity estimations has been found to be more robust with the proposed method.

#### 5.4.2 Performance of the Extended Kalman Filter in the FTP Cycle

Figure 5.15 shows the performance of the EKF in the last phase of an FTP cycle. Three differently aged TWCs are shown. In order to demonstrate the robust filter convergence, tests have been performed with different initial values for the storage capacity  $SC$  at 10, 30, 50, and 70 mol/m<sup>3</sup>. For reference purposes, additionally the engine speed  $n_{eng}$  and the engine exhaust  $\lambda_{exh}$  are shown. The filter performance is good, the three TWCs can be clearly separated and  $SC$  converges stably to identical curves for one single TWC.

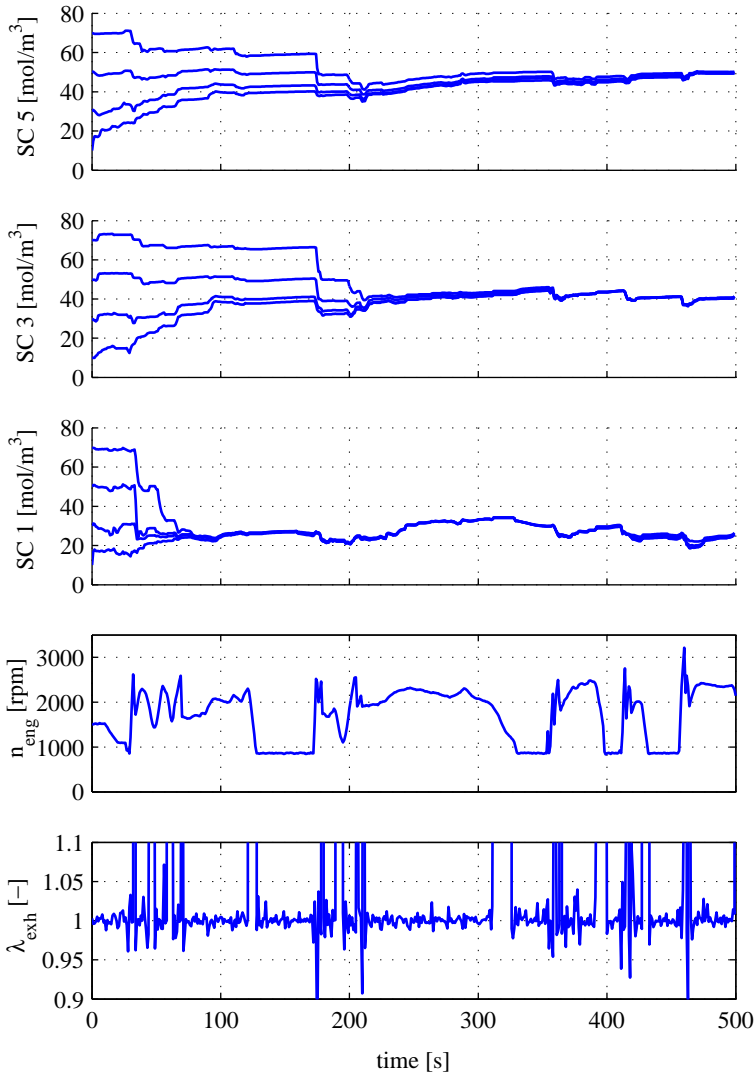


Figure 5.15: Estimated storage capacities  $SC$  with different initial values. The EKF was tuned for fast convergence. TWC 1 is considerably aged (at  $1100\text{ }^\circ\text{C}$ ), TWC 3 moderately aged (at  $900\text{ }^\circ\text{C}$ ), and TWC 5 is fresh, see Section 2.5.  $n_{eng}$  denotes the engine speed,  $\lambda_{eng}$  the engine exhaust air-to-fuel ratio.

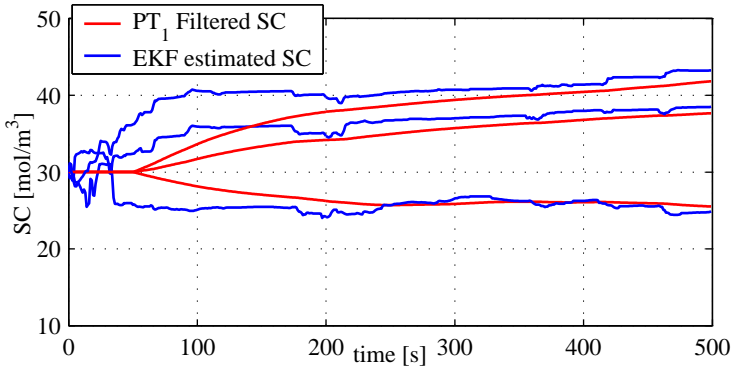


Figure 5.16: Estimated storage capacities of differently aged TWCs (at 1100 °C, 900 °C, and fresh, see Section 2.5). The EKF has been tuned for slow convergence. The red signals have been low pass filtered with a time constant of 100 s.

All cycles were recorded with active  $\lambda$  feedback and feedforward (compensator for the wall-wetting and intake manifold dynamics) controllers. A TWC controller was not used. The system was not especially excited. The air-to-fuel ratio  $\lambda$  was controlled to a constant value of 1, except during fuel cut-offs. No special strategy for the depletion of the stored oxygen in the TWC after the fuel cut-offs was utilised. The filter was configured with a rather large covariance for  $SC$  in order to provide fast convergence. However, this led to quite unsteady  $SC$  signals. With such unsteady signals, it is of course difficult to identify the  $SC$  of the TWC within narrow limits. Therefore, the covariance should be chosen much smaller in practice, in order to provide a smooth signal of the estimated  $SC$ .

A “bad” TWC should be identified within one test cycle such as FTP. This does not mean that  $SC$  has to be exactly known at the end of the cycle. It only has to be determined, whether its value lies above or below a critical limit. Therefore, a strategy is recommended, whose model is most accurate, where  $SC$  is critical. The EKF is initialised with the critical value. The estimated  $SC$  is then heavily filtered under operation. If it starts to increase after initialisation, the TWC is good. If it starts decreasing, a malfunction may be indicated. This is demonstrated in Figure 5.16. The filter has been configured to converge slowly. Additionally, the identified storage capacity has been low pass filtered with a time constant of 100 s. If the critical value has been assumed to be 30 mol/m<sup>3</sup>, the “bad” TWC can easily be identified.

The example presented here is of course somewhat academic, since TWCs

close to the critical value are hardly identifiable as easy as this example might indicate. The result is to be understood as a basis, which can be improved in many ways with suitable filter techniques and/or statistical tools.

One of the major advantages of the EKF is that no extra excitation is necessary. The excitation provided under normal operation conditions of the engine is sufficient for a robust performance.

## 5.5 Conclusion

A control-oriented physical model of the exhaust gas aftertreatment system including the TWC, the upstream wide-range and the downstream switch-type  $\lambda$  sensors has been developed. It consists of three modules, including the raw exhaust gas composition, the TWC, and the switch-type  $\lambda$  sensor. In the first module, the engine-out mole fractions of  $O_2$  (including NO), CO (including HC), and  $H_2$  are calculated. The second module is the TWC, where the outlet concentrations of the three components are calculated. The TWC model consists of three finite elements, each containing three state variables. These are the temperature and the occupancies of O and CO. The third module consists of an algebraic switch-type  $\lambda$  sensor model, where the voltage output is calculated from the three gas components. Apart from the oxygen input, output, and storage behaviour, the deactivation of the TWC by carbonaceous species has been accounted for. Additionally, the water-gas shift reaction has been included, which is dependent on the TWC deactivation and the ageing. The entire model reflects the input/output behaviour of the real system very well under a wide range of engine operating points and ageing levels of the TWC. It has been shown that the ageing of the TWC can be characterised with one single parameter, the storage capacity.

The model has been incorporated in an extended Kalman filter which serves as a state observer and simultaneously estimates the storage capacity by means of parameter identification. Hence, it can be applied for control and diagnosis purposes. It has been demonstrated that the filter can robustly identify the ageing level of the TWC within the last part of the FTP cycle. This is achieved without any special excitation of the raw exhaust  $\lambda$  or other control inputs. The filter appears to be a promising tool for TWC diagnosis.



# 6 Control of a Three-Way Catalytic Converter

## 6.1 Introduction

The extended Kalman filter presented in the previous chapter cannot only be used for TWC diagnosis, but also for the development of an observer-based controller of the TWC. It has been shown in Chapter 3 that the performance of the TWC in terms of conversion rates of CO, NO, and HC apart from the steady-state air-to-fuel ratio also depends on the levels of the stored species. This becomes very clear, when the air-to-fuel ratio of the raw exhaust is switched between lean and rich at low frequencies. Both simulation and measurement results revealed that during the filling or depleting of the TWC with oxygen, the conversion rates are increased temporarily, although the inlet  $\lambda$  is permanently far away from stoichiometry. Therefore, a TWC controller aims at keeping the TWC in a state, where the highest conversion rates are expected. It is clear that this goal cannot be achieved with a  $\lambda$  control system, as has been described in Section 1.4, because the state of the TWC is not regarded in that strategy. Therefore, the  $\lambda$  controller has to be extended accordingly or simply replaced by a TWC controller, since a “ $\lambda = 1$ ” concept also aims at the performance of the TWC.

Various types of TWC controllers have been presented in the literature. In [89], a concept was developed, where the oxygen storage level is estimated from an observer. Additionally, parameters are identified using a recursive Markov estimate method. The storage level is used as the control variable. The complete control and identification concept developed in this thesis follows basically the ideas presented in [89], however, with a considerably refined modelling, identification and control approach. A model-based controller was also presented in [6] and [7]. Here, an observer is utilised which estimates the oxygen storage level of the TWC. The observer is based on a nonlinear model, which mainly consists of an oxygen storage (integrator) with nonlinear filling and depletion functions, dependent on the inlet conditions (temperatures, mass flow) and  $\lambda$ . The controller, which is a neuro-fuzzy approximation of a model predictive controller, aims at keeping the stored oxygen at a level, where the TWC’s maximum conversion rates are obtained. A model-based control con-

cept which uses wide-range  $\lambda$  sensors both upstream and downstream of the TWC was presented in [39]. Again, a nonlinear observer estimates the oxygen storage level, which is then controlled. The observer incorporates an extended Kalman filter which is supported by the downstream  $\lambda$  sensor.

A description of the concepts in use at present in production-type control systems can be found in e. g. [97]. Usually, a switch-type  $\lambda$  sensor is used downstream of the TWC. A slow PI controller aims at keeping the sensor's voltage output at a constant level. The purpose is to keep the upstream  $\lambda$  controller calibrated and to compensate for potential sensor offsets. These can be obtained from the steady-state integrator value of the I-controller. Thus, the controller is also used for sensor diagnosis.

In the following, different potential control strategies will be discussed first. Then, a model-based controller of the TWC will be derived, which apart from the main control goal also provides a means for the diagnosis of the upstream  $\lambda$  sensor. Finally, a selection of measurement results is presented and discussed.

## 6.2 Control of TWCs and $\lambda = 1$ Strategies

### 6.2.1 Challenges of TWC Control

As has been pointed out in the previous section, a strategy which only uses TWC upstream sensor information is not sufficiently robust because of the potential offset of  $\lambda$  sensors. Only a small error may lead to a slightly lean or rich balanced exhaust gas, which causes the levels of stored oxygen or other species in the TWC to drift away slowly from their optimal values in terms of the conversion rates. In a first approach, which is also used in state-of-the-art engine control systems, the  $\lambda$  controller is calibrated with a switch-type  $\lambda$  sensor located downstream of the TWC. The setup is depicted in Figure 6.1. The location of the switch is quite robust during the sensor's lifetime. Hence, a voltage level close to the location of the switch is chosen as a setpoint for the controller, usually around 600 mV. If the control variable is the setpoint for the  $\lambda$  controller, and if a PI controller is used, the steady-state value of the integrator is equal to the steady-state offset of the sensor. This information can be used for diagnosis purposes.

Apart from the optimal steady-state conversion rates of the TWC, also other aspects should be considered, when designing a TWC controller. The conversion rates should also be optimal under dynamic conditions, i. e., when disturbances of the inlet  $\lambda$  occur. These are caused by the differences between the air path (via intake manifold) and the fuel path dynamics (via wall-wetting). These differences can only partly be compensated in practice. Especially dur-

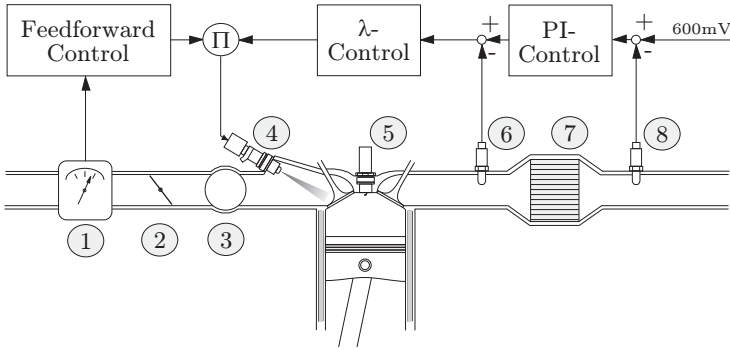


Figure 6.1: Sketch of an extended  $\lambda$  control system with the following components: 1 Air mass flow meter; 2 Throttle; 3 Intake manifold; 4 Fuel injection valve; 5 Spark plug; 6  $\lambda$  sensor upstream; 7 TWC; 8  $\lambda$  sensor downstream. Notice that the feedback  $\lambda$  controller adjusts the injection time by means of a factor. The reason for this has been explained in Section 1.4.

ing heavy transients such as sudden changes of the desired engine load, temporary excursions of  $\lambda$  of at least 0.5% even in a well calibrated system may occur. If the TWC is kept in a well-balanced state, such excursions can be damped because of the TWC's ability to store or release oxygen. However, measurements have revealed that this mechanism is somewhat limited, i. e., aggressive (fast and considerable) excursions can be damped only partly, even with fresh TWCs. Especially the CO conversion has been found to be sensitive towards aggressive TWC operation, imposed by the  $\lambda$ /feedforward controller or by an aggressive TWC controller. This has also been shown in [7]. This clearly implies that the compensation of the intake manifold- and the wall-wetting dynamics as well as the  $\lambda$  controller are still very important. The TWC controller can only compensate for "failures" of these controllers to a rather limited degree.

Another important aspect is the appearance of fuel cut-offs. These occur frequently with a manual transmission. During a fuel cut-off, the TWC is filled with oxygen, which must be depleted, when the fuel injection is reset. It goes without saying that a fast recovery of the TWC is desirable.

The concepts with a slow PI controller of the downstream sensor voltage actually account for the problem of the upstream sensor offset and implicitly for the sensitivity to  $\lambda$  disturbances, since the controller only imposes signals with a small bandwidth. However, two major problems arise with the concept.

Firstly, for a recovery after a fuel cut-off, these controllers are usually too slow. A separate feedforward strategy has to be used. Secondly, especially downstream of fresh TWCs, the sensor signal exhibits a partly very weak sensitivity to changes in the TWC's state. In other words, it is very hard to obtain a stable control system around stoichiometry, since the sensor is almost "blind" and only reacts, when considerable deviations from the TWC's desired state are reached.

To summarise, the main challenges are robust balancing or rather disturbance rejection of the TWC of any ageing level, stable operation of fresh TWCs with very weak downstream sensor information, and fast recovery after fuel cut-offs. All this should be achieved with a limited control bandwidth in order to avoid additional aggressive excursions from stoichiometry, which have a negative impact on the conversion rates, namely of CO.

### 6.2.2 Observer based TWC Control Strategies

From the considerations in the previous section, it becomes clear that a state observer should be used, which on the one hand allows the estimation of the TWC's state and on the other hand can operate even with a temporarily "inert" signal at the TWC outlet. The extended Kalman filter presented in the previous chapter provides a good estimate of the storage levels even distributed in the axial direction, since three discrete cells are considered. In the following, concepts are discussed, which make use of this filter.

#### Cascade and Direct Control Structure

For the setup of the TWC controller structure, basically two possibilities can be taken into account. In a cascade structure, the TWC controller generates a setpoint for the inner  $\lambda$  controller, similar to the structure presented in Figure 6.1. In a direct control structure, no explicit  $\lambda$  controller is used. Instead of the setpoint for the  $\lambda$  controller, the TWC controller directly adjusts the amount of injected fuel. Both setups are illustrated in Figure 6.2. Notice that any TWC feedforward controller has been omitted for the sake of simplicity. At first sight, a direct control scheme appears to be a more reasonable choice, because cascade systems always impose considerable limitations concerning the bandwidth of the outer control loops. However, in this case, these limitations are already imposed by the physical setup as has been explained above.  $\lambda$  variations have to be suppressed at the TWC inlet as far as possible, since they have a deteriorating impact on the conversion rates. Therefore, the inner  $\lambda$  controller has to be fast, whereas the outer controller should have a substantially limited bandwidth. Thus, also a direct controller should exhibit a high bandwidth with

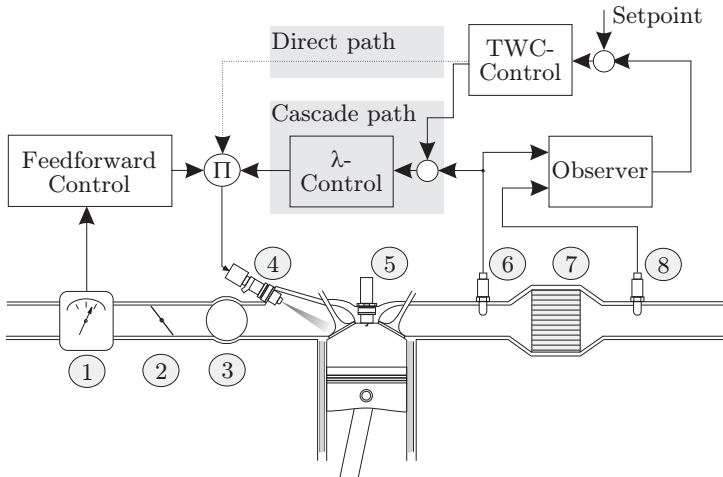


Figure 6.2: Sketch of the cascade and the direct TWC control system with the following components: 1 Air mass flow meter; 2 Throttle; 3 Intake manifold; 4 Fuel injection valve; 5 Spark plug; 6  $\lambda$  sensor upstream; 7 TWC; 8  $\lambda$  sensor downstream.

respect to the TWC inlet  $\lambda$ . Under this premise, a cascade control approach is more straightforward and simpler to realise.

A second aspect is the operation of the engine under conditions, where the TWC controller is switched off. This is the case during start-up before TWC light-off and before the downstream switch-type  $\lambda$  sensor is ready. During this time, the engine is operated with the  $\lambda$  controller only, namely with the feedforward controller immediately after engine ignition, and with the feedback controller after the first few seconds. Also after fuel cut-offs, special measures to deplete the oxygen from the TWC are easier to implement, when a cascade structure is used.

In the previous section, it has been shown that a cascade control approach with integrating behaviour provides the possibility for the diagnosis of the  $\lambda$  sensor. This could of course also be achieved with the EKF. However, tests have shown that the filter operates more robust when used for the identification of the TWC storage capacity only.

To summarise, a direct control structure does not really bring any substantial advantage as compared to a cascade system because of the physical limitations regarding the bandwidth of the “inner” ( $\lambda$ -) and the “outer” (TWC-) control

loops. Moreover, the cascade controller is simpler to be realised and adjusted to operating conditions, where only a  $\lambda$  controller is needed. For these reasons, a cascade structure was chosen for the TWC controller.

### Control Objective and Feedback Signals

The goal of the TWC controller is to maximise the conversion rates of  $\text{NO}_x$ , CO, and HC, or accordingly, to minimise the concentrations of these species at the TWC outlet. From a steady-state point of view, the conversions of CO and HC increase with an increasing  $\lambda$ . The opposite is true for the  $\text{NO}_x$ , where the conversion rate dramatically decreases with  $\lambda > 1$ , see Figure 1.2. When the dynamic operation of the TWC is considered, tests have revealed that an increasing variance of the  $\lambda$  signal leads to a deteriorated CO conversion, whereas the NO and HC conversions might be improved, if the variance is imposed by a controller, which keeps the TWC well balanced around stoichiometry. This is also in agreement with the results presented in [7]. Mathematically, the control goal with respect to both the steady-state dependence of the conversion rates and the variance or “energy” of the control signal  $\lambda - 1$  can be expressed with a quadratic cost function which is to be minimised:

$$\min_{\lambda} J_{exh} = \int_0^t \left( r \cdot (\lambda(\tau) - 1)^2 + q_{\text{CO}} \cdot c_{\text{CO}}(\tau)^2 \dots \right. \\ \left. + q_{\text{HC}} \cdot c_{\text{HC}}(\tau)^2 + q_{\text{NO}_x} \cdot c_{\text{NO}_x}(\tau)^2 \right) d\tau \quad (6.1)$$

$r$  and  $q_i$  are weighting factors.

Potential control variables are the states of the observer, i. e., the occupancies  $\theta_{\text{O}}$  and  $\theta_{\text{CO}}$ , and the temperature in each cell. From these state variables, the concentrations of CO,  $\text{O}_2$ , and  $\text{H}_2$  can be calculated in each cell. Finally, also the voltage output of the switch-type  $\lambda$  sensor  $U_{\lambda st}$  could be used, as is done in modern production-type engine control systems.

As has been pointed out in the previous section, the downstream  $\lambda$  sensor signal is almost “blind” under operating conditions close to the desired state, especially downstream of fresh TWCs. Therefore, this signal has been disregarded as a suitable choice for the feedback controller. Notice that this only concerns the controller, the signal is of course indispensable for the observer.

An obvious choice for the control variables are the concentrations of CO,  $\text{O}_2$ , or  $\text{H}_2$ . Theoretically, an optimal controller could be designed, which directly aims at the minimisation of CO and  $\text{O}_2$ . Notice that the latter includes the  $\text{NO}_x$ . However, this leads to a rather complicated problem formulation because of the highly nonlinear correlation between the state variables and the concentrations. Therefore, a considerably simpler approach is proposed.

Instead of the concentrations, the occupancies are controlled under the premise of minimal accumulated CO and O<sub>2</sub> concentrations. In other words, the set-points of the controlled state variables are derived from optimisation considerations, where the concentrations of CO and O<sub>2</sub> are to be minimised. Hence, the actual controller only has to ensure robust input disturbance rejection and tracking behaviour with a limited bandwidth.

Theoretically, both the occupancies of carbon monoxide,  $\theta_{CO}$ , and oxygen,  $\theta_O$ , could be controlled. However,  $\theta_{CO}$  only exhibits very slow dynamics. Additionally, it cannot be controlled entirely independently of  $\theta_O$ . In other words, controlling  $\theta_O$  keeps  $\theta_{CO}$  stable within a small range, because the sum of the two occupancies cannot exceed 1. It will be shown that this has to be accounted for when sensor diagnosis is applied, but can be neglected otherwise. Therefore, the control of  $\theta_O$  is assumed to be sufficient.

Having determined the control variable, the question remains, of whether all cells or only one single cell should be controlled. Basically, the last cell is directly related with the TWC outlet concentrations of the critical species. A simple approach might therefore aim at controlling this cell, only. Tests have shown, however, that the control especially of fresh TWCs with this strategy is difficult, because of the large buffering effect of the first two cells. A high controller order is required to account for this buffering effect, i. e., the TWC dynamics have to be reflected in the controller. This is of course an overhead, since the crucial information is already available from the nonlinear observer, where the TWC dynamics are naturally reflected, as well. For the direct control of the oxygen storage levels of the three cells provided by the observer, only a very simple control structure is sufficient, as will be shown further below. Hence, controlling all three cells is certainly the best choice for a stable and robust operation of a TWC, irrespective of its state of ageing.

From the considerations above, the methodology for obtaining the setpoint maps of the oxygen occupancies is derived in the following. Starting point are the TWC outlet concentrations of CO and O<sub>2</sub> which are to be minimised. These concentrations are equal to the ones in the channel of the last cell, i. e.,  $c_{CO,3}^{ch}$  and  $c_{O_2,3}^{ch}$ . They have been derived in the previous chapter and are repeated here for convenience:

$$c_{O_2,3}^{ch} = \frac{\dot{V}_{rel} c_{O_2,2}^{ch}}{\dot{V}_{rel} + D_{O_2} \left( 1 - \frac{D_{O_2}}{D_{O_2} + 0.5 (k_1 \theta_{V,3} + k_6 \theta_{CO,3}) SC} \right)}$$

$$c_{CO,3}^{ch} = \frac{\dot{V}_{rel} c_{CO,2}^{ch}}{\dot{V}_{rel} + D_{CO} \left( 1 - \frac{D_{CO}}{D_{CO} + (k_2 \theta_{O,3} + k_5 \theta_{V,3}) SC} \right)}$$

The concentrations are dependent on the occupancies and temperature of cell 3 and additionally on the inlet concentrations  $c_{O_2,2}^{ch}$  and  $c_{CO,2}^{ch}$ , which are in turn dependent on the states of the preceding cells 1 and 2 and on the inlet conditions  $\lambda_{exh}$  and  $T_{exh}$ . The goal is to obtain an expression, which calculates the optimal occupancy of oxygen from the state and inlet variables under the assumption that all other state and inlet variables remain constant. "Optimal" means with respect to a weighted sum of the squared concentrations. Mathematically, this can be expressed as follows:

*Find an optimal steady-state oxygen occupancy of cell 3*

$$\theta_{O,3}^{opt} = f \left( \theta_{O,1}, \theta_{O,2}, \theta_{CO,1}, \theta_{CO,2}, \theta_{CO,3}, T_{s,1}, T_{s,2}, T_{s,3}, \lambda_{exh}, T_{exh}, \dot{V}_{rel} \right) \quad (6.2)$$

*which minimises sum of the weighted squared steady-state concentrations of O<sub>2</sub> and CO, according to*

$$\min_{\theta_{O,3}(t)} J(t) = q_1 \cdot c_{O_2,3}^{ch}(t)^2 + q_2 \cdot c_{CO,3}^{ch}(t)^2 \quad (6.3)$$

*given the constant state and input variables in the function f.*

An alternative approach, which simplifies the optimisation problem considerably, is to maximise the conversion efficiencies of cell 3 instead of minimising the concentrations of CO and O<sub>2</sub>. The conversion efficiency of species  $i$  can be expressed as follows:

$$\eta_i = 1 - \frac{c_{i,out}}{c_{i,in}} \quad (6.4)$$

Thereby, a value of 1 means full conversion, 0 denotes no conversion. Inserting the concentrations  $c_{O_2,3}^{ch}$  and  $c_{CO,3}^{ch}$  in (6.4) leads to the following conversion efficiencies:

$$\begin{aligned} \eta_{O_2} &= 1 - \frac{\dot{V}_{rel}}{\dot{V}_{rel} + \mathcal{D}_{O_2} \left( 1 - \frac{\dot{V}_{rel}}{\mathcal{D}_{O_2} + 0.5(k_1\theta_{V,3} + k_6\theta_{CO,3})SC} \right)} \\ \eta_{CO} &= 1 - \frac{\dot{V}_{rel}}{\dot{V}_{rel} + \mathcal{D}_{CO} \left( 1 - \frac{\dot{V}_{rel}}{\mathcal{D}_{CO} + (k_2\theta_{O,3} + k_5\theta_{V,3})SC} \right)} \end{aligned} \quad (6.5)$$

Instead of formulating a new cost function, the problem is further simplified by inspecting the conversion efficiencies. These are dependent on volumetric flow ( $\dot{V}$ ), the temperatures, and on the occupancies of O and CO in cell 3. It is assumed that the dependence of the diffusion coefficients on the temperature only plays a minor role and that they are identical for CO and O<sub>2</sub>. Hence, for



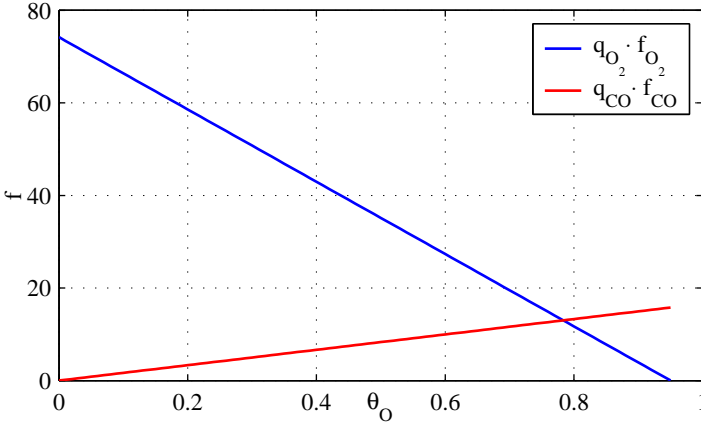


Figure 6.3:  $f_{O_2}$  and  $f_{CO}$  at 750 K, with  $\theta_{CO,3} = 0.05$  and  $q_{O_2}/q_{CO} = 0.5$ .

one specific engine operating point, which determines  $\dot{V}$ , only the following terms  $f_{O_2}$  and  $f_{CO}$  are dependent on the state variables of cell 3:

$$\begin{aligned} f_{O_2} &= 0.5 \cdot (k_1\theta_{V,3} + k_6\theta_{CO,3}) \\ f_{CO} &= k_2\theta_{O,3} + k_5\theta_{V,3} \end{aligned} \quad (6.6)$$

From (6.5) it is clear that maximising the conversion efficiencies is equivalent to maximising  $f_{O_2}$  and  $f_{CO}$ . An example of these two functions is depicted in Figure 6.3. With a specific occupancy of CO and constant reaction rates  $k_i$ ,  $f_{O_2}$  is maximal with  $\theta_{O,3} = 0$  and then linearly strictly decreasing with increasing  $\theta_{O,3}$ . The opposite is true for  $f_{CO}$ . This function is minimal with  $\theta_{O,3} = 0$  and from there strictly increasing. Hence, any setpoint for  $\theta_{O,3}$  is a compromise between the conversion efficiencies of CO and  $O_2$ . This is of course expected. A simple and straightforward approach is now to choose the setpoint such that the weighted functions  $f_{O_2}$  and  $f_{CO}$  are equal:

$$\begin{aligned} q_{O_2} \cdot f_{O_2} &= q_{CO} \cdot f_{CO} \\ q_{O_2} \cdot \frac{1}{2} (k_1\theta_{V,3} + k_6\theta_{CO,3}) &= q_{CO} \cdot (k_2\theta_{O,3} + k_5\theta_{V,3}) \end{aligned} \quad (6.7)$$

Notice that the choice of the weighting parameters is limited to the following

conditions:

$$\begin{aligned} \frac{q_{O_2}}{q_{CO}} \min(f_{O_2}) &< \max(f_{CO}) \\ \frac{q_{O_2}}{q_{CO}} \max(f_{O_2}) &> \min(f_{CO}) \end{aligned} \quad (6.8)$$

From (6.7), a setpoint for  $\theta_{O,3}$  can now be calculated as follows:

$$\theta_{O,3}^{sp} = \frac{\frac{q_{O_2}}{q_{CO}} \frac{k_1}{2} - k_5 + \left( -\frac{q_{O_2}}{q_{CO}} \frac{k_1}{2} + \frac{k_6}{2} + k_5 \right) \theta_{CO,3}}{\frac{q_{O_2}}{q_{CO}} \frac{k_1}{2} + k_2 - k_5} \quad (6.9)$$

Notice that the reaction constants  $k_i$  are dependent on the temperature. With this result, a balance between the conversion efficiencies of lean and rich species can be maintained, irrespective of changing engine operating points or TWC deactivation ( $\theta_{CO}$ ).

The setpoints for cells 1 and 2 are determined from steady-state considerations. Hence, they can be calculated from the nonlinear state-space model, which has been presented in the previous chapter. Thereby, the steady-state vector  $\mathbf{x}^{stst}$  is obtained from the following expression:

$$\mathbf{0} = \mathbf{f}(\mathbf{x}^{stst}, \lambda_{exh}^{stst}) \quad \text{where} \quad \theta_{O,3}^{stst} = \theta_{O,3}^{sp} \quad (6.10)$$

The steady-state vector  $\mathbf{x}^{stst}$  and the corresponding  $\lambda_{exh}^{stst}$  can be calculated using a solver for nonlinear equation systems, such as *fsolve* from the Matlab™ optimisation toolbox [64]. Notice that  $\theta_{O,3}^{sp}$ ,  $\mathbf{x}^{stst}$ , and  $\lambda_{exh}^{stst}$  are dependent on the operating point of the engine, which determines the mass flow  $\dot{m}_{exh}$  and the temperature  $T_{exh}$  of the raw exhaust gas. Hence, maps have to be generated for the setpoints of the occupancies of oxygen in the three cells. An example of these maps is shown in Figure 6.4. Interestingly, the setpoints decrease significantly with higher engine speeds and loads. This is a result of the fact that with higher temperatures, sorption processes become more efficient.

The procedure just described allows a fully automated determination of the setpoint maps for the oxygen occupancies in all cells, which are to be controlled. The balance of the TWC between the conversion efficiencies of lean and rich species can be clearly adjusted with the parameter  $q_{O_2}/q_{CO}$ : A higher value shifts the balance slightly to the lean side, i. e., to an improved conversion rate of reducing species, and vice versa. Hence, a simple way has been found to handle the trade-off between the conversion of NO on the one hand and CO or HC on the other hand.

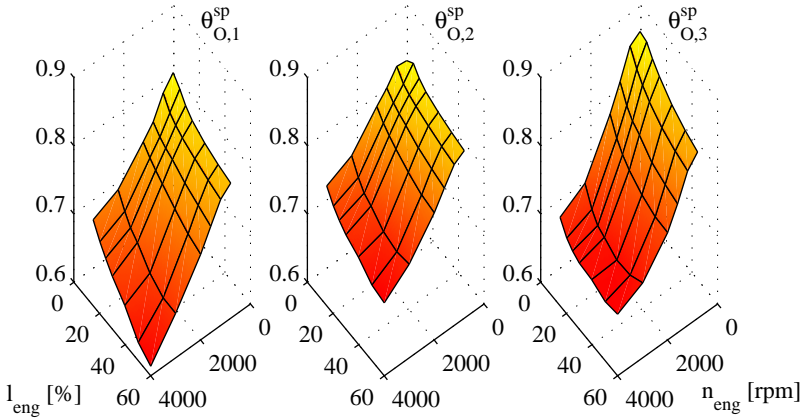


Figure 6.4: Setpoint maps of the oxygen occupancies with  $q_{O_2}/q_{CO} = 1$  dependent on the engine speed ( $n_{eng}$ ) and load ( $l_{eng}$ ). Notice that some axes are reversed.

### Control Methodology

For the control of the oxygen storage levels or rather occupancies, various possibilities can be taken into account. When evaluating these, the following aspects were particularly considered:

- **Simplicity:** The controller should be as simple as possible and not consume much CPU power.
- **Parametrisation:** It should be possible to parameterise the controller easily without the need of extended measurement or tuning campaigns.
- **Observer based:** The observer provides a very good, nonlinear estimate of the storage levels/occupancies. The controller should make use of these quantities, i. e., a state feedback controller is preferred.

The first claim rules out nonlinear strategies or optimal strategies with a finite time horizon, such as model predictive control. Notice that the high level of disturbances at the inlet and the necessity of a low bandwidth additionally cancel out the advantages of this type of strategies. To account for the nonlinearity of the system, an LPV (linear parameter variation) approach is sufficient regarding the inherent stability of the system and the necessity of only low bandwidths. On the other side of the spectrum of complexity, a PI(D) controller exhibits a very simple structure. However, for the parametrisation, a simple and clear

methodology is required. A very simple and straightforward approach is the use of a state feedback controller, which can be parameterised using the LQG or  $H_\infty$  method. Both strategies allow a transparent implementation and adaptation of the specifications to the whole range of operating points and are thus suitable for the automated design of an LPV controller. Because only a slow controller with a correspondingly low bandwidth is required, it has been decided that an LQ state feedback regulator is sufficient for the task. Its design, implementation and performance on the engine testbench will be presented in the following section.

## 6.3 Control of the Relative Oxygen Storage Levels

The estimated oxygen occupancies or relative oxygen storage levels shall be controlled with a linear quadratic (LQ) state feedback regulator. Together with the (extended) Kalman filter, the complete control scheme forms an LQG (linear quadratic gaussian) controller. This type of controller is well documented in the literature, see [91] or [26]. Therefore, the method in general will be only discussed briefly. However, specific aspects, such as stability and design parameters will be addressed in more detail. In the following, the LQ control algorithm and its application for TWC control including the realisation using LPV will be discussed. Then, a selection of measurement results will be presented. Finally, the estimation of the offset of the wide-range  $\lambda$  sensor at the TWC inlet will be addressed.

### 6.3.1 Design of an LQ Regulator for the TWC

Since an LPV approach is chosen to account for the nonlinearity of the system, the locally linearised system is considered to be time-invariant. Hence, a time-invariant LQ regulator with an infinite time horizon can be designed. The problem formulation and solution is briefly summarised here for convenience [40].

Consider a linear, time-invariant plant

$$\begin{aligned}\dot{\mathbf{x}}(t) &= \mathbf{A}\mathbf{x}(t) + \mathbf{B}\mathbf{u}(t) \\ \mathbf{x}(0) &= \mathbf{x}_0\end{aligned}\tag{6.11}$$

with the reference output

$$\mathbf{y}(t) = \mathbf{C}\mathbf{x}(t)\tag{6.12}$$

Find the control input  $\mathbf{u}_{opt}(t)$ , which minimises the quadratic cost function

$$J(\mathbf{u}) = \int_0^{\infty} (\mathbf{x}^T(t)\mathbf{Q}\mathbf{x}(t) + \mathbf{u}^T(t)\mathbf{R}\mathbf{u}(t)) dt \quad (6.13)$$

where

$$\begin{aligned} [\mathbf{A}, \mathbf{B}] &\rightarrow \text{controllable(stabilisable)} \\ [\mathbf{A}, \mathbf{C}] &\rightarrow \text{observable(detactable)} \\ \mathbf{Q} &= \mathbf{C}^T\mathbf{C} \\ \mathbf{R} &> 0 \quad \text{and diagonal} \end{aligned} \quad (6.14)$$

This constrained optimal control problem can be converted to an unconstrained optimisation problem using Lagrange multipliers. The derivation of the solution can be looked up in e. g. [26].

The optimal controller minimising the cost function (6.13) can be expressed in the following manner:

$$\mathbf{u}_{opt}(t) = -\mathbf{R}^{-1}\mathbf{B}^T\mathbf{K}_{\infty}\mathbf{x}(t) \quad (6.15)$$

where  $\mathbf{K}_{\infty}$  is the only positive-definite (positive-semidefinite if  $[\mathbf{A}, \mathbf{B}]$  is stabilisable and  $[\mathbf{A}, \mathbf{C}]$  is detactable) solution of the following algebraic Riccati equation:

$$\mathbf{0} = -\mathbf{A}^T\mathbf{K} - \mathbf{K}\mathbf{A} + \mathbf{K}\mathbf{B}\mathbf{R}^{-1}\mathbf{B}^T\mathbf{K} - \mathbf{Q} \quad (6.16)$$

Basically, the LQ regulator exhibits guaranteed phase and gain margins. However, in combination with a Kalman filter, i. e., in an LQG setup, no robustness margins are guaranteed. This can be overcome with a so called loop transfer recovery (LTR) procedure for non-minimum phase systems [36]. However, care must be taken, since LTR may involve an increase of the control signal energy, which should be avoided here, as has been discussed in the previous section. Since the plant is nonlinear, only local robustness margins can be investigated anyway. However, only a low bandwidth of the controller is required and the system is inherently stable. Hence, no problems with the robustness are expected. The control loop will be inspected more thoroughly further below.

The structure of the state feedback controller is very simple. In fact, for each state variable, a P-controller results. The plant is not inherently integrating, hence, a steady-state offset of the state variables might occur. To avoid this, the plant is extended with an integrator, in order to provide good tracking performance.

## Realisation of the LQ Regulator

As has been discussed above, only the relative oxygen storage levels or rather occupancies  $\theta_{O,i}$  will be controlled. Therefore, the system is linearised in a range of operating points, where the steady-state variables and setpoint maps have been obtained with the procedure described in 6.2.2. The temperatures  $T_{s,i}$  and occupancies  $\theta_{CO,i}$  are also obtained from this procedure. They are treated as parameters. The dynamics of the engine and the wide-range  $\lambda$  sensor including the  $\lambda$  controller are neglected. The control variable is  $\lambda_{exh}$ . The exhaust gas mass flow  $\dot{m}_{exh}$  and temperature  $T_{exh}$  are constant in one operating point. Thus, the dynamics and the input matrices  $\mathbf{A}_{\theta_O}$  and  $\mathbf{B}_{\theta_O}$  are obtained as follows:

$$\begin{aligned}\mathbf{A}_{\theta_O} &= \left. \frac{\partial \mathbf{f}_{\theta_O}(\mathbf{x}_{\theta_O}, \lambda_{exh})}{\partial \mathbf{x}_{\theta_O}} \right|_* \\ \mathbf{B}_{\theta_O} &= \left. \frac{\partial \mathbf{f}_{\theta_O}(\mathbf{x}_{\theta_O}, \lambda_{exh})}{\partial \lambda_{exh}} \right|_*\end{aligned}\quad (6.17)$$

Subscript \* denotes a steady-state operating point.  $\mathbf{x}_{\theta_O}$  is the reduced state vector, which only consists of the oxygen occupancies.  $\mathbf{f}_{\theta_O}(\mathbf{x}_{\theta_O}, \lambda_{exh})$  stands for the corresponding set of nonlinear state equations.

As has been mentioned before, the plant is extended with an integrator in order to enhance the tracking performance of the controller. The state of the last cell mainly determines the outlet gas composition of the TWC. Remember that the setpoint maps have been obtained from the conversion efficiencies of this cell. Therefore, it is important that the relative oxygen level of this cell does not exhibit any steady-state control error. Hence, the extension of the plant is only attached to the occupancy of cell 3. With the state equation of the extension

$$\dot{x}_e = \delta\theta_{O,3} \quad (6.18)$$

and the integrator gain  $K_I$ , the linearised state-space model of the extended plant can be expressed as follows:

$$\begin{aligned}\begin{bmatrix} \delta \dot{\mathbf{x}}_{\theta_O} \\ \dot{x}_e \end{bmatrix} &= \begin{bmatrix} \mathbf{A}_{\theta_O} & 0 \\ [0 & 0 & 1] & 0 \end{bmatrix} \begin{bmatrix} \delta \mathbf{x}_{\theta_O} \\ x_e \end{bmatrix} + \begin{bmatrix} \mathbf{B}_{\theta_O} \\ 0 \end{bmatrix} [\delta \lambda_{exh}] \\ [\delta y] &= [\mathbf{C}_{\theta_O} \quad K_I] \begin{bmatrix} \delta \mathbf{x}_{\theta_O} \\ x_e \end{bmatrix}\end{aligned}\quad (6.19)$$

$\delta$  denotes the difference of the actual value of a variable from the nominal trajectory.  $\delta y$  is a fictive output. Notice that the output matrix is used as a tuning parameter for the determination of  $\mathbf{Q}$ , see (6.14).

Having derived the linearised state-space model of the TWC, the specific cost function for this problem can be formulated:

$$\begin{aligned}
 J(\delta\lambda_{\text{exh}}) = & \int_0^{\infty} (q_{\theta_{O,1}}\delta\theta_{O,1}^2 + q_{\theta_{O,2}}\delta\theta_{O,2}^2 + q_{\theta_{O,3}}\delta\theta_{O,3}^2 + \dots \\
 & \dots + K_I^2 x_e^2 + r\delta\lambda_{\text{exh}}^2) dt
 \end{aligned} \tag{6.20}$$

$q_{\theta_{O,i}}$  denotes the  $i$ th diagonal element of the matrix  $\mathbf{Q}$ . With the tuning parameters  $q_{\theta_{O,i}}$ ,  $K_I$ , and  $r$ , the performance of the controller can be adjusted. Notice that the variance or signal energy of  $\delta\lambda_{\text{exh}}$  can be directly ‘‘punished’’ with the parameter  $r$ . Hence, when  $\mathbf{Q}$  is determined, the balance between the conversion rates of  $\text{NO}_x$ , HC, and CO can be directly adjusted with  $q_{\text{O}_2}/q_{\text{CO}}$  from the previous section and  $r$ . Thus, the LQ regulator in this form offers a surprisingly transparent possibility to balance the TWC.

The choice of  $\mathbf{Q}$  and  $K_I$  is basically driven by the demand for robust tracking behaviour and efficient inlet disturbance rejection. At first sight, it is reasonable to put a lot of weight on the last cell, since this cell mainly drives the TWC outlet concentrations. However, with this, the buffer effect of the first two cells is somewhat neglected, which can have a destabilising effect on the control system. This is exactly the problem with control systems aiming at the voltage of the switch-type  $\lambda$  sensor located downstream of the TWC. In fact, tests have shown that a fast recovery of the second cell after heavy disturbances or fuel cut-offs enhances both the stability of the system and the ability to damp  $\lambda$  excursions substantially. The first cell is naturally the one, where most of the conversion occurs in the model, since ageing is assumed to affect the whole TWC homogeneously. The buffering effect is only limited here. Hence, less weight is to be put on the state of this cell. The integrator should only affect the system ‘‘on the long run’’, i. e., very slowly. It is mainly necessary to balance out offsets of the wide-range  $\lambda$  sensor at the inlet of the TWC. This is used for the sensor diagnosis, as will be shown in the result section. All these considerations above lead to the following choice of parameters:

$$q_{\theta_{O,1}} = 0; \quad q_{\theta_{O,2}} = 10^2; \quad q_{\theta_{O,3}} = 1; \quad K_I = 0.02^2$$

With this set of parameters, disturbances at the input are damped well. The tracking behaviour of the last cell is not very good. This is not a big problem during normal operation, since the setpoints of the occupancies only vary little. However, after a fuel cut-off, cells 1 and 2 recover fairly quickly, but oxygen depletion of cell 3 is far too slow. Therefore, a feedforward procedure has been implemented for the recovery after a fuel cut-off. Thereby, the engine is operated 0.5% rich as long as the oxygen occupancy level of the third cell is more than 10% above the setpoint. With this relatively small deviation

from stoichiometry, extensively low oxygen levels of the first two cells can be avoided.

The choice of the other two parameters  $r$  and  $q_{O_2}/q_{CO}$  and their influence on the conversion rates will be discussed and demonstrated in the result section further below. The structure of the complete realised control system including the extended Kalman filter is depicted in Figure 6.5.

As has been mentioned already, nonlinearities of the model have been accounted for using LPV. This means that the controller structure is fixed, but the parameters such as feedback gains or the integrator gain in the case focused on here change with the engine operating point. If the variation of these control parameters is slower than the controller dynamics, their dynamics can be neglected. Hence, they can be implemented by means look-up tables. Notice that the (LQ) parameters  $r$  and  $\mathbf{Q}$  have been kept constant here for all operating points. Alternatively, they could also be adjusted in an LPV approach, for example, if a specific bandwidth or other criteria for the controller performance are required. Here, only the system matrices  $\mathbf{A}_{\theta_O}$  and  $\mathbf{B}_{\theta_O}$  vary dependent on the engine operating point.

## Robustness Analysis

For the analysis of the robustness, the plant was linearised in the steady-state operating points corresponding to the setpoint maps, see Section 6.2.2. Using the linearised system, an LQG controller was designed with the  $\mathbf{Q}$  and  $\mathbf{R}$  matrices, which were used for the extended Kalman filter and the LQ regulator. Of course, robust stability of this linearised system does not guarantee the robustness of the overall nonlinear system. However, sufficiently high gain and phase margins in all operating points at least indicate that no major stability problems are to be expected.

The design of the LQG controller is well documented in the literature (see [26] or [91]) and shall not be discussed here. The Nyquist plot of the open loop gain  $L_e(s)$  for all tested operating points is shown in Figure 6.6.  $L_e(s)$  is the product of the plant transfer function  $G(s)$  and the controller transfer function  $K(s)$ :

$$\begin{aligned} L_e(s) &= G(s) \cdot K(s) \\ &= \left( \mathbf{C} [s\mathbf{I} - \mathbf{A}]^{-1} \mathbf{B} + \mathbf{D} \right) \cdot \left( \mathbf{G} [s\mathbf{I} - \mathbf{A} + \mathbf{B}\mathbf{G} + \mathbf{H}\mathbf{C}]^{-1} \mathbf{H} \right) \end{aligned} \quad (6.21)$$

$\mathbf{A}$ ,  $\mathbf{B}$ ,  $\mathbf{C}$ ,  $\mathbf{D}$  are the system matrices of the linearised plant. Notice that the plant is extended with an integrator element as has been discussed in the LQ regulator design section above.  $\mathbf{G}$  denotes the state feedback gain matrix of the LQ



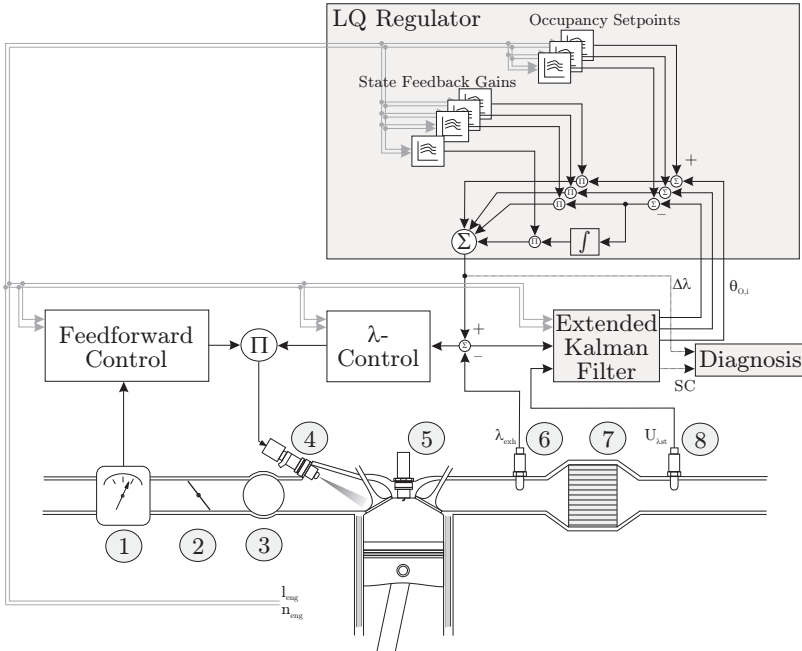


Figure 6.5: Sketch of the entire realised control system including the LQ regulator and the extended Kalman filter. The numbers refer to the following components: 1 Air mass flow meter; 2 Throttle; 3 Intake manifold; 4 Fuel injection valve; 5 Spark plug; 6  $\lambda$  sensor upstream; 7 TWC; 8  $\lambda$  sensor downstream.

regulator.  $\mathbf{H}$  is the observer gain matrix of the Kalman filter. Notice that  $\mathbf{G}$  and  $\mathbf{H}$  have been obtained from the reduced state-space models as described in the corresponding sections above and in Chapter 5. In order to fit into (6.21), zero elements were added according to the omitted feedback signals in the design.

From the Nyquist plot, it can be seen that ample robustness margins are obtained for all operating points. From the point of view of stability, no major problems are expected.

### Adaptation to TWC Ageing

The dynamics of the TWC change with ageing because of the decreasing storage capacity. This has to be taken into account, both for the design of the

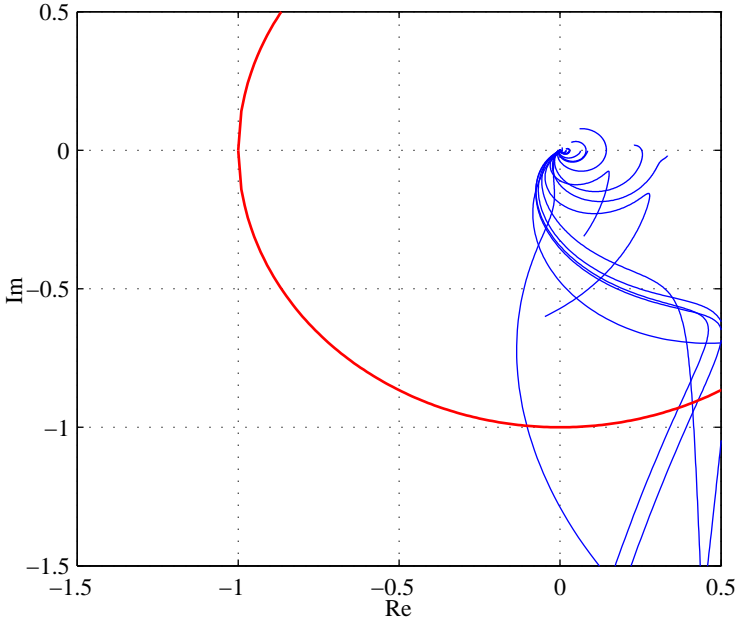


Figure 6.6: Nyquist diagram for all operating points of the loop gain function  $L_e(s)$ . The range of operating points includes engine speeds between 800 and 4000 rpm, and engine loads between 15 and 60%.

setpoint maps and the maps of the state feedback gains. Hence, these maps have to be extended by one dimension, to include the dependence on the storage capacity. Another approach might be to include this dependence by means of heuristic linear or quadratic functions. The choice depends on the resources which are available in the control unit. Since the storage capacity only changes slowly, no problems are expected from the adaptation. In the experiments presented here, the former approach was used.

### 6.3.2 Controller Performance on the Engine Test Bench

To illustrate the performance of the TWC controller, the results are presented in three parts. In the first part, engine load steps and a fuel cut-off sequence with an adjacent oxygen depletion phase is shown both with the  $\lambda$  controller only and with the TWC controller in comparison. In the second part, an example of

an FTP cycle measurement is presented. Finally, the accumulated amounts of NO, HC, and CO obtained with differently aged TWCs and differently balanced control setpoints are compared to the ones obtained from a  $\lambda = 1$  strategy. The experiments presented in the first and in the second parts have been performed with a moderately aged TWC (at 900 °C, see Section 2.5).

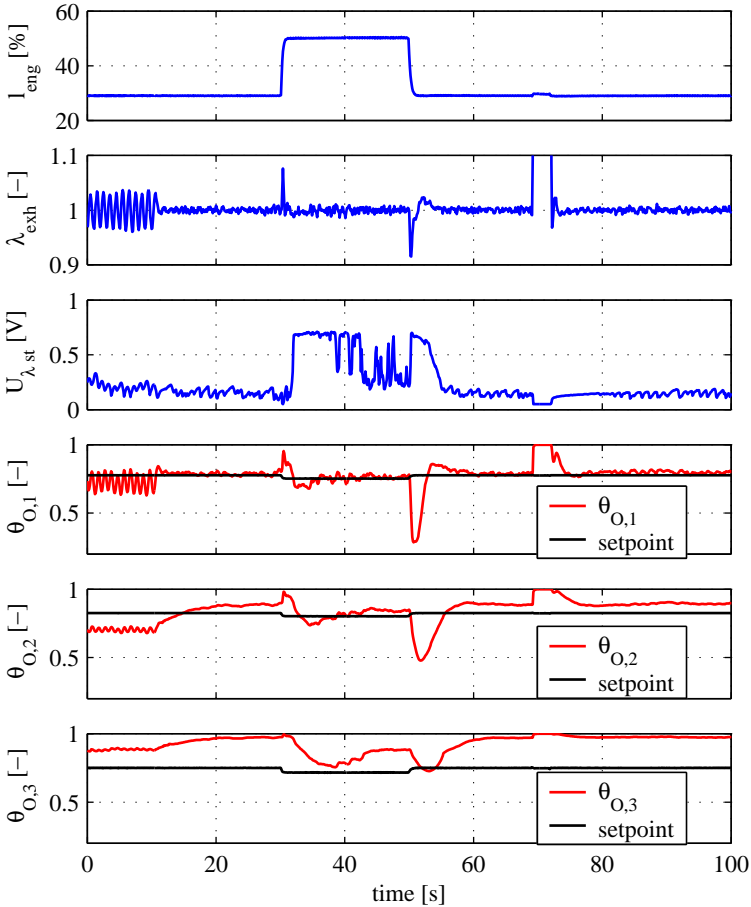


Figure 6.7: Performance with a  $\lambda$  controller only during load steps and a fuel cut-off. The test has been performed at an engine speed of 1500 rpm with a moderately aged TWC (at 900 °C, see Section 2.5).

## 6 Control of a Three-Way Catalytic Converter

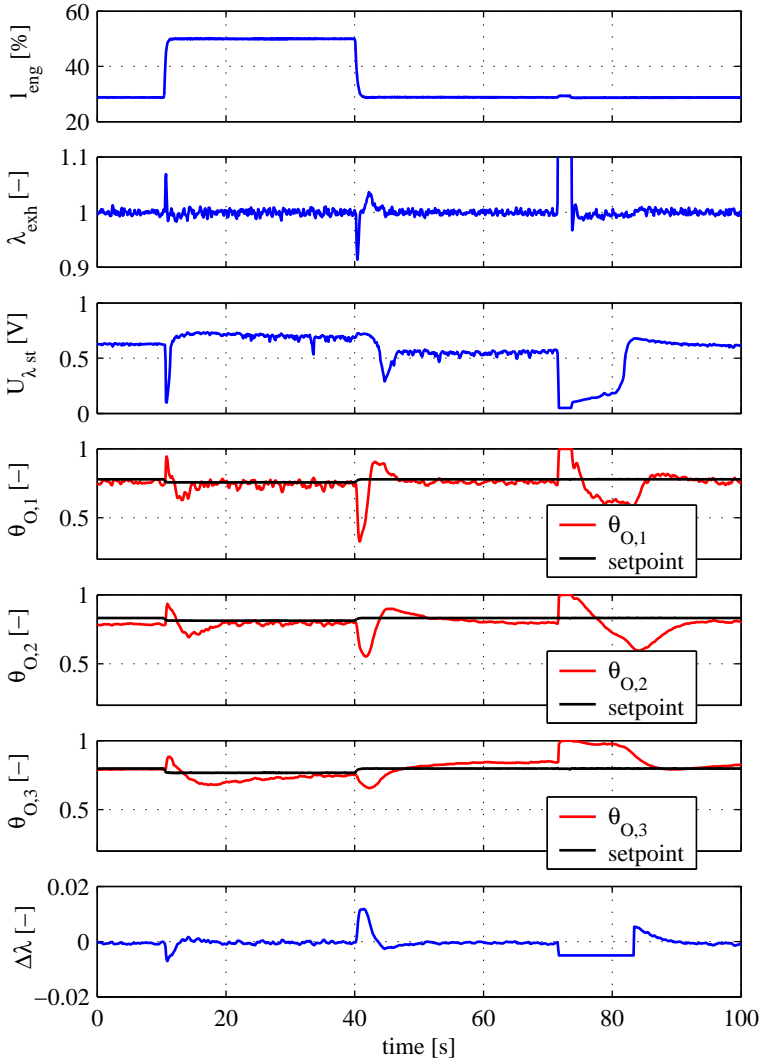


Figure 6.8: Performance of the TWC controller during load steps and a fuel cut-off. The test has been performed at an engine speed of 1500 rpm with a moderately aged TWC (at 900 °C, see Section 2.5). The ratio of the conversion efficiencies  $q_{O_2}/q_{CO}$  was 1.

Figure 6.7 shows the engine load, the raw exhaust  $\lambda$ , the switch-type  $\lambda$  sensor voltage, and the oxygen occupancies of the three cells during two load steps and a fuel cut-off. Only a  $\lambda = 1$  strategy was applied, i. e., no TWC controller was used. For comparison, the setpoints of a TWC controller with a desired conversion ratio  $q_{O_2}/q_{CO}$  of 1 are shown, as well. In order to obtain a well-balanced TWC,  $\lambda_{exh}$  was excited with a high frequency during the first 10 seconds. At 30 s, the load was switched from 30 to 50% and back to 30% at 50 s. These load changes were imposed by a step of the throttle angle. At 70 s, the fuel was cut during approximately 10 s to emulate a fuel cut-off. The whole procedure was performed at an engine speed of 1500 rpm. Since the dynamics of the intake manifold and the wall-wetting cannot be perfectly compensated, a lean peak occurs at a sudden increase of the load. The fuel path dynamics cannot follow the air, which flows directly into the cylinder. The opposite is true, when a load step to a lower level is imposed. A peak of  $\lambda_{exh}$  to the rich side occurs. When the fuel is cut-off,  $\lambda_{exh}$  of course increases, theoretically to infinity.

It can be observed that the wide-range  $\lambda$  sensor obviously exhibits a slight rich offset. Hence, the  $\lambda$  controller shifts the balance slightly to the lean side, which results in a switch-type  $\lambda$  sensor voltage well below 300 mV and leads to high oxygen storage levels. Notice that the level of the first cell seems to be quite robust against the  $\lambda$  offset, whereas the second and particularly the third cells are more sensitive. This can be explained with the fact that in the first cell, still reasonable amounts of all species, i. e.,  $O_2$ ,  $CO$ , and  $H_2$  are present. This is not the case in the following cells, which leads to a considerably increased ratio between the oxygen storage and the oxygen depletion reaction rates under lean operation or vice versa under rich operation. This effect is more pronounced with fresh TWCs, which makes them particularly hard to be controlled stably. Notice that this is not reflected by a model which consists of only one single cell. A further interesting phenomenon is the dependence of the oxygen occupancies on the engine load. Especially the occupancy of the third cell stabilises at a lower level, when the engine is operated at a higher load. This is also reflected in the setpoint maps, see Figure 6.4. Notice however, that a part of this effect might also be caused here by a load dependent  $\lambda$  sensor offset. Since the TWC is generally balanced slightly lean in this example, the effect of the fuel cut-off is rather limited. The oxygen occupancies of all three cells converge relatively fast to the value before the fuel cut-off occurred. However, these levels are quite high, so the test with this configuration is not very meaningful.

Figure 6.8 shows the same test as above, with load changes and a fuel cut-off. This time, the TWC controller is in use. Therefore, also the output signal of the controller,  $\Delta\lambda$  is depicted. Generally, the balance of the TWC is considerably improved as compared to before. This clearly shows that the TWC controller

can make up for offsets of the upstream wide-range  $\lambda$  sensor. The disturbances are damped reasonably well. The tracking behaviour is good, even after the fuel cut-off, where the desired state is recovered after approximately 20 s. This is mainly achieved by the feedforward controller. From  $\Delta\lambda$  it can be seen that the TWC is operated 0.5% rich during approximately 15 s after resetting the fuel injection. Notice that the oxygen occupancies of cells 1 and 2 are considerably decreased during TWC recovery. If the LQ regulator was used during this period, both cells would be tightly controlled, leading to a very slow recovery of cell 3. As soon as the regulator is activated again, i. e., at approximately 85 s, the occupancies of cells 1 and 2 quickly converge to the setpoints.

All in all, it can be stated that the controller performs well, both during load steps and after fuel cut-offs. Similar results are obtained at other operating points. With this, the controller is ready for an assessment, where its performance is tested on differently aged TWCs in FTP cycles.

The data for the FTP cycles, which have been used in this investigation, were recorded from a vehicle with a manual transmission. As a consequence, a considerable number of fuel cut-offs occur. Thereby, two main challenges arise. First, when the cut-off occurs during a gear-shift sequence, the closing of the clutch and simultaneous increase of the load leads to a sudden increase of the air mass flow, which may cause a lean peak, as has been demonstrated above. If a fuel cut-off occurred because of the sudden release of the gas pedal before opening the clutch, the lean peak enters a TWC, which is considerably filled with oxygen. This may lead to a lean break through, which goes hand in hand with an NO peak at the TWC outlet. The second problem is the fuel cut-off because of a deceleration phase before a stand-still of the vehicle. In that case, the oxygen has to be depleted during engine idle operation, where the combustion is relatively bad and only a small mass throughput is present. Hence, the oxygen depletion is very slow. Moreover, it is natural that after the standstill, a sudden acceleration occurs, which is connected with several gear shifts. This brings us back to the first problem. It can be said that the FTP cycle with a vehicle equipped with manual transmission is suitable to challenge both the (input) disturbance rejection and the tracking properties of the TWC controller.

Figures 6.9 and 6.10 show the performance of the TWC controller during the last part of an FTP cycle. In Figure 6.9, the  $\lambda$  sensor signals and the occupancies of O and CO are depicted. Figure 6.10 shows the corresponding TWC control output signals, the concentrations of NO, HC, and CO, and the temperatures upstream and downstream of the TWC. For reference, the engine speed signal is shown in both figures. The TWC in use was moderately aged (at 900 °C, see Section 2.5). The TWC control setpoints were adjusted to a conversion ratio  $q_{O_2}/q_{CO}$  of 1.

The tracking behaviour of the controller is generally good. However, recov-

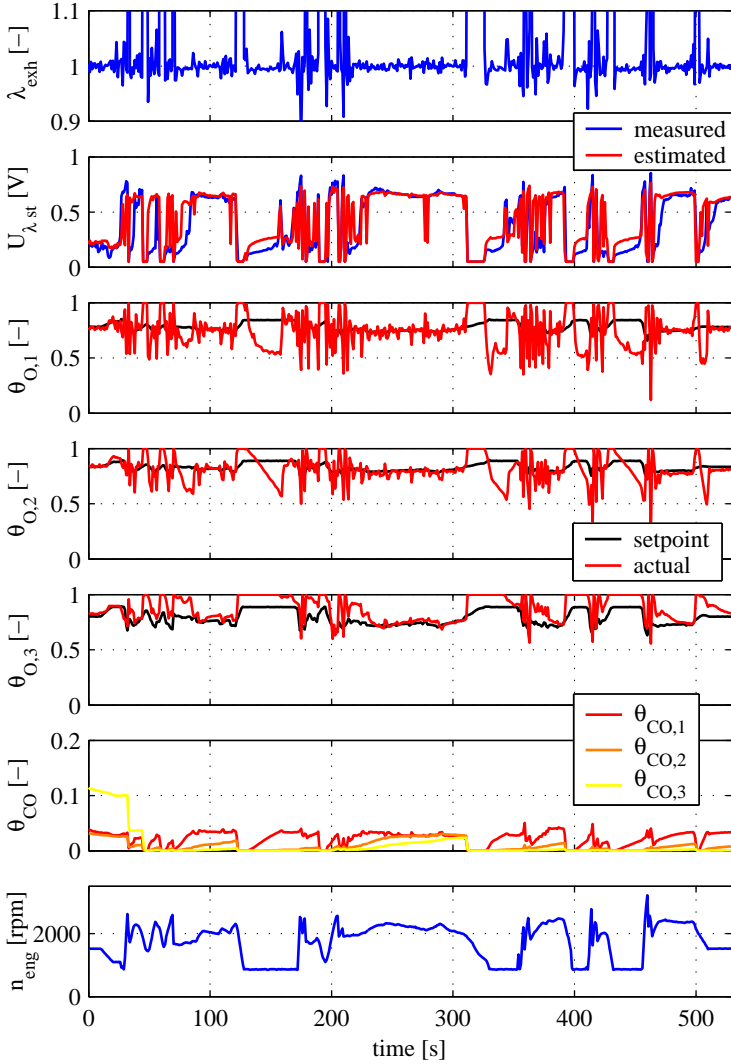


Figure 6.9: Performance of the TWC controller during the last part of an FTP cycle, part I: The raw exhaust  $\lambda$ , the measured and EKF estimated switch-type  $\lambda$  sensor signals, the occupancies of O and CO, and the engine speed are shown. The TWC in use was moderately aged at  $900\text{ }^{\circ}\text{C}$ , see Section 2.5. The ratio of the conversion rates  $q_{\text{O}_2}/q_{\text{CO}}$  was set to 1.

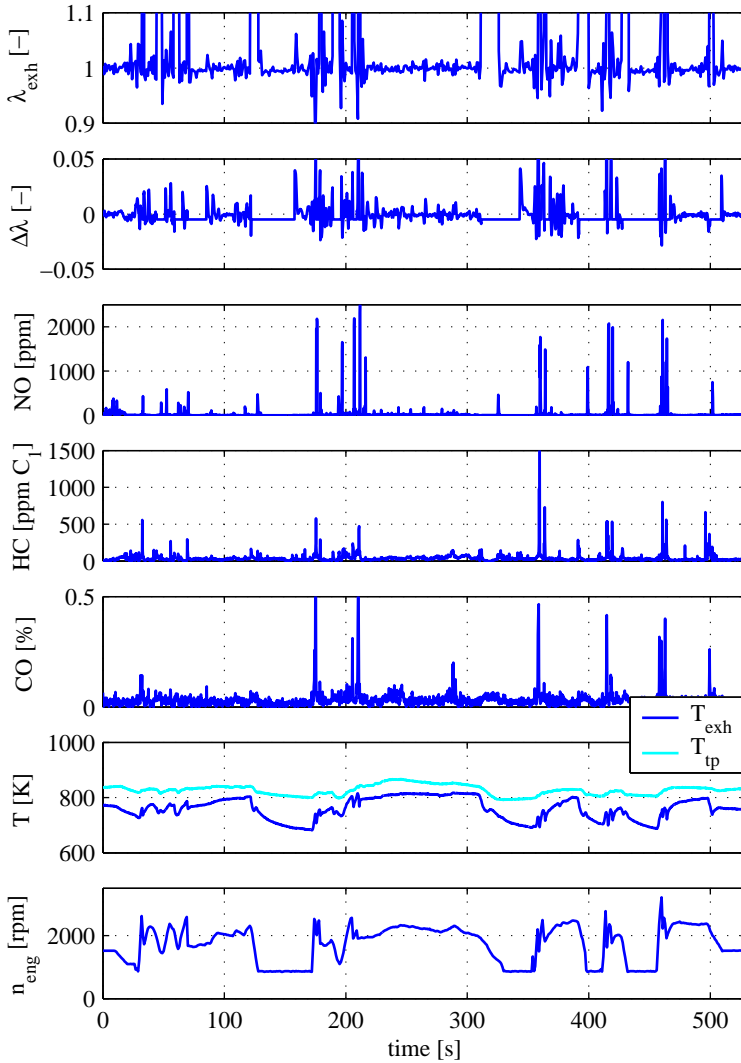


Figure 6.10: Performance of the TWC controller during the last part of an FTP cycle, part II: The raw exhaust  $\lambda$ , the TWC controller output, the concentrations of NO, HC, and CO, the temperatures, and the engine speed are shown. The TWC in use was moderately aged at  $900\text{ }^{\circ}\text{C}$ , see Section 2.5. The ratio of the conversion rates  $q_{\text{O}_2}/q_{\text{CO}}$  was set to 1.



ery of the TWC after fuel cut-offs during engine idle phases is very slow, as has been expected. The oxygen level of the last cell remains very high during engine idle phases after resetting the fuel injection, although a permanent  $\lambda$  offset of 0.5% to the rich side is imposed, as can be seen from the control signal  $\Delta\lambda$ . Since the oxygen occupancies of the first two cells reach considerably low levels during these oxygen depletion phases, a higher  $\lambda$  offset has not been taken into account.

From the concentration measurements, it can be seen that considerable peaks mainly occur, where the oxygen occupancies are far off the setpoint. This confirms that the control of the occupancies is a suitable strategy for the improvement of the conversion rates.

The deactivation or rather the CO occupancies remain low during the entire cycle. This is of course dependent on the storage capacity  $SC$  and thus on the TWC ageing. During the operation in a cycle with frequent fuel cut-offs, this form of deactivation is not expected to cause major problems. However, long constant driving conditions under slightly rich conditions, such as on a (free) motorway, might eventually lead to a higher occupancy of CO in the TWC. The only cure would be to temporarily operate the engine slightly lean. Since the internal states including the deactivation of the TWC are accessible with the here developed extended Kalman filter, the deactivation can be firstly monitored and secondly depleted without emitting high loads of NO. However, this has not been investigated and shall therefore not be discussed further.

The most important question regarding the TWC controller is, of course, whether the conversion rates of NO, HC, and CO can be improved or at least stabilised and adjusted with the weighting factor  $q_{O_2}/q_{CO}$ . For this purpose, a number of FTP cycles (last part only) with differently aged TWCs and with various controller configurations were performed. Since only the instantaneous mole fractions  $y_i$  could be measured, they had to be integrated with the exhaust gas mass flow in order to obtain the accumulated mass:

$$m_{(\text{NO,HC,CO})} = \sum_1^n y_{(\text{NO,HC,CO})} \frac{R_{exh} M_{(\text{NO,HC,CO})}}{\mathfrak{R}} \dot{m}_{exh} h_s \quad (6.22)$$

$R_{exh}$  denotes the specific gas constant of the exhaust gas. A value of 287 J/kgK was assumed.  $h_s$  is the sampling time. Since the  $C_1$  equivalent of the total HC was measured, a molar mass of 14 g/mol was assumed, which corresponds to an H/C ratio of 2. The method for obtaining the total masses of the exhaust gas species is of course quite inaccurate as compared to bag measurements. Especially since mostly small concentrations are measured, only slight drifts of the measurement devices may significantly distort the results. However, the absolute values are not so important here, since only a part of the FTP cycle with a

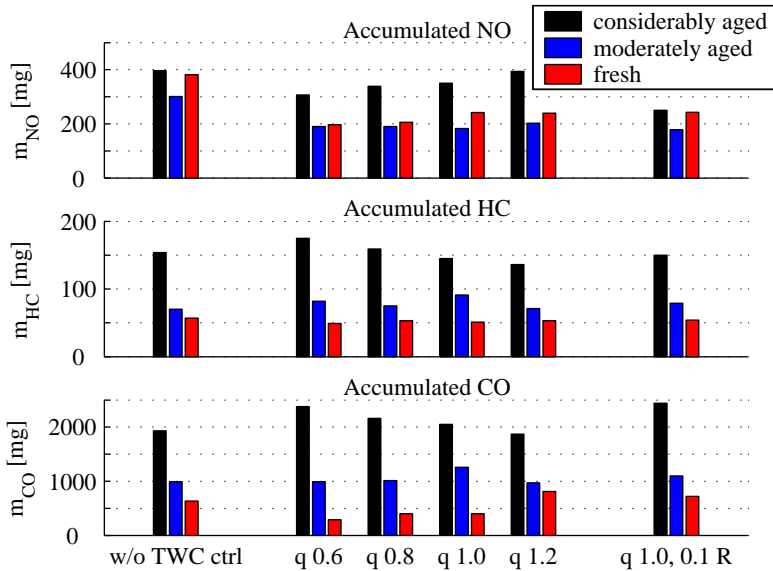


Figure 6.11: Accumulated amounts of NO, HC, and CO during the last part of an FTP cycle. “Considerably aged” and “moderately aged” refers to ageing at 1100 °C and 900 °C, respectively, see Section 2.5. “q” refers to the conversion rate ratio  $q_{O_2}/q_{CO}$ . “0.1 R” refers to the controller with a reduced weighting of the control signal energy.

warm engine could be measured and no underfloor TWC was used. Therefore, the attention should be focused on the comparison between the differently aged TWCs and controller configurations, rather than on the absolute values of the accumulated masses.

The results for three differently aged TWCs (considerably aged, moderately aged, and fresh) are depicted in Figure 6.11. Thereby, six tests were performed with each TWC. In the first test, the cycle was performed with a  $\lambda = 1$  controller only, no TWC controller was in use. In tests 2-5, the LQ regulator was used with conversion rate ratios  $q_{O_2}/q_{CO}$  of 0.6, 0.8, 1.0, and 1.2. The final test was performed with a ratio of 1.0 and a weighting factor for the control variable decreased by one order of magnitude, which leads to a more aggressive controller with a higher bandwidth. As has been mentioned already, only the last (hot) part of the FTP cycle has been recorded with the engine being hot. This was done for two reasons: Firstly, there were no possibilities for climate conditioning in the test cell. Secondly, engine shut-off and restart could not

be performed in a sufficiently reproducible manner. Notice that only a close-coupled TWC was in use.

The results of the considerably aged TWC meet the expectations fairly well. With an increasing conversion rate ratio  $q_{O_2}/q_{CO}$ , the NO emissions increase, whereas the HC and CO emissions decrease. With the TWC controller in use, the performance is slightly better than with a  $\lambda$  controller only. With a more aggressive TWC controller, the NO conversion is significantly improved at the cost of the CO conversion, which is slightly deteriorated. Hence, when choosing a parametrisation, the performance of the second TWC should be taken into account. If this converter is able to oxidise the CO efficiently, a more aggressive controller can be used for the close-coupled TWC.

Considering the results of the moderately aged and the fresh TWCs, the picture is not as clear as for the considerably aged one. The main reason is certainly the very low concentrations, which cannot be covered with sufficient accuracy by the measurement equipment in use. Another reason might be that the reproducibility of the measurements is too low to resolve the small differences between the different controller configurations. This is actually the good news: Less aged TWCs seem to be less sensitive to the controller configuration, at least, when the conversion efficiencies are concerned. However, it can be clearly seen that the use of the TWC controller is very important for the balance of the TWC. Especially the conversion rate of NO is significantly improved when the TWC controller is used. The reason is the generally better adjusted oxygen storage levels, which has already been shown in Figures 6.7 and 6.8. Fresher TWCs only recover very slowly or not at all from a fuel cut-off, if no TWC control strategy is used.

To summarise, it can be stated that TWC controller tuning should mainly focus on more aged converters. Depending on the underfloor TWC (and of course on the emission limits enforced by legislation), a more aggressive strategy can be implemented, which improves the NO conversion at the cost of the CO. As for less aged TWCs, a robust balance is required in order to avoid high oxygen storage levels, which deteriorate the NO conversion. With this prerequisite met, fresher TWCs always perform better with respect to the three critical species addressed by legislation.

### 6.3.3 Sensor Diagnosis

As has been mentioned already, the TWC controller can be used for the diagnosis of the wide-range  $\lambda$  sensor located upstream of the TWC. With an offset of this sensor, the TWC observer states are shifted, which results both in different oxygen occupancies and a modified estimated voltage of the switch-type  $\lambda$  sensor. The extended Kalman filter drives the voltage back to the measured

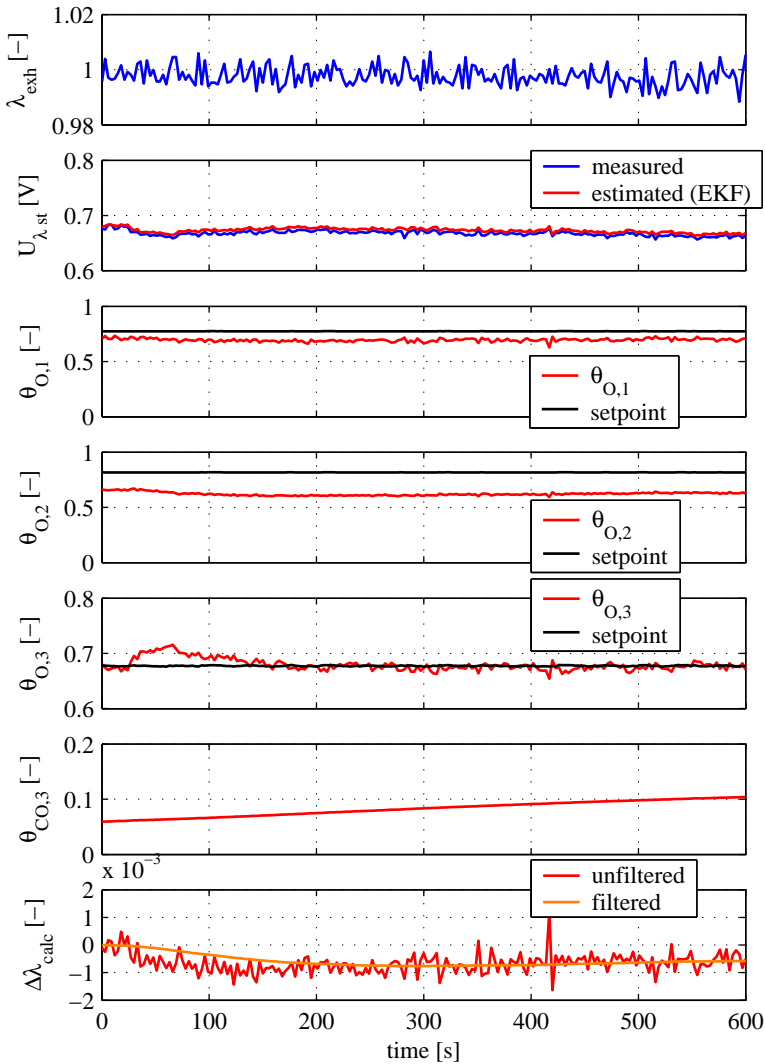


Figure 6.12: Test of the upstream wide-range  $\lambda$  sensor diagnosis without correction of the error occurring from drifting CO occupancies. An offset of +0.1% is added to  $\lambda_{exh}$  at 20 s. The TWC control output  $\lambda_{calc}$  has been normalised to zero at the beginning of the experiment.

value, whereas the controller forces the oxygen occupancies to the setpoints. This is achieved by the integrating part of the TWC controller. Hence, when the new steady-state level is reached, the integrator compensates for the offset of the wide-range  $\lambda$  sensor at the inlet of the TWC. The output of TWC controller can thus be interpreted as the sensor offset, because it is actually the setpoint for the  $\lambda$  controller due to the cascade structure. This procedure was tested on the test bench. The engine was run in steady-state conditions with the TWC controller used. The sensor signal was then distorted by 0.1%. The result is shown in Figure 6.12. The disturbance was imposed at approximately 20 s. Since the  $\lambda$  controller immediately reacts, no excursion can be seen in the  $\lambda_{exh}$ -signal. However, from the switch-type  $\lambda$  sensor signal and from the occupancies, it can be seen that the system was disturbed. The control signal  $\Delta\lambda$ , which has been normalised to 0 at the beginning of the experiment, follows the error within approximately 100 s. The signal has been additionally filtered for illustration. Unfortunately, the initially correctly indicated error drifts away after about 200 s. Notice that this goes hand in hand with the drift of the deactivation of cell 3. The problem is that the setpoints of the oxygen occupancies are not adjusted to the catalyst deactivation, i. e., to the CO occupancies. If these occupancies are increasing as in the example presented here, the controller has to shift the  $\lambda$  to the lean side to maintain the desired oxygen occupancy. Hence,  $\Delta\lambda$  drifts to the lean side. Theoretically, this should be accounted for, if the conversion rate ratios are to be maintained exactly, as can be seen from (6.9). As far as the overall conversion efficiency of the TWC is concerned, this adjustment is not crucial, as has been demonstrated above. However, for the detection of small  $\lambda$  sensor offsets, this cannot be neglected. Therefore, the difference between the actual CO occupancy and its calculated steady-state value has been taken into account using (6.9) and the controller gain  $K_3$  of cell 3 for the correction of the calculated sensor error.

$$\Delta\lambda_{corr} = \Delta\lambda + \frac{\left(-\frac{q_{O_2}}{q_{CO}} \frac{k_1}{2} + \frac{k_6}{2} + k_5\right) \Delta\theta_{CO,3}}{\frac{q_{O_2}}{q_{CO}} \frac{k_1}{2} + k_2 - k_5} K_3 \quad (6.23)$$

The result of this correction is presented in Figure 6.13. Now, the indicated offset remains at the correct value, the sensor offset can be accurately determined with this method. Thus, this method is suitable for the diagnosis of the wide-range  $\lambda$  sensor.

The example presented here is of course somewhat academic, since everything runs under nice steady-state conditions. During transient operation, such a robust and accurate result could hardly be obtained. However, in reality, the

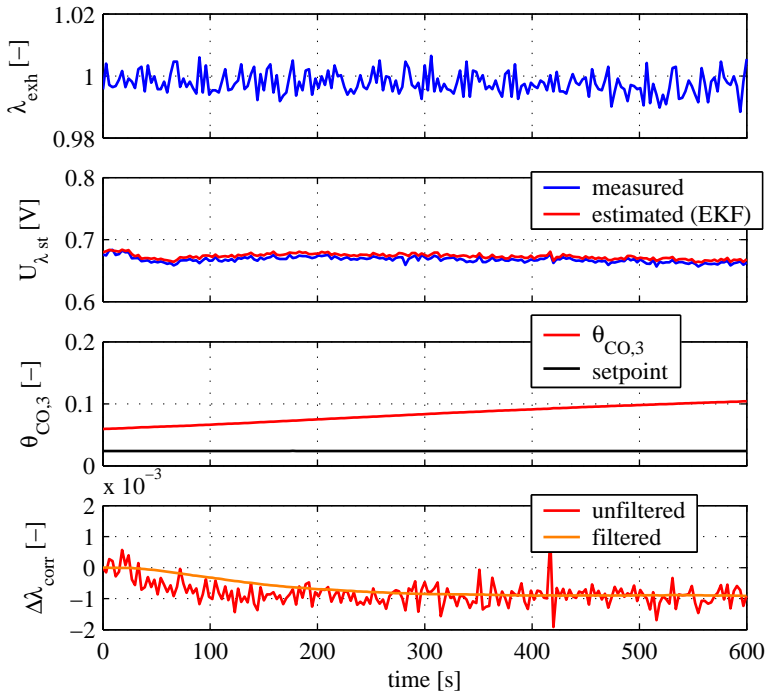


Figure 6.13: Test of the upstream wide-range  $\lambda$  sensor diagnosis with correction of the error occurring from drifting CO occupancies. An offset of +0.1% is added to  $\lambda_{exh}$  at 20 s. The corrected TWC control output  $\lambda_{corr}$  has been normalised to zero at the beginning of the experiment.

goal of the diagnosis is not to detect such small offsets quantitatively as in the example, but rather significant faults occurring from sensor malfunctions.

An open question is of course the reliability of the switch-type sensor, on which the concept is based. This problem has not been investigated here. However, a hint can be given about how it can be approached. The main challenge is to differ between errors of the upstream and the downstream sensors. If there is a satisfactory solution at all, this can only be obtained by investigating the dynamics of the observer, especially the interaction of the sensor signals and the oxygen occupancies. It is likely that this behaviour is differently influenced by distortions of the two sensor signals. If the types of behaviours can be reliably separated, the diagnosis of the downstream sensor can be realised.

## 6.4 Conclusion

A controller for the relative oxygen levels or rather the oxygen occupancies has been derived. Thereby, an LQ regulator with an integrator extension for the third cell has been found to be suitable, since it directly uses the estimated states of the nonlinear observer with a very simple P-control structure for each element. The regulator is adjusted to the engine operating points using LPV. It is implemented in a cascade structure, where it adjusts the setpoint of the  $\lambda$  controller. With the chosen configuration it has been found to exhibit ample robustness margins in a wide range of engine operating points.

The setpoints for the oxygen levels at different engine operating points are obtained from an automated offline procedure, where the ratio between the modelled conversion rates of CO and O<sub>2</sub> can be directly chosen. With this ratio, the TWC can be balanced between lean and rich operation, which directly influences the conversion rates of the critical species, NO, HC, and CO. The conversion rates of CO and NO have been found to be additionally dependent on the variance of the control signal, which can be directly adjusted with the weighting in the cost function of the LQ regulator. For aged TWCs, a more aggressive controller improved the NO conversion significantly, whereas the CO conversion was slightly deteriorated.

For a robust damping of the  $\lambda$  disturbances at the TWC inlet, the second cell has to be controlled tightly during normal operation. In order to provide fast recovery after a fuel cut-off, a feedforward controller had to be implemented. Thereby, the engine is operated slightly rich, until the oxygen occupancy of cell 3 approaches the setpoint.

The controller was tested on the last part of an FTP cycle with frequent fuel cut-offs due to a manual transmission of the vehicle. The accumulated emissions could be slightly reduced downstream of a considerably aged TWC. For fresher converters, especially the NO conversion was substantially improved as compared to a simple  $\lambda$  controller because of a better lean/rich balance. It was found that the conversion rates of the three critical species can be adjusted with two tuning parameters, the ratio between the conversion rates of the modelled CO and O<sub>2</sub>, and with the weighting of the control signal in the quadratic cost function of the LQ regulator.

Since the LQ regulator is extended with an integrator, offsets of the wide-range  $\lambda$  sensors are compensated. Because the control signal is the setpoint for the  $\lambda$  controller, it can be interpreted as this offset under steady-state conditions. This has been successfully tested. A sensor offset of 0.1% could be reliably detected on the engine test bench.





# 7 Conclusions

The increasingly stringent limits for the emission of NO, HC, and CO during the recent years and in the future make an active control mechanism of the TWC indispensable. Additionally, legislation dictates the persistent monitoring of the exhaust gas aftertreatment system including an indication to the driver in case of malfunctions. Both monitoring and control concepts rely on  $\lambda$  sensor information downstream of the TWC. Thereby, these sensor signals can be heavily distorted by the hydrogen concentration in the exhaust gas. This hydrogen concentration in turn is subject to the dynamics of the TWC, which are dependent on the operating condition of the engine and the ageing level of the converter.

In this thesis, a control and diagnosis strategy has been developed which not only accounts for the oxygen storage dynamics, but also predicts the hydrogen concentration levels and their influence on the  $\lambda$  sensors.

Throughout the thesis, only close-coupled TWCs with a wide-range  $\lambda$  sensor upstream and a switch-type  $\lambda$  sensor downstream have been focused on. Underfloor converters have not been considered.

For the investigation of the TWC's dynamic behaviour in terms of storage and exhaust gas composition, a detailed 1-D model has been derived. The model is capable of reflecting well the transient response of the gas components to low-frequency  $\lambda$  excitations for various engine operating points and ageing levels. A special focus has been placed on the components subject to legislation (NO, HC, CO) and significant for the  $\lambda$  sensor outputs ( $O_2$ ,  $H_2$ ). It has been found that apart from the oxygen storage, a rather slow deactivation process has an impact on the dynamics of the TWC, especially under rich engine operation. Thereby, the catalyst surface is slowly covered by hydrocarbons, which leads to a reduced activity of the water-gas shift and the steam-reforming reactions. Hence, the ratio between  $H_2$ , CO, and HC is still changing long after the stored oxygen has been depleted. It has been shown that even the conversion rate of NO can deteriorate with advanced deactivation under rich operation.

In order to determine how the gas components influence the signal of the switch-type  $\lambda$  sensor, a detailed model has been developed, which accounts for the diffusion through the protection layer and the reaction kinetics both on the electrodes and on the electrolyte. The dependence of the sensor signal on the most important species such as CO,  $H_2$ , and HC is reflected accurately. It has

been found that high voltage outputs, which are measured under rich operation, can only be established with the presence of  $H_2$  or  $CO$ , rather than with a shortage of  $O_2$  only. In other words, the chemical potential of the oxidation of rich species drives the sensor voltage output during rich operation.

From the results of the detailed sensor and TWC models, it has been concluded that a control and diagnosis strategy has to account for the oxidation or production of  $H_2$  in the TWC and its influence on the switch-type  $\lambda$  sensor. Therefore, a simplified control-oriented model has been deduced from the complex models. The model accounts for the oxygen storage and the TWC deactivation by a  $CO$  storage mechanism. Thereby, three components are considered, namely  $O_2$ ,  $CO$ , and  $H_2$ . The  $NO_x$  are incorporated in the  $O_2$  concentration, whereas the  $HC$  are included in  $CO$ . Additionally, the temperatures are calculated. The model consists of three consecutive cells which account for the axial distribution of the state variables. The switch-type  $\lambda$  sensor has been modelled by means of an algebraic function. The inlet gas concentrations to the TWC have been calculated by means of a simple exhaust gas model derived from stoichiometric considerations and heuristic functions obtained from measurements. The complete model is capable of very accurately reflecting the transient behaviour of the system in a wide range of operating points and TWC ageing levels.

The control-oriented model has been used for the development of an extended Kalman filter, which serves as an observer of states such as the oxygen storage levels and for the online identification of the storage capacity. The former is used for control, the latter for diagnosis purposes and for the adaptation of the controller. The online estimation algorithm has been found to perform robustly, the storage capacity of differently aged TWCs was identified with arbitrary initial values within a few hundred seconds.

For the control of the oxygen storage levels, an LQ regulator with an integrator extension has been designed. The controller has been embedded in a cascade structure. Hence, the TWC-controller output is the setpoint for the  $\lambda$ -control system. The nonlinearity has been accounted for by means of LPV (Linear Parameter Variation). The LQ regulator design has been preferred because of its simple controller structure and the transparent meaning of the design parameters. A TWC controller mainly follows two goals: First, disturbances at the inlet occurring from temporary mismatches of the fuel and air path dynamics, which cannot be handled by the wall-wetting compensator or  $\lambda$ -feedback controller should be damped. Secondly, the TWC should be kept in a state where heavy disturbances can be buffered and any offsets of the wide-range  $\lambda$  sensor located upstream can be compensated for. A substantially increased weighting of the oxygen storage level of the second cell brought the best results in terms of stability especially of less aged TWCs and of emissions.

However, a feedforward strategy had to be implemented to allow a sufficiently fast depletion of the stored oxygen after a fuel cut-off. For the setpoints for the regulator, a procedure has been developed which automatically creates setpoint maps. Thereby, only one parameter has to be specified which adjusts the ratio between the conversion rates of reducing and oxidising species. With a second tuning parameter, the signal energy of the control variable can be adjusted. The signal energy has been found to directly influence the conversion rates of CO and NO.

The controller brought an improvement of the conversion rates of NO, CO, and HC for all ageing levels, as compared to a  $\lambda = 1$  strategy. The better balance of fresher TWCs resulted in a significantly improved conversion rate of NO. When an aggressive controller was used, the NO emissions of a considerably aged TWC could be roughly cut in half at the cost of a 20% increase of the CO and with no impact on the HC emissions. A strategy has been developed to estimate the offset of the upstream wide-range  $\lambda$  sensor using the integrator extension of the LQ regulator. An offset of 0.1% could be reliably detected on the engine test bench.

The strategy presented here offers a variety of starting points for further developments. Some of the most obvious which are recommended by the author are listed in the following:

- *Extension to the underfloor TWC:* Modern exhaust gas aftertreatment systems consist of two TWCs. An extension to the second converter is straightforward. Depending on its conversion capabilities, the controller can be parameterised accordingly.
- *Ageing of the downstream switch-type  $\lambda$  sensor:* Similar to an offset of the upstream  $\lambda$  sensor, a changing behaviour of the device influences the performance and behaviour of the extended Kalman filter. This should be properly analysed, since it might offer the possibility of differentiating between distortions of the signals of the two  $\lambda$  sensors.
- *Estimation of the NO and HC concentrations:* The simple and physically transparent model structure offers the possibility of extensions. It is very likely that the model can be extended to accurately estimate the NO and HC concentrations without substantially increasing the consumption of CPU power. With such an extension, at least the diagnosis could be directly based on the conversion rates instead of the storage capacity.
- *Temperature sensor downstream of the TWC:* With a temperature sensor located downstream of the TWC, the Kalman filter could be supported

## 7 Conclusions

with an additional signal. This would improve the robustness and reliability of the diagnosis and definitely clear the path towards diagnosis of the downstream  $\lambda$  sensor.

# A Determination of $\lambda$ from Exhaust Gas Components:

## A.1 Evaluation Procedure for the Exhaust Gas Measurements

The following problems arise when evaluating the data which has been recorded with the equipment described in Section 2.2

- The measurements of CO/CO<sub>2</sub> only produce the concentrations scaled to the dried exhaust gas.
- The NO concentration measurements are distorted because of quenching of the chemiluminescence reaction by H<sub>2</sub>O and CO<sub>2</sub>.
- The sum of the mole fractions measured with the mass spectrometer (H<sub>2</sub>, O<sub>2</sub>, H<sub>2</sub>O, N<sub>2</sub>) is scaled to 1.
- Water and nitrogen calibrations are not accurate. N<sub>2</sub> calibration is performed at a concentration of 99.5%. Water is calibrated with humid air, which is supposed to be saturated at room temperature.

These problems make the following data evaluation procedure necessary:

1. Recalibration of the water and nitrogen concentration measurements at the engine running in steady-state conditions.
2. Calculation of the wet CO/CO<sub>2</sub> concentrations.
3. Calculation of the corrected NO concentration.
4. Rescaling of the mass spectrometer measurements.

### Recalibration of H<sub>2</sub>O, N<sub>2</sub>, and CO<sub>2</sub>

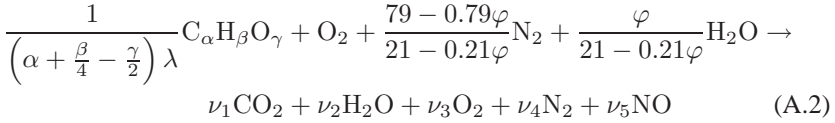
For the recalibration of the H<sub>2</sub>O and N<sub>2</sub> measurements, the engine is run in steady-state conditions at 10% lean from stoichiometry, i. e.,  $\lambda = 1.1$ . Since the measurements are performed downstream of the TWC, it can be assumed

## A Determination of $\lambda$ from Exhaust Gas Components:

that the concentrations of  $\text{H}_2$ ,  $\text{CO}$ , and  $\text{HC}$  are zero. The offset of the  $\lambda$  sensor is basically unknown. However, it is assumed to be quite accurate far lean from stoichiometry and downstream of the TWC. Its maximum offset is assumed to be 0.5%. The  $\lambda$  measured at this point is  $\lambda^{cal}$ . In order to determine the theoretically correct concentrations of  $\text{CO}_2$ ,  $\text{H}_2\text{O}$ ,  $\text{N}_2$ , and  $\text{O}_2$  at this calibration point, a very simple combustion calculation is performed. It is assumed that only  $\text{CO}_2$ ,  $\text{H}_2\text{O}$ ,  $\text{O}_2$ ,  $\text{N}_2$ , and  $\text{NO}$  occur in the exhaust downstream of the TWC at  $\lambda = 1.1$ . The gasoline consists of carbon (C), hydrogen (H) and oxygen (O) at ratios obtained from an analysis performed at the Swiss Federal Laboratories for Materials Testing and Research (EMPA). Traces of N and other compounds are neglected. The composition of the humid air is assumed to be

$$(21 - 0.21\varphi) \cdot \text{O}_2 + (79 - 0.79\varphi) \cdot \text{N}_2 + \varphi \cdot \text{H}_2\text{O} \quad (\text{A.1})$$

where  $\varphi$  is the water concentration in % in the humid air. Thus, the overall combustion reaction can be expressed as follows:



Thereby, the coefficients are

$$\begin{aligned} \nu_1 &= \frac{\alpha}{\left(\alpha + \frac{\beta}{4} - \frac{\gamma}{2}\right) \lambda^{cal}} \\ \nu_2 &= \frac{\frac{\beta}{2}}{\left(\alpha + \frac{\beta}{4} - \frac{\gamma}{2}\right) \lambda^{cal}} + \frac{\varphi}{21 - 0.21\varphi} \\ \nu_3 &= 1 - \frac{1}{\lambda^{cal}} - \frac{1}{2} \nu_5 \\ \nu_4 &= \frac{79 - 0.79\varphi}{21 - 0.21\varphi} - \frac{1}{2} \nu_5 \end{aligned} \quad (\text{A.3})$$

The coefficient for  $\text{NO}$ ,  $\nu_5$ , is obtained from measurements, which are corrected in this point as follows:

$$y_{\text{NO}}^{cal} = y_{\text{NO}}^{meas} (1 + q_{\text{H}_2\text{O}} y_{\text{H}_2\text{O}}^{cal} + q_{\text{CO}_2} y_{\text{CO}_2}^{cal}) \quad (\text{A.4})$$

$q_{\text{H}_2\text{O}}$  and  $q_{\text{CO}_2}$  denote the correction factors for the compensation of the distortion occurring from the quenching of the chemiluminescence reaction in the  $\text{NO}$  measurement device by  $\text{H}_2\text{O}$  and  $\text{CO}_2$ .

As has been shown in Section 2.2, CO<sub>2</sub> is measured in the dehumidified exhaust gas. The relation of the dry and the wet CO<sub>2</sub> mole fractions is

$$y_{\text{CO}_2}^{\text{dry}} = \frac{y_{\text{CO}_2}^{\text{wet}}}{1 - y_{\text{H}_2\text{O}} + y_{\text{H}_2\text{O}}^{\text{dry}}} \quad (\text{A.5})$$

$y_{\text{H}_2\text{O}}^{\text{dry}}$  is the mole fraction of the water in the dehumidified exhaust gas. It corresponds to the saturation concentration of water at 5 °C, which is the operating temperature of the Horiba device.

The mole fractions of CO<sub>2</sub> and H<sub>2</sub>O can be obtained from (A.3) and inserted in (A.5), leading to

$$\begin{aligned} y_{\text{CO}_2}^{\text{dry}} &= \frac{\nu_1}{\sum_{i=1}^5 \nu_i} \cdot \frac{1}{1 - \frac{\nu_2}{5} + y_{\text{H}_2\text{O}}^{\text{dry}}} \\ &= \alpha \left\{ \left( \frac{\beta}{4} + \frac{\gamma}{2} \right) (1 + y_{\text{H}_2\text{O}}^{\text{dry}}) - \frac{\beta}{2} + \dots \right. \\ &\quad \left. + \frac{100(1 + y_{\text{H}_2\text{O}}^{\text{dry}}) - \varphi}{21 - 0.21\varphi} \left( \alpha + \frac{\beta}{4} - \frac{\gamma}{2} \right) \lambda^{\text{cal}} \right\}^{-1} \end{aligned} \quad (\text{A.6})$$

This allows the calculation of a correction factor for the CO<sub>2</sub> concentration, i. e.,

$$y_{\text{CO}_2}^{\text{dry}} = f_{\text{CO}_2} y_{\text{CO}_2}^{\text{meas}} \quad (\text{A.7})$$

From  $\lambda^{\text{cal}}$ , the calibration mole fractions of water, nitrogen, and CO<sub>2</sub> can be calculated:

$$\begin{aligned} y_{\text{H}_2\text{O}}^{\text{cal}} &= \frac{\nu_2(\lambda^{\text{cal}})}{\sum_{i=1}^5 \nu_i(\lambda^{\text{cal}})} \\ y_{\text{N}_2}^{\text{cal}} &= \frac{\nu_4(\lambda^{\text{cal}})}{\sum_{i=1}^5 \nu_i(\lambda^{\text{cal}})} \\ y_{\text{CO}_2}^{\text{cal}} &= \frac{\nu_1(\lambda^{\text{cal}})}{\sum_{i=1}^5 \nu_i(\lambda^{\text{cal}})} \end{aligned} \quad (\text{A.8})$$

## A Determination of $\lambda$ from Exhaust Gas Components:

The calibration mole fraction of NO has already been calculated in (A.4). The sum of the mole fractions obtained from the mass spectrometer ( $\xi_i$ ) is scaled to 1. Notice that there are no hydrogen or hydrocarbons present, hence:

$$\begin{aligned}\xi_{\text{N}_2}^{\text{cal}} &= \frac{y_{\text{N}_2}^{\text{cal}}}{1 - y_{\text{CO}_2}^{\text{cal}} - y_{\text{NO}}^{\text{cal}}} \\ \xi_{\text{H}_2\text{O}}^{\text{cal}} &= \frac{y_{\text{H}_2\text{O}}^{\text{cal}}}{1 - y_{\text{CO}_2}^{\text{cal}} - y_{\text{NO}}^{\text{cal}}}\end{aligned}\quad (\text{A.9})$$

The goal is now to derive correction factors  $f_{\text{H}_2\text{O}}$  and  $f_{\text{N}_2}$  for the water and the nitrogen mole fractions. These will be valid in all operating conditions, since the ion currents are proportional to the partial pressures in the focused operating region, see also Section 2.2.

The sum of corrected fractions has again to be scaled to 1. Hence, the correction factors have to adjust the fractions *after* scaling, they cannot be obtained by simply dividing the measured ( $\xi_i^{\text{meas}}$ ) by the calculated mole fractions ( $\xi_i^{\text{cal}}$ ). The new mole fractions after scaling are

$$\begin{aligned}\xi_{\text{H}_2\text{O}}^{\text{cal}} &= \frac{f_{\text{H}_2\text{O}} \xi_{\text{H}_2\text{O}}^{\text{meas}}}{\xi_{\text{O}_2}^{\text{meas}} + f_{\text{N}_2} \xi_{\text{N}_2}^{\text{meas}} + f_{\text{H}_2\text{O}} \xi_{\text{H}_2\text{O}}^{\text{meas}}} \\ \xi_{\text{N}_2}^{\text{cal}} &= \frac{f_{\text{N}_2} \xi_{\text{N}_2}^{\text{meas}}}{\xi_{\text{O}_2}^{\text{meas}} + f_{\text{N}_2} \xi_{\text{N}_2}^{\text{meas}} + f_{\text{H}_2\text{O}} \xi_{\text{H}_2\text{O}}^{\text{meas}}}\end{aligned}\quad (\text{A.10})$$

Solving for the correction factors yields the desired result:

$$\begin{aligned}f_{\text{H}_2\text{O}} &= \frac{\xi_{\text{O}_2}^{\text{meas}}}{\frac{\xi_{\text{H}_2\text{O}}^{\text{meas}}}{\xi_{\text{H}_2\text{O}}^{\text{cal}}} - \xi_{\text{H}_2\text{O}}^{\text{meas}} \left(1 + \frac{\xi_{\text{N}_2}^{\text{cal}}}{\xi_{\text{H}_2\text{O}}^{\text{cal}}}\right)} \\ f_{\text{N}_2} &= \frac{\xi_{\text{O}_2}^{\text{meas}}}{\frac{\xi_{\text{N}_2}^{\text{meas}}}{\xi_{\text{N}_2}^{\text{cal}}} - \xi_{\text{N}_2}^{\text{meas}} \left(1 + \frac{\xi_{\text{H}_2\text{O}}^{\text{cal}}}{\xi_{\text{N}_2}^{\text{cal}}}\right)}\end{aligned}\quad (\text{A.11})$$

With these correction factors, the scaled mole fractions obtained from the mass



spectrometer can be calculated as follows:

$$\begin{aligned}
\xi_{\text{H}_2} &= \frac{\xi_{\text{H}_2}^{meas}}{\xi_{\text{H}_2}^{meas} + \xi_{\text{O}_2}^{meas} + f_{\text{H}_2\text{O}} \xi_{\text{H}_2\text{O}}^{meas} + f_{\text{N}_2} \xi_{\text{N}_2}^{meas}} \\
\xi_{\text{O}_2} &= \frac{\xi_{\text{O}_2}^{meas}}{\xi_{\text{H}_2}^{meas} + \xi_{\text{O}_2}^{meas} + f_{\text{H}_2\text{O}} \xi_{\text{H}_2\text{O}}^{meas} + f_{\text{N}_2} \xi_{\text{N}_2}^{meas}} \\
\xi_{\text{H}_2\text{O}} &= \frac{f_{\text{H}_2\text{O}} \xi_{\text{H}_2\text{O}}^{meas}}{\xi_{\text{H}_2}^{meas} + \xi_{\text{O}_2}^{meas} + f_{\text{H}_2\text{O}} \xi_{\text{H}_2\text{O}}^{meas} + f_{\text{N}_2} \xi_{\text{N}_2}^{meas}} \\
\xi_{\text{N}_2} &= \frac{f_{\text{N}_2} \xi_{\text{N}_2}^{meas}}{\xi_{\text{H}_2}^{meas} + \xi_{\text{O}_2}^{meas} + f_{\text{H}_2\text{O}} \xi_{\text{H}_2\text{O}}^{meas} + f_{\text{N}_2} \xi_{\text{N}_2}^{meas}} \quad (\text{A.12})
\end{aligned}$$

### Wet CO/CO<sub>2</sub> Concentrations

The CO/CO<sub>2</sub> measurement device only provides concentrations related to the dehumidified exhaust gas. Since water is measured, as well, the CO/CO<sub>2</sub> concentrations related to the wet, i. e., total exhaust can be obtained. However, the calculation is somewhat awkward, since the water concentration has to be obtained from the mass spectrometer measurements, which in turn makes the use of the CO/CO<sub>2</sub> concentrations necessary.

The wet CO/CO<sub>2</sub> mole fractions are calculated as follows:

$$\begin{aligned}
y_{\text{CO}_2}^{wet} &= y_{\text{CO}_2}^{dry} (1 - y_{\text{H}_2\text{O}} + y_{\text{H}_2\text{O}}^{dry}) \\
y_{\text{CO}}^{wet} &= y_{\text{CO}}^{dry} (1 - y_{\text{H}_2\text{O}} + y_{\text{H}_2\text{O}}^{dry}) \quad (\text{A.13})
\end{aligned}$$

The water fraction is obtained from the mass spectrometer measurements. These have to be scaled to the total exhaust gas:

$$\begin{aligned}
y_{\text{H}_2\text{O}} &= \xi_{\text{H}_2\text{O}} (1 - y_{\text{CO}_2}^{wet} - y_{\text{CO}}^{wet} - y_{\text{NO}}^{corr} - y_{\text{HC}}) \\
&= \xi_{\text{H}_2\text{O}} (1 - y_{\text{CO}_2}^{wet} - y_{\text{CO}}^{wet} - \dots \\
&\quad - y_{\text{NO}}^{meas} (1 + q_{\text{H}_2\text{O}} y_{\text{H}_2\text{O}} + q_{\text{CO}_2} y_{\text{CO}_2}^{wet}) - y_{\text{HC}}) \quad (\text{A.14})
\end{aligned}$$

The simplest way to solve for the H<sub>2</sub>O, CO, CO<sub>2</sub>, and NO concentrations, is to start with the water. Inserting (A.13) in (A.14) and solving for the desired water fraction  $y_{\text{H}_2\text{O}}$  yields after some algebra

$$y_{\text{H}_2\text{O}} = \frac{\zeta_1^{\text{NO}} \xi_{\text{H}_2\text{O}} (1 - (\zeta_2^{\text{NO}} y_{\text{CO}_2}^{dry} + y_{\text{CO}}^{dry}) (1 + y_{\text{H}_2\text{O}}^{dry}) - y_{\text{NO}}^{meas} - y_{\text{HC}})}{1 - \zeta_1^{\text{NO}} \xi_{\text{H}_2\text{O}} (\zeta_2^{\text{NO}} y_{\text{CO}_2}^{dry} + y_{\text{CO}}^{dry})} \quad (\text{A.15})$$

## A Determination of $\lambda$ from Exhaust Gas Components:

where

$$\zeta_1^{\text{NO}} = \frac{1}{1 + q_{\text{H}_2\text{O}} y_{\text{NO}}^{\text{meas}}} \quad (\text{A.16})$$

$$\zeta_2^{\text{NO}} = 1 + q_{\text{CO}_2} y_{\text{NO}}^{\text{meas}}. \quad (\text{A.17})$$

With the known water concentration,  $y_{\text{CO}_2}$  and  $y_{\text{CO}}$  can be obtained easily from (A.13).

### Corrected NO Concentration

Now that the  $\text{H}_2\text{O}$  and the wet  $\text{CO}_2$  concentrations are known, the corrected NO concentration can be calculated as follows:

$$y_{\text{NO}}^{\text{corr}} = y_{\text{NO}}^{\text{meas}} (1 + q_{\text{H}_2\text{O}} y_{\text{H}_2\text{O}} + q_{\text{CO}_2} y_{\text{CO}_2}^{\text{wet}}) \quad (\text{A.18})$$

### Rescaling of the Mass Spectrometer Measurements

The sum of mole fractions provided by the mass spectrometer is scaled to 1. Since four species are not measured by this device, the fractions have to be rescaled such that the sum of all species becomes 1. This is done in a straightforward manner:

$$y_i |_{i=\text{H}_2, \text{H}_2\text{O}, \text{N}_2, \text{O}_2} = \xi_i |_{i=\text{H}_2, \text{H}_2\text{O}, \text{N}_2, \text{O}_2} \cdot (1 - y_{\text{CO}_2}^{\text{wet}} - y_{\text{CO}}^{\text{wet}} - y_{\text{NO}}^{\text{corr}} - y_{\text{HC}}) \quad (\text{A.19})$$

## A.2 Error Calculation

The goal of this error calculation is to obtain the maximum error in  $\lambda$ , calculated from the maximum errors of the measurements devices.

Generally, the total maximum error is calculated from the first order Taylor approximation, i. e., for a general function

$$y = f(x_1, x_2, \dots, x_n) \quad (\text{A.20})$$

the total maximum error is calculated from the maximum errors in  $x_i$ , i. e.,  $\Delta x_i$ , as follows:

$$\Delta y = \sum_{i=1}^n \Delta x_i \frac{\partial f}{\partial x_i} \quad (\text{A.21})$$

Hence, the total error of  $\lambda$  calculated from the measured exhaust gas components

$$\lambda = \frac{2y_{\text{CO}_2} + y_{\text{CO}} + 2y_{\text{O}_2} + y_{\text{NO}} + y_{\text{H}_2\text{O}}}{2y_{\text{CO}_2} + 2y_{\text{CO}} + y_{\text{H}_2} + \left(2x + \frac{y}{2}\right) y_{\text{C}_x\text{H}_y} + y_{\text{H}_2\text{O}}}$$

is then

$$\begin{aligned} \Delta\lambda = & \Delta y_{\text{CO}_2} \frac{\partial\lambda}{\partial y_{\text{CO}_2}} + \Delta y_{\text{CO}} \frac{\partial\lambda}{\partial y_{\text{CO}}} + \Delta y_{\text{O}_2} \frac{\partial\lambda}{\partial y_{\text{O}_2}} + \Delta y_{\text{NO}} \frac{\partial\lambda}{\partial y_{\text{NO}}} \dots \\ & + \Delta y_{\text{H}_2\text{O}} \frac{\partial\lambda}{\partial y_{\text{H}_2\text{O}}} + \Delta y_{\text{H}_2} \frac{\partial\lambda}{\partial y_{\text{H}_2}} + \Delta y_{\text{HC}} \frac{\partial\lambda}{\partial y_{\text{HC}}}. \end{aligned} \quad (\text{A.22})$$

The maximum mole fraction errors of the exhaust gas components  $\Delta y_i$  have to be calculated following the evaluation procedure described in the previous section. This is done using the “fundamental” errors, i. e., measurement errors, which are:

**Errors in the gasoline analysis** The ratio of the species in the gasoline, i. e., C:H:O, is  $\alpha:\beta:\gamma$ . The errors are thus  $\Delta\alpha$ ,  $\Delta\beta$ , and  $\Delta\gamma$ .

**Errors in the air composition** The composition of the air entering the cylinder is not exactly known. The errors are thus  $\Delta y_{\text{O}_2}^{\text{air}}$ ,  $\Delta y_{\text{N}_2}^{\text{air}}$ , and  $\Delta y_{\text{H}_2\text{O}}^{\text{air}}$ .

**Error in the  $\lambda^{\text{cal}}$**  The water and nitrogen concentrations are calibrated at an operating point of the engine, whose accuracy is dependent on the  $\lambda$  sensor. The maximum error of this sensor in the calibration point, i. e., 10% lean of stoichiometry, is  $\Delta\lambda^{\text{cal}}$ .

**Error in the temperature of the CO/CO<sub>2</sub> device** The exhaust gas is dehumidified by cooling the exhaust and removing condensed water by a rotating drain separator. It is assumed that the dehumidified air is saturated with water at the cooling temperature. This temperature is not exactly known, its maximum error is  $\Delta T^{\text{cool}}$ . The error of the water concentration in the dehumidified exhaust, i. e.,  $\Delta y_{\text{H}_2\text{O}}^{\text{dry}}$ , can be calculated from Antoine’s law, see Section 2.2.

**Error in the exhaust gas measurements** The errors of exhaust gas measurements depend on the stability, i. e., drift of the measurements on the calibration gas, on the linearity of the measurement device, on the ambient conditions, and on the data communication from the device to the data collecting computer. All these influences are collected in the total errors of the exhaust gas components. Notice that these are the errors of the absolute measurements, i. e., of the dry mole fractions of CO and

## A Determination of $\lambda$ from Exhaust Gas Components:

$\text{CO}_2$  and of the scaled mole fractions of the mass spectrometer. The errors are thus  $\Delta y_{\text{NO}}$ ,  $\Delta y_{\text{HC}}$ ,  $\Delta y_{\text{CO}}^{\text{dry}}$ ,  $\Delta y_{\text{CO}_2}^{\text{dry}}$ ,  $\Delta \xi_{\text{H}_2}$ ,  $\Delta \xi_{\text{O}_2}$ ,  $\Delta \xi_{\text{H}_2\text{O}}$ , and  $\Delta \xi_{\text{N}_2}$ .

The total errors in (A.22) have to be determined from the known errors following the data evaluation process and applying (A.21). Hence, the total errors  $\Delta y_{\text{H}_2\text{O}}$ ,  $\Delta y_{\text{H}_2}$ , and  $\Delta y_{\text{O}_2}$  have to be calculated using (A.9), (A.11), and (A.12).  $\Delta y_{\text{CO}}$  and  $\Delta y_{\text{CO}_2}$  are obtained using (A.13).  $\Delta y_{\text{NO}}$  and  $\Delta y_{\text{HC}}$  are known and can be inserted directly. The calculation of the errors is straightforward. The derivation of the complete formalism requires a lot of awkward algebra, which can be easily obtained using a tool such as Maple or similar. A much more convenient method is to calculate the derivatives in (A.22) numerically.

## B TWC Model

### B.1 Derivation of the Mass Balance Equation

The mass balance equations of the TWC model contain a somewhat unexpected term at the end, which equalizes the slight error which is being made by not applying a consistent diffusion model, such as the Stefan-Maxwell equations. The mass balance for the gas channel (3.1) is repeated here for convenience:

$$\begin{aligned} \rho_g \varepsilon \frac{\partial w_i}{\partial t} &= \varepsilon D_{eff} \frac{\partial^2 w_i}{\partial z^2} - \frac{\dot{m}}{A_{cs}} \frac{\partial w_i}{\partial z} - D_i A_{geo} (\rho_g w_i - \rho_{wc} v_i) \\ &\quad + w_i \sum_i D_i A_{geo} (\rho_g w_i - \rho_{wc} v_i) \end{aligned}$$

The first term on the right-hand side is the diffusion term, followed by the convection term and a source term, which accounts for the radial diffusion.

Generally, the mass balance for one species reads as follows (without axial diffusion):

$$\begin{aligned} \frac{\partial m_i}{\partial t} &= \dot{m}_i(z) - \dot{m}_i(z + dz) - \Delta \dot{m}_i(z) \\ &= -\frac{\partial \dot{m}_i}{\partial z} dz - \Delta \dot{m}_i(z) \end{aligned} \quad (\text{B.1})$$

Thereby,  $\Delta \dot{m}_i(z)$  denotes the mass transfer in the radial direction:

$$\Delta \dot{m}_i(z) = D_i A_{geo} (\rho_g w_i - \rho_{wc} v_i) \quad (\text{B.2})$$

Expressing the mass of species  $i$ ,  $m_i$ , with the mass fraction  $w_i$ , the mass balance becomes:

$$\begin{aligned} \frac{\partial(mw_i)}{\partial t} &= -\frac{\partial(\dot{m}w_i)}{\partial z} dz - \Delta \dot{m}_i(z) \\ m \frac{\partial w_i}{\partial t} + w_i \frac{\partial m}{\partial t} &= -\dot{m} \frac{\partial w_i}{\partial z} dz - w_i \frac{\partial \dot{m}}{\partial z} - \Delta \dot{m}_i(z) \end{aligned} \quad (\text{B.3})$$

When the balances of all species are summed, the total mass balance is ob-

tained:

$$m \frac{\partial (\sum_i w_i = 1)}{\partial t} + \frac{\partial m}{\partial t} = -\dot{m} \frac{\partial (\sum_i w_i = 1)}{\partial z} dz - \frac{\partial \dot{m}}{\partial z} dz - \sum_i \Delta \dot{m}_i(z)$$

$$\frac{\partial m}{\partial t} = -\frac{\partial \dot{m}}{\partial z} dz - \sum_i \Delta \dot{m}_i \quad (\text{B.4})$$

Inserting the total mass balance (B.4) in the one for the species  $i$ , (B.3) leads to

$$m \frac{\partial w_i}{\partial t} + w_i \left[ -\frac{\partial \dot{m}}{\partial z} dz - \sum_i \Delta \dot{m}_i(z) \right] =$$

$$-\dot{m} \frac{\partial w_i}{\partial z} dz - w_i \frac{\partial \dot{m}}{\partial z} dz - \Delta \dot{m}_i(z)$$

$$m \frac{\partial w_i}{\partial t} = -\dot{m} \frac{\partial w_i}{\partial z} dz - \Delta \dot{m}_i(z) + w_i \sum_i \Delta \dot{m}_i(z) \quad (\text{B.5})$$

If the radial mass transfer was consistent, the last term would be zero and drop out.

## B.2 Model Parameters

In the following, all parameters of the TWC model are listed. For the geometry parameters, physically reasonable values were chosen. The values for the reaction enthalpies were obtained from the NIST Chemistry Webbook<sup>1</sup>. The kinetic parameters were obtained from a calibration procedure, which has been described in Section 3.3.3.

Table B.1: Enthalpies of the produced/consumed species.

enthalpy	[kJ/mol]
$\Delta H_{\text{NO}}$	90.3
$\Delta H_{\text{CO}}$	-110.5
$\Delta H_{\text{CO}_2}$	-393.5
$\Delta H_{\text{C}_3\text{H}_6}$	20.4
$\Delta H_{\text{H}_2\text{O}}$	-241.8
$\text{Ce}_2\text{O}_3 + \frac{1}{2}\text{O}_2(\text{g}) \rightarrow 2\text{CeO}_2$	-190.5

<sup>1</sup><http://webbook.nist.gov/chemistry/>

Table B.2: Geometry and material parameters of the TWC model.

Parameter	Description	Unit	Value
$A_{cat}$	Specific catalytic active surface	$\text{m}^2/\text{m}^3$	12500
$A_{cs}$	Catalyst cross-sectional area	$\text{m}^2$	5e-3
$A_{geo}$	Specific geometric catalyst surface	$\text{m}^2/\text{m}^3$	2250
$A_{TWC}$	Outer TWC surface	$\text{m}^2$	0.023
$c_{p,g}$	Specific heat capacity (gas phase)	J/(kgK)	1100
$c_s$	Specific heat capacity (solid phase)	J/(kgK)	500
$D_{eff}$	Gas dispersion coefficient	kg/(ms)	0.1
$D_{chan}$	Diameter gas channel	m	1.5e-3
$D_{wc}$	Washcoat thickness	m	5e-5
$V_{TWC}$	TWC volume	$\text{m}^3$	4.5e-4
$\alpha$	Heat-transfer coefficient TWC $\rightarrow$ exhaust	W/( $\text{m}^2\text{K}$ )	82.3
$\alpha_{TWC}$	Heat-transfer coefficient TWC $\rightarrow$ ambient	W/( $\text{m}^2\text{K}$ )	47.0
$\varepsilon$	Volume fraction of gas phase	-	0.8
$\varepsilon_{wc}$	Washcoat porosity	-	0.4
$\lambda_g$	Heat conductivity gas phase	W/(mK)	0.05
$\lambda_s$	Heat conductivity solid phase	W/(mK)	50
$\rho_s$	Density solid phase	$\text{kg}/\text{m}^3$	7850
$\Sigma_{v,H_2}$	Diffusion volume $\text{H}_2$	$\text{cm}^3/\text{mol}$	6.12
$\Sigma_{v,H_2O}$	Diffusion volume $\text{H}_2\text{O}$	$\text{cm}^3/\text{mol}$	13.1
$\Sigma_{v,CO}$	Diffusion volume CO	$\text{cm}^3/\text{mol}$	18.0
$\Sigma_{v,CO_2}$	Diffusion volume $\text{CO}_2$	$\text{cm}^3/\text{mol}$	26.9
$\Sigma_{v,C_3H_6}$	Diffusion volume $\text{C}_3\text{H}_6$	$\text{cm}^3/\text{mol}$	61.5
$\Sigma_{v,NO}$	Diffusion volume NO	$\text{cm}^3/\text{mol}$	10.6
$\Sigma_{v,O_2}$	Diffusion volume $\text{O}_2$	$\text{cm}^3/\text{mol}$	16.3
$\Sigma_{v,N_2}$	Diffusion volume $\text{N}_2$	$\text{cm}^3/\text{mol}$	18.5

Table B.3: Reaction scheme and parameters of the TWC model.

Reaction	O r1	O r2	s / A (-) / (s <sup>-1</sup> )	E (kJ/mol)
$O_2(g) + 2* \rightarrow 2O^*$	1	1	0.0017	
$2O^* \rightarrow O_2(g) + 2*$	1	-	1.46e12	231.6
$CO(g) + * \rightarrow CO^*$	1	1	0.295	
$CO^* \rightarrow CO(g) + *$	1	-	1.26e5	-6.5
$H_2(g) + 2* \rightarrow 2H^*$	1	1	0.0141	
$2H^* \rightarrow H_2(g) + 2*$	1	-	1.05e15	173.9
$NO(g) + * \rightarrow NO^*$	1	1	0.0127	
$NO^* \rightarrow NO(g) + *$	1	-	8.26e19	116.4
$C_3H_6(g) + 4* \rightarrow C_3H_5^{***} + H^*$	1	1	9.01e-5	
$C_3H_5^{***} + H^* \rightarrow C_2H_6(g) + 4*$	1	1	5.15e1	28.1
$CO^* + O^* \rightarrow CO_2(g) + 2*$	1	1	2.29e9	86.1
$2H^* + O^* \rightarrow H_2O(g) + 3*$	1	1	4.64e11	48.8
$C_3H_5^{***} + 5O^* \rightarrow$ $3CO^* + 2H_2O(g) + H^* + 4*$	1	1	1.25e6	33.5
$NO^* + * \rightarrow N^* + O^*$	1	1	1.74e2	-77.1
$N^* + O^* \rightarrow NO^* + *$	1	1	3.94e2	76.9
$2N^* \rightarrow N_2(g) + 2*$	2	-	2.04e13	116.4
$Ce_2O_3 + \frac{1}{2}O_2(g) \rightarrow 2CeO_2$	1	1	0.00013	
$Ce_2O_3 + H_2O(g) + 2* \rightarrow 2CeO_2 + 2H^*$	1	1	4.02e-6	-90.6
$C_3H_6(g) + 12CeO_2 \rightarrow$ $3CO(g) + 3H_2O(g) + 6Ce_2O_3$	1	1	1.18e10	121.8
$CO(g) + 2CeO_2 \rightarrow CO_2(g) + Ce_2O_3$	1	1	7.22e8	118.1
$H_2(g) + 2CeO_2 \rightarrow H_2O(g) + Ce_2O_3$	1	1	2.51e6	65.5

\* denotes a vacant site on the noble metal. Superscript \* stands for adsorbed species (on the noble metal). The second and the third rows contain the orders of reactants 1 and 2, respectively.



# C Switch-Type Sensor Model

## C.1 Model Parameters

The parameters of the switch-type  $\lambda$  sensor model have been generally obtained from the literature, where available. Model tuning was kept as little as possible.

In Table C.1 the geometry parameter of the sensor model and the boundary conditions are shown. Only one operating point was investigated. All parameters have been obtained in this investigation.

Table C.1: Geometry parameters and boundary conditions.

Parameter	Description	Unit	Value
$A_{\text{electrode}}$	Electrode surface	$\text{m}^2$	1e-4
$A_{\text{sensor}}$	Specific diffusion cross-sectional area	$\text{m}^2/\text{m}^3$	1e5
$d_{\text{diff}}$	Strength diffusion layer	$\mu\text{m}$	10
$\epsilon/q$	Porosity/Tortuosity factor	-	0.01
$L_{\text{electrode}}$	Adsorption capacity	$\text{mol}/\text{m}^2$	1.5e-5
$T_{\text{exh}}$	Exhaust gas temperature	K	915
$p_{\text{exh}}$	Exhaust gas pressure	Pa	1e5
$T_{\text{sensor}}$	Sensor temperature	K	930

Table C.2 shows the kinetic parameters of the electrode model. All parameters have been obtained from the literature, except for the pre-exponential factor of the hydrogen desorption, which was adjusted to reflect the sensitivity of the sensor towards hydrogen more accurately.

Table C.2: Reaction scheme and parameters of the sensor electrode model.

Reaction	O r1	O r2	s / A (-) / (s <sup>-1</sup> )	E (kJ/mol)	source
$O_2(g) + 2* \rightarrow 2O^*$	1	1	0.003		[48]
$2O^* \rightarrow O_2(g) + 2*$	1	-	5e12	215-60 $\theta_O$	[48]
$CO(g) + * \rightarrow CO^*$	1	1	0.84		[48]
$CO^* \rightarrow CO(g) + *$	1	-	1e13	125.6	[48]
$H_2(g) + 2* \rightarrow 2H^*$	1	1	0.05		[48]
$2H^* \rightarrow H_2(g) + 2*$	1	-	5e15	75.4	[48] <sup>1</sup>
$NO(g) + * \rightarrow NO^*$	1	1	0.5		[77]
$NO^* \rightarrow NO(g) + *$	1	-	2.6e8	34.3	[77]
$H_2O(g) + * \rightarrow H_2O^*$	1	1	0.1		[48]
$H_2O^* \rightarrow H_2O(g) + *$	1	-	1e13	45.2	[48]
$CO^* + O^* \rightarrow CO_2(g) + 2*$	1	1	1e15	100-50 $\theta_O$	[48]
$O^* + H^* \rightarrow OH^* + *$	1	1	1e12	10.5	[48]
$OH^* + * \rightarrow O^* + H^*$	1	1	1e8	20.9	[48]
$OH^* + O^* \rightarrow H_2O^* + *$	1	1	9e16	62.8	[48]
$H_2O^* + * \rightarrow OH^* + O^*$	1	1	1.8e13	154.9	[48]
$2OH^* \rightarrow H_2O^* + O^*$	2	-	1e15	51.5	[48]
$NO^* + * \rightarrow N^* + O^*$	1	1	8.3e4	56.5	[77]
$NO^* + N^* \rightarrow N_2(g) + O^* + *$	1	1	2e9	87.8	[71]
$2N^* \rightarrow N_2(g) + 2*$	2	-	3e10	120	[71]

\* denotes a vacant site on the noble metal. Superscript \* stands for adsorbed species (on the noble metal). The second and the third rows contain the orders of reactants 1 and 2, respectively.

In Table C.3 the parameters of the electrolyte model II are presented. Since only one operating point was investigated, the parameters are constant. It is expected that they are dependent on the temperature, when more operating points are considered. Most probably, an Arrhenius Ansatz would cover the temperature dependence sufficiently well.

<sup>1</sup>The original value for A is 1e12 s<sup>-1</sup>. This modification improved the total result substantially.

Table C.3: Parameters of the electrolyte model II.

Parameter	Unit	Value
$k_{f,\text{CO}}/k_f$	-	1e-1
$k_{f,\text{H}}/k_f$	-	1e9
$k_{a,\text{H}}/k_a$	-	5e1

The parameters of the electrolyte model III are presented in Table C.4. Where provided in temperature dependent form, they have been obtained from the literature [67], [75]. Parameters which are constant, have been found in this investigation. Notice that these parameters are based on the assumption that the surface occupancy of vacant sites is 1.

Table C.4: Parameters of the electrolyte model III.

Reaction	Parameter
$\text{CO}^* + \text{O}^\otimes \rightarrow \text{CO}_2(\text{g})$	$4.96\text{e}15 \cdot e^{-312900/\mathfrak{R}T_{\text{sensor}}}$
$\text{CO}_2(\text{g}) \rightarrow \text{CO}^* + \text{O}^\otimes$	$4.48\text{e}-25 \cdot e^{0.0299 \cdot T_{\text{sensor}}}$
$\text{H}^* + \text{OH}^\otimes \rightarrow \text{H}_2\text{O}^* + \otimes$	$3.75\text{e}2 \cdot e^{-66110/\mathfrak{R}T_{\text{sensor}}}$
$\text{H}_2\text{O}^* + \otimes \rightarrow \text{H}^* + \text{OH}^\otimes$	$2.06\text{e}-3 \cdot e^{0.0016 \cdot T_{\text{sensor}}}$
$\text{H}^* + \text{H}_2\text{O}^\otimes \rightarrow \text{H}_2\text{O}^* + \text{H}^\otimes$	$1.47\text{e}6 \cdot e^{-155400/\mathfrak{R}T_{\text{sensor}}}$
$\text{H}_2\text{O}^* + \text{H}^\otimes \rightarrow \text{H}^* + \text{H}_2\text{O}^\otimes$	$6.38\text{e}-7 \cdot e^{0.0110 \cdot T_{\text{sensor}}}$
$\text{O}^* + \otimes \rightarrow \text{O}^\otimes + *$	0.0009
$\text{O}^\otimes + * \rightarrow \text{O}^* + \otimes$	0.0005
$\text{H}_2\text{O}^\otimes + \otimes \leftrightarrow \text{OH}^\otimes + \text{H}^\otimes$	$9.92\text{e}2 \cdot e^{-72400/\mathfrak{R}T_{\text{sensor}}}$
$\text{H}^\otimes + \text{O}^{2-} \leftrightarrow \text{OH}^\otimes$	$1.75\text{e}2 \cdot e^{205500/\mathfrak{R}T_{\text{sensor}}}$
$\text{O}^{2-} + \otimes \leftrightarrow \text{O}^\otimes$	2.9
$\text{H}_2\text{O}(\text{g}) + \otimes \leftrightarrow \text{H}_2\text{O}^\otimes$	$1.96\text{e}-6 \cdot e^{49200/\mathfrak{R}T_{\text{sensor}}}$



# D Observer of a Three-Way Catalytic Converter

## D.1 Model Parameters

The kinetic parameters of the control-oriented TWC model are presented in Table D.1. They have been obtained from the calibration procedure described in Section 5.3. Calibration was performed for all TWCs simultaneously.

The parameters of the switch-type  $\lambda$  sensor model are depicted in Table D.2. The sensor was always heated, the sensor temperature was not controlled under operation. The parameters have been obtained from measurement data using a nonlinear least-squares algorithm.

In Table D.3 the geometry, material, and thermodynamical parameters are shown. Except for  $\alpha_{TWC}$ , which was obtained from the calibration routine, all parameters have been obtained from physical considerations or from the literature.

Table D.1: Reaction scheme and parameters of the control-oriented TWC model.

Reaction	A (s <sup>-1</sup> )	E (kJ/mol)
$\frac{1}{2}\text{O}_2(\text{g}) + * \rightarrow \text{O}^*$	$8.01\text{e}0 \text{ s}^{-1}(\text{mol}/\text{m}^3)^{-1}$	-22.8
$\text{CO}(\text{g}) + \text{O}^* \rightarrow \text{CO}_2(\text{g}) + *$	$1.64\text{e}1 \text{ s}^{-1}(\text{mol}/\text{m}^3)^{-1}$	-0.094
$\text{H}_2(\text{g}) + \text{O}^* \rightarrow \text{H}_2\text{O}(\text{g}) + *$	$5.44\text{e}16 \text{ s}^{-1}(\text{mol}/\text{m}^3)^{-1}$	221.0
$\text{H}_2\text{O}(\text{g}) + * \rightarrow \text{H}_2(\text{g}) + \text{O}^*$	$7.80\text{e}14 \text{ s}^{-1}$	220.0
$\text{CO}(\text{g}) + \eta_{\text{CO}}* \rightarrow \text{CO}^{\eta_{\text{CO}}}$	$3.46\text{e}6 \text{ s}^{-1}$	113.0
$\frac{1}{2}\text{O}_2(\text{g}) + \text{CO}^{\eta_{\text{CO}}*} \rightarrow \text{CO}_2(\text{g}) + \eta_{\text{CO}}*$	$7.93\text{e}9 \text{ s}^{-1}(\text{mol}/\text{m}^3)^{-1}$	173.0
$\eta_{\text{CO}}$	12	

\* denotes a vacant site on the noble metal. Superscript \* stands for adsorbed species.

Table D.2: Parameters of the control-oriented switch-type  $\lambda$  sensor model.

Parameter	Unit	Value
$A_{\lambda st}$	V	0.3
$B_{\lambda st}$	1/ppm	0.5
$C_{\lambda st}$	1/ppm	110
$D_{\lambda st}$	1/ppm	0.099
$E_{A,\lambda st}$	V	0.061
$E_{E,\lambda st}$	J/mol	-3000
$F_{\lambda st}$	V	0.085

Table D.3: Geometry, material, and thermodynamic parameters of the control-oriented TWC model.

Parameter	Description	Unit	Value
$A_{geo}$	Specific geometric catalyst surface	$m^2/m^3$	2250
$c_{p,g}$	Specific heat capacity (gas phase)	J/(kgK)	1100
$c_s$	Specific heat capacity (solid phase)	J/(kgK)	500
$D_{eff}$	Gas dispersion coefficient	kg/(ms)	0.1
$D_{chan}$	Diameter gas channel	m	$1.5e-3$
$V_{TWC}$	Catalytic converter volume	$m^3$	$4.5e-4$
$\alpha$	Heat-transfer coefficient TWC $\rightarrow$ exhaust	W/( $m^2K$ )	82.3
$\alpha_{TWC}$	Heat-transfer coefficient TWC $\rightarrow$ ambient	W/( $m^2K$ )	47.0
$\varepsilon$	Volume fraction of gas phase	-	0.8
$\lambda_s$	Heat conductivity solid phase	W/(mK)	50
$\rho_s$	Density solid phase	$kg/m^3$	7850
$\phi_{H_2/CO}$	H <sub>2</sub> /CO ratio (raw exhaust)	-	0.25
$a_{\eta_{comb}}$	Coefficient exhaust gas model	-	$1.765e-2$
$b_{\eta_{comb}}$	Coefficient exhaust gas model	1/K	$-1.26e-5$
$\Sigma_{v,H_2}$	Diffusion volume H <sub>2</sub>	$cm^3/mol$	6.12
$\Sigma_{v,CO}$	Diffusion volume CO	$cm^3/mol$	18.0
$\Sigma_{v,O_2}$	Diffusion volume O <sub>2</sub>	$cm^3/mol$	16.3
$\Delta H_{CO_2}$	Reaction Enthalpy of CO oxidation	kJ/mol	-283.0
$\Delta H_{H_2O}$	Reaction Enthalpy of H <sub>2</sub> oxidation	kJ/mol	-241.8

# Bibliography

- [1] P.W. Atkins. *Physikalische Chemie (in German)*. VCH Verlagsgesellschaft, Weinheim, 1st (German) edition, 1988. [34](#)
- [2] T.S. Auckenthaler, C.H. Onder, and H.P. Geering. Modelling of a Solid-Electrolyte Oxygen Sensor, *SAE paper 2002-01-1293*, 2002. [28](#), [59](#)
- [3] T.S. Auckenthaler, C.H. Onder, and H.P. Geering. Aspects of dynamic Three-Way Catalyst behaviour including oxygen storage. In *4th IFAC Symposium on Advances in Automotive Control, paper 122*, Salerno, Italy, 2004. [103](#)
- [4] T.S. Auckenthaler, C.H. Onder, and H.P. Geering. Online Estimation of the Oxygen Storage Level of a Three-Way Catalyst, *SAE paper 2004-01-0525*, 2004. [28](#), [84](#)
- [5] T.S. Auckenthaler, C.H. Onder, H.P. Geering, and J. Frauhammer. Modeling of a Three-Way Catalytic Converter with Respect to Fast Transients of  $\lambda$ -Sensor Relevant Exhaust Gas Components. *Ind. Eng. Chem. Res.*, 43:4780, 2004. [29](#)
- [6] M. Balenovic. *Modeling and Model-Based Control of a Three-Way Catalytic Converter*. PhD thesis, Technical University of Eindhoven, 2002. [25](#), [30](#), [36](#), [37](#), [56](#), [84](#), [131](#)
- [7] M. Balenovic, T. Backx, and T. de Bie. Development of a Model-Based Controller for a Three-Way Catalytic Converter, *SAE paper 2002-01-0475*, 2002. [131](#), [133](#), [136](#)
- [8] S. Baltisberger. *Entwicklung eines NO-Messgeräts zur arbeitsspielauf-lösenden Abgasanalyse an Verbrennungsmotoren (in German)*. Diss. ETH No. 11593, ETH Zürich, 1996. [18](#)
- [9] H. Bauer. *Kraftfahrtechnisches Taschenbuch (in German)*, Robert Bosch GmbH. Vieweg, Braunschweig, 23rd edition, 1999. [4](#), [5](#), [6](#), [9](#)

- [10] D.D. Beck and J.W. Sommers. Impact of Sulfur on Three-Way Catalysts: Comparison of Commercially produced Pd and Pt-Rh Monoliths. In A. Frennet and J.-M. Bastin, editors, *Catalysis and Automotive Pollution Control III*, volume 96, Brussels, 1995. 37, 39
- [11] B.I. Bertelsen. The U.S. Motor Vehicle Emission Control Programme. *Platinum Metals Review*, 45(2):50–59, 2001. 4
- [12] J. Birk. *Rechnergestützte Analyse und Lösung nichtlinearer Beobachtungsaufgaben (in German)*. PhD thesis, Universität Stuttgart, 1992. 122, 123
- [13] G.C. Bond and R.H. Cunningham. Alkane Transformations in Supported Platinum Catalysts. *Journal of Catalysis*, 166:172–185, 1997. 37
- [14] J.W. Bozek, R. Evans, C.D. Tyree, and K.L. Zerafa. Operating Characteristics of Zirconia Galvanic Cells (Lambda Sensors) in Automotive Closed-Loop Emission Control Systems, *SAE paper 920289*, 1992. 59, 69, 92
- [15] A. D. Brailsford and E. M. Logothetis. A steady-state diffusion model for solid-state gas sensors. *Sensors and Actuators, B: Chemical*, 7:39–67, 1985.
- [16] A. D. Brailsford and E. M. Logothetis. Selected aspects of gas sensing. *Sensors and Actuators, B: Chemical*, 52(1-2):195–203, 1998. 59
- [17] A. D. Brailsford, E. M. Logothetis, M. Yussouff, and J.T. Woestman. Estimation of the Switch Point of an Exhaust Gas Oxygen Sensor in General Exhaust Environments, *SAE paper 950531*, 1995.
- [18] A. D. Brailsford, M. Yussouff, and E. M. Logothetis. Theory of gas sensors. *Sensors and Actuators, B: Chemical*, pages 135–138, 1993. 68, 69
- [19] A. D. Brailsford, M. Yussouff, and E. M. Logothetis. Steady state model of electrochemical gas sensors with multiple reactions. *Sensors and Actuators, B: Chemical*, B 35-36:392–397, 1996. 68, 69
- [20] A. D. Brailsford, M. Yussouff, and E. M. Logothetis. Theory of gas sensors: Response of an electrochemical sensor to multi-component gas mixtures. *Sensors and Actuators, B: Chemical*, B 34:407–411, 1996.



- [21] A. D. Brailsford, M. Yussouff, and E. M. Logothetis. First-principles model of the zirconia oxygen sensor. *Sensors and Actuators, B: Chemical*, B 44:321–326, 1997. 59
- [22] A. D. Brailsford, M. Yussouff, E. M. Logothetis, and M. Shane. Steady-state model of a zirconia oxygen sensor in a simple gas mixture. *Sensors and Actuators, B: Chemical*, B 24-25:362–365, 1995.
- [23] E.P. Brandt, Y. Wang, and J.W. Grizzle. Dynamic Modeling of a Three-Way Catalyst for SI Engine Exhaust Emission Control. *IEEE Transactions on Control Systems Technology*, 8(5):767–776, 2000. 84
- [24] T. Bunluesin, R.J. Gorte, and G.W. Graham. Studies of the water-gas-shift reaction on ceria-supported Pt, Pd, and Rh: implications for oxygen-storage properties. *Applied Catalysis B: Environmental*, 15:107–114, 1998. 37
- [25] R. Burch and T.C. Watling. Kinetics and Mechanism of the Reduction of NO by C<sub>3</sub>H<sub>8</sub> over Pt/Al<sub>2</sub>O<sub>3</sub> under Lean-Burn Conditions. *Journal of Catalysis*, 169:45–54, 1997. 37
- [26] J.B. Burl. *Linear Optimal Control: H<sub>2</sub> and H<sub>∞</sub> methods*. Addison Wesley Longman, Inc., Menlo Park, CA, 1999. 142, 143, 146
- [27] Cambustion. HFR400 Fast FID, Quick User Guide (V1.1), 1997. 19
- [28] Cambustion. fNO<sub>x</sub>400 Fast Response NO Measurement System, Reference Manual, 1999. 19
- [29] B. Campbell, R. Farrington, G. Inman, S. Dinsdale, D. Gregory, D. Eade, and J. Kisenyi. Improved Three-Way Catalyst Performance Using an Active Bias Control Regeneration System, *SAE paper 2000-01-0499*, 2000. 36, 39
- [30] M. Carriero, M. Miorali, and C. Gommelini. Poisoning of Lambda Sensor: An Experimental Method to Measure the Lambda Sensor Switch Velocity and Its Effect on Air-Fuel Ratio Excursion, *SAE paper 982647*, 1998. 66
- [31] D. Chatterjee. *Detaillierte Modellierung von Abgaskatalysatoren (in German)*. PhD thesis, Ruprecht-Karls-Universität, 2001. 25, 37
- [32] C.-T. Chen. *Linear system theory and design*. Oxford University Press, New York, 1999. 123

- [33] T. Collier, C. Burgess, M. Brogan, B. Campbell, A. Finch, and K. Reavell. Measurement of Gasoline Exhaust Hydrogen Emissions, *SAE paper 2004-01-0592*, 2004. 21
- [34] R. Dictor. A Kinetic Study of the Water-Gas Shift Reaction over Rh/Al<sub>2</sub>O<sub>3</sub> Catalysts. *Journal of Catalysis*, 106:458–463, 1987. 38, 45
- [35] Dieselnet. URL: <http://www.dieselnet.com>, 2004. 4, 5, 6
- [36] J.C. Doyle and G. Stein. Robustness with Observers. *IEEE Transactions on Automatic Control*, 24(4):607–611, 1979. 143
- [37] Baker D.R. and Verbrugge M.W. Mathematical analysis of potentiometric oxygen sensors for combustion-gas streams. *AICHE Journal*, 40:1498–1514, 1994. 61, 68, 70
- [38] P. Eastwood. *Critical topics in exhaust gas aftertreatment*. Engineering Design Series. Research Studies Press Ltd., Baldock, Hertfordshire, 2000. 9
- [39] G. Fiengo, J.W. Grizzle, and J.A. Cook. Experimental Results on Dual-UEGO Active Catalyst Control. In *Advances in Automotive Control, IFAC Symposium*, Salerno, Italy, 2004. 80, 132
- [40] H.P. Geering. *Regelungstechnik, Mathematische Grundlagen, Entwurfsmethoden, Beispiele (in German)*. Springer Verlag, Berlin, 4th edition, 1996. 119, 142
- [41] H.P. Geering, C.H. Onder, C.A. Rodunder, D. Dyntar, and D. Matter. ICX-3 - A Flexible Interface Chip for Research in Engine Control. In *Proceedings of the FISITA 2002 World Automotive Congress, Paper Code FV02V315*, pages 1–4, Helsinki, 2002. 16
- [42] H. Germann, S. Tagliaferri, and H.P. Geering. Differences in Pre- and Post-Converter Lambda Sensor Characteristics, *SAE paper 960335*, 1996. 28, 80
- [43] K.S. Goto. *Solid state electrochemistry and its applications to sensors and electronic devices*, volume 45 of *Materials Science Monographs*. Elsevier BV, Amsterdam, 1st edition, 1988. 61, 68, 69
- [44] W. Göpel and H.-D. Wiemhöfer. *Statistische Thermodynamik (in German)*. Spektrum Akademischer Verlag, Heidelberg, 2000. 34

- [45] P. Granger, C. Dathy, J.J. Lecompte, L. Leclercq, M. Prigent, G. Mabilon, and G. Leclercq. Kinetics of the NO and CO Reaction over Platinum Catalysts - I. Influence of the Support. *Journal of Catalysis*, 173:304–314, 1998. 67
- [46] J.S. Hepburn and H.S. Gandhi. The Relationship Between Catalyst Hydrocarbon Efficiency and Oxygen Storage Capacity, *SAE paper 920831*, 1992. 86
- [47] J.B. Heywood. *Internal Combustion Engine Fundamentals*. Automotive Technology Series. McGraw-Hill, New York, 1988. 3
- [48] D.A. Hickman and L.D. Schmidt. Steps in CH<sub>4</sub> Oxidation on Pt and Rh Surfaces: High-Temperature Reactor Simulations. *AIChE Journal*, 39(7):1164–1177, 1993. 66, 180
- [49] Horiba. Motor Exhaust Gas Analyzer MEXA-1300FRI, Instruction Manual, 1994. 20
- [50] F.P. Incropera and D.P. DeWitt. *Fundamentals of Heat and Mass Transfer*. John Wiley & Sons, New York, 4th edition, 1996. 30, 31, 33
- [51] G.A. Ingram and S. Gopichandra. On-line Oxygen Storage Capacity Estimation of a Catalyst, *SAE paper 2003-01-1000*, 2003. 80, 108
- [52] R.A. Jackson, J.C. Peyton Jones, J. Pan, J.B. Roberts, and P.R.N. Childs. Chemical Aspects of the Dynamic Performance of a Three-Way Catalyst, *SAE paper 1999-01-0312*, 1999. 26
- [53] E. Jobson, Smedler. G., P. Malmberg, H. Bernler, O. Hjortsberg, I. Gottberg, and A. Rosén. Nitrous Oxide Formation Over Three-Way Catalyst, *SAE paper 940926*, 1994. 37
- [54] E. Jobson, O. Hjortsberg, S.L. Andersson, and I. Gottberg. Reactions Over a Double Layer Tri-Metal Three-Way Catalyst, *SAE paper 960801*, 1996. 25, 29, 35, 37, 38, 56
- [55] E. Jobson, M. Laurell, E. Högberg, H. Bernler, S. Lundgren, G. Wirmark, and G. Smedler. Deterioration of Three-Way Automotive Catalysts, Part I - Steady State and Transient Emission of Aged Catalyst, *SAE paper 930937*, 1993. 29
- [56] E.W. Kamen and J.K. Su. *Introduction to Optimal Estimation*. Advanced Textbooks in Control and Signal Processing. Springer-Verlag, London, 1999. 117

- [57] S. Klett, M. Piesche, H. Weyl, H.-M. Wiedenmann, U. Schneider, and H. Neumann. Numerical and Experimental Analysis of the 3D Flow-Pattern in Exhaust Gas Sensors, *SAE paper 2004-01-1118*, 2004. [59](#), [62](#)
- [58] G.C. Koltsakis and A.M. Stamatelos. Modeling dynamic phenomena in 3-way catalytic converters. *Chemical Engineering Science*, 54:4567–4578, 1999. [25](#)
- [59] G. Linka. *Untersuchungen zur Elektrodenkinetik der Kohlendioxid- und Sauerstoffreduktion an Spitzenelektroden auf stabilisiertem Zirkondioxid (in German)*. PhD thesis, Universität Dortmund, 1982. [68](#)
- [60] L. Ljung. *System Identification, Theory for the User*. Prentice Hall Information and System Sciences Series. Prentice Hall PTR, London, 2nd edition, 1999. [123](#)
- [61] M. Locatelli. *Modeling and Compensation of the Fuel Path Dynamics of a Spark Ignited Engine*. Diss. ETH No. 15700, ETH Zürich, 2004. [17](#)
- [62] T. Maillot, Y. Madier, R. Taha, J. Barbier Jr, and D. Duprez. Spillover of oxygen species in the steam reforming of propane on ceria-containing catalysts. *Studies in surface science and catalysis*, 112:267–275, 1997. [38](#)
- [63] E.A. Mason and A.P. Malinauskas. *Gas Transport in Porous Media: The Dusty-Gas Model*, volume 17 of *Chemical Engineering Monographs*. Elsevier, Amsterdam, 1st edition, 1983. [63](#)
- [64] Mathworks. *Optimization Toolbox User's Guide*. 2004. [40](#), [106](#), [140](#)
- [65] J. Mizusaki, K. Amano, S. Yamauchi, and K. Fueki. Electrode reaction at Pt, O<sub>2</sub>(g)/stabilized zirconia interfaces. Part I: Theoretical consideration of reaction model. *Solid State Ionics*, 22:323–330, 1987. [68](#), [71](#)
- [66] J. Mizusaki, K. Amano, S. Yamauchi, and Kazuo Fueki. Electrode reaction at Pt, O<sub>2</sub>(g)/stabilized zirconia interfaces. Part II: Electrochemical measurements and analysis. *Solid State Ionics*, 22:323–330, 1987. [71](#)
- [67] J. Mizusaki, T. Hiroaki, I. Kensuke, M. Tajika, I. Koshiro, H. Maruyama, and H. Katsuhiko. Kinetics of the electrode reaction at the H<sub>2</sub>-H<sub>2</sub>O porous Pt/stabilized zirconia interface. *J. Electrochem. Soc.*, 141(6):1674–1683, 1994. [68](#), [71](#), [72](#), [73](#), [181](#)

- [68] J. Mizusaki, H. Tagawa, Y. Miyaki, S. Yamauchi, K. Fueki, I. Koshiro, and K. Hirano. Kinetics of the electrode reaction at the CO-CO<sub>2</sub>, porous Pt/stabilized zirconia interface. *Solid State Ionics*, 53-56:126–134, 1992. 68, 71
- [69] A. Mizutani, T. Okawa, H. Matsuzaki, H. Kubota, and S. Hosogai. Oxygen Sensor For CNG Application As ULEV or Tighter Emission Vehicle, *SAE paper 980264*, 1998. 62
- [70] D.R. Monroe, M.H. Krueger, D.D. Beck, and M.J. D’Aniello Jr. The effect of sulfur on three-way catalysts. In A. Crucq, editor, *Catalysis and automotive pollution control II*, volume 71, Brussels, Belgium, 1990. Elsevier. 39
- [71] A.J.L. Nievergeld. *Automotive exhaust gas conversion: reaction kinetics, reactor modelling and control*. PhD thesis, Techn. Univ. Eindhoven, 1998. 67, 180
- [72] U. Nowak, J. Frauhammer, and U. Nieken. A fully adaptive algorithm for parabolic partial differential equations in one space dimension. *Comput. Chem. Eng.*, 20(5):547–561, 1996. 39
- [73] C.H. Onder. *Modellbasierte Optimierung der Steuerung und Regelung eines Automobilmotors (in German)*. Diss. ETH No. 10323, ETH Zürich, 1993. 15, 59, 92
- [74] C.H. Onder, C.A. Rodunder, and H.P. Geering. Model Identification for the A/F Path of an SI Engine, *SAE paper 970612*, 1997. 74
- [75] S. Onuma, A. Kaimai, K. Kawamura, Y. Nigara, T. Kawada, J. Mizusaki, H. Inaba, and H. Tagawa. Electrochemical Oxidation in a CH<sub>4</sub>-H<sub>2</sub>O System at the Interface of a Pt Electrode and Y<sub>2</sub>O<sub>3</sub>-Stabilized ZrO<sub>2</sub> Electrolyte. *J. Electrochem. Soc.*, 145(3):920 – 925, 1998. 71, 73, 181
- [76] S. Onuma, A. Kaimai, K. Kawamura, Y. Nigara, T. Kawada, J. Mizusaki, and H. Tagawa. Influence of the coexisting gases on the electrochemical reaction rates between 873 and 1173 K in a CH<sub>4</sub>-H<sub>2</sub>O/Pt/YSZ system. *Solid State Ionics*, 132:309–331, 2000. 66, 71, 72, 73
- [77] G.A. Papapolymerou and L.D. Schmidt. Unimolecular Reactions of NO, N<sub>2</sub>O, NO<sub>2</sub>, and NH<sub>3</sub> on Rh and Pt. *Langmuir*, 1:488–495, 1985. 67, 180
- [78] K.N. Pattas, A.M. Stamatelos, P.K. Pistikopoulos, G.C. Koltsakis, P.A. Konstantinidis, E. Volpi, and E. Leveroni. Transient Modeling of 3-Way Catalytic Converters, *SAE paper 940934*, 1994. 25

- [79] J.C. Peyton Jones and R.A. Jackson. Potential and pitfalls in the use of dual exhaust gas oxygen sensors for three-way catalyst monitoring and control. *IMEchE Proceedings, Part D: Journal of Automobile Engineering*, 217:475–487, 2003. 29, 59, 80
- [80] J.C. Peyton Jones, R.A. Jackson, and J.B. Roberts. The Importance of Reversible Deactivation Dynamics for On-Board Catalyst Control and OBD Systems, *SAE paper 2002-01-0067*, 2002. 84
- [81] J.C. Peyton Jones, R.A. Jackson, J.B. Roberts, and P. Bernard. A Simplified Model for the Dynamics of a Three-Way Catalytic Converter, *SAE paper 2000-01-0652*, 2000. 84
- [82] S.F. Potamianou and K.A.Th. Thoma. A study of ion transport in zirconia through computer modeling. *Solid State Ionics*, 71/72:533–536, 1994. 61
- [83] W.H. Press, S.A. Teukolsky, William T. Vetterling, and Brian P. Flannery. *Numerical Recipes in C*. Cambridge University Press, New York, 2nd edition, 1992. 40, 125
- [84] R.C. Reid, J.M. Prausnitz, and B.E. Poling. *The properties of gases and liquids*. McGraw-Hill, New York, 4th edition, 1986. 31, 63
- [85] N.L. Robertson and J.N. Michaels. Oxygen Exchange on Platinum Electrodes in Zirconia Cells: Location of Electrochemical Reaction Sites. *J. Electrochem. Soc.*, 137(1):129–135, 1990. 68
- [86] C.A. Roduner, C.H. Onder, and H.P. Geering. Automated design of an air/fuel controller for an SI engine considering the three-way catalytic converter in the  $H_\infty$  approach. In *5th IEEE Mediterranean Conference on Control and Systems*, pages 1–7, Cyprus, 1997. 9, 17
- [87] T. Schmitz, D. Hassel, and F.-J. Weber. Zusammensetzung der Kohlenwasserstoffe im Abgas unterschiedlicher Fahrzeugkonzepte (in German). Technical Report Jül-3646, Forschungszentrum Jülich, 1999. 62
- [88] E. Shafai. *Fahrzeugemulation an einem dynamischen Verbrennungsmotor-Prüfstand* (in German). Diss. ETH No. 9080, ETH Zürich, 1990. 15
- [89] E. Shafai, C. Roduner, and H.P. Geering. Indirect adaptive control of a three-way catalyst, *SAE paper 961038*, 1996. 84, 131

- [90] M. Shelef and R. W. McCabe. Twenty-five years after introduction of automotive catalysts: what next? *Catalysis today*, 62:35–50, 2000. 4, 9
- [91] S. Skogestad and I. Postlethwaite. *Multivariable Feedback Control, Analysis and Design*. John Wiley & Sons Ltd., Chichester, UK., 1<sup>st</sup> edition, 1996. 142, 146
- [92] J. Slotine and W. Li. *Applied Nonlinear Control*. Prentice Hall, Englewood Cliffs, New Jersey, 1991. 123
- [93] G. Smedler, S. Eriksson, M. Lindblad, H. Bernler, S. Lundgren, and E. Jobson. Deterioration of Three-Way Automotive Catalysts, Part II - Oxygen Storage Capacity at Exhaust Conditions, *SAE paper 930944*, 1993. 29
- [94] K.J. Åström and B. Wittenmark. *Adaptive Control*. Addison-Wesley, New York, 1995. 123
- [95] A. Trovarelli. *Catalysis by Ceria and Related Materials*, volume 2 of *Catalytic Science Series*. Imperial College Press, London, 2002. 9, 36, 37
- [96] Pfeiffer Vacuum. Massenspektrometer 2002-2004, brochure (in German), 2002. 21
- [97] R. Van Basshuysen and F. Schäfer. *Handbuch Verbrennungsmotor, Grundlagen, Komponenten, Systeme, Perspektiven (in German)*. Vieweg Verlag, Braunschweig, 2nd edition, 2002. 124, 132
- [98] M. Weibel, F. Garin, P. Bernhardt, G. Maire, and M. Prigent. Influence of water in the activity of catalytic converters. In A. Crucq, editor, *Catalysis and Automotive Pollution Control II*, volume 71, Brussels, 1990. 38, 45
- [99] G. Welch and G. Bishop. An Introduction to the Kalman Filter, URL:[http://www.cs.unc.edu/~welch/media/pdf/kalman\\_intro.pdf](http://www.cs.unc.edu/~welch/media/pdf/kalman_intro.pdf), 2004. 117, 118
- [100] W.R. Williams, C.M. Marks, and L.D. Schmidt. Steps in the Reaction  $\text{H}_2 + \text{O}_2 \leftrightarrow \text{H}_2\text{O}$  on Pt: OH Desorption at High Temperature. *J. Phys. Chem.*, 96:5922–5931, 1992. 67
- [101] J.T. Woestman, A.D. Brailsford, M. Shane, and E.M. Logothetis. A model of the transient response of mass-transfer limited gas sensors. *Sensors and Actuators B*, 45:27–33, 1997.

## *Bibliography*

- [102] P. Zarchan and H. Musoff. *Fundamentals of Kalman Filtering*, volume 190 of *Progress in Astronautics and Aeronautics*. AIAA American Institute of Astronautics and Aeronautics, 2000. [117](#), [125](#)



# Curriculum Vitae

## Personal Data

Name: Theophil Sebastian Auckenthaler  
Date of birth: March 21, 1970  
Parents: Jörg Auckenthaler and Dorothea Auckenthaler-Hauser

## Education

1977–1983 Primary school in Küsnacht ZH, Switzerland  
1983–1989 Gymnasium in Zürich, Switzerland  
1989 Matura, typus B  
1990–1997 Studies in mechanical engineering, Swiss Federal Institute of Technology (ETH) Zurich, Switzerland  
Main subjects Automatic Control and Fluid Mechanics  
1997 Diploma as *Dipl. Masch.-Ing. ETH*  
1999–2005 Doctoral student and research assistant at the Measurement and Control Laboratory, Swiss Federal Institute of Technology (ETH) Zürich, Switzerland

## Professional Experience

1997-1999 Development Engineer, ABB Power Generation, Baden, Switzerland